

Magnetic soft mode behaviour investigated
via Multi-Spin Flip Raman Spectroscopy on
near surface $\text{Cd}_{1-x}\text{Mn}_x\text{Te}/\text{Cd}_{1-y}\text{Mg}_y\text{Te}$
Quantum wells



Dissertation zur Erlangung des
naturwissenschaftlichen Doktorgrades
der Julius-Maximilians-Universität Würzburg

vorgelegt von
Christian Kehl
aus Werneck

Würzburg, 2010

Eingereicht am: 02. Dezember 2010
bei der Fakultät für Physik und Astronomie

1. Gutachter: Prof. Dr. J. Geurts
2. Gutachter: Prof. Dr. W. Ossau
der Dissertation

1. Prüfer: Prof. Dr. J. Geurts
2. Prüfer: Prof. Dr. W. Ossau
3. Prüfer: Prof. Dr. W. Kinzel
im Promotionskolloquium

Tag des Promotionskolloquiums: 28. März 2011

Doktorurkunde ausgehändigt am:

für meine Eltern und Großeltern

Contents

1	Introduction	1
2	Theory and Basics	5
2.1	Cd(Mn)Te Properties	5
2.1.1	CdTe	5
2.1.2	CdMnTe	8
2.2	Semimag. Semiconductors	9
2.2.1	Mn states	9
2.2.2	Magnetization	10
2.2.3	Exchange interaction among Mn-ions	11
2.2.4	s/p-d exchange interaction	13
2.3	Quantum Well	18
2.3.1	CdMnTe/CdMgTe Quantum Well	18
2.3.2	Magnetic anisotropy of the valence band	25
2.3.3	The limit: Total Anisotropy	30
2.4	Theory of Multi-SFRS	32
2.4.1	Raman spectroscopy	32
2.4.2	Macroscopic view	33
2.4.3	Microscopic view	34
2.4.4	PR Raman scattering	36
2.4.5	Multi-PR Raman scattering	39
2.5	Kavokin's theory	43
3	Setup and samples	51
3.1	Two-Colour experiment	51
3.2	QW samples	53
4	Results: 030807A-I	55
4.1	PL - characteristics -	55
4.1.1	Identification of PL-signals	55
4.1.2	Below-barrier excitation	61
4.1.3	Above-barrier excitation	66
4.1.4	Two-colour excitation	68
4.1.5	Conclusion of the PL behaviour	69
4.2	Influencing the Mn-g-factor	70
4.2.1	Mn-g-factor determination	70
4.2.2	Varying above-barrier excitation	71

4.2.3	Dependence on B-field	74
4.2.4	Temperature dependence aspect	75
5	Magnetic soft mode	77
6	Cap impact	83
6.1	13nm cap	83
6.2	15nm cap	89
6.3	17nm cap	93
6.4	19nm cap	97
6.5	Conclusion of 031709BI-IV	100
7	Discussion PL	105
8	Summary	115
9	Zusammenfassung	119
10	Indices	123
	Bibliography	133
	List of pictures	137
	List of tables	139
A	Phys. & math. add-ons	141
A.1	k p theory	141
A.2	BRILLOUIN function and band splitting	143
A.3	Magnetic polaron in 2D in its exchange field	145
A.4	Bloch equations	148
A.5	Auxiliary calculations	149
	A.5.1 Differential equation	149
	A.5.2 Stationary State	151
A.6	QW Exciton spins in an external B-field	152
B	Formality	153

Chapter 1

Introduction

"Smaller, faster, cheaper" are the keywords for the development of data storage media in the chip-producing industries for more than twenty years. Latest fashioned and promising for discovering a new way of data storage is spintronics. This is a branch of science and technology which employs both the charge and the spin of the carrier (electron). This requires materials which exhibit both ferromagnetic and semiconductor properties in order to combine permanent (i.e. stable and non-vanishing) magnetic storage and the conventional electronics of semiconductors in one device [ZLR10].

Basic research was required on low-dimensional semiconductor heterostructures with the most recent focus on nonmagnetic semiconductor host materials that can be partially substituted by a small amount of transition-metal ions like Mn^{2+} and Co^{2+} that promote magnetism.

These studies triggered the ongoing discussion about a carrier-induced ferromagnetic phase transition in diluted-magnetic II-VI semiconductors (DMS) through RKKY--interaction [HWA⁺97]. In this context theoretical studies on the coherent dynamics of localized spins (e.g.: Mn-ions) coupled with a two-dimensional hole gas (2DHG) in DMS QWs was done by K.V. KAVOKIN [Kav99]. His main result is the time evolution of the (Mn^{2+}) spin system in an in-plane magnetic field affected by a 2DHG, resulting in the reduction of its Larmor frequency and thus of the Mn-g-factor under the influence of an oscillating effective field of holes. This is called magnetic soft mode behaviour [KAK⁺09].

The experimental access to the Mn-g-factor is Multi-Spin-Flip Raman scattering, also called Multi-Paramagnetic-Resonance (PR) Raman scattering. A lot of research was done on this method by resonantly exciting Mn^{2+} -ions in $\text{Cd}_{1-x}\text{Mn}_x\text{Te}$ QW structures embedded in $\text{Cd}_{1-y}\text{Mg}_y\text{Te}$ in the 1990th by STÜHLER et al [SHSW94], [SSD⁺95], [SSD⁺96], [Stü95].

This research status is the motivation for this thesis, using Multi-PR Raman spectroscopy in this thesis under the new aspect of embedding a $\text{Cd}_{1-x}\text{Mn}_x\text{Te} / \text{Cd}_{1-y}\text{Mg}_y\text{Te}$ QW close to the surface resulting in a near-surface-induced p-doping of the QW. Moreover, the hole concentration in the QW is tuned by photo-generated carriers through above-barrier laser illumination. Simultaneously, Multi-PR Raman scattering is induced by resonant QW-excitation. In these two-colour experiments the carrier influence on the Mn-g-factor is probed. The result is the influence of the Multi-PR signals

by photo-generated carrier (holes) using a two-colour experiment i.e. one light source exciting above and one resonantly below the QW barrier.

Figure 1.1 gives an overview of the new aspects done in this thesis (red) and the already existing research procedure by STÜHLER et al (black).

For the experiment a resonant monochromatic light source is needed to serve as

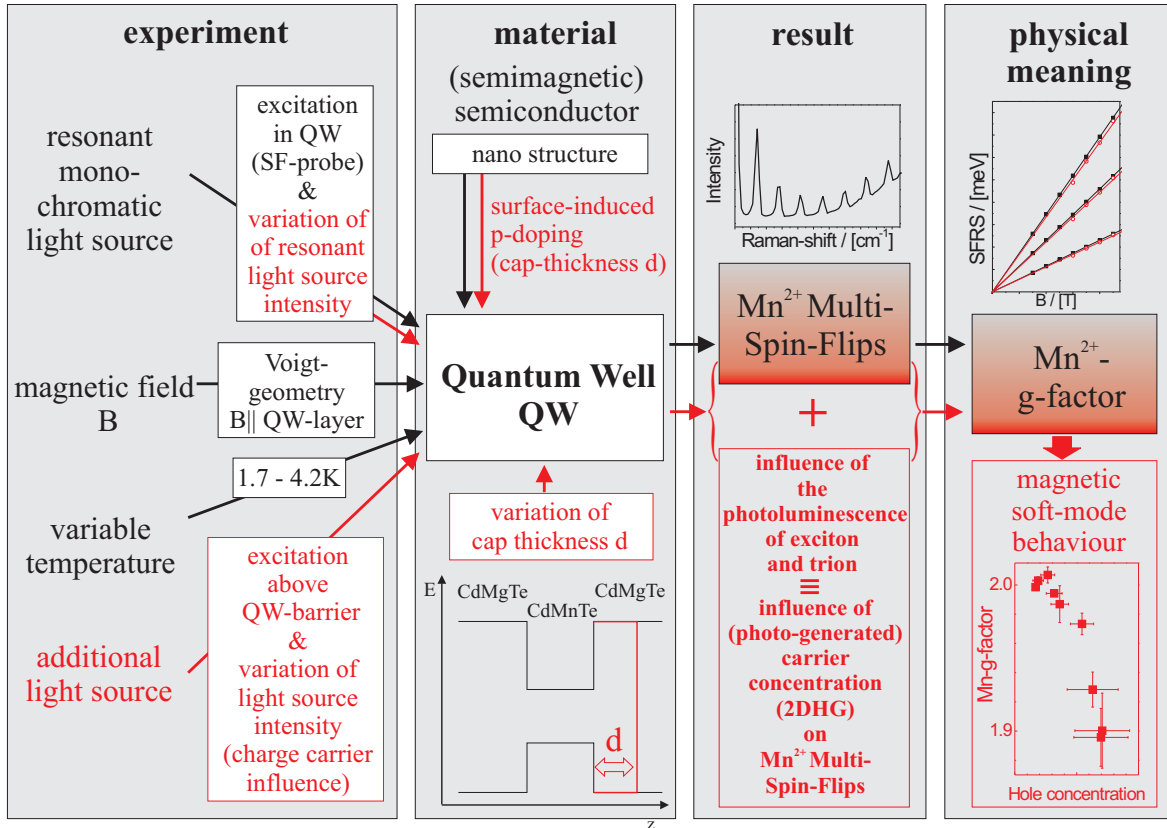


Figure 1.1: Chart of the main research blocks used for achieving the interesting results in this thesis. The first blocks present the requirements to both the experiment and the material for observing and investigating the Multi-Spin-Flip signals in general (black). The additional requirements for observing the soft mode behaviour via Multi-Spin Flip Raman spectroscopy are marked red.

a probe for the Multi-Spin Flips which appear at small temperatures (here: 1.7 - 4.2K) and in an applied magnetic field perpendicular to the growth direction (z) of the semimagnetic QW. The two-dimensional hole gas (2DHG) in the QW is induced by embedding the QW close to the surface (cap layer thickness: 13-19nm) resulting in a near-surface induced p-doping of the QW. This 2DHG and thus the hole concentration is mainly influenced by varying the illumination intensity from above barrier causing photo-generated carriers. Using two light sources which excite below and above barrier (two-colour excitation) in a tuneable external magnetic field gives access to the investigation of the Mn²⁺ Multi-Spin Flips under the influence of varying the concentration of a 2DHG. The physical meaning of the Multi-SF signals in an external magnetic field can be summarised in the Mn-g-factor (gradient of Spin Flip Raman signal: SFRS vs. B-field). The Mn-g-factor is reduced under the influence of the 2DHG. This is called

magnetic soft mode behaviour which was theoretically predicted by K.V. KAVOKIN [Kav99]. The experimental confirmation of these theoretical predictions is the main content in this thesis.

According to these theoretical predictions, the aim of the present thesis is to investigate the magnetic soft mode behaviour of the Mn-g-factor influenced by a varying 2DHG in near-surface doped $\text{Cd}_{1-x}\text{Mn}_x\text{Te}/\text{Cd}_{1-y}\text{Mg}_y\text{Te}$ QW samples. The thesis falls into the following categories. The theoretical and basic background is given in **Chapter 2** starting with the lattice and electronic properties of the host material CdTe. The next section points out the meaning of the partial substitution of Mn-ions in CdTe and its effects on the magnetization of CdMnTe, the exchange interaction of neighboured Mn-ions and the s/p-d exchange interaction of its conduction band and valence band, respectively. This is followed by the description of the semimagnetic quantum well states ($\text{Cd}_{1-x}\text{Mn}_x\text{Te} / \text{Cd}_{1-y}\text{Mg}_y\text{Te}$) and its resulting magnetic anisotropy of the heavy hole valence band. After that, a brief introduction into the macroscopic and microscopic theoretical description of Raman spectroscopy is given, followed by the criteria for observing paramagnetic and Multi-paramagnetic Raman scattering.

Chapter 3 describes the experimental setup and how the QW samples are investigated using the two-colour illumination. The structure of the samples and their parameters are briefly summarised in the same chapter.

The characteristic properties of these samples are representatively discussed in detail using the sample with a well width of 12.0nm and a cap thickness of 17.5nm (030807A-I) in **Chapter 4**. In the first section the PL-signals are identified. Then, the PL-behaviour is investigated under the influence of varying below-barrier, above-barrier and two-colour excitation power. With this knowledge the Mn-g-factor is influenced using the two-colour excitation in an external magnetic field perpendicular to the growth direction in the next section. The below-barrier excitation serves as a probe for the Multi-PR signals, while the above-barrier excitation is responsible for the main influence of the 2DHG. Furthermore the procedure of the Mn-g-factor determination, the dependence of the Mn-g-factor on the varying above-barrier illumination and the external B-field is discussed in this section followed by its temperature dependence. The interpretation of these observations takes place in **Chapter 5** based on the theoretical predictions and calculations of K.V. KAVOKIN [Kav99] [KAK⁺09]. Accentuating that this thesis presents the experimental confirmation of the theoretical predicted *magnetic soft mode behaviour* is the main content of this chapter.

Four samples with a well width of 10.0nm each and different cap layer thicknesses of 13.0-19.0nm (031709B-I-IV) are investigated under the influence of varying cap thickness on the PL-behaviour (i.e. on the 2DHG) and on the Mn-g-factor in **Chapter 6**. The results of these investigations based on the observed PL-behaviour are discussed and interpreted in **Chapter 7** under the aspect of near-surface doping of the QW and tunnelling processes to the surface.

Finally, a summary pointing out the main results and interpretations of the magnetic soft mode behaviour in near-surface located CdMnTe/CdMgTe QWs is given in **Chapter 8**.

Chapter 2

Theory and Basics

2.1 Properties of CdTe and CdMnTe

2.1.1 Base material CdTe

Crystal structure Semiconductor heterostructures based on the binary II-VI semiconductor CdTe are investigated in this thesis. Like most of the II-VI semiconductors CdTe has a zinc blende crystal structure as shown in Figure 2.1

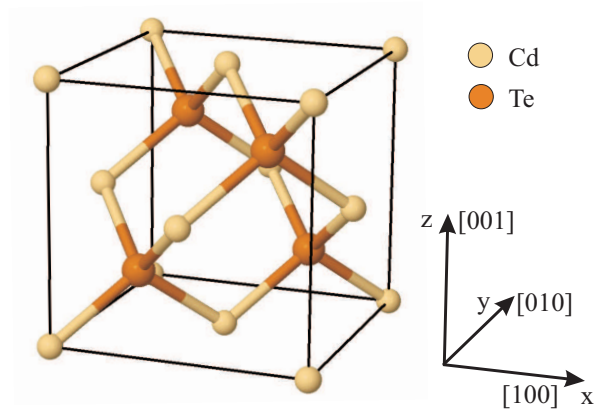


Figure 2.1: Unit cell of a zinc blende CdTe crystal [ope08]. There is no inversion centre due to point group symmetry T_d [DDJ08].

This structure consist of two face-centred cubic cationic and anionic lattices, respectively which are displaced by a $(\frac{1}{4}, \frac{1}{4}, \frac{1}{4})$ of the unit cell diagonal. Each ion (Cd and Te respectively) has four nearest neighbours of the opposite binding partner in a tetrahedral geometry. The nearest neighbour distance in this zinc blende structure is $\frac{\sqrt{3}}{4}a$ with a as the lattice constant.

The chemical bond of II-VI semiconductors takes place between the s-electron of the cation (Cd) and the p-electron of the anion (Te) of neighboured ions¹ i.e. a sp^3 hy-

¹electronic configuration of the atoms: Cd $4d^{10}5s^2$ and Te $4d^{10}5s^2p^4$

bridisation of the electron states with four equivalent orbitals in tetrahedral order. The bonding sp^3 states in the crystal constitute the valence band, while the conduction band originates from their antibonding counterpart. Due to different electronegativity of the involved ions, the sp^3 -hybrid atomic orbital has a partial ionic character. The lattice constant of CdTe is $a = 6.486 \text{ \AA}$ (at 300K) [RNPZ74] and thus the $Cd-Te$ bond length is 2.809 \AA .

Electronic band structure The band structure of CdTe is shown in Figure 2.2. CdTe has its fundamental band gap E_g at the Brillouin zone centre at the Γ -point and is thus a direct band gap semiconductor. Most optical emissions in this thesis take place close to $k = 0$ at the Γ -point. The energetically lowest conduction band of a zinc blende

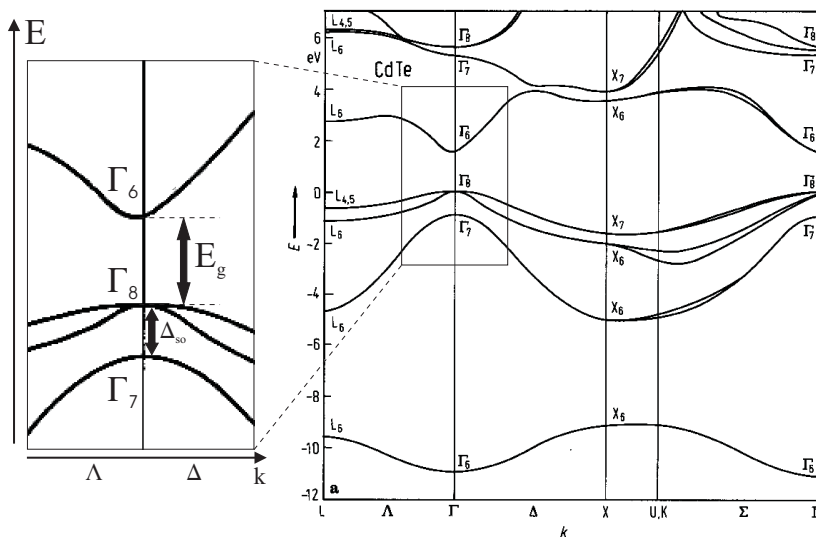


Figure 2.2: Nonlocal pseudo potential calculations for the electronic structure of CdTe [CC76]. The left hand side shows to larger scale the relevant part of the whole band structure. The band gap energy $E_0 = E_g = 1.605 \text{ eV}$ at 4.2K. $\Delta_{so} = 0.938 \text{ eV}$ is the split-off energy of Γ_7 - and Γ_8 , due to the spin-orbit exchange interaction. The k -space directions are defined as follows: $X = (001)$, $K = (110)$ and $L = (111)$ according to [CC76].

crystal is formed by anti-binding molecular σ -orbital. The electronic states of this s-like Γ_6 - conduction band² are twice spin-degenerated with a total angular momentum of $1/2$. In contrast to the conduction band, the energetically highest valence band plays the role of the binding molecular π -orbital which mainly stems from p-like atomic orbitals. Therefore the orbital overlap among the crystal atoms is increased [YC01]. These valence band states split off at $k = 0$ into a Γ_8 -quadruple and Γ_7 -duplet. The total angular momentum of the quadruple and the duplet is $J = 3/2$ and $J = 1/2$, respectively ($L=1$ and $S=1/2$). This split-off energy Δ_{so} at $k = 0$ is shown in Figure 2.2 and is caused by spin-orbit exchange interaction. For the case $k \neq 0$ the Γ_8 -valence band splits into two branches with different band curvature. Due to their different effective masses these two branches are called light hole (LH) band and heavy hole

²the nomenclature of the bands is due to symmetry properties in group theory

(HH) band with the z-component of the total angular momentum $m_J = \pm 1/2$ and $m_J = \pm 3/2$, respectively. The band gap of CdTe bulk material is 1.606eV [Fur88] (calculated: 1.605eV [CC76]) at 4.2K and at room temperature 1.528eV [Fur88].

Due to the s-like electron wave function the energy dispersion of the Γ_6 -band near the Γ -point ($\vec{k} = 0$) can be approximately described by an isotropic and parabolic relation

$$E^{CB} = E_g + \frac{\hbar^2 k^2}{2m_e^*} \quad (2.1)$$

where m_e^* is the effective mass of the crystal electron.

Now the focus lies on the p-like Γ_8 -valence band which is energetically above the Γ_7 -band (split-off band). Due to this relatively large energetic distance of these two bands the Γ_7 -band is neglected for further analytical descriptions of the experimental results. This approximation leads back to the Luttinger model [LK55] [Lut56].

According to LUTTINGER [Lut56] the energy momentum operator of a hole in the Γ_8 -band is:

$$H^{VB} = \frac{\hbar^2}{2m_0} \left[\left(\gamma_1 + \frac{5}{2}\gamma_2 \right) \vec{\nabla}^2 - 2\gamma_3 \left(\vec{J}\vec{\nabla} \right)^2 + 2(\gamma_3 - \gamma_2) \left(\nabla_x^2 J_x^2 + \nabla_y^2 J_y^2 + \nabla_z^2 J_z^2 \right) \right] \quad (2.2)$$

with Kohn-Luttinger parameter for CdTe $\gamma_1 = 4.118$, $\gamma_2 = 1.0810$, $\gamma_3 = 1.9515$ [NNL88] and the 4×4 matrices of the total momentum J_x, J_y, J_z .

The x-, y-, and z-axis coincide with the crystallographic axes [Dya08]. The first terms in (2.2) have spherical/parabolic symmetry. By contrast the last term makes the iso-energetic surfaces of the light and heavy holes anisotropic, i.e. the energy branches do not have a simple parabolic form (Warping-Term) [Dya08]. Compared to [Lut56], equation (2.2) is presented here without the influence of an external magnetic field. Introduced by LUTTINGER [Lut56] the fourfold degenerated states of the valence band can be described in the frame work of the degenerated perturbation theory in the following 4×4 matrices of the total momentum components³:

$$J_x = \begin{pmatrix} 0 & \sqrt{3}/2 & 0 & 0 \\ \sqrt{3}/2 & 0 & 1 & 0 \\ 0 & 1 & 0 & \sqrt{3}/2 \\ 0 & 0 & \sqrt{3}/2 & 0 \end{pmatrix} \quad (2.3)$$

$$J_y = \begin{pmatrix} 0 & i\sqrt{3}/2 & 0 & 0 \\ -i\sqrt{3}/2 & 0 & i & 0 \\ 0 & -i & 0 & i\sqrt{3}/2 \\ 0 & 0 & -i\sqrt{3}/2 & 0 \end{pmatrix} \quad (2.4)$$

$$J_z = \begin{pmatrix} 3/2 & 0 & 0 & 0 \\ 0 & 1/2 & 0 & 0 \\ 0 & 0 & -1/2 & 0 \\ 0 & 0 & 0 & -3/2 \end{pmatrix} \quad (2.5)$$

³canonical basis $Y_m^{3/2}$ with $m = \frac{3}{2}, \frac{1}{2}, -\frac{1}{2}, -\frac{3}{2}$

In this case the quantization axis is $\langle 001 \rangle$ coordination axis. J_x , J_y and J_z fulfill the commutation relations of the momentum components $[J_x, J_y] = iJ_z$.

These matrices will be used later on for describing the total Hamiltonian of a quantum well in an external B-field of several directions x and z in subsection 2.3.2.

2.1.2 CdMnTe

The formation of the ternary semiconductor $\text{Cd}_{1-x}\text{Mn}_x\text{Te}$ takes place by substituting the fraction x of Cd^{2+} cations by Mn^{2+} (iso-electronic configuration $(3d)^5(4s)^2$). The two $4s$ -electrons of the iso-electronic Mn are involved in the sp^3 -bond. Both the symmetry of the cubic unit cell and the translation invariancy are disturbed by this purely stochastic implantation. To get a theoretical access for band structure calculation or lattice dynamics in ternary semiconductors, the **V**irtual **C**rystal **A**pproximation (VCA) method is used as a well adapted tool. In the framework of VCA, pseudopotentials instead of the actual potentials are taken to "recover" the symmetry properties of the CdTe-crystal.

As a result the band gap E_g of mixed crystals like $\text{Cd}_{1-x}\text{Mn}_x\text{Te}$ shows approximately a linear dependence on the Mn-concentration x . CdTe as well as $\text{Cd}_{1-x}\text{Mn}_x\text{Te}$ are semiconductors with a direct band gap which increases with increasing Mn-concentration and can be described as follows [Fur88]:

$$E_g(4.2K) = (1.606 + 1.592x) \text{ eV} \quad (2.6)$$

The lattice constant of $\text{Cd}_{1-x}\text{Mn}_x\text{Te}$ decreases with increasing Mn-concentration. The decrease is proportional to x according to VEGARD's law. Thus the lattice constant of $\text{Cd}_{1-x}\text{Mn}_x\text{Te}$ is [BSG81] [RNPZ74]:

$$a = (6.486 - 0.148x) \text{ \AA} \quad (2.7)$$

This change in lattice constant is due to the smaller bond length of MnTe compared to CdTe. It should be mentioned here that $\text{Cd}_{1-x}\text{Mn}_x\text{Te}$ bulk zinc blende structure is only stable to a maximum Mn-concentration of about 77 % [Fur88]. Pure MnTe bulk material has a NiAs structure [RVV06].

The CdMnTe samples investigated in this thesis are epilayers on zinc blende due to a maximum Mn-concentration of about 1%.

2.2 Semimagnetic semiconductors

The partial substituent of the replaced group-II-element by a transition metal in a II-VI-semiconductor changes both its optical and its magnetic properties. The most applied transition metal is manganese (Mn). For a III-V-semiconductor like GaAs the built-in of Mn causes both doping properties and magnetic properties while in a II-VI-semiconductor Mn causes only magnetic properties and doping in a II-VI-material can be done separately.

2.2.1 Electronic states of manganese

Manganese is substituting the group-II element in a II-VI-semiconductor and is twofold ionized. The half-filled 3d-shell of Mn^{2+} is responsible for the semimagnetic properties of the II-VI basic material like CdTe. The $(3d)^5$ electrons are not influencing the band structure. According to HUND's rule these electrons form a ${}^6S_{5/2}$ -multiplet with $J = S = \frac{5}{2}$ in the ground state [Fur88].

Flipping of one of these spins cause an excited state of the free Mn^{2+} $S = \frac{3}{2}$ und $L \neq 0$ shown in Figure 2.3. Electronic transitions from the ground state 6S in any of the excited states are generally forbidden due to parity rules and selection rules $\Delta S = 0$. Each of these excited states is located at a higher energy than the ground state and thus they are less important in this thesis. In a crystal field where the Mn-ion interacts with its four neighbouring anions the selection rules of Mn^{2+} soften due to spin-orbit coupling and the lack of inversion symmetry of the crystal environment [Fur88]. As a consequence transitions from all excited states of the 4G state are possible. This is the reason for the internal Mn-transition seen in photoluminescence spectra at 2.2eV [Fur88]. For this transition, the band gap of the Mn containing semiconductor must be larger than 2.2eV (i.e. the Mn-content x of $Cd_{1-x}Mn_xTe$ must be $x > 0.37$ to fulfill this criterion). The ground state ${}^6S_{5/2}$ has no orbital angular momentum. Thus it is a matter of pure spin magnetism with a g-factor of 2. In an external magnetic field $B \parallel z$ the z-component of the total spin m_s splits into six equidistant spin states (compare Figure 2.3) showing a linear ZEEMAN behaviour as follows:

$$E_{PR} = m_s \cdot g_{Mn} \cdot \mu_B \cdot B \quad (2.8)$$

with the spin quantum number $m_s \in \{-\frac{5}{2}, -\frac{3}{2}, -\frac{1}{2}, \frac{1}{2}, \frac{3}{2}, \frac{5}{2}\}$ and μ_B is the BOHR magneton⁴. The magnetic field (B-field) causes a symmetry reduction of the states from T_d to S_4 .

Within this ZEEMAN sextet a spin-flip transition $\Delta m_s = 1$ with energy

$$E_{PR} = g \cdot \mu_B \cdot B \quad (2.9)$$

causes the so called paramagnetic resonance (PR) signal⁵ of Mn^{2+} . This $\Delta m_s = 1$ transition of a few hundreds of μeV (depending on the applied B-field) can be monitored in Raman spectroscopy measurements known as Spin Flip Raman Spectroscopy (SFRS)

⁴ $\mu_B = \frac{e\hbar}{2m_e}$

⁵also called EPR = electronic paramagnetic resonance signal

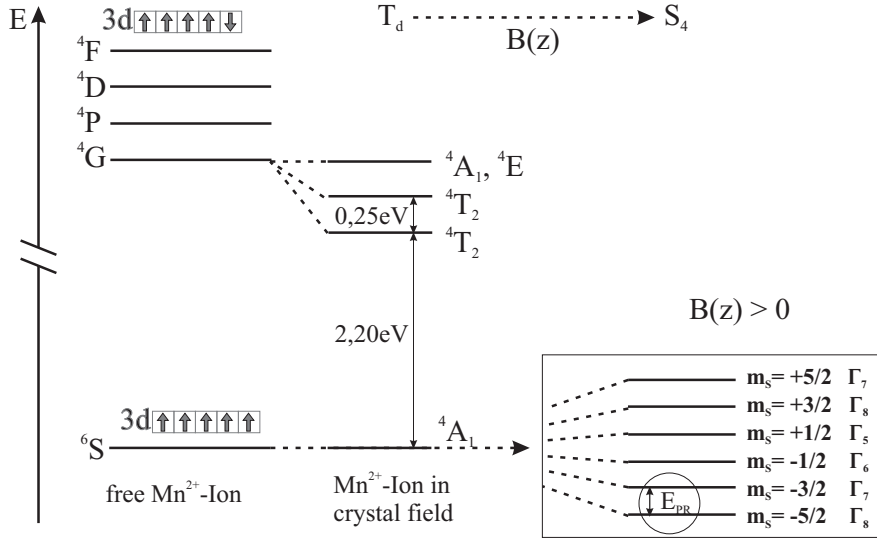


Figure 2.3: Scheme of energy states. (Left) splitting of free Mn^{2+} with spectroscopic notation $(2S+1)L$. (Middle) Mn^{2+} in crystal field (symmetry T_d). (Right) splitting of its ground state in an external B-field (symmetry S_4) [Fur88].

or Paramagnetic Resonance (PR) Raman Spectroscopy. The investigation of these PR-signals in small semimagnetic quantum wells (QW) under the influence of photo-generated carriers is one of the key issues of this thesis.

2.2.2 Magnetizations of non-interacting Mn-ions

For a Mn-concentration of about $x < 0.01$ in a ternary semiconductor compound like $\text{Cd}_{1-x}\text{Mn}_x\text{Te}$ the embedded Mn-ions are isolated from each other [Fur88]. Therefore the thermal expectation value $\langle S_z \rangle$ of the total spin z-component of an isolated Mn-ion in the ground state influenced by an external B-field B ($B \parallel z$) can be described as:

$$\langle S_z \rangle = -S \cdot \mathfrak{B}_S \left(\frac{g_{Mn} \mu_B S B}{k_B T_{Mn}} \right) \quad (2.10)$$

where

- S : Total spin of the Mn-ion $S=5/2$
- g_{Mn} : g-factor of the Mn-3d electrons
- T_{Mn} : Mn-temperature
- \mathfrak{B}_S : Brillouin function
- μ_B : BOHR magneton $\mu_B = \frac{e\hbar}{2m_e}$

The Brillouin function can be written as:

$$\mathfrak{B}_S(y) = \frac{2S+1}{2S} \coth \left(\frac{2S+1}{2S} \cdot y \right) - \frac{1}{2S} \coth \left(\frac{1}{2S} \cdot y \right) \quad (2.11)$$

Here, "y" is a function of the B-field and has its origin in the following consideration: An external B-field causes an orientation of the Mn-ions in a semimagnetic semiconductor and can be described as:

$$U_{magnetization}(B) = -\mu_{mag} \cdot B = g_{Mn} \cdot \mu_B \cdot S \cdot B \quad (\mu_{mag}: \text{magnetic moment}) \quad (2.12)$$

This order is perturbed by temperature T:

$$U_{thermal} = k_B \cdot T \quad (k_B: \text{BOLTZMANN constant}) \quad (2.13)$$

Thus the spin orientation of the Mn-ions and their total spin is dependent on these mentioned effects, describing y as follows:

$$y(B) = \frac{-U_{magnetization}(B)}{U_{thermal}} = \frac{g_{Mn} \cdot \mu_B \cdot S}{k_B \cdot T} \cdot B \quad (2.14)$$

Concluding all these basic tools the magnetization M of a semimagnetic layer containing non-interacting Mn-ions has the following equation:

$$M = xN_0g_{Mn}\mu_B \frac{5}{2} \mathfrak{B}_S \left(\frac{5}{2} \cdot \frac{g_{Mn}\mu_B B}{k_B T_{Mn}} \right) \quad (2.15)$$

N_0 is the cation density per volume and x is the ratio of Mn-occupied cation lattice sites.

2.2.3 Exchange interaction among Mn-ions

In the previous subsection the Mn-ions were expected to be isolated at $x < 0.01$. Now, dealing with Mn-concentrations $x > 0.01$ the interaction of Mn-ions with each other has to be taken into account. This interaction consists of two parts of exchange: The first and main part is the isotropic antiferromagnetic exchange of next neighbour (NN) spins, also called super exchange. The second part is the anisotropic exchange interaction with the DZYALOSHINSKY-MORIYA exchange [Dzy58] [Mor60] and the magnetic dipole-dipole exchange interaction. Both are about two orders of magnitude smaller than the isotropic exchange. Due to its very small contribution the magnetic dipole-dipole interaction can be neglected beyond.

As already mentioned the super exchange interaction is the coupling of two neighbouring Mn-ions. This coupling takes place by virtual hopping processes through the 4p orbitals of Te-Ions which are located in between the Mn-ions [LHE88] [SLT+86] and is supported by p-d hybridisation.

The coupling of two Mn-ions is antiferromagnetic and thus it reduces the thermal expectation value $\langle S_z \rangle$ of the Mn spins in the B-field. According to LARSON et al. [LE89] the total spin Hamiltonian of the "d-d exchange interaction" can be written as follows:

$$H_{d-d} = - \sum_{\alpha, \beta} \vec{S}_{1, \alpha} J_{\alpha, \beta}(\vec{R}_{12}) \vec{S}_{1, \beta} \quad (2.16)$$

$$= H_{iso} + H_{DM} \quad (2.17)$$

$\vec{S}_{1,\alpha}$ is the α -component ($\alpha = x, y, z$) of the Mn-ion spin 1 located at \vec{R}_1 and $\vec{S}_{2,\beta}$ is the β -component ($\beta = x, y, z$) of the Mn-ion spin 2 located at \vec{R}_2 , respectively. $J_{\alpha,\beta}$ is the exchange tensor and $\vec{R}_{12} = \vec{R}_1 - \vec{R}_2$ is the distance of the spins. This tensor product can be concluded to the sum of an isotropic part (H_{iso}) and an anisotropic part (H_{DM}) shown in (2.17).

The **isotropic part** is the HEISENBERG-Hamiltonian

$$H_{iso} = -J(\vec{R}_{12})\vec{S}_1\vec{S}_2 \quad (2.18)$$

with the exchange constant of the isotropic exchange interaction $J(\vec{R}_{12})$ which is equal to the exchange constant of NN spins ($J(\vec{R}_{NN})$). According to [LHEC85] the main part for $J(\vec{R}_{NN})$ with about 95% is caused by the previously discussed super exchange. $J(\vec{R}_{NN})$ for CdMnTe is calculated⁶ as -5.6K [LE89] (-7.6K [LHE88]). $J(\vec{R}_{NN})$ is negative i.e. it is an antiferromagnetic coupling. The next nearest neighbour exchange constant is also negative but is expected to be about four times smaller [LHEC85].

$J(\vec{R}_{NN})$ can also be determined experimentally either from magnetization steps in high temperature measurements of the magnetic susceptibility (explained by [Kel04] and [SLT⁺86] $J(\vec{R}_{NN}) = -6.9K$) or from the Raman shift of the " $M = 0$ "-transition ($S = 0 \rightarrow S = 1$) of antiferromagnetically coupled pairs of NN Mn-ions ([Stü95] $J(\vec{R}_{NN}) = -6.11K$).

Due to this isotropic exchange and depending on the temperature and Mn-concentration, $\text{Cd}_{1-x}\text{Mn}_x\text{Te}$ can emerge in three different magnetic phases [Fur88]:

- paramagnetic phase for low Mn-concentration x and/or high temperature
- spin-glass phase ("frozen" disorder) for $x < 65\%$ and low temperature
- antiferromagnetic phase for $x > 65\%$ and low temperature

The **anisotropic DZIALOSHINSKY-MORIYA** [Dzy58] [Mor60] **part** of the exchange interaction can be expressed for two Mn-ions in neighbouring cation sites by

$$H_{DM} = -\vec{D}(\vec{R}_{12})(\vec{S}_1 \times \vec{S}_2). \quad (2.19)$$

For CdMnTe the vector \vec{D} is perpendicular to the plane defined by the two Mn-ions and the Te-ion placed in between. For more details of the orientation of \vec{D} see [Mor60]. This exchange interaction is about one magnitude smaller than the isotropic one ($|\vec{D}| = 0.30K$ [LE89])

It results from the spin-orbit coupling which leads to an excited state of one of the neighbouring magnetic ions. Thus the ground-state ion and the excited ion interact with each other.

The anisotropic exchange interaction can cause a weakening of the selection rules. The reason is that states in which its Hamiltonian of the isotropic part is diagonal, can be mixed (i.e. off-diagonal matrix elements appear).

In conclusion, due to the formation of antiferromagnetic (af) cluster of next-neighbour (NN) Mn spins causing strong d-d exchange interaction among each other, a strongly

⁶ab initio calculations

concentration-dependent part of the Mn-spins does not contribute or only partially contribute to the magnetization of the diluted magnetic semiconductor material. Thus the primal fraction of manganese x of the ternary DMS contributing to the magnetization must be replaced by a smaller value x_{eff} ($M \propto x_{eff} \langle S^z \rangle$). The cluster formation of $\text{Cd}_{1-x}\text{Mn}_x\text{Te}$ increases with increasing x . The maximum of x_{eff} is at an actual Mn-concentration of $x = 15\%$ (corresponds to $x_{eff} \cong 6\%$ [Zeh98]).

In addition a further parameter T_0 is introduced to consider the Mn-Mn exchange interaction. It is a phenomenological fitting parameter which retards the relative fast saturation of B_S at ideal paramagnetism. This is on the one hand caused by long ranging antiferromagnetic exchange interaction among Mn-spins of next nearest neighbours and so on [BRH⁺87]. On the other hand it is caused by magnetization contributions of different Mn-cluster which do not follow the Brillouin function $\mathfrak{B}_{5/2}$. This parameter is summed up to the temperature T_{Mn} in (2.10). Later on in subsection 2.2.4 both parameters x_{eff} and T_0 are included for further considerations.

2.2.4 s/p-d exchange interaction

The exchange interaction of the localized electrons of the Mn-3d shell with the s-like conduction band and the p-like valence band is the most important property of semimagnetic semiconductors. It is responsible for the GIANT ZEEMAN effect and GIANT FARADAY effect [KG02].

To describe formally a semiconductor containing localized magnetic moments a KONDO-like exchange term H_{exch} [Liu61] is added to the original Hamiltonian H_0 [Fur88]. Thus the total Hamiltonian H_T is

$$\begin{aligned} H_T &= H_0 + H_{exch} \\ &= H_0 + \sum_i J^{sp-d}(\vec{r} - \vec{R}_i) \vec{S}_i \vec{J} \end{aligned} \quad (2.20)$$

Amongst others H_0 consists of the Landau quantization and the intrinsic ZEEMAN effect⁷ ($H_{intZeeman}$) described by the Hamiltonian, in the case of a nonzero B-field

$$H_{Landau} = \frac{1}{2m^*}(\vec{p} - e\vec{A})^2 \quad \text{and} \quad H_{intZeeman} = g^* \mu_B \hat{\sigma} \vec{B} \quad (2.21)$$

respectively⁸.

According to FURDYNA [Fur88] in wide-gap DMS it is very convenient to neglect the operators in (2.21) which are responsible for non-exchange cyclotron splitting and spin splitting⁹. Reasons are that in wide gap materials like CdMnTe the effective masses m^* are large and the sp-band g-factors g^* are at the order of unity.

Subsequently the region of interest of the Hamiltonian in (2.20) is

$$H_{exch} = - \sum_i J(\vec{r} - \vec{R}_i) \vec{S}_i \vec{J} \quad (2.22)$$

⁷ordinary sp-band spin splitting

⁸ m^* : effective mass, \vec{A} : vector potential, g^* : "band" g-factor of the electron, \vec{J} spin of the electron, \vec{B} external B-field

⁹[Fur88],R46

with the spin operator \vec{S}_i and the position vector \vec{R}_i of the i -th Mn-ion, while \vec{r} and \vec{J} are the position vector and the spin operator of the band electron, respectively. The exchange operator is denoted by J^{sp-d} . The sum acts on all Mn-ions in the whole crystal.

Using the operators $S_i^\pm = S_i^x \pm iS_i^y$ and $J^\pm = J^x \pm iJ^y$ respectively (c.f. [CTDL99]) the exchange Hamiltonian in (2.22) can be rewritten:

$$H_{exch} = - \sum_i J(\vec{r} - \vec{R}_i) (S_i^z J^z + \frac{1}{2} S_i^+ J^- + \frac{1}{2} S_i^- J^+) \quad (2.23)$$

The summands $\frac{1}{2} S_i^+ J^-$ and $\frac{1}{2} S_i^- J^+$ correspond to Raman scattering at the spins of the Mn-ions. The $\frac{1}{2} S_i^+ J^-$ summand represents the simultaneous Spin Flip process of a Mn-ion ($\Delta m = +1$) and a charge carrier ($\Delta m = -1$). The summand $S_i^z J^z$ causes a strong band splitting in an external B-field. The above Hamiltonian (2.23) is non-diagonal in the basis of H_0 (Table 2.1 shown later) because of the Spin Flip terms $\frac{1}{2} S_i^+ J^-$ and $\frac{1}{2} S_i^- J^+$.

In consideration of the extremely extended wave functions of the band electrons in the lattice which allows to average over several lattice sites, the Hamiltonian in (2.22) can be approximated with two helpful tools: (i) The VCA¹⁰ replaces the summation over all Mn lattice sites by summation over all cation lattice sites and weighting the summation value with the Mn-content x (\vec{S}_i is replaced by $x\vec{S}_i$). (ii) The mean field approximation considers that the single spins \vec{S}_i can be replaced by the thermal expectation value $\langle \vec{S} \rangle$. $\langle \vec{S} \rangle = \langle S^z \rangle$ if an external B-field is aligned along z-direction.

Using these approximations (2.22) transforms to:

$$H_{exch} = -x \langle S^z \rangle J^z \sum_j J^{sp-d}(\vec{r} - \vec{R}_j) \quad (2.24)$$

H_{exch} includes the periodicity of the lattice and thus it is allowed to use the same wave functions for solving the exchange interaction problem as those used for diagonalising H_0 . These BLOCH functions are listed in Table 2.1 for the conduction band (CB), the valence band (VB) and the split-off band.

energy band	$ J, J_z\rangle$	u_{J, J_z}
Γ_6	$\varphi_5 = 1/2, +1/2\rangle$	$S \uparrow$
Γ_6	$\varphi_6 = 1/2, -1/2\rangle$	$S \downarrow$
Γ_8	$\varphi_1 = 3/2, +3/2\rangle$	$(1/\sqrt{2})(X + iY) \uparrow$
Γ_8	$\varphi_2 = 3/2, +1/2\rangle$	$(i/\sqrt{6})[(X + iY) \downarrow - 2Z \uparrow]$
Γ_8	$\varphi_3 = 3/2, -1/2\rangle$	$(1/\sqrt{6})[(X - iY) \uparrow + 2Z \downarrow]$
Γ_8	$\varphi_4 = 3/2, -3/2\rangle$	$(1/\sqrt{2})(X - iY) \downarrow$
Γ_7	$\varphi_7 = 1/2, +1/2\rangle$	$(1/\sqrt{3})[(X + iY) \downarrow + Z \uparrow]$
Γ_7	$\varphi_8 = 1/2, -1/2\rangle$	$(i/\sqrt{3})[-(X - iY) \uparrow + Z \downarrow]$

Table 2.1: Basis Bloch functions of Γ_6 - (conduction band), Γ_8 - (valence band) and Γ_7 -band (split-off band) [[Fur88], [LK55]].

¹⁰Virtual Crystal Approximation mentioned in subsection 2.1.2

Note that the wave functions $|S\rangle$, $|X\rangle$, $|Y\rangle$ and $|Z\rangle$ describing the bond in a zinc blende crystal are directed along the Cartesian coordinates transform under symmetry group T_d like nuclear s -, p_x -, p_y -, p_z -orbitals [LK55]. Taking account of the spin orbit interaction i.e. $\vec{l} \cdot \vec{s}$ - coupling, the states of the valence band (Γ_8 and Γ_7) must be described in a new basis. A new possible basis for diagonalising H_0 is shown in Table 2.1. The spins are represented by up and down arrows.

Now the Hamiltonian (2.24) can be diagonalised in the basis of Table 2.1 as well. Furthermore the primary interest is in the behaviour of the bottom of the conduction band Γ_6 and the top of the valence band Γ_8 close to the Γ -point. Under these two aspects and neglecting the Γ_7 -band¹¹ H_{exch} can be expressed by the following matrices:

$$H_{exch}^{CB} = \begin{pmatrix} 3A & 0 \\ 0 & -3A \end{pmatrix} \quad (2.25)$$

for the conduction band Γ_6 with the basis $|1/2, +1/2\rangle$ and $|1/2, -1/2\rangle$ and

$$H_{exch}^{VB} = \begin{pmatrix} 3B & 0 & 0 & 0 \\ 0 & B & 0 & 0 \\ 0 & 0 & -B & 0 \\ 0 & 0 & 0 & -3B \end{pmatrix} \quad (2.26)$$

for the valence band Γ_8 with basis $|3/2, +3/2\rangle$, $|3/2, +1/2\rangle$, $|3/2, -1/2\rangle$, $|3/2, -3/2\rangle$ [GGG78] [Lut56]. The matrix elements A and B are

$$A = -\frac{1}{6}N_0\alpha x_{eff} \langle S^z \rangle \quad \text{and} \quad B = -\frac{1}{6}N_0\beta x_{eff} \langle S^z \rangle \quad (2.27)$$

respectively; with $N_0 = 4/a^3$ the cation density, $\alpha = \langle S | J^{sp-d} | S \rangle$ and $\beta = \langle X | J^{sp-d} | X \rangle$ the exchange integrals of conduction band and valence band. In (2.27) x is replaced by its smaller value x_{eff} because of the formation of antiferromagnetic (af) cluster of next-neighbour (NN) Mn spins causing strong d-d exchange interaction among each other (mentioned previously in subsection 2.2.3).

From first order perturbation theory one obtains the eigenvalues of the conduction band and valence band energy shift - i.e. the band splitting of each spin branch $m_{s,j}$ with respect to its spectral position without an applied B-field - at the Γ -point

$$\Delta E_{\Gamma_6} = xN_0\alpha \langle S_z \rangle m_s \quad \text{with} \quad m_s = \pm \frac{1}{2} \quad (2.28)$$

$$\Delta E_{\Gamma_8} = \frac{1}{3}xN_0\beta \langle S_z \rangle m_j \quad \text{with} \quad m_j = \pm \frac{1}{2}, \pm \frac{3}{2} \quad (2.29)$$

with the thermal expectation value $\langle S^z \rangle$ (2.10) in subsection 2.2.2 with a modified Brillouin function \mathfrak{B}_S :

$$\langle S_z \rangle = -S \cdot \mathfrak{B}_S \left(\frac{g_{Mn}\mu_B S B}{k_B(T_{Mn} + T_0)} \right) \quad (2.30)$$

¹¹valid due to relative large energetic distance to the Γ_8 -band $\Delta_{CdTe}=0.938\text{eV}$ [CC76]

Where $S = 5/2$ and T_0 is the already mentioned (subsection 2.2.3) phenomenological fitting parameter which is caused by long ranging antiferromagnetic exchange interaction among Mn-spins of next nearest neighbours and next next nearest neighbours and so on [BRH⁺87].

The experimental determination of α and β can be realized by magneto photoluminescence (PL) and magneto Raman measurements ¹². The determined values of the exchange integrals for $\text{Cd}_{1-x}\text{Mn}_x\text{Te}$ are [GPF79]:

$$N_0\alpha = 0.22eV \text{ and } N_0\beta = -0.88eV \quad (2.31)$$

In addition it has to be mentioned that according to $\langle S^z \rangle$ in (2.30) the energy splitting by sp-d exchange interaction is strongly dependent on the temperature of Mn-ion spin system. The tendency $\alpha > 0$, $\beta < 0$ and $|\alpha| < |\beta|$ applies to all semimagnetic materials. The origins of this tendency are two competing effects influencing the magnitude of the exchange integral [BFC83]. On the one hand the value of the exchange integral is determined by direct 1/r-potential exchange (Coulomb) among band electrons and Mn-3d electrons. The effect exists both for the s-like conduction band and for the p-like valence band, resulting in a parallel (*ferromagnetic*) alignment of band electron spins and Mn-ion spins. This leads to a positive contribution to the exchange integral. On the other hand the value of the exchange integral is affected by the kinetic exchange originating from the hybridization of the 3d-electrons and the s- (p-) band electrons. This exchange interaction causes an *antiferromagnetic* alignment of the Mn-ion spins and the band electron spins. Due to symmetry conditions, the s-d hybridization between the d-orbitals and the conduction band states is not possible at the Γ -point [BFC83]. Thus the conduction band splitting is only caused by the ferromagnetic direct potential exchange. In contrast, for the VB state the negative contribution of the p-d hybridization prevails the positive contribution of direct exchange and causes an antiferromagnetic coupling and thus a negative exchange integral.

In principle the splitting is qualitatively identical to "ordinary" spin splitting which takes place in nonmagnetic semiconductors with two and four spin levels for Γ_6 and Γ_8 , respectively. BUT the situation differs from the nonmagnetic semiconductor case primarily by the fact that the magnitude of the spin splitting is extremely large (GIANT ZEEMAN EFFECT), so that its behaviour is determined primarily by the properties of the magnetization i.e. it varies with temperature and is not necessarily linear in B-field [Fur88]. For this argument a distinction of cases must be made concerning the BRILLOUIN function with parameter $y \equiv \frac{g_{Mn} \cdot \mu_B \cdot S}{k_B} \cdot \frac{B}{T}$ (2.11):

- high B-field or small temperature ($y \gg 1$): $\mathfrak{B}_S(y) = \frac{2S+1}{2S} \coth\left(\frac{2S+1}{2S} \cdot y\right) - \frac{1}{2S} \coth\left(\frac{1}{2S} \cdot y\right)$
- low B-field or high temperature ($y \ll 1$): $\mathfrak{B}_S \approx \frac{S+1}{3S} \cdot y$ [Dya08]

i.e. for low B-field or high temperature \mathfrak{B}_S is linear in y and thus \mathfrak{B}_S has a linear behaviour in the magnetic field B . This is demonstrated for the BRILLOUIN function

¹²from magneto PL ($\alpha - \beta$) can be determined while from band electron Spin Flip position vs. B-field in Raman measurements α can be determined separately

\mathfrak{B}_S and the expectation value $\langle S_z \rangle$ of the total angular momentum S of the Mn-ions at increasing B-field and additionally under the aspect of different total angular momentum S and at varying temperature T in Figure 2.4, respectively.

Concluding from Figure 2.4, the saturation onset of the BRILLOUIN function starts

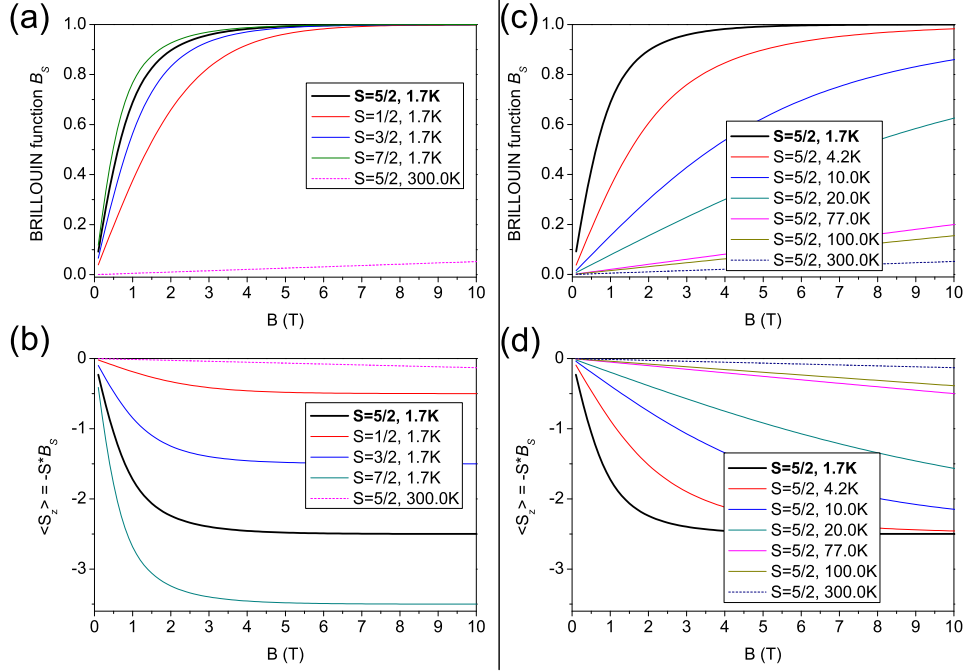


Figure 2.4: BRILLOUIN function \mathfrak{B}_S ((a), (c)) and the expectation value $\langle S_z \rangle$ of the total angular momentum of the Mn-ions S ((b), (d)) in an external B-field. Both are discussed under the aspect of different total angular momentum S ((a), (b)) and varying temperature T ((c), (d)). The thick black lines emphasise the case the Mn-ion ($S=5/2$) under the main temperature of investigation ($T=1.7\text{K}$). (Calculation: MATHEMATICA 7.0).

both at increasing S and at decreasing temperature T . Thus at the same temperature e.g. Europium-ions ($S=7/2$) saturate at lower B-fields than Mn-ions ($S=5/2$). Further information concerning the band splitting under the aspects of varying temperature and the total angular momentum are presented in appendix A.2.

According to [Fur88] the selection rules remain the same as for a nonmagnetic semiconductor. A schematic sketch of the bottom of the conduction band (Γ_6) and the top of the valence band (Γ_8) for a wide gap semimagnetic semiconductor and its spin splitting in a magnetic field B is shown in Figure 2.5. The dipole allowed transitions in Faraday configuration in circular and linear polarisation (σ^+ , σ^- and Π) are highlighted with black vertical arrows. σ^+ and σ^- stand for transitions among states with $\Delta m = \pm 1$ while Π represents transitions among states with $\Delta m = 0$. The maximum splitting of the CB is given by $xN_0\alpha \langle S_z \rangle$ while the maximum splitting of the VB (i.e. of the HH-states) is determined by $xN_0\beta \langle S_z \rangle$ (cf.(2.28) and (2.29), respectively).

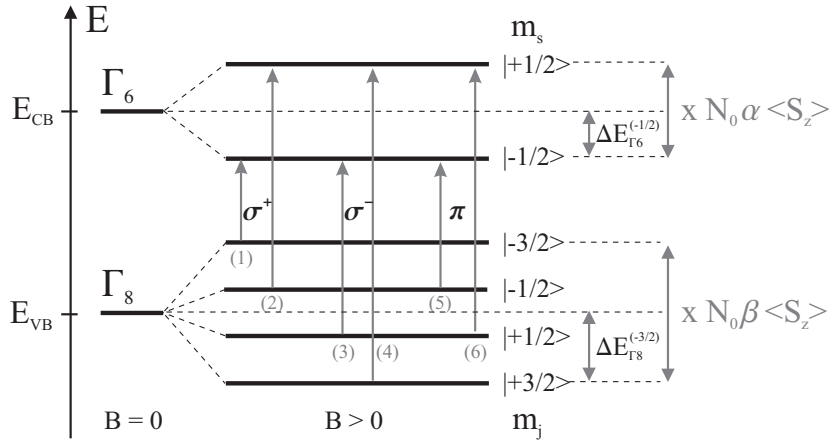


Figure 2.5: Schematic sketch of the bottom of the conduction band (Γ_6) and the top of the valence band (Γ_8) for a wide gap semimagnetic semiconductor and the spin splitting in a magnetic field B . The arrows represent the dipole allowed transitions in Faraday configuration. These are two circular polarizations σ^+ and σ^- ($\Delta m = \pm 1$) and one linear polarization Π ($\Delta m = 0$) [Fur88].

2.3 CdMnTe/CdMgTe Quantum Well and its anisotropy in an external magnetic field

2.3.1 CdMnTe/CdMgTe Quantum Well

Growing thin layers of different energy-gap-sized semiconductors in alternating sequences, the resulting structure is called a quantum well (QW). If there is only material A embedded between layers of material B where $E_B > E_A$, this is called a single QW with A the well material and B the barrier material. More than one of these alternations "B A B" are called Multi Quantum well and superlattice¹³, respectively. The investigated samples in this thesis have single QW close to the surface which will be discussed later on.

There is a variety of possibilities to combine semiconductors forming QWs. The two main parameters are the already mentioned energy gap and the lattice constant. In Figure 2.6(a) these two parameters are plotted against each other. The coloured background of the plot is associated with the visible spectrum of light. The white squared frame in Figure 2.6(b) is plotted in more detail in Figure 2.6(b) and shows the region of interest of the QW samples investigated in this thesis. The filled symbols in Figure 2.6(b) mirror the parameters of the QWs, either of $\text{Cd}_{0.994}\text{Mn}_{0.006}\text{Te}$ well embedded in $\text{Cd}_{0.80}\text{Mg}_{0.20}\text{Te}$ barriers or $\text{Cd}_{0.99}\text{Mn}_{0.01}\text{Te}$ well embedded in $\text{Cd}_{0.80}\text{Mg}_{0.20}\text{Te}$ barriers. A detailed sample description is given later on in section 3.2.

The thickness of the well material (the well width L) quantizes the energetic sublevels inside the QW in growth direction (see (2.32)). This is called the electronic confinement. Thus depending on the well thickness the transition energies of the

¹³superlattice: the width of the barrier material B between the wells is so small that the extending QW wavefunctions into the barrier can overlap building subbands over the whole structure.

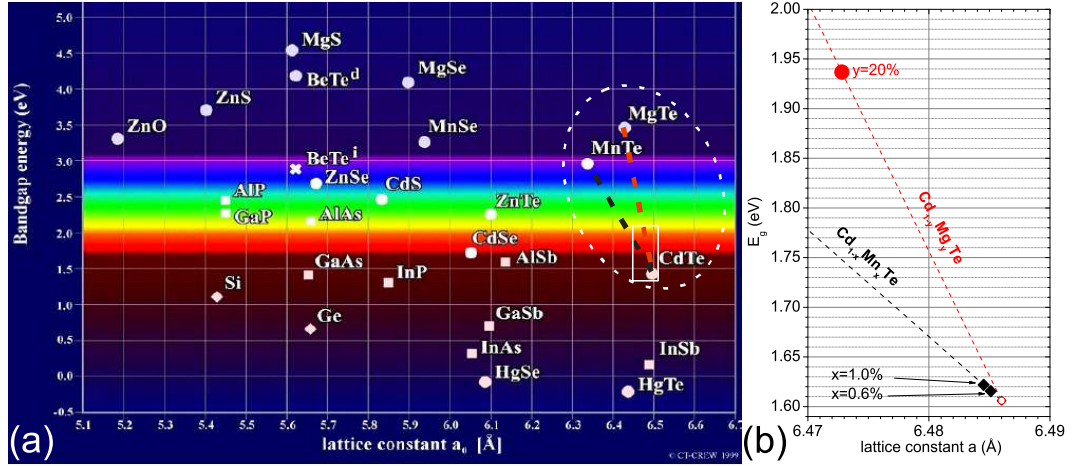


Figure 2.6: (a) "Bandgap Energy vs. lattice constant" chart of the most common semiconductor materials in zinc blende structure at room temperature. Signed in a dashed white oval the region of interest for the investigated samples in this thesis. (b) In detail, the region of interest of the sample parameters investigated in this thesis marked with a white squared frame in (a).

QW can be tuned by the growth sequence. Furthermore using ternary materials e.g. Cd_{1-x}Mn_xTe for the growth procedure provides the opportunity of lattice matching and mismatching, respectively. That means the difference between the lattice constant of two materials e.g. A grown on B can be influenced by the fraction of x in the ternary material B. As a consequence the interface between the materials A and B can be tuned to be stressed, tensioned or lattice matched. As can be seen from Figure 2.6(b) the lattice constants of the well and the barrier material are not lattice matched. The lattice mismatch is about 0.2%¹⁴.

The QWs of interest in this thesis are Cd_{1-x}Mn_xTe/Cd_{1-y}Mg_yTe with x=0.01 and y=0.20. The minimum excitation energies are in the visible red spectral range (low energy side) for the well and also in the higher energetically visible red range for the barrier. This is monitored in Figure 2.6 with the dashed straight lines (black and red), respectively.

Starting from infinite potential barriers and a well width L, the resulting wavefunctions

	Cd _{1-x} Mn _x Te	Cd _{1-y} Mg _y Te
a (Å)	(6.486-0.148x) [BSG81] [RNPZ74]	(6.486-0.066y) [MDP ⁺ 09]
E _g (eV)	(1.606+1.592x) (4.2K) [Fur88]	(1.606+1.654y) [WHS ⁺ 93] [TBF ⁺ 94]

Table 2.2: Energy gap and lattice constant of CdMnTe- and CdMgTe-bulk material.

(alternating parity with n=1, 2, 3...) lead to the energy [Dav98]:

$$E_n = \frac{\hbar^2}{2m} \left(\frac{n\pi}{L} \right)^2 \quad (2.32)$$

¹⁴($a_{barrier} - a_{well}/a_{barrier}$)

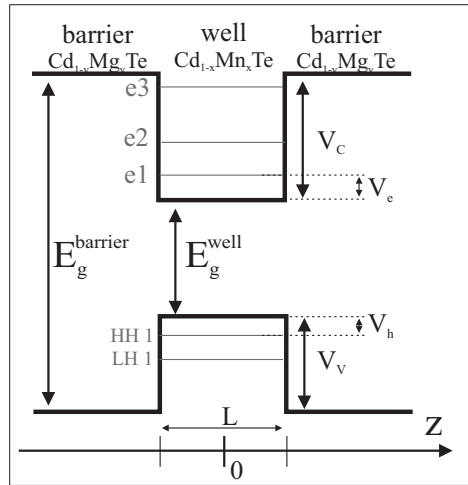


Figure 2.7: Scheme of a CdMnTe/CdMgTe QW of width L grown along z direction. E_g^{well} and $E_g^{barrier}$ denote the bandgap energy of the well and barrier material, respectively. V_C and V_V are the potential well depth of the CB and VB, respectively. V_e and V_h are the confinement energies of electron- and hole-states in the well. According to (2.32): $V_e=0.0379\text{eV}$ for $L=10\text{nm}$ and $V_e=0.0263\text{eV}$ for $L=12\text{nm}$ while $V_h=0.0188\text{eV}$ for $L=10\text{nm}$ and $V_h=0.0130\text{eV}$ for $L=12\text{nm}$ (using $m_e^*=0.0992$ [NNL88] and $m_H^*H=0.2$). The electron- and hole-states are denoted by e1, e2, e3 and HH1, LH1, respectively.

To describe the states in a finite QW shown in Figure 2.7 no analytical solution exists. A possible method to determine the QW states is to use the envelope-function approximation. Therefore the following conditions are necessary [Bas88]: (i) the different layers can be described by the band structure of the bulk material, (ii) the single layers can be taylored by the Bloch functions u_l and (iii) the Bloch functions are identical for both material layers. Thus the single particle wave functions of each band can be described by the following linear combination ¹⁵:

$$\psi(\vec{r}) = \sum_l f_l^{A,B}(\vec{r}) \cdot u_l(\vec{r}) \quad (2.33)$$

with the envelope functions $f^{A,B}(\vec{r})$. The potential fluctuation is along z -axis while the potential shows translation invariancy in the xy -plane¹⁶ and the particle motion can be described by a plain wave leading to a separation Ansatz:

$$f_l^{A,B}(\vec{r}) = \varphi_l^{A,B}(z) \cdot \exp(i\vec{k}_\perp \vec{r}_\perp) \quad (2.34)$$

where \vec{k}_\perp is said to be equal for both materials.

In the following, the SCHRÖDINGER equation under the effective-mass approximation is used for describing a subband state in the QW. This means the lattice periodic potential for which the motion of free charge carriers must be described by

¹⁵A and B stand for CdMgTe and CdMnTe, respectively

¹⁶ $(x, y) \equiv \vec{r}_\perp$ and $(k_x, k_y) \equiv \vec{k}_\perp$

the Bloch functions is not taken into account. Instead, a flat devolution of the potential is taken where the carriers move with an effective mass. This effective mass has to make allowance for the lattice periodic potential.

$$\left(-\frac{\hbar^2}{2m_{A,B}} \nabla_z^2 + \frac{\hbar^2}{2m_{A,B}} \vec{k}_\perp^2 + V \right) \varphi^{A,B}(z) = E \varphi^{A,B}(z) \quad (2.35)$$

with the effective mass in A and B, respectively and the potential height V of the well. The conduction band edge energy of the well material is chosen to be zero. At the interfaces the steadiness of $\varphi^{A,B}(z)$ and $\frac{1}{m_{A,B}} \cdot \frac{d}{dz} \varphi^{A,B}(z)$ must be valid. Thus the subband energies E can be determined. The wave vectors $k_{A,B}$ and E are connected as follows [Bas88]:

$$k_B = \frac{\sqrt{2m_B E}}{\hbar} \quad \text{and} \quad k_A = \frac{\sqrt{2m_A(V - E)}}{\hbar} \quad (2.36)$$

In good approximation the masses of the ternary (CdTe-based) materials building the QW are the effective masses of CdTe. These effective masses are given by the Luttinger parameters mentioned in subsection 2.1.1.

- in z-direction [YC01] [LHHS97]: $m_{HH} = (\gamma_1 - 2\gamma_2)^{-1} \cdot m_e$
- in the interface plane [YC01]:

$$m_{HH}^\perp = (\gamma_1 + \gamma_2)^{-1} \cdot m_e$$

$$m_{LH}^\perp = (\gamma_1 - \gamma_2)^{-1} \cdot m_e$$

m_{HH} and m_{LH} are the heavy hole mass and the light hole mass, respectively and m is the rest mass of the free electron.

The different masses lead to the lifting of the degeneracy at the Γ -point. As presented in Figure 2.8 the T_d -symmetry is reduced to the D_{2d} -symmetry and thus the Γ_8 -band (VB) splits to a Γ_6 -band (HH) and a Γ_7 -band (LH).

Excitons Up to now the Coulomb interaction between electron and hole was neglected in optical transitions. This interaction causes the coupling of the photo-generated electron-hole pairs (e-h pairs). This bound state is called an exciton. The general SCHRÖDINGER equation for the two-particle problem in the 3D case is [Dav98]:

$$\left[\left(E_C - \frac{\hbar^2}{2m_e^*} \nabla_e^2 \right) - \left(E_V + \frac{\hbar^2}{2m_h^*} \nabla_h^2 \right) - \frac{e^2}{4\pi\epsilon_r\epsilon_0|\vec{r}_e - \vec{r}_h|} \right] \cdot \varphi(\vec{r}_e, \vec{r}_h) + [V_e(\vec{r}_e) + V_h(\vec{r}_h)] \cdot \varphi(\vec{r}_e, \vec{r}_h) = E \cdot \varphi(\vec{r}_e, \vec{r}_h) \quad (2.37)$$

For the sake of simplicity the LH- and HH-valence bands are assumed to be parabolic. The potentials V_e and V_h are the confinement energies of the electron and the hole in a QW, respectively (see Figure 2.7). V_e and V_h are only functions of z in layered structures. ϵ_r is the static dielectric constant taking into account the screening of the Coulomb-interaction by the polarisability of the lattice and bonding electrons.

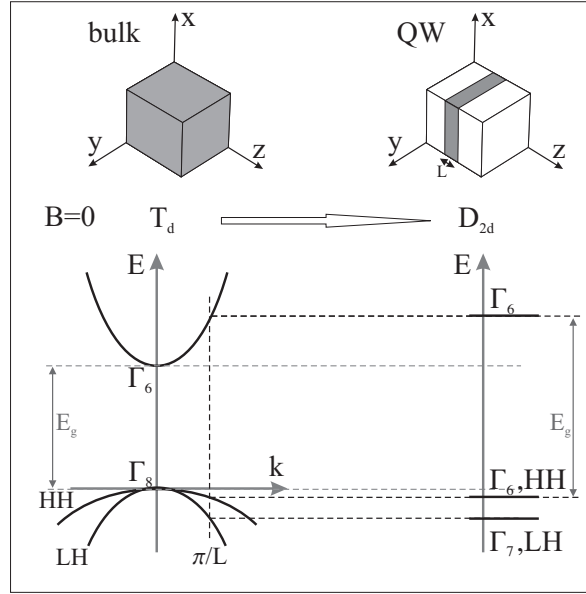


Figure 2.8: Schematic overview of bulk material and QW comparing their symmetry and dispersion relation $E(k)$

3D Excitons Starting with the 3D exciton case the potentials V_e and V_h vanish in (2.37). Analogue to the hydrogen model the SCHRÖDINGER equation can be solved using a transformation to relative coordinate and centre of mass coordinate (\vec{r} and \vec{R}) and an Ansatz of separation. Thus the exciton wave function is:

$$\varphi(\vec{r}, \vec{R}) = \frac{1}{\sqrt{V}} \exp(i\vec{K}\vec{R}) \phi_{nlm}(\vec{r}) \quad (2.38)$$

with V the crystal volume, \vec{K} the eigenvalue of the centre of mass momentum. ϕ_{nlm} are the known hydrogen eigenfunctions where the modified mass $\mu = (m_e^* m_h^* / (m_e^* + m_h^*))$ and the effective BOHR radius $a_0 = (4\pi\epsilon_r\epsilon_0\hbar^2) / (\mu e^2)$ is taken into account. Thus the binding energy of the 3D exciton in the hydrogen model is:

$$E_{bind}^n(3D) = \frac{\mu e^4}{32(\pi\epsilon_r\epsilon_0)^2\hbar^2} \cdot \frac{1}{n^2} = 13.6eV \cdot \left(\frac{\mu}{m_e\epsilon_r^2} \right) \cdot \frac{1}{n^2} \quad (2.39)$$

with n the main quantum number. The total energy of a free exciton including the kinetic energy of the centre of mass movement is:

$$E_n(3D) = E_g + \frac{\hbar^2 K^2}{2(m_e^* + m_h^*)} - E_{bind}^n(3D) \quad (2.40)$$

A rough estimation of the free 3D exciton energy depending on Mn-content could be made according to [LR84]:

$$E_{freeX}^{3D} = 1.595 + 1.592x \quad (2.41)$$

x	$E_{freeX}(\text{Cd}_{1-x}\text{Mn}_x\text{Te}) / (\text{eV})$
0.0066	1.60562
0.0100	1.61092
0.0200	1.62684
0.0400	1.65868

Table 2.3: $\text{Cd}_{1-x}\text{Mn}_x\text{Te}$ free-exciton energies for different Mn-contents. $x = 0.66\%$ and $x = 1.00\%$ are Mn-contents of the samples investigated in this thesis according to (2.41)

2D Excitons By using the effective mass approximation (flat potentials) the relative motion of an exciton in a QW can be described as [Dav98]:

$$\left[\left(E_C - \frac{\hbar^2}{2m_e^*} \frac{\partial^2}{\partial z_e^2} \right) - \left(E_V + \frac{\hbar^2}{2m_h^*} \frac{\partial^2}{\partial z_h^2} \right) - \frac{e^2}{4\pi\epsilon_r\epsilon_0|\vec{r}_e - \vec{r}_h|} \right] \cdot \varphi(\vec{r}, z_e, z_h) + [V_e(z_e) + V_h(z_h)] \cdot \varphi(\vec{r}, z_e, z_h) = E \cdot \varphi(\vec{r}, z_e, z_h) \quad (2.42)$$

The remaining wave function depends on the relative in-plane coordinate \vec{r} of the well and both former z-components.

Due to the fact that a QW well is neither purely 3D nor purely 2D, according to [He91] a fractional-dimensional space is used to simplify the mathematical treatments. This model treats the anisotropic interaction (i.e. an anisotropic potential) in the 3D space as isotropic one in a lower fractional-dimensional space, where the dimension α is determined by the degree of anisotropy. The aim is to solve the SCHRÖDINGER equation in a noninteger-dimensional space where the interactions experience an isotropic environment. Hence in this space the problem of the QW exciton is reduced to the hydrogen-like atom with the binding energy in an α D space [MLC92]:

$$E_{bind}^n(\alpha D) = \frac{E_{bind}^n(3D)}{\left[n + \frac{\alpha-3}{2} \right]^2} \quad (2.43)$$

For $\alpha = 3$ the exciton binding energy is back at the 3D case. For $\alpha = 2$ and $n = 1$ the binding energy in the 2D case is four times larger than in the 3D one.

According to MATHIEU et al. [MLC92] the 1s exciton binding energy¹⁷ E_{Bind}^X depending on the well width L is plotted in Figure 2.9. The dimension α is expressed by

$$\alpha = 3 - e^{-\beta} \quad (2.44)$$

with

$$\beta = \frac{\frac{2}{k_b} + L}{a_0^*}. \quad (2.45)$$

The numerator in (2.45) takes into account the spreading of the e-h pair into the barriers by a length characteristic of the motion in growth direction z . k_b is the wave vector of the particle (electron and hole) in the barrier which considers the well depth (V_C, V_V), the effective masses of electron ($m_e^* = 0.0992$) and heavy hole ($m_{HH} = m_e(\gamma_1 - 2*\gamma_2)^{-1}$;

¹⁷ $n = 1$

$\gamma_1 = 3.61, \gamma_2 = 0.97$ [LHHS97]) and the well width L . a_0^* represents the mean value of the 3D BOHR radius dependent on the well width L and the already mentioned effective masses of electron and HH. The physical meaning of β corresponds to the ratio of a length characteristic of the electron and hole motions with respect to the well width L , to a length characteristic of the e-h relative motion with respect to the Coulomb interaction. In Figure 2.9 the relevant well widths for this thesis are marked

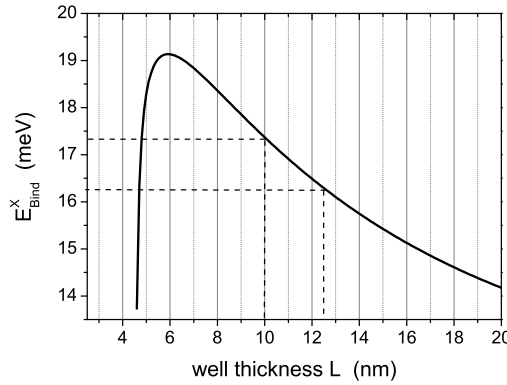


Figure 2.9: Theoretical calculations of the exciton binding energy depending on the well width L of a $\text{Cd}_{0.99}\text{Mn}_{0.01}\text{Te}/\text{Cd}_{0.80}\text{Mg}_{0.20}\text{Te}$ QW following [MLC92]. The dashed lines mark the well widths of relevance in this thesis.

by dashed lines.

strain Strain is a further influence on the excitonic states and should be discussed briefly. In general the lattice constant of the well material is strained by growing on the barrier material. There are two cases of modifications that can occur. The first one produces both an upward shift in the CB and a downward shift in the VB. Thus the band gap is increased by an amount of δE_H which originates from the hydrostatic component of the strain. The second and more important case is responsible for separating the LH and HH. They are pushed in opposite directions with respect to their energetic centre position by δE_S . "S" stands for the shear component of the strain. For convention [ZE96]:

- $\delta E_{H,S} > 0$: compressive strain
- $\delta E_{H,S} < 0$: tensile strain

Thus the degeneracy of the VB is cancelled and the strained bandgap energy is [AJBM01]:

$$E = E_g + \Delta E(HH) = E_g + \delta E_H + \frac{1}{2}\delta E_S \quad (2.46)$$

$$E = E_g + \Delta E(LH) = E_g + \delta E_H - \frac{1}{2}\delta E_S \quad (2.47)$$

with

$$\delta E_H = (a_c - a_v) \left(\frac{2S_{12}}{S_{11} + S_{12}} + 2 \right) \frac{a_{\text{barrier}} - a_{\text{well}}}{a_{\text{well}}} \quad (2.48)$$

$$\delta E_S = 2b \left(\frac{2S_{12}}{S_{11} + S_{12}} - 1 \right) \frac{a_{\text{barrier}} - a_{\text{well}}}{a_{\text{well}}} \quad (2.49)$$

where a_c and a_v are the deformation potentials for CB and VB. S_{ij} is the elastic constant of the unstrained well material. $a_{\text{barrier},\text{well}}$ are the unstrained lattice constants of the barrier and the well, respectively.

2.3.2 Magnetic anisotropy of the valence band

Applying a magnetic field to bulk CdMnTe the valence band splitting is isotropic to any field direction. This is different in a quantum well. There are two extreme cases of applying a magnetic field. One is parallel and the other one is perpendicular to the growth direction. In **back scattering geometry** and $\vec{k} \parallel \vec{z}$ these two mentioned cases are called:

- Faraday geometry where $\vec{B} \parallel \vec{z}$
- Voigt geometry where $\vec{B} \perp \vec{z}$

These B-field geometries cause different kind of valence band splitting while the conduction band has quite similar splitting behaviour which is shown in Figure 2.10. Both

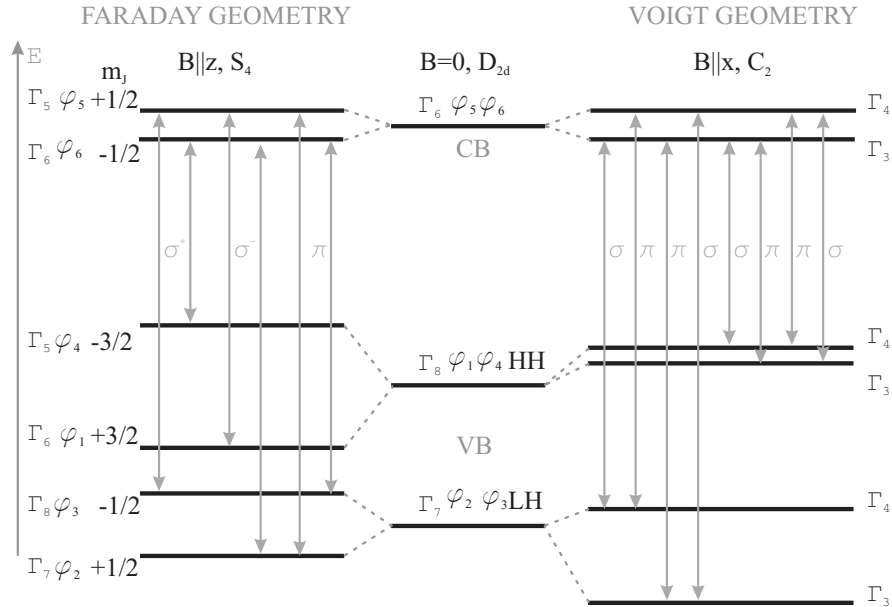


Figure 2.10: Schematic valence splitting of a quantum well depending on the B-field direction (Faraday and Voigt) according to [MDSW97] [PwMd+93] [Kac91]. In Faraday geometry the QW D_{2d} symmetry is reduced to S_4 while it is reduced to C_2 symmetry in Voigt geometry. The vertical double arrows represent the optically allowed transitions in the magnetic field

cases cause a symmetry reduction and thus cancel symmetry degeneracy of both the CB and the HH- and LH states of the VB. The already mentioned Bloch functions $|J, m_J\rangle$ ¹⁸ of the CB and VB in Tab.(2.1) are basis functions for of the irreducible representation of the band states in bulk material (T_d -symmetry) and can also be used for the QW symmetry D_{2d} and its additionally reduced symmetry in Faraday geometry S_4 . Again these Bloch functions are:

$$\varphi_1 = |3/2, +3/2\rangle; \varphi_2 = |3/2, +1/2\rangle; \varphi_3 = |3/2, -1/2\rangle; \varphi_4 = |3/2, -3/2\rangle$$

and

$$\varphi_5 = |1/2, +1/2\rangle; \varphi_6 = |1/2, -1/2\rangle$$

for the Γ_8 - (VB) and Γ_7 -band (split-off band), respectively.

For the Voigt geometry and thus for C_2 -symmetry the following linear combinations of φ_i can be used for the irreducible representations Γ_3 and Γ_4 :

Derived from HH states of the VB:

$$\begin{aligned} \phi_1 &= (1/\sqrt{2}) |\varphi_1 + \varphi_4\rangle, \Gamma_3 \\ \phi_4 &= (1/\sqrt{2}) |\varphi_1 - \varphi_4\rangle, \Gamma_4 \end{aligned}$$

Derived from LH states of the VB:

$$\begin{aligned} \phi_2 &= (1/\sqrt{2}) |\varphi_2 + \varphi_3\rangle, \Gamma_3 \\ \phi_3 &= (1/\sqrt{2}) |\varphi_2 - \varphi_3\rangle, \Gamma_4 \end{aligned}$$

Derived from CB states:

$$\begin{aligned} \phi_5 &= (1/\sqrt{2}) |\varphi_5 + \varphi_6\rangle, \Gamma_4 \\ \phi_6 &= (1/\sqrt{2}) |\varphi_5 - \varphi_6\rangle, \Gamma_3 \end{aligned}$$

BUT these linear combinations are not yet eigenstates of the former Hamiltonian!

Figure 2.10 also shows the dipole transitions in both B-field geometries. Due to the fact that the same eigenfunctions can be used both for the QW in Faraday geometry and for the bulk material, the same selection rules for transitions between CB and VB are valid. $\sigma^{+/-}$ represent the right hand and left hand circular polarization, respectively. The linear polarization is called π and is not detectable in back scattering geometry. In this thesis Faraday geometry is only used to determine the Mn-concentrations of the investigated samples which is described later on.

In contrast to the latter mentioned geometry there are different transitions in Voigt geometry with in general four σ - and four π -dipole transitions.

- σ : polarization of the incident/scattered light is **perpendicular** to \vec{B}
- π : polarization of the incident/scattered light is **parallel** to \vec{B}

¹⁸ $J_z|\varphi\rangle = m_J|\varphi\rangle$

These polarizations will be picked up again when the PR- and Multi-PR-signals are discussed.

Before the discussion about the total Hamiltonian in Faraday and Voigt geometry is started some "limitations" have to be mentioned.

A sufficient confinement of the QW is an urgent condition for discussing the QW Hamiltonian. This means that the splitting of the bandstates is clearly smaller than the height of the potential well. Additionally, the split-off band due to its relatively large energetic distance from the HH- and LH-states can be neglected like in bulk CdMnTe. Due to smaller contributions to the Hamiltonian by intrinsic Zeeman effects of the carriers and by Landau quantization these effects can also be neglected.

According to these limitations the band Hamiltonian can be written ($\vec{k}_\perp = 0$)¹⁹:

$$H = H_{QW} + H_{exch} \quad (2.50)$$

In matrix representation of the QW Hamiltonian by using its basis function $\psi_i(z)\varphi_i$, H_{QW} can be expressed by the following matrices for CB (i=5, 6) and VB (i=1, 2, 3, 4):

$$H_{QW}^{CB} = \begin{pmatrix} E_{CB1} & 0 \\ 0 & E_{CB1} \end{pmatrix} \quad (2.51)$$

and

$$H_{QW}^{VB} = \begin{pmatrix} E_{HH1} & 0 & 0 & 0 \\ 0 & E_{LH1} & 0 & 0 \\ 0 & 0 & E_{LH1} & 0 \\ 0 & 0 & 0 & E_{HH1} \end{pmatrix} \quad (2.52)$$

respectively. $\psi_i(z)$ represent the envelope functions of the first subbands of HH and LH and of the CB electrons. For discussing the exchange interaction and its Hamiltonian H_{exch} the same approximations as for the bulk material in subsection 2.2.4 can be used. Thus in 2.24 the different B-field configurations for Faraday ($\vec{B} \parallel \vec{z}$) and Voigt ($\vec{B} \perp \vec{z}$) have to be taken into account.

$$\text{Faraday geometry} \quad H_{exch} = -x_{eff} \langle S^z \rangle J^z \sum_j J^{sp-d}(\vec{r} - \vec{R}_j) \quad (2.53)$$

$$\text{Voigt geometry} \quad H_{exch} = -x_{eff} \langle S^x \rangle J^x \sum_j J^{sp-d}(\vec{r} - \vec{R}_j) \quad (2.54)$$

To get H_{exch} in the matrix expression the spin-matrices J_z (see: (2.5)) and J_x (see: (2.3) [Lut56] where ($J_x = 1/2(J^+ + J^-)$)) in the basis φ_i in Faraday and Voigt geometry are used for expressing the CB. Due to its pure spin component the usual Pauli-matrices are used for the VB.

¹⁹ \vec{k}_\perp is the directions perpendicular to k_z (i.e.: x and y go to infinity)

Faraday geometry Using the above mentioned spin- and Pauli-matrices the exchange interaction Hamiltonian of the CB and VB in Faraday geometry ($\vec{B} \parallel \vec{z}$) is:

$$H_{exch}^{CB} = \begin{pmatrix} 3AP_{55} & 0 \\ 0 & -3AP_{66} \end{pmatrix} \quad (2.55)$$

and

$$H_{exch}^{VB} = \begin{pmatrix} 3BP_{11} & 0 & 0 & 0 \\ 0 & BP_{22} & 0 & 0 \\ 0 & 0 & -BP_{33} & 0 \\ 0 & 0 & 0 & -3BP_{44} \end{pmatrix} \quad (2.56)$$

with the constants

$$A = -\frac{1}{6}N_0\alpha x_{eff} \langle S^z \rangle \quad \text{and} \quad B = -\frac{1}{6}N_0\beta x_{eff} \langle S^z \rangle \quad (2.57)$$

where $N_0\alpha = 0.22eV$ and $N_0\beta = -0.88eV$ are the exchange constants of the CdTe conduction band and valence band, respectively.

These constants are nearly the same like in the bulk material in subsection (2.2.4) but with a different band splitting due to the weighting factor:

$$P_{mn} = \int_{DMS} \psi_m(z)\psi_n(z)dz \quad (2.58)$$

This factor is based on the presumption that the charge carrier is located only in the semimagnetic part of the structure (DMS) although this charge carrier has an overlapping part of the wave function into the nonmagnetic barrier. The obvious reason is, the s/p-d exchange interaction takes place only in the semimagnetic part of the structure.

As can be seen from the above matrices the CB- and VB-matrix are diagonal in the basis $\psi_i(z)\varphi_i$. Thus the band splitting behaviour is similar to that of the bulk material. As a consequence the dipole selection rules for transitions between the CB and VB in the QW are equivalent to the bulk ones. The states split symmetrically due to the fact that the on-diagonal elements in this case are $P_{11} = P_{44}$, $P_{22} = P_{33}$ and $P_{55} = P_{66}$ (because: $\psi_1(z) = \psi_4(z)$, $\psi_2(z) = \psi_3(z)$, $\psi_5(z) = \psi_6(z)$).

This description is adequate for the samples in this thesis. The well width and well depth values are sufficient to neglect m_J -state-specific leakage of the wave function into the barriers.

Voigt geometry The situation is much more complicated in Voigt geometry. Substituting (2.3) into (2.54) one obtains:

$$H_{exch}^{CB} = \begin{pmatrix} 0 & 3CP_{56} \\ 3CP_{56} & 0 \end{pmatrix} \quad (2.59)$$

and

$$H_{exch}^{VB} = \begin{pmatrix} 0 & \sqrt{3}DP_{12} & 0 & 0 \\ \sqrt{3}DP_{12} & 0 & 2DP_{23} & 0 \\ 0 & 2DP_{23} & 0 & \sqrt{3}DP_{34} \\ 0 & 0 & \sqrt{3}DP_{34} & 0 \end{pmatrix} \quad (2.60)$$

with the constants

$$C = -\frac{1}{6}N_0\alpha x_{eff} \langle S^x \rangle \quad \text{and} \quad D = -\frac{1}{6}N_0\beta x_{eff} \langle S^x \rangle \quad (2.61)$$

Taking the eigenvector of matrix (2.61) ($hh \uparrow, lh \uparrow, lh \downarrow, hh \downarrow$) where hh and lh are the eigen functions of the HH- and LH-states and the arrows represent their corresponding spin-states, respectively. Thus it is easy to see that the off-diagonal components $\sqrt{3}DP_{12}$ and $\sqrt{3}DP_{34}$ in matrix (2.60) are responsible for the HH-LH-mixing .

Tension and confinement on the one hand are responsible for one distinct direction of the crystal (here: z-axis) as well as for the HH-LH-splitting ΔE_{HH-LH} . On the other hand the external B-field causes a distinct direction in the QW plane (here: x-axes). Thus the behaviour of the QW is strongly dependent on the ratio of ΔE_{HH-LH} to the strength of the exchange interaction between holes and Mn-ions.

It is useful to present H in a new basis different from $\psi_i(z)\varphi_i$. This new basis and its functions $\Psi_i(z)\varphi_i$ are assimilated to the C_2 -symmetry of the Voigt geometry. In other words a basis transformation is done by looking up valid functions fitting to group theory tables of C_2 -symmetry. Therefore the CB of the total Hamiltonian H for $\Psi_5(z)$ and $\Psi_6(z)$ is:

$$H_{CB} = \begin{pmatrix} E_{CB1} + 3CP_{55} & 0 \\ 0 & E_{CB1} - 3CP_{66} \end{pmatrix} \quad (2.62)$$

Due to the on-diagonal matrix form the band splitting of the CB in Voigt geometry is similar to the one in bulk material and Faraday geometry.

For the functions $\Psi_1(z)$, $\Psi_2(z)$, $\Psi_3(z)$ and $\Psi_4(z)$ the VB Hamiltonian is

$$H_{VB} = \begin{pmatrix} 0 & \sqrt{3}DP_{12} & 0 & 0 \\ \sqrt{3}DP_{12} & \Delta E_{HH-LH} + 2DP_{22} & 0 & 0 \\ 0 & 0 & \Delta E_{HH-LH} - 2DP_{33} & \sqrt{3}DP_{34} \\ 0 & 0 & \sqrt{3}DP_{34} & 0 \end{pmatrix} \quad (2.63)$$

In this matrix $E_{HH} = 0$ and ΔE_{HH-LH} ²⁰ is negative for all samples investigated in this thesis. That means that the HH-state is above the LH-state.

Getting closer to the experimental observation done in Voigt geometry, KACH-LISHVILI did some simulations - using similar matrix expressions as mentioned above - on the VB confinement energy behaviour in QWs with an in-plane magnetic field [Kac91]. The results of these simulations are shown in Figure 2.11. The magnetic field on the hole subbands in a semimagnetic CdMnTe superlattice²¹ shows that an additional mechanism of coupling between HH- and LH-subbands, independent of the in-plane wavevectors (\vec{k}_x, \vec{k}_y) and resulting from the exchange interaction (2.54) is possible if the field is applied to the layer planes. A qualitatively similar behaviour occurs in single semimagnetic QWs. The exchange induced coupling between HHs and LHs modifies the Zeeman effect in a rather complicated way as mentioned above. It replaces the crossing of the confinement energy bands by an anticrossing. Concerning

²⁰ $\Delta E_{HH-LH} = E_{LH1} - E_{HH1}$

²¹Multi-QW structure with overlapping well wave functions among the single QWs caused by thin barriers thicknesses forming subbands.

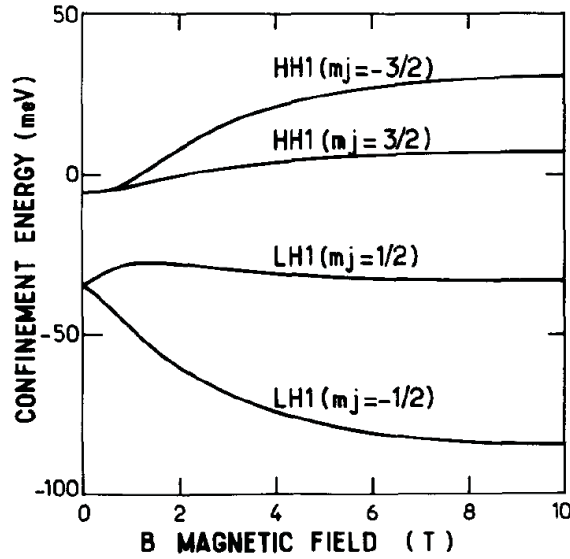


Figure 2.11: According to [Kac91] the calculated confinement energy of the HH1- and LH1-band states depending on the external B-field perpendicular to the growth axis z of a CdMnTe quantum well.

a symmetrical splitting of the bands with increasing B-field in Faraday geometry the "HH1($m_j = 3/2$)" and "LH1($m_j = 1/2$)" would cross at a certain B-field meant by "crossing". In Voigt geometry this is not the case as shown in Figure 2.11. The "HH1($m_j = 3/2$)"- and "LH1($m_j = 1/2$)"-states do not split symmetrically with respect to their opposite spin branch "HH1($m_j = -3/2$)" and "LH1($m_j = -1/2$)", respectively. These branches do not cross (anti-crossing) in contrast to the Faraday splitting but they are flattened and parallel to each other with increasing B-field. Thus it is not valid anymore to talk about the former eigenstates $|3/2, +3/2\rangle$, $|3/2, +1/2\rangle$, $|3/2, -1/2\rangle$, $|3/2, -3/2\rangle$ [PwMd+93]. As can be seen from Figure 2.11, the states named "HH1($m_j = 3/2$)" and "LH1($m_j = 1/2$)" have a more HH-like characteristic than the other two states due to their weak magnetic field dependence. This is depending on the well width and the Mn concentration in good agreement with the experimentally observed behaviour [PwMd+93] [Kac91].²²

2.3.3 The limit of a total anisotropic quantum well

Due to the anisotropy of the quantum well, the HH total momentum has only a component perpendicular to the plane $\langle J_x \rangle = \langle J_y \rangle = 0$. This causes the g-factor anisotropy of the hole. The pure z-component of the HH total momentum can not be influenced by a magnetic field aligned in any in-plane direction. As a result the splitting of the HH-state in Voigt geometry does not exist for an extremely anisotropic QW [Bas88]. The HH-LH-mixing is responsible for observing a HH-splitting in Voigt geometry. As mentioned in the previous subsection the structural behaviour strongly depends on the ratio ΔE_{HH-LH} and the strength of the exchange interaction among holes and Mn-ions.

²²This behaviour is also observed in ZnSe-based diluted magnetic semiconductors [CAB+97]

This ratio can be influenced by both the width of the QW and the Mn concentration. The splitting behaviour in Faraday and Voigt geometry depending on the Mn concentration and the well width is discussed and simulated in the thesis of STÜHLER and MEYER [Stü95] .

The total anisotropy is connected to a large HH-LH splitting and small terms of exchange interaction which result in neglecting the off-diagonal elements in (2.60). As mentioned before these off-diagonal elements combine the HH- and LH-states. Now the H_{VB} is diagonal and the HH- and LH-states constitute independent subsystems. According to STÜHLER and MEYER the LH subsystem splits twice as large as the HH subsystem for the case of total anisotropy. The subsystem of the HHs is degenerated in energy.

Again: The HH-states in a magnetic field in Voigt geometry do not change their energy because of non-existing in-plane components of total angular momentum (of HH). Thus the eigenstates of HH can be described in the projection of the total angular momentum J_z on the growth direction \vec{z} : $J_z = \pm 3/2$.

2.4 Theory of Multi-Spin Flip Raman Scattering

This section is used to answer the question how visible light with the order of eV can couple to the solid state body by exciting elementary excitations with the order of μeV like (Multi) Spin-Flip also called (Multi) **P**aramagnetic **R**esonance (PR) signals. In the following subsections there is a brief introduction in Raman scattering followed by the macroscopic and microscopic views of how elementary excitations in general can be either generated or annihilated before PR- and Multi-PR-signals are discussed.

2.4.1 Raman spectroscopy -a brief introduction-

Raman spectroscopy is an inelastic scattering process of monochromatic light at gases, liquids or solids leading to elementary excitations within these phases. These elementary excitations can either be generated (Stokes process S) or annihilated (Anti-Stokes process AS). Single particle excitations e.g. Spin Flip processes as well as collective excitations e.g. phonons are possible.

Thus the energy of the scattered light $\hbar\omega_S$ is shifted by the energy value of elementary excitation $E_A = \hbar\omega_A$ in relation to the incoming energy of the Laser $\hbar\omega_L$.

$$\hbar \cdot \omega_S = \hbar \cdot \omega_L \pm \hbar \cdot \omega_A \quad (2.64)$$

The "+" and "-" in (2.64) stands for the Anti-Stokes process and the Stokes process, respectively. Subsequent, only the Stokes process of the Spin Flip Raman measurements are taken into account. These Stokes shifts of the Multi Spin Flip signals are named **Spin Flip Raman Signals (SFRS)**²³ or Multi PR signals. The momentum conservation is given by:

$$\vec{k}_S = \vec{k}_L \pm (\vec{q} + \vec{G}) \quad (2.65)$$

where the k -vector of the scattered light \vec{k}_S is expressed by the incoming laser light vector \vec{k}_L , the pseudo wave vector \vec{q} and the reciprocal lattice vector \vec{G} . This pseudo wave vector \vec{q} and its reciprocal lattice vector \vec{G} satisfy the momentum conservation of collective excitations (e.g. phonons). \vec{G} can be assumed to be zero due to the fact that the wave vector of the visible light is small with respect to the size of the Brillouin zone (BZ) ($|\vec{k}_L - \vec{k}_S| \ll 2\pi/a$). Thus the wave vectors of the considered elementary excitations are close to the Γ -point of the BZ.

In general the energy and momentum conservation for the whole Raman process is requested but for the sub-Raman-processes the energy conservation is satisfied within the HEISENBERG uncertainty²⁴. It should be mentioned that the paramagnetic resonance (PR) of the Mn-ions investigated in this thesis have no pseudo momentum. The difference in momentum of the laser light and the scattered light in (2.65) is transferred to the whole crystal.

²³equivalent to the Raman shift in phonon spectra

²⁴ $\Delta E \Delta t \geq \hbar/2$

2.4.2 Macroscopic view of inelastic light scattering at elementary excitations

The interaction between the light and a solid is represented by electron hole (e-h) pairs. This is the easiest way to explain how visible light can couple to the solid state body to excite elementary excitations.

In general the susceptibility $\chi(\omega)$ of the solid describes its reaction on an incoming electromagnetic wave \vec{E}_L with frequency ω_L . $\chi(\omega)$ leads to the polarization \vec{P} and contains as the main information the electron transition energies and in addition the information about the crystal structure, the pressure and the temperature of the solid. In other words the electro magnetic wave interacts with the solid, inducing a polarization. Phonons (atomic vibrations of the solid) modulate $\chi(\omega)$ which leads to the Stokes part of the polarisations [YC01]:

$$\vec{P}_S = \varepsilon_0 \cdot \chi' \cdot Q \cdot \vec{E}_L \quad (2.66)$$

This part oscillates frequency-shifted with respect to the laser light $\vec{P}_S = \vec{P}_S(\omega_L - \omega_A)$. Q is the lattice deformation coordinate of the excitation. For Spin-Flip excitations Q is replaced by the magnetic dipole moment M [HL78]. $\chi' = \partial\chi/\partial Q$ is the second order TAYLOR approximation of the electric susceptibility. This approximation is valid due to the fact that the laser frequency ω_L is much higher than the resonance frequency of the lattice ω_0 . The induced polarization $\vec{P}_{S/AS}$ in general contains the information about the Stokes- and Anti-Stokes shift of elementary excitations²⁵:

$$\vec{P}_{S/AS} \propto \cos \left[(\vec{k}_L + \vec{q})\vec{r} - (\omega_L + \omega_0)t \right] + \cos \left[(\vec{k}_L - \vec{q})\vec{r} - (\omega_L - \omega_0)t \right] \quad (2.67)$$

where the first term in (2.67) is representing the Anti-Stokes and the second term the Stokes process, respectively. The Raman scattering cross section can be expressed by [HL78]

$$\frac{d\sigma}{d\Omega} \propto \omega_L \cdot \omega_S^3 \cdot |\vec{e}_S \cdot \chi' \cdot \vec{e}_L|^2 \quad (2.68)$$

where \vec{e}_L and \vec{e}_S are the polarization vectors of the intrinsic and the scattered light, respectively²⁶. Considering that χ is modulated by a classical magnetic dipole precessing in an external B-field ($\hbar\omega_{Larmor} = g\mu_B = \hbar\omega_A$) χ' can be determined and (2.68) changes to [HL78]:

$$\frac{d\sigma}{d\Omega} \propto |(\vec{e}_S \times \vec{e}_L)^+|^2 \quad (2.69)$$

with $(\vec{e}_S \times \vec{e}_L)^+ = (\vec{e}_S \times \vec{e}_L)^x + i(\vec{e}_S \times \vec{e}_L)^y$ describing circularly polarized light. The z-axis is defined by the direction of the external magnetic field.

Observing an elementary excitation of a Mn^{2+} -spin $\Delta m_S = 1$ is only allowed under the following conditions (selection rules). For this case of irradiation with polarization in σ^+ with respect to the z-axes. The scattered light is then analyzed with linear

²⁵for more details c.f.: [YC01]

²⁶see also [Stü95]

polarization (π) along z-direction (90-degree scattering geometry). Or the other way round, irradiating with π -polarized light is followed by analyzing the σ^- -polarized light. Thus it is not possible to irradiate with σ^+ -polarized light and analyzing π -polarized light in backscattering geometry, simultaneously.

But all measurements in this thesis were done in back scattering geometry. For this case and using linear polarized light, equation (2.69) can be rewritten as

$$\frac{d\sigma}{d\Omega} \propto |(\vec{e}_S \times \vec{e}_L) \times \vec{e}_B|^2 \quad (2.70)$$

with the B-field direction \vec{e}_B . In back scattering geometry $d\sigma/d\Omega = 0$ when:

- general: the B-field and direction of detection coincide (= Faraday geometry)
- $\vec{e}_S \parallel \vec{e}_L$ in Voigt geometry²⁷

but in the case of Voigt geometry $d\sigma/d\Omega$ reaches its maximum for crossed polarization of \vec{e}_S and \vec{e}_L . In dipole approximation only Spin-Flip transitions of $\Delta m_s = \pm 1, \pm 2$ are allowed e.g. in CdMnTe bulk material.

2.4.3 Microscopic view of inelastic light scattering at elementary excitations

The fundamental description of light scattering in solids starts with the Hamiltonian (H) of the solid in an electromagnetic field. This Hamiltonian can be split into three parts:

$$H = H_{solid} + H_{exch} + H_R \quad (2.71)$$

with

- H_{solid} describes all unperturbed systems of the crystal (e.g.: lattice, electrons, Mn-spins etc.) and their electronic, phononic and spin excitations
- $H_{exch} = H_i + H_{eR}$ where H_i describes the exchange interaction of excitations among each other (electron \leftrightarrow phonon, charge carrier \leftrightarrow Mn-ions) and H_{eR} stands for the electron-radiation interaction
- H_R represents the Hamiltonian of the incident and scattered photons

It should be mentioned that all Raman measurements done in this thesis are *resonant* Raman measurements. Thus, only the resonant Raman scattering conditions will be discussed in this subsection²⁸.

The scattering probability from initial $|i\rangle$ to final $|f\rangle$ state with energy E_i and E_f

²⁷Voigt geometry: $\vec{k}_L \perp \vec{B}$)

²⁸for more details see [YC01]

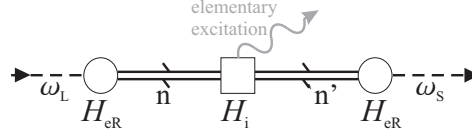


Figure 2.12: One of six permutations describing Stokes Raman scattering via Feynman diagrams is shown according to [YC01]. The circles and squares are vertexes representing the electron radiation interaction Hamiltonian H_{eR} and the electron-phonon (or carrier Mn-ion) interaction Hamiltonian H_i . The parallel lines between the vertexes represent the e-h pairs (intermediate states).

can be derived from FERMI's Golden Rule. In terms of perturbation theory the first vertex in Figure 2.12 can be described as follows:

$$\sum_n \frac{\langle n | H_{eR} | i \rangle}{[\hbar\omega_i - (E_n - E_i)]} \quad (2.72)$$

This is one term out of three forming the scattering probability for the Feynman diagram in Figure 2.12. E_n is the energy of the intermediate state $|n\rangle$. The whole scattering probability for an elementary excitation ($P_{elemexc}$)- under the assumption that the final state is again the electron ground state (= initial state) - has the form:

$$P_{elemexc}(\omega_S) = \left(\frac{2\pi}{\hbar} \right) \left| \sum_{n,n'} \frac{\langle f | H_{eR}(\omega_S) | n' \rangle \langle n' | H_i | n \rangle \langle n | H_{eR}(\omega_L) | i \rangle}{[\hbar\omega_L - (E_n - E_i)][\hbar\omega_L - \hbar\omega_0 - (E_{n'} - E_i)]} \right|^2 \cdot \delta[\hbar\omega_L - \hbar\omega_0 - \hbar\omega_S] \quad (2.73)$$

For completeness: to receive the whole off-resonance scattering probability the five mentioned permutations of Figure 2.12 must be added to (2.73) (cf. [YC01]).

When either the incoming (ω_L) or scattered light (ω_S) is energetically close to an electronic excitation energy this is understood as *resonant Raman scattering*. That means that the non-resonant terms (the mentioned permutations above) can be regarded as a small constant C . Thus, (2.73) represents the strongest contribution. Assuming that the initial electronic state is the ground state $|0\rangle$ of the semiconductor with $E_0 = 0$ i.e. no existing electron-hole pair and the resonant intermediate state is denoted as $|a\rangle$ and energy E_a , the scattering probability for a given elementary excitation (like a PR-signal) in the vicinity of E_a can be approximated:

$$P_{res} \approx \left(\frac{2\pi}{\hbar} \right) \left| \frac{\langle 0 | H_{eR}(\omega_S) | a \rangle \langle a | H_i | a \rangle \langle a | H_{eR}(\omega_L) | 0 \rangle}{[E_a - \hbar\omega_L][E_a - \hbar\omega_S]} + C \right|^2 \quad (2.74)$$

Summing over ω_S removes the delta function in (2.73) [YC01]. The difference between $\hbar\omega_L$ and $\hbar\omega_S$ is equal to the energy of the elementary excitation. This is very small compared to the electronic energies. The case $E_a = \hbar\omega_L$ stands for the incoming resonance and $E_a = \hbar\omega_S$ is the outgoing resonance. These two denominators only vanish simultaneously for special circumstances [YC01].

When either the incident ($\hbar\omega_L$) or the scattered photon energy ($\hbar\omega_S$) is resonant with E_a the denominator vanishes and the scattering probability (2.74) would diverge. An

option to deal with this unphysical situation is to assume that $|a\rangle$ has a finite lifetime τ_a due to radiative and nonradiative decay processes [YC01]. Thus E_a can be replaced by the complex energy $E_a - i\Gamma_a$. Where Γ_a is the damping constant with the relation $\Gamma_a = \hbar/\tau_a$.

Assuming that the resonant state E_a is a discrete state (e.g. an excitonic state) and is energetically well separated from other intermediate states, the scattering probability of an elementary excitation in the vicinity of the state E_a can be expressed as

$$P_{res} \approx \left(\frac{2\pi}{\hbar} \right) \left| \frac{\langle 0 | H_{eR}(\omega_S) | a \rangle \langle a | H_i | a \rangle \langle a | H_{eR}(\omega_L) | 0 \rangle}{[E_a - \hbar\omega_L - i\Gamma_a][E_a - \hbar\omega_S - i\Gamma_a]} \right|^2 \quad (2.75)$$

Using now (2.75), the differential cross section and thus the transition amplitude of a three step resonant Raman scattering process can be written as [HL78]:

$$\frac{d\sigma}{d\Omega} \propto P_{res} \quad (2.76)$$

The paramagnetic resonance (PR) Raman scattering is an example for a three step resonant Raman scattering process mentioned above. The scattering process and its mechanism will be described in detail in the next subsection.

2.4.4 Paramagnetic Resonance Raman scattering

First the difference between the PR-signal and the so called band Spin Flip should be pointed out.

The PR-signal is the Spin Flip ($\Delta m_s = 1$) in the half filled 3d-shell of the Mn-ion ground state between two ZEEMAN-split and formerly degenerated spin states shown earlier in Figure 2.3. As a result the previously mentioned three step scattering process let the Mn-ion get from its ground state to an excited one (e.g. $m_s = -5/2 \rightarrow m_s = -3/2$). PR-Raman scattering can be seen as "atomic spectroscopy" on Mn-ions inside a solid state body.

In contrast, the band Spin Flip of an electron is a Spin Flip from one spin subband to its opposite spin subband in the GIANT-ZEEMAN-split conduction band caused by the external B-field. An electron with e.g.: spin-up is photo-excited to its dipole allowed spin-splitted state. An already existing electron with spin-down in the other spin-split state recombines. The magnetic spin quantum number m_s of the electron is changed by ± 1 (e.g. $m_s = +1/2 \rightarrow m_s = -1/2$). This two step scattering process needs therefore n-doped semimagnetic semiconductors to get the condition of an already existing electron in one of the spin-split states. From this kind of measurements the exchange constants α and β of the CB and VB, respectively can be determined.

The light scattering at the Mn-ion spins is an indirect excitation process. Via sp-d exchange interaction a photo-excited e-h pair causes the Spin Flip at Mn-ions. The band states of the semiconductor are the intermediate states of the resonant Raman process. An exchange interaction Hamiltonian H_i connects the band states and the Mn-ions. In the case of PR-Raman scattering this exchange interaction Hamiltonian is H_{exch} , known from subsection 2.2.4. According to the previous subsection this three step Raman process can be described by (2.75), replacing H_i by H_{exch} .

The band states²⁹ involved in the scattering process can be determined from H_{exch} i.e. from the sp-d exchange interaction of the Mn-ions and the photo-excited charge carriers.

As a reminder to subsection 2.2.4:

$$H_{exch} \propto -\alpha \vec{S} \vec{J}_{electron} \text{ and } H_{exch} \propto -\beta \vec{S} \vec{J}_{hole} \quad (2.77)$$

respectively, where $\vec{S} \vec{J}_{electron, hole}$ can be written as

$$S^z J^z + \frac{1}{2} S^+ J^- + \frac{1}{2} S^- J^+. \quad (2.78)$$

The first term in (2.78) represents the Rayleigh scattered light. The second term causes a SF of the Mn-ion with $\Delta m_S = +1$ which has its origin in a Stokes PR-Raman scattering process due to sp-d exchange. Simultaneously a (virtual) spin flip of the electron (hole) with $\Delta m_J = -1$ is involved in the scattering process. Term three represents the Anti-Stokes process i.e. the reduction of the Mn-spin energy in the B-field by $\Delta m_S = -1$.

The scattering mechanism is shown in Figure 2.13 and can be described in three steps according to [PPV⁺83]:

1. Transition of an electron from the VB to a virtual (real) state in the CB by Laser photon absorption
2. Spin Flip of a Mn 3d-shell electron spin $\Delta m_S = +1$ due to sp-d exchange interaction and a virtual Spin Flip of the CB electron (VB hole) $\Delta m_J = -1$
3. Recombination of an electron from a real (virtual) CB state to the VB band by photon emission

This Spin Flip in the Mn-ion is equivalent to the excitation of the Mn-ion by a value $E_{PR} = g_{Mn} \mu_B B$. After the scattering process the electronic system has returned to the initial state (ground state). At high B-fields ($\geq 3.0T$) the splitting of the VB and CB due to GIANT-ZEEMAN effect is much larger than the linear ZEEMAN splitting of the ${}^6S_{5/2}$ -Mn ground state. Therefore, only one of the dipole transitions in the scattering process can be resonant, the other intermediate state is virtual. This virtual state is represented in Figure 2.13 as a dashed line between the two spin splitted CB states. Paying attention to the dipole selection rules ($\Delta m_J = 0, \pm 1$) of the transition in step 1 and 3 of the scattering mechanism, there are six possible transitions i.e. three possibilities for each PORTO-notation³⁰ in Voigt geometry shown in Figure 2.14. For simplicity only the spin splitted bands of VB and CB are shown with their real transitions and without any virtual states and the Mn-states, respectively. As can be seen from Figure 2.14 out of each cross polarization configuration³¹ one electron-induced and two hole-induced Mn-Spin Flips are possible. All measurements in this thesis were done in $-z(\pi, \sigma)z$ configuration and have hole-induced Mn-Spin Flips.

²⁹ Γ_8 VB with $J_{hole} = 3/2$ and Γ_6 CB with $J_{electron} = 1/2$

³⁰e.g.: $-z(\pi, \sigma)z \equiv$ "direction of k_L (polarization of laser light, polarization of scattered light) direction of k_S "

³¹i.e. in- and out-going polarization are perpendicular to each other

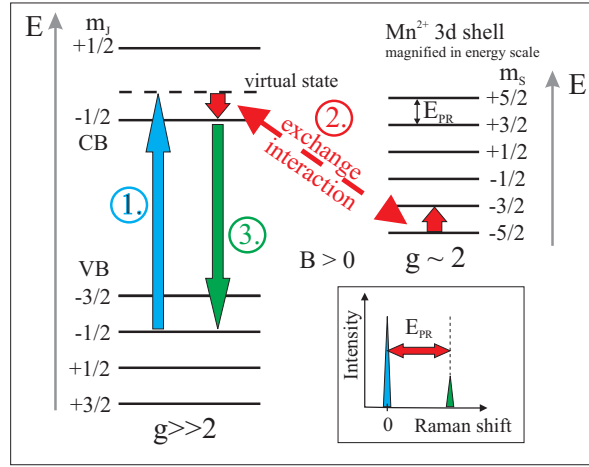


Figure 2.13: Scheme of the three step PR-transition in bulk material. Due to the fact that E_{PR} is only a few hundred μeV [PPV⁺83] the Zeeman-split states of the Mn-ion is presented in an enlarged energy scale with respect to the band splittings of CB and VB, respectively. The inset shows a schematic PR-Raman spectrum. The PR-signal is shown with a green peak and the red arrow represents its energy red-shift relative to the laser line (blue).

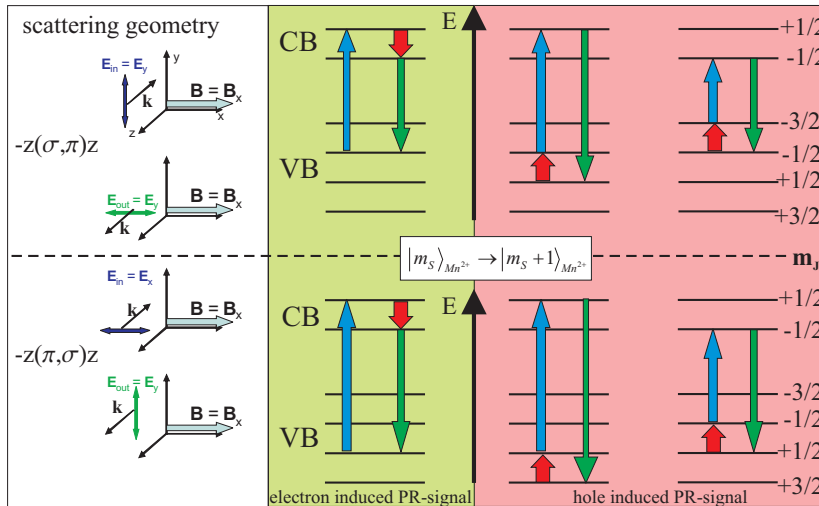


Figure 2.14: Selection rules for PR-Raman scattering in Voigt geometry with $\Delta m_J = 0, \pm 1$ according to [PPV⁺83]. Left hand side: Highlighted in white: PORTO-notation of the selection rules. Middle and right: spin splitted bands in Voigt geometry; green: electron-induced spin flip; red: hole induced Spin Flip.

2PR-Raman scattering implies a second order PR-Raman scattering process ($\Delta m_S = 2$). Its scattering probability can be derived very similar to the procedure above. Now the numerator of one of the possible permutations of the 12 Feynman diagrams with four vertices consists of four terms. The summation runs over three intermediate states. Due to huge band splitting compared to the manganese ${}^6S_{5/2}$ -ground state, resonance is achievable only with one of the electronic band states. Both others virtually take part in the scattering process.

The dipole selection rules of backscattering geometry for $\Delta m_S = 2$ in Voigt configuration are presented in Figure 2.15 according to [PPV⁺83]. Two hole-hole processes

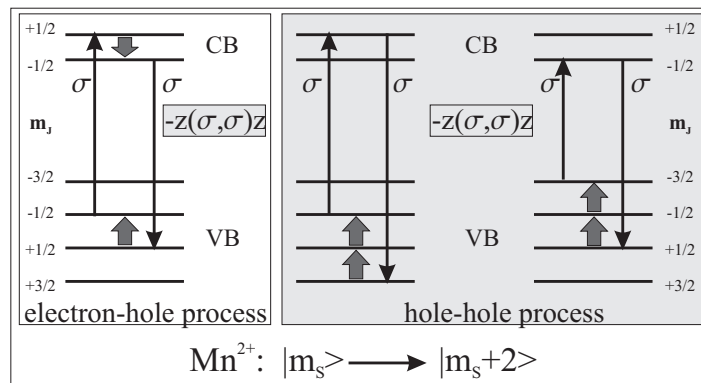


Figure 2.15: 2PR Raman scattering in Voigt configuration

and one electron-hole process can occur, where the virtual SF-transitions either take place both in the VB or one in the CB and one in the VB. In dipole approximation the n PR-Ramanscattering for $n > 2$ i.e. $\Delta m_S > 2$ is forbidden in CdMnTe bulk material. The situation of the n PR-Ramanscattering for $n > 2$ completely changes for the case of semimagnetic quantum wells, being discussed in the next sub section.

2.4.5 Multi Paramagnetic Resonance Raman scattering

I.A. MERKULOV and K.V. KAVOKIN explain the phenomenon of Multi-PR Raman scattering in a demonstrative way by means of a time-dependent formalism [KM97] ([RS83] [SSD⁺95]) called "**exchange box model**". The possibility to describe the Multi-PR Raman scattering with the formalism for the PR-Raman scattering in bulk material is restricted³². But the advantage of a time-dependent formalism delivers a demonstrative picture of the intermediate state devolution (in time). Thus the dynamic of the intermediate state can be described by a quasi-classical precession of Mn^{2+} -spins in an effective magnetic field (see below).

There are three physical phenomena which are involved in this time-dependent formalism and which are closely connected. These are

³²The eigenvalues of the polaron operator as an intermediate state of the scattering process are not taken into account

1. a DMS QW with its (*HH-spin anisotropy* in Voigt geometry mentioned in previous sections,
2. a 2D *electron-hole pair* which is connected with
3. a 2D *polaron formation* of Mn^{2+} -spins inside this QW.

For the formalism some general considerations are made:

The QW VB has an ideal and total anisotropy i.e. no HH-spin splitting in an external magnetic field in Voigt geometry (i.e. two-fold degenerated spins) and thus no HH-LH mixing (see subsection 2.3.3). Therefore the HH-spins are oriented along the growth direction (z)³³ with $m_J = \pm 3/2$.

The e-h pair is a localized exciton consisting of a CB electron and a heavy hole of the energetically highest VB subband excited by linear polarized light. This localized exciton is the intermediate state of the Raman scattering process. Due to the anisotropy of the HH-spins the HH of the exciton is responsible for the exchange interaction with the Mn^{2+} -spins forming a (2D) magnetic polaron (see A.3) [MK95].

A magnetic polaron in general is a system of aligned magnetic ions (here: Mn-ions) within the volume of a charge carrier wave function (here: exciton-HH wave function) which is schematically shown in Figure 2.16. The HH of the exciton which is from

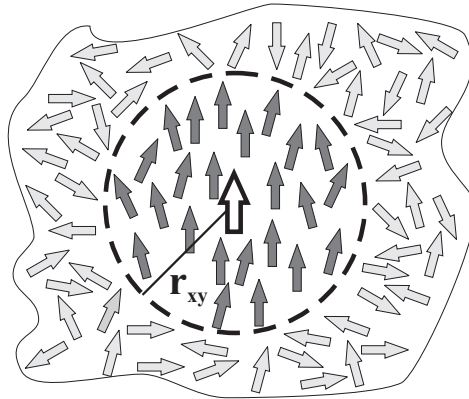


Figure 2.16: Scheme of magnetic polaron: White arrow is the exciton-HH centred in its localisation volume V (dashed circle) with localization radius r_{xy} . The grey arrows in general represent the Mn-ion spins. Dark grey spins are affected by the hole wave function within r_{xy} .

now on called "the HH" and the Mn-ions are coupled by strong exchange interaction with the Hamiltonian for localized states (see appendix A.3, second term in equation (A.18)):

$$H_{exch} = -\frac{1}{3}\beta \sum_i \left[\vec{J}\vec{S}_i |\Psi(\vec{R}_i)|^2 \right] \quad (2.79)$$

with the HH wave function $\Psi(\vec{R}_i)$ with spin \vec{J} at the position \vec{R}_i of the i -th Mn-ion with spin \vec{S}_i . (2.79) considers according to [MK95]³⁴ a hole interacting with the sum

³³this is valid for QWs of low width

³⁴based on [RS83]

over the Mn^{2+} -spins within the hole volume $\vec{I} = \sum_i \vec{S}_i$. This is based on a formal assumption that the hole wave function Ψ is constant within the localization region V and zero outside i.e. $|\Psi(\vec{R}_i)|^2 \propto \frac{1}{V}$ for all \vec{R}_i inside V and zero outside V , respectively. This is called the "**exchange box model**".

The main property of the exchange interaction for Multi-PR Raman scattering is its anisotropy. The reason for is that there is no total HH angular momentum component in the plane of the QW ($\langle J_x \rangle = \langle J_y \rangle = 0$). Thus the HH with a constant momentum projection m_J on the z-direction allows transitions in Voigt geometry which have different projections \vec{I}_x of the total Mn^{2+} -spin \vec{I} within the HH volume V on $\vec{B}_{ext} \parallel \vec{x}$. From theory of magnetic poltroons (see appendix A.3,(A.18)) the exchange interaction between HHs and Mn^{2+} -spins can be expressed by an exchange field \vec{B}_{exch} , which is caused by a HH ($J_z = \pm 3/2$) at the location of the Mn^{2+} -spin, oriented along growth direction z:

$$\vec{B}_{exch}(\vec{R}_i) = - \frac{1}{g_{Mn}\mu_B} \frac{\beta}{3} \cdot |\Psi(\vec{R}_i)|^2 \vec{J} \quad (2.80)$$

The Multi-PR scattering is strongly dependent on $\vec{B}_{exch}(\vec{R}_i)$ and thus on $|\Psi(\vec{R}_i)|^2$ of the localized exciton. The variation of the QW width L influences $\vec{B}_{exch}(\vec{R}_i)$ because a decreasing L causes an increasing $|\Psi(\vec{R}_i)|^2$ [Stü95].

From eigenvalues of the total 2D polaron Hamiltonian (A.19):

$$H = \sum_i g_{Mn}\mu_B \vec{S}_i \left(\vec{B}_{ext} + \vec{B}_{exch} \right) \quad (2.81)$$

the Multi-PR scattering process can be demonstrated in an easy way. The result is the quasi-classical precession of the total Mn^{2+} -spin \vec{I} with Larmor frequency

$$\omega_L = \frac{g_{Mn}\mu_B}{\hbar} \sqrt{(B_{ext}^2 + B_{exch}^2)} \quad (2.82)$$

in an effective magnetic field

$$\vec{B}_{eff} = \vec{B}_{ext} + \vec{B}_{exch} \text{ where } \vec{B}_{ext} \perp \vec{B}_{exch} \quad (2.83)$$

Mechanism The mechanism of the time-dependent formalism can be described demonstratively in three time-steps.

The excitation of an exciton in the magnetic field B_{ext} in Voigt at $t=0$ is connected with a polaron formation of total Mn^{2+} -spin \vec{I} within the HH-volume and simultaneously "switching on" the exchange field B_{exch} caused by the exciton-HH. During the lifetime of the exciton the total Mn^{2+} -spin \vec{I} precesses around \vec{B}_{eff} with the Larmor frequency ω_L (Figure 2.17a).

At the time $t=T$ when the exciton recombines the precession around \vec{B}_{eff} stops instantaneously and B_{exch} "switches off". The projection $I_x(t=T)$ of $\vec{I}(t)$ on \vec{B}_{ext} changed its value compared to $I(0)$ at the beginning of the scattering process (Figure 2.17b). Thus the Mn-system is in an excited state at the end of the scattering process. The

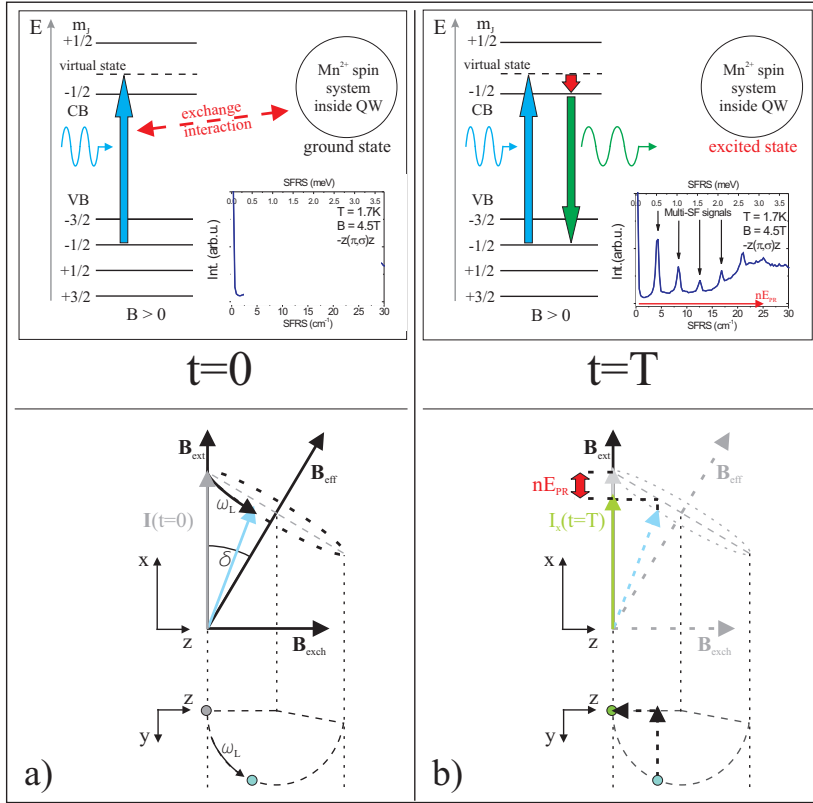


Figure 2.17: **Scheme of Multi-PR-Raman scattering.** a) "switching on" the exchange field (B_{exch}) via HH-exciton excitation and exchange interaction with the QW Mn^{2+} -spin system. b) "switching off" the exchange field (B_{exch}) via HH-exciton recombination leaving the QW Mn^{2+} -spin system in an excited state. Observable by Multi-PR-Raman scattering (inset of above figures)

angle δ between B_{ext} and B_{eff} is given by

$$\sin\delta = \frac{\vec{B}_{exch}}{\sqrt{(B_{ext}^2 + B_{exch}^2)}} \quad (2.84)$$

and is used for calculating the expectation value of the alteration of the projection \vec{I} on \vec{B}_{ext} :

$$N(t) = |I_x(t) - I_x(0)| = I \cdot \sin^2\delta \cdot (1 - \cos(\omega_L t)) \quad (2.85)$$

In the frame work of the "Virtual-Crystal" approximation it can be written for an arbitrary $|\Psi(\vec{R}_i)|^2$:

$$N(t) = \int_V dV \rho_{Mn} S \cdot \sin^2\delta \cdot (1 - \cos(\omega_L t)) \quad (2.86)$$

with the density of Mn-ions ρ_{Mn} and $S=5/2$.

So far all considerations are done at $T = 0K$. For $T \neq 0K$, $S = 5/2$ in (2.86) must be replaced by the expectation value $\langle S \rangle (B_{ext}, T)$

$$N(t) = \int_V dV \rho_{Mn} \langle S \rangle (B_{ext}, T) \cdot \sin^2\delta \cdot (1 - \cos(\omega_L t)) \quad (2.87)$$

The probability of observing an n -th order Mn-SF at a certain time t after the exciton excitation is discussed in detail in [Stü95]. This thesis takes a shortcut to the result without discussing the analytical details. Ending up with the probability of emitting a scattered photon of energy $\hbar \cdot \omega_i - ng_{Mn}\mu_B B_{ext}$ is

$$P_n(t) = \int_0^\infty dt e^{-\frac{t}{\tau}} \frac{N(t)^n}{n!} e^{-N(t)} \quad (2.88)$$

considering the limited lifetime τ ($\approx 1ps$ [Stü95]) of the intermediate state. This probability offers no information of the polarization of the scattered light. According to [SSD⁺95] "*no selection rules are effective*" so that there is no need to discuss transition probabilities in detail here³⁵. The majority of the Multi-PR-Raman measurement were done in crossed geometry (π, σ) .

2.5 Theoretical prediction of K.V. Kavokin

This section emphasises the experimental confirmation of K.V. Kavokin's theoretical prediction of influencing the Mn g-factor by hole concentration in a semimagnetic QW. The first section presents the theoretical prediction of K.V. Kavokin according to his publication in 1999 ([Kav99]). This prediction is based on the RKKY³⁶ [Yos57]-mechanism, i.e. in the case of this thesis the indirect exchange correlation of Mn-ions via holes confined in the QW. The subsequent section gives a brief overview of the Raman setup used for confirming his theory. Then the experimental results are presented and discussed.

The subject of K.V. Kavokin's publication in 1999 (cf. [Kav99]) is the analysis of the dynamics of the coupled spin systems of 2D hole gas (2DHG) and magnetic ions in a quantum well applying an in-plane magnetic field using a mean-field approach. It is predicted by K.V. Kavokin that the Larmor frequency ω_L of the magnetic ions interacting with the hole gas depends on the hole gas concentration. Thus ω_L of the localized spins is reduced under the influence of the oscillating effective field of holes. Hence, it is assumed that the z -axis is parallel to the growth direction while the x -axis defines the direction of external magnetic field $\vec{B}_{ext} (\equiv \vec{B})$ in the QW plane.

The following Hamiltonian describes both the spin system of holes (heavy holes) and the system of the Mn-ions and their interaction in DMS:

$$H_S = a \sum_{i,j} (\hat{J}_j \hat{S}_i) \delta(\vec{r}_j^C - \vec{r}_i^I) + H_{SS} + \sum_i (\vec{B} \cdot \hat{S}_i) \quad (2.89)$$

- a : parameter of the exchange interaction between the spin system of holes and Mn-ions
- \hat{J}_j and \vec{r}_j^C : operator of spin and position vector of the j -th carrier (here heavy holes $J = 3/2$), respectively

³⁵more details are presented in [Stü95]

³⁶Ruderman-Kittel-Kasuya-Yoshida, e.g. [RK54]

- \hat{S}_i and \vec{r}_i^I : operator of spin and position vector of the i -th magnetic ion, respectively.

The first term represents the carrier-ion (here: hole-Mn²⁺) exchange interaction³⁷. The second term stands for the superexchange interaction of adjacent Mn-ions mentioned in subsection 2.2.3 and the third term is the ZEEMAN energy of the Mn-ions in an external magnetic field \vec{B} . The smaller ZEEMAN energy of the heavy holes is neglected. For the holes both the strong spin-orbit interaction and the quantum well confinement (mentioned earlier) are included in this theory i.e. degenerated HH and LH-subbands appear at the top of the VB.

For the further discussion of the two spin systems the focus lies on the evolution of spin-density vectors of ions and holes averaged over the QW. For that reason the exchange field B_{exch} mentioned in subsection 2.4.5 is discussed now within a mean-field approach. Therefore the carrier-ion interaction is represented in terms of exchange fields which are proportional to the average spins of holes and Mn-ions, respectively. These exchange fields affect Mn-ion and hole spins, respectively. According to [Kav99] neither the holes nor the Mn-ions create in-plane components of mean fields which act upon each other.

The mean fields are expressed by:

$$\text{Mean field of holes: } \vec{b}_{hi}(t) = a |\psi_h(z_i)|^2 \vec{j}(t) \quad (2.90)$$

$$\text{Mean field of Mn-ions: } \vec{B}^I(t) = a \sum_i |\psi_h(z_i)|^2 \vec{s}_i(t) \quad (2.91)$$

with the hole-spin density \vec{j} parallel to the z-axis and the average values \vec{s}_i of the operators \hat{S}_i . $\psi_h(z_i)$ is again the wave function of holes determined by the confinement potential of the QW. According to KAVOKIN: *The mean spin evolves under the z component of these fields. The extreme anisotropy of the exchange interaction of spins averaged over entire ensembles of holes and magnetic ions plays the decisive role in their spin dynamics,...*[Kav99].

The nonscalar part of H_{SS} [FSN96] is likely the main reason for the relaxation of Mn²⁺-spins and the rapid spin relaxation of holes ($< 1ps$) is caused by the interaction with the Mn-ion subsystem in DMS QWs. Due to considerable wave vectors³⁸ this relaxation should be more effective for Fermi-edge holes in modulation-doped structures (even at low temperatures). Without going into details of this scope, the theoretically discussed hole-spin relaxation supported by experimentally confirmed short spin-decay times [CAB⁺97] is important for the analysis of the coherent spin dynamics in the system discussed below.

Now, the dynamics of mean-spin density of Mn-ions is described by \vec{s}_i . These dynamics are influenced by both the external magnetic field B ³⁹ and the exchange field $\vec{b}_{hi} \parallel z$ -axis caused by holes (HH) in each monolayer (with index i) of the semimagnetic QW

³⁷ \hat{J}_j and \hat{S}_i enclosed by the brackets represent their scalar product

³⁸ k_z -vectors in QWs are beyond the Γ -point of the BZ and yield an energy contribution $E \propto k_z^2$

³⁹Subsequently B_{ext} will be named B which is parallel to x-axis.

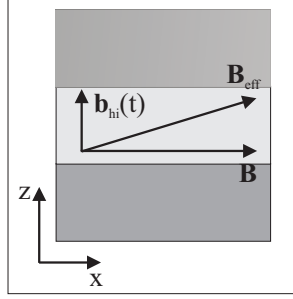


Figure 2.18: B-field directions of the external B-field B and the mean field of holes b_{hi} according to [Kav99]

leading to an effective B-field mentioned earlier.

Under the experimental conditions in this thesis and in the work of e.g. [CAB⁺97] the following approximation can be made:

$$B \gg b_{hi} \quad (2.92)$$

which is valid because the external applied field is of the order of a few Tesla ($1\text{T} \leq 5\text{T}$) in these experiments and $b_{hi} \leq 0.1\text{T}$ [HWA⁺97] for a completely polarised 2DHG ($n_h = 10^{11}\text{cm}^{-2}$). As a consequence \vec{s}_i is directed very close to the external B-field vector \vec{B} during hole (exciton) lifetime and during the evolution of the spin system. Thus the time evolution of each \vec{s}_i and therefore of Mn^{2+} -spins can be described by the following differential equations:

$$\dot{s}_{iz} = -Bs_{iy} - \frac{s_{iz} - s_{0z}[b_{hi}(t)]}{T_2} \quad (2.93)$$

$$\dot{s}_{iy} = Bs_{iz} - b_{hi}(t)s_{ix} - \frac{s_{iy}}{T_2} \quad (2.94)$$

$$s_{ix} = s_{0x}(B) \quad (2.95)$$

which represents the BLOCH equations for the applications in this thesis (see appendix A.4). The approximation of (2.92) leads to $s_{ix} = s_{0x}(B)$ in (2.95) where $s_{0x}(B)$ and $s_{0z}(b_{hi})$ are the equilibrium values of the corresponding spin-density components in B and b_{hi} , respectively [Kav99]. T_2 represents the transverse ionic spin relaxation time (compare A.4).

Due to the interaction of holes with the Mn-ions the spin relaxation of holes is very fast. According to CROOKER et al [CAB⁺97] the experimentally determined spin relaxation time of holes is $\tau_{sh} < 1\text{ps}$. This is shorter than any other relaxation time in the Mn^{2+} -spin system ($> 100\text{ps}$) and also shorter than the Larmor precession period in usually applied external magnetic fields ($20 - 100\text{ps}$). Under these conditions the dynamical interaction between the spin subsystem of holes and Mn-ions can be described as "a time-dependent hole-spin density $j(t)$ governed by the instant value of the Mn-ion exchange field" [Kav99]:

$$j(t) = j[B_z^I(t)] \quad (2.96)$$

i.e. a direct time-dependent connection can be made between the mean-field of holes and the mean field of Mn-ions and thus the system of equations (2.95) becomes closed.

Now (2.95) is multiplied by $a \cdot |\psi_h(z_i)|^2$ and summed over i to solve the system of equations (see appendix A.5.1).

$$\dot{B}_z^I = -BB_y^I - \frac{1}{T_2} \left[B_z^I - a^2 \cdot W \cdot s_{0x}(B) \cdot \frac{j(B_z^I)}{B} \right] \quad (2.97)$$

$$\dot{B}_y^I = BB_z^I - a^2 \cdot W \cdot s_{0x}(B) \cdot j(B_z^I) - \frac{B_y^I}{T_2} \quad (2.98)$$

This is a set of equations for components of \vec{B}^I with $W \equiv \sum_i |\psi_h(z_i)|^4$. According to K.V. KAVOKIN the stationary states of (2.98) relate to $B_y^I = 0$ and B_z^I is defined by (see appendix A.5.2):

$$BB_z^I - a^2 \cdot W \cdot s_{0x}(B) \cdot j(B_z^I) = 0 \quad (2.99)$$

Only one solution $B_z^I = 0$ exists for (2.99), when

$$\zeta = a^2 \cdot W \cdot \frac{s_{0x}(B)}{B} \cdot \left. \frac{dj(B_z^I)}{dB_z^I} \right|_{B_z^I=0} \leq 1 \quad (2.100)$$

If $\zeta > 1$ there are three stationary states. One state with $B_z^I = 0$ is unstable and the others which are located symmetrically with respect to $B_z^I = 0$ are stable. These two stable states represent saturated magnetization of holes as well as a nonzero z component of the Mn-spin density. The physical meaning of these two stable states is the carrier-induced ferromagnetic transition (see [HWA⁺97]) for a zero in-plane B-field. This transition can be induced by decreasing the temperature because of the temperature dependence of $s_{0x}(B)/B$. Summarizing: $\zeta \leq 1$ represents the paramagnetic phase of the system, while $\zeta = 1$ is the phase transition point. $\zeta > 1$ describes the ferromagnetic phase. Later on in this section, these phases are presented in Figure 2.19 in connection with the corresponding precession of the mean spin of Mn-ions

In the case of small oscillations of the spin system between stationary states on both sides of the transition (black dots in Figures 2.19b and c), the equations (2.97) and (2.98) can be seen as linear near their corresponding stationary state⁴⁰. Satisfying now the condition (2.100), the eigenfrequency of the oscillating vector \vec{B}_I can be expressed by [Kav99]:

$$\omega \approx B\sqrt{1-\zeta} \quad (2.101)$$

with μ_B and \hbar taken as unity.

As can be seen from the above equation the Larmor frequency ω of the mean field of Mn-ions is always below the precession frequency of free Mn^{2+} -spins at equal external field B . Thus the Mn-g-factor is less than 2 under these circumstances.

Summarizing equation (2.101), ω depends on the following parameters:

- hole wave function $\psi_h(z_i)$: $W = \sum_i |\psi_h(z_i)|^4$

⁴⁰i.e. it is assumed that the system can be seen as a radial 2dim. harmonic oscillator in the y - z plane

- equilibrium value of the corresponding spin-density component in B , denoted here as $s_{0x}(B)$, where $s_{0x}(B)/B$ can be seen as the susceptibility of the Mn^{2+} -spin density which is T-dependent
- paramagnetic susceptibility of the hole gas $\frac{dj(B_z^I)}{dB_z^I}$ with respect to the z-component of the mean field of Mn-ions B_z^I

From (2.90) and (2.91) and finding $B^I(t)$ under the appropriate initial conditions, the time-dependent exchange fields $b_{hi}(t)$ produced by holes at ions of each monolayer can be obtained. Using now (2.95), the time-dependent ion spin densities can be calculated. $b_{hi}(t)$ represents the driving force of the system. For further detailed analysis see [Kav99]. The result is that the ends of the spin-density vectors \vec{s}_i , move synchronously along similar orbits for $t \gg \tau_{sh}$:

$$\vec{s}_i(t) = s_{0x}(B) \left\{ \vec{e}_x + aj_0\tau_{sh} |\psi_h(z_i)|^2 e^{-\frac{t}{T_2}} \left[\vec{e}_z(1-\zeta)^{-\frac{1}{2}} \sin \omega t + \vec{e}_y \cos \omega t \right] \right\} \quad (2.102)$$

with $\tilde{T}_2 = T_2/(1-\zeta/2)$ the renormalized damping time⁴¹.

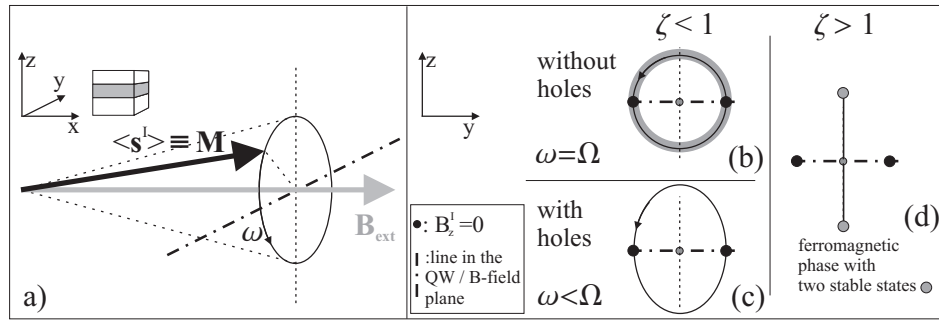


Figure 2.19: (a) Precession of the mean spin of Mn-ions $\langle s^I \rangle$ with respect to the external B-field. (b) and (c) represent the paramagnetic phase $\zeta \leq 1$. (b) Precession of $\langle s^I \rangle$ in the y-z-plane in the absence of holes. The dash-dotted line is in the plane of the QW while the dotted line is in the direction of the exchange B-field. If $\langle s^I \rangle$ deflects from the QW-plane the Zeeman energy increases (grey ring apart from the black circles in (b)). The precession frequency ω is equal to the Larmor frequency of free Mn^{2+} -spins Ω . The black circles represent $B_z^I = 0$. (c) Due to the exchange interaction between the normal-to-plane components of the spin of holes and of Mn-ions, the (Zeeman) energy shift is reduced in the presence of holes causing an elliptical precession of \mathbf{M} . ω is smaller than the Larmor frequency of free Mn^{2+} -spins. (d) represents the ferromagnetic phase with two stable states located symmetrically with respect to $B_z^I = 0$ (grey circles) where each corresponds to the saturated magnetization of holes and a non zero z component of $\langle s^I \rangle$ [Kav99].

The whole effect discussed here is an entirely dynamical one and can be verified according to its physical background. Initially, by the photo-generation of an e-h pair (i.e. switching-on the exchange field $B_{exch} \perp B_{ext}$) the mean spin of Mn-ions $\langle s^I \rangle$ deflects from the QW plane and thus from the direction of the external B-field and starts to precess around $\vec{B}_{eff} = \vec{B}_{ext} + \vec{B}_{exch}$. After the e-h recombination (i.e. switching-off

⁴¹assuming $B \gg 1/T_2$

the exchange field B_{exch}) the mean spin of Mn-ions $\langle s^I \rangle$ precesses around the external magnetic field $B \parallel x$ (see Figure 2.19(a)). During the deflection of $\langle s^I \rangle$ out of the QW plane it has to be distinguished between two cases:

- deflection of $\langle s^I \rangle$ in the absence of holes
- deflection of $\langle s^I \rangle$ in the presence of holes

In the absence of holes the deflection of $\langle s^I \rangle$ causes an increase in its ZEEMAN energy (proportional to the second power of the deflection angle). From the underlined part of (2.102) with $\zeta = 0$ it can be pointed out that the y- and z-components are classically conjugated variables of a large spin with its main direction along x (see Figure 2.19(b)). Thus the Larmor precession can be considered as an oscillation in this parabolic potential [KM97]. In this case the head of $\langle s^I \rangle$ describes a circle.

In the case of holes are present in the QW, the energy shift (due to increasing Zeeman energy) is reduced to the benefit of the exchange interaction between the z-components⁴² of the hole-spins and the Mn^{2+} -spins during the deflection. The head of $\langle s^I \rangle$ describes an ellipse shown in Figure 2.19(c). Due to the fact that this energy has a negative quadratic behaviour with the deflection angle, the interaction with holes results in a decrease of the eigenfrequency of the system i.e. the rigidity of the system is lowered proportional to $(1 - \zeta)$. *"Such a softening of oscillation modes is typical of systems undergoing phase transitions"* [Kav99].

It should be briefly discussed why this frequency shift is not related with the Knight shift of NMR⁴³ frequency. The Knight shift in general is the effect of the contact interaction between the conduction electron spin and the nuclear spin which leads to a small frequency shift in the nuclear resonance frequency [Blu04]. The interacting electrons can be considered in terms of an effective field which is acting on the local ion spins. This can be understood like the electrons hop on and off a given nucleus. The nucleus experiences a net hyperfine coupling which is the result of averaging over all the electron spin orientations. The static average of the hyperfine interactions causes the Knight shift. In a non-zero static magnetic field this net hyperfine coupling will be non-zero, because this B-field will polarize the electron spins. Thus the external B-field and the exchange field of the electrons are parallel to each other.

In contrast here in K.V. KAVOKIN's theory, due to the heavy hole spin anisotropy in QWs the exchange field is perpendicular to the QW-plane and in this case perpendicular to the external B-field. The time average of the hole exchange field is zero. The Knight shift is a static effect while the effect discussed here is dynamic.

So far K.V. KAVOKIN described the effect of the magnetic soft mode behaviour in a quantum mechanical formalism. For a more demonstrative picture of K.V. KAVOKIN's theoretical description it follows a semi-classical description.

An Ansatz is made with the already mentioned Bloch equations (see appendix A.4) neglecting any relaxation processes i.e. $T_1, T_2 \rightarrow \infty$:

$$\frac{d\vec{M}}{dt} = \gamma \cdot \vec{M} \times \left[\vec{B} + \vec{B}_h(t) \right] \quad (2.103)$$

⁴²normal-to-plane components

⁴³nuclear magnetic resonance

where $\gamma = g_{Mn}\mu_B/\hbar$, \vec{B} and $\vec{B}_h(t)$ are the external magnetic field (along the x-axis) and the exchange field of polarized holes (along the z-axis), respectively. For the sake of simplicity \vec{M} stands for the mean spin of Mn-ions (cf. Figure 2.19). It is considered that the holes possess the maximal anisotropic (hole-)g-factor, so that the exchange field of the Mn-ion spins acts on the hole spins only in the case when the projection of the magnetic moment of Mn-ions on the z-direction is non-zero (i.e. $M_z \neq 0$). In the exchange field of the Mn-ion spins the polarisation degree of the 2DHG (i.e. the magnetization) is proportional to M_z which deflects from the x-y plane by the angle θ . Thus $B_h \propto M_z$ leads to

$$B_h = \kappa \cdot M_z \quad (2.104)$$

The exchange field of holes \vec{B}_h in turn acts on the magnetic moment \vec{M} with a typical positive feedback. This results in an additional momentum, which increases the deflection of \vec{M} from the x-y plane (i.e. M_z) and is proportional to θ . In this case the head of \vec{M} describes an elliptical precession (cf. Figure 2.19c). Due to the higher magnetic susceptibility of the 2DHG (proportional to this additional torque) more time is required for the recovery of \vec{M} in the state for $M_z = 0$ and $\theta = 0$, respectively. Thus the reason for retarding the precession of \vec{M} ($\omega < \Omega$) is the presence of the 2DHG.

Assuming now in (2.103) like in the quantum-mechanical description $|\vec{B}\rangle \gg |\vec{B}_h\rangle$ thus $M_{y,z} \ll M_x$ with $M_x \approx M = \text{const}$ and $\theta \ll 1$, $B_y = 0$ and $B_z \equiv B_h = \kappa \cdot M_z$ it follows

$$\begin{aligned} \frac{dM_x}{dt} &= 0 \\ \frac{dM_y}{dt} &= -\gamma (M_x \cdot \kappa \cdot M_z - M_z \cdot B) \\ \frac{dM_z}{dt} &= -\gamma \cdot M_y \cdot B \end{aligned} \quad (2.105)$$

This set of equations can be seen as a radial harmonic oscillator in the y-z plane solving its differential equations with the Ansatz $M_y = M_1 \sin(\omega t)$ and $M_z = M_2 \cos(\omega t)$ and using $\Omega = \gamma \cdot B$, $\chi_{Mn} = M/B$. It is ending up with an equation similar to (2.101)

$$\omega = \Omega \sqrt{1 - \chi_{Mn} \cdot \kappa} \quad (2.106)$$

From its definition in (2.104), κ is proportional to the hole spin susceptibility χ_h .

In the end of reference [Kav99], K.V. KAVOKIN made an outline how to proof this theory experimentally. The soft mode behaviour can either be influenced by varying temperature close to the transition point or by influencing the hole concentration inside the QW.

Furthermore, he mentioned that the effect discussed above might be the reason for the shift of Larmor frequency observed in [CAB⁺97]. It was attempted to describe quantitatively the results that the concentration of holes was essentially time dependent and the carriers might be overheated due to high power of the used pump pulse. Nevertheless K.V. KAVOKIN came to the conclusion that investigations on modulation-doped structures containing equilibrium holes, or on undoped structures under controllable

continuous-wave (cw) illumination, would provide more feasible and detailed information on the behaviour of the spin system.

This thesis will point out in the next sections that the effect above can be investigated under the condition of modulation-doped (surface-doped) QWs *and* controllable continuous-wave illumination. Using Multi-PR-Raman scattering to investigate modulation-doped semimagnetic QWs gives access to the Mn^{2+} -spin system. The hole concentration can be influenced by an additional cw illumination.

The setup for these Two-Colour experiments is described in the next section.

Chapter 3

Setup and samples

3.1 Two-Colour experiment: Combining Multi-PR Raman scattering with an additional light source

For this thesis a low-temperature and resonant Raman setup is used for investigating the $\text{Cd}_{1-x}\text{Mn}_x\text{Te}/\text{Cd}_{1-y}\text{Mg}_y\text{Te}$ quantum wells, which is shown in Figure 3.1. The tuneable Dye-Laser (red: *Pyridine2* spectral range: 675-783nm i.e.:1.58-1.84eV) is pumped by the Ar^+ -Laser with the green 514.5nm-line (2.41eV). *Pyridine2* was chosen for resonant excitation of the (lowest) QW-states. Depending on the Mn-content of the samples ($x=0.6\%$ and 1.0%) the lowest transition energies are between 1.60eV and 1.61eV¹. A detailed sample description will follow in a subsequent section.

The Ar^+ -Laser is used simultaneously as an additional light source with excitation energy above the $\text{Cd}_{1-y}\text{Mg}_y\text{Te}$ barrier ($E_g(\text{Cd}_{.80}\text{Mg}_{.20}\text{Te})=1.94\text{eV}$)² realized by a beam splitter between the pump laser and the Dye-Laser.

The samples were investigated in an optical bath-cryostat with a split coil magnet mostly at a He-bath temperature of 1.7K. Some additional measurements were performed at temperatures up to 4.2K. The B-fields up to 4.5 T were applied in the sample plane ($B\parallel x$) in Voigt geometry. The signals were detected by a charge-coupled device (CCD) linked to a subtractive triple spectrometer, providing a spectral resolution of about 0.5 cm^{-1} ($65\text{ }\mu\text{eV}$). The attenuators in Figure 3.1 tune the power of both laser-light sources. The polariser and analyser are used in cross polarisation (π, σ) for all measurements in this thesis.

The photoluminescence (PL) and Raman spectra were measured with the tuneable Dye-Laser and the additional light provided by the Ar^+ -Laser. The motivation for this two-colour experiment is that the Dye-Laser is used to probe the Multi-PR signals, while simultaneously the charger carrier concentration inside the QW is tuned by the above barrier illumination from the additional light. The ideal alignment is given when both light spots on the sample overlap.

On the one hand the shape and height of the characteristic PL of the QW is dependent

¹cf.: Table:2.3

²according to Table 2.2

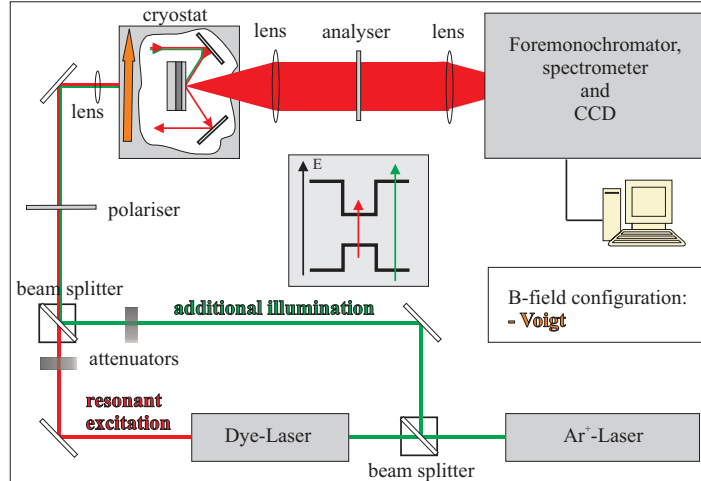


Figure 3.1: Scheme of the two-colour Raman setup. The centred grey inset shows the CdMnTe/CdMgTe QW scheme; the vertical arrows represent the above-barrier excitation by additional illumination (green) and the below-barrier exciton by the Dye-Laser (red)

on the power of the Dye-Laser P_b and its spectral position with respect to the QW gap and on the other hand it is dependent on the power of the additional illumination P_a (demonstrated in subsequent sections). This means that the Ar⁺-Laser can be utilized to tune the hole concentration in the QW while the Dye-Laser is used in the low-power range of a few μW to probe the Multi-PR Raman signals. Essentially, the low-power range avoids the Dye-Laser to induce a non-negligible contribution to the hole concentration. The reason for this setup configuration is that the efficiency of the carrier generation by the Dye-Laser would depend on the B-field, because of the GIANT-ZEEMAN shift of the semimagnetic QW-states. In contrast, the above barrier excitation (i.e. the non-resonant excitation) guarantees the independence of the carrier generation efficiency from the B-field.

3.2 CdMnTe/CdMgTe quantum well samples

The investigated samples in this thesis were grown in Warsaw at the Institute of Physics, Polish Academy of Sciences by Prof. Dr. Grzegorz Karczewski's group. The samples consist of single $\text{Cd}_{1-x}\text{Mn}_x\text{Te}/\text{Cd}_{1-y}\text{Mg}_y\text{Te}$ -QWs each, grown by molecular-beam epitaxy (MBE) on a GaAs substrate oriented in (001)-orientation followed by a thick CdTe buffer of $4.1\mu\text{m}$. Their main parameters are represented in Table 3.1.

The samples 031907B-I to IV originate from the same growth procedure with different cap thicknesses and equivalent Mn-concentration. This was achieved by step-wise partly masking the wafer during the growth procedure of the cap layer till the desired cap thickness was reached [Kra07]. The differences between sample 030807A-I and samples 031907B-I-IV are the well width (12nm and 10nm), the Mn-concentration, the cap thickness (see Table 3.1) and the barrier thicknesses with $0.5\mu\text{m}$ and $1.1\mu\text{m}$, respectively. The Mn-concentration of the quantum well was determined via magneto-photoluminescence (magneto-PL) in Faraday-geometry. With the aid of equation (2.29) the effective Mn-concentration was determined from the BRILLOUIN-fit of the magneto-PL plot³. The magneto-PL-investigated samples are marked with (*). It is guaranteed that the samples 031907B-II to IV have the same Mn-content as the investigated 031907B-I sample because of their derivation from the same growth process. This is the reason for investigating the Mn-content only at one sample out of four from the samples series 031907B-I-IV.

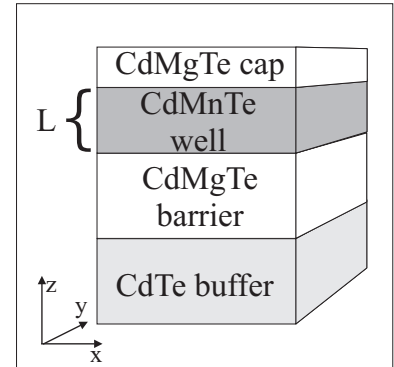


Figure 3.2: QW

sample	Mn x/(%)	Mg y/(%)	well width L/(nm)	cap thickness/(nm)
030807A-I	0.67*	20	12.0	17.5
031907B-I	1.00*	20	10.0	13.0
031907B-II	1.00	20	10.0	15.0
031907B-III	1.00	20	10.0	17.0
031907B-IV	1.00	20	10.0	19.0

Table 3.1: Sample list with the most important parameters of the single $\text{Cd}_{1-x}\text{Mn}_x\text{Te}/\text{Cd}_{1-y}\text{Mg}_y\text{Te}$ -quantum wells.

All the samples are nominally undoped i.e. no doping elements are incorporated during the MBE growth process. Instead they are near-surface doped, positioning the QW close to the surface i.e. by growing only a very thin cap layer. Thus the surface states in combination with the cap thickness play a major role for influencing the carrier concentration (here: holes) inside the QW by photo-generated carriers. This is experimentally demonstrated and discussed later on in section 4.1.

³PL-signal vs. applied B-field

In the subsequent sections sample 030807A-I is used to demonstrate K.V. Kavokin's theoretical prediction. The same effects will be investigated at the other four samples under the aspect of varying cap thickness.

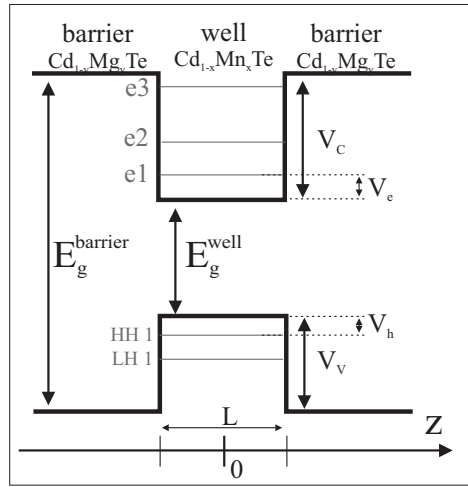


Figure 3.3: QW sample scheme

sample	Mn x: /(%)	Mg y: /(%)	L /(nm)	V_e /(meV)	V_h /(meV)	V_C /(meV)	V_V /(meV)
030807A-I	0.67	20	12.0	24	12	185*	123*
031907B-I-IV	1.00	20	10.0	38	19	181*	121*

Table 3.2: Sample properties of the single $\text{Cd}_{1-x}\text{Mn}_x\text{Te}/\text{Cd}_{1-y}\text{Mg}_y\text{Te}$ -quantum wells are estimated using the equations in section 2.3.1. (*) Band off-set: $V_C/V_V=60/40$

Chapter 4

Experimental results of a near-surface doped CdMnTe/CdMgTe QW (030807A-I)

4.1 Photoluminescence - characteristics -

4.1.1 Identification of photoluminescence signals

Demonstrated at a below-barrier excited QW photoluminescence spectrum shown in Figure 4.1 the typical electronic features for this kind of QW samples will be discussed in this subsection. In Figure 4.1 the transitions belonging to the lowest sublevel ($e1$, HH1) of the QW are identified by the exciton energy X at 1.6210eV, the positive trion T^+ at 1.6181eV and the impurity-bound exciton A at 1.6151eV. The exciting laser line L is positioned in resonance with the "blue" shoulder of the exciton signal.

The exciton and its binding energy in a QW were already discussed in section 2.3.1. A simple and general description of a trion is given by a charged exciton i.e. either a positive one consisting of an exciton and an additional hole or a negative one because of an additional electron (cf. [HCS⁺00] [SOS⁺95]). The following experimental subsections demonstrate and discuss the PL-signals under the aspect of their laser power dependence und thus the influence of photo-generated carriers on the PL-signals and their shape respectively. Prior to that the different regimes of charge carrier density in low dimensions and their effects on the electronic excitation and quasi-particles are briefly discussed.

Carrier density regimes Considering a bulk semiconductor in general the absorption of photons causes different kind of quasi-particles dependent on its charge carrier density. Depending on the excitation intensity, KLINGSHIRN [Kli07] distinguishes three types of regimes with gradual boundaries:

- low density regime

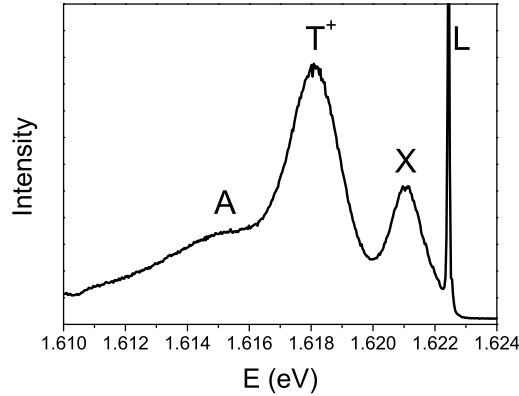


Figure 4.1: QW PL spectrum for below-barrier excitation at a Dye-Laser power $P_b \approx 6\mu\text{W}$. From the high to the low energy scale can be seen the Dye-Laser line (L) 1.6224eV, the exciton signal (X) 1.6210eV, the positive trion signal (T^+) 1.6181eV and the impurity-bound exciton (A) 1.6151eV.

- intermediate density regime
- high density regime

The **low density regime** starts from a semiconductor in the ground state with its VB completely filled with electrons and an empty CB. The low intensity of the incident light excites single e-h pairs which determine the optical properties either in the excitonic states or in the continuum. Additionally these excitons have the opportunity of forming bound exciton complexes caused by defects.

The **intermediate density regime** is reached with increasing excitation power. This regime is characterised by the fact that the excitons are still good quasi-particles, but they interact with each other. These interactions may be caused e.g. by elastic and inelastic scattering processes between excitons and at higher temperatures between excitons and free carriers. Furthermore coherent and incoherent interaction processes can cause the formation of biexcitons and trions (charged excitons). The biexciton, consisting of two electrons and two holes, in the hydrogen-model can be compared to the H_2 molecule and more to the positronium molecule. The constituent parts of the trion (the more relevant quasi-particle concerning this thesis), were already discussed above. Besides the exciton, the trion can also be observed in the PL-measurements mostly in QWs due to its increasing binding energy with decreasing well width [RPV00]. A more detailed discussion of the trion will follow later on in this subsection.

The **high density regime** or better known as the regime of electron-hole plasma (EHP) is reached at even higher excitation power compared to the intermediate density regime. The excitons lose their identity as individual quasi-particles by forming a new collective phase, the electron-hole plasma i.e. a certain electron is no longer bound to a specific hole. The formerly sharp PL-peaks of exciton and trion signals, respectively end up in a broadened and asymmetric peak called Fermi-edge singularity (FES). The FES marks the onset of the EHP [KBB⁺04] and is caused by multiple scattering processes involving electrons (or holes) near the Fermi level [HCS⁺00].

In the intermediate and high density regime the consequence of the PAULI principles and correlation effects with increasing carrier concentration have to be considered. Individually, these effects would cause an energy blue-shift and red-shift in e.g. PL-spectra, respectively.

At first neglecting any spin relevance, the increase of carrier concentration weakens the Coulomb-exchange interaction between e and h due to the presence of additional charge carriers. This is called **screening**. Thus the exciton binding energy E_{Bind}^X is decreased, leading to a blue-shift in its energetic position. The screening effect is most pronounced in bulk material and is reduced in a QW because the screening is less effective in growth direction (z). There, the screening is due to the wave functions of the well and not due to the barrier wave functions.

The **phase-space filling** has also a blue-shifting effect on the PL-signal due to the fact that only unoccupied states can be used to form an exciton. This plays an important role in low dimensional semiconductors [Kli07]. In detail: up to the electron hole plasma the carriers are not randomly distributed. The exchange interaction of identical fermions forbids two electrons (holes) with parallel spin to be in the same energy state (PAULI principle). Consequently their total repulsive Coulomb energy is reduced i.e. the total energy of the electron system is lowered (blue-shifted) [Kli07].

In the regime of high carrier density there is an increasing probability of finding both the differently charged carriers and the carriers of opposite spin next to each other. This is caused by correlation effects. The corresponding correlation energy lowers the energy of the e-h-pair system [Kli07] and thus increases the exciton binding energy for the whole e-h-pair system. Consequently the exciton PL-energy red-shifts due to the renormalisation of the bandgap and ends up at the Fermi-edge singularity mentioned above. According to [Kli07] the correlation energy is a "*reminder*" of the Coulomb interaction among electrons and holes which is responsible for the formation of excitons at low densities.

The sum of these two effects above is called the exchange and correlation energy. The effects can be seen in chapter 6 for a blue-shifting exciton and trion signal in the low-power range before it returns to its initial value (for the exciton) or red-shifts (for the trion signal) with further increasing illumination power.

Trion or charged exciton The existence of these quasi-particles based on the hydrogen model was theoretically predicted by LAMBERT in the late sixties [Lam58]. The positively charged trion (T^+) was the hydrogen equivalent of H_2^+ and the negative trion of H^- . The first experimental confirmation of negative trions in CdTe-based QWs was published by KHENG et al [KCdA⁺93]. The observation of the positive trions in CdTe-based QW was reported e.g. by BRINKMANN et al [BKV⁺98]¹. All the trions investigated in this thesis are positively charged. The combination of a near-surface single QW and the photo-generated carriers by above and/or below-barrier excitation² causes a majority of holes inside the QW as the nucleus for the creation of positive trions. Subsequently all discussion and explanations will refer to positive trions.

Starting with the exciton in a QW already mentioned in section 2.3.1 the focus is now

¹overview articles of positive trions in CdMnTe/CdMg(Zn)Te QWs by Kossacki et al. [Kos03], [KBB⁺04]

²possible mechanisms will be discussed in detail in 7

located on its spin system in an external magnetic field. Figure 4.2a schematises the Zeeman splitting of the spin states of the exciton. Due to the QW confinement the sublevels energetically close to the VB maximum are HH sublevels. Thus the lowest possible exciton excitations in the QW are HH excitons. The exciton is created by a photon which has either the total spin $+1$ (σ^+) or -1 (σ^-). As a consequence light of polarisation σ^+ couples to an electron of $-1/2$ spin ($s_z^{electron} = -1/2$) and a hole of spin $+3/2$ ($s_z^{hole} = +3/2$), light of polarisation σ^- couples the other way round. $S_z = s_z^{electron} + s_z^{hole}$ is the net spin z-component of the exciton in Figure 4.2. A brief explanation of the exciton spin system for individual spin presentation and net spin presentation is given in A.6.

As mentioned previously a positively charged trion consists of one electron and two

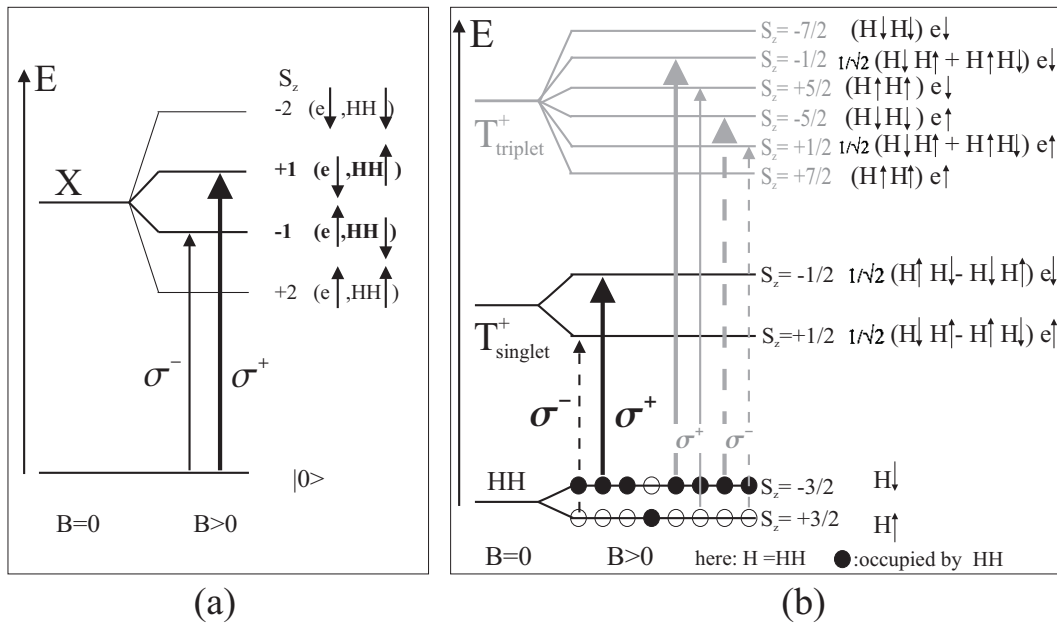


Figure 4.2: Spin system of (a) the exciton and (b) the trion in the QW with their net spin z-component S_z with and without an applied magnetic field in Faraday configuration according to SHIELDS et al. [SPRM95], [SOS⁺95]. Thicker vertical arrows represent stronger excitations due to higher hole population of the appropriate state. The black dots represent the holes.

holes. The spins couple to the total spin S and its z-component S_z . Analogously to H_2^+ the possible trion states can be distinguished by the symmetry of the spin part of their wave function $|S, S_z\rangle$ either forming a singlet or triplet state which is shown in Figure 4.2b. Due to PAULI principle the system with two identical fermions requires a total wave function which is anti-symmetric upon exchange of its particles. That means either the (hole-) spin part of the wave function is symmetric and the spatial part anti-symmetric or vice versa [SPRM95]. This is the case when the hole spins couple to either a singlet state with total hole spin 0 or a triplet with a total (hole-)spin quantum number of 3 with its (hole) z-component $s_z^{hole} + s_z^{hole} = +3, 0, -3$ (see Figure 4.2b) The total z-component of the trion $S_z = s_z^{electron} + s_z^{hole} + s_z^{hole}$ can be written for the

- singlet state: $S_z = s_z^{electron} + 0 = \pm 1/2$ with an anti-symmetric hole spin part of

the wave-function and

- triplet state: $S_z = \pm 1/2, \pm 5/2, \pm 7/2$ with a symmetric hole spin part of the wave-function.

Without an external magnetic field the lowest energy state of the positive trion is the singlet state (Figure 4.2b). The net spin in the singlet state is the electron spin in the positive trion. Thus the ZEEMAN splitting of T^+ is affected by the e-CB-splitting alone. Subsequently only the singlet-state which is the relevant one for this thesis will be discussed.

An interband transition (vertical lines in Figure 4.2b) creates a T^+ by exciting an e-h pair binding to a second excess hole. By the recombination of the electron and the hole under photon emission, a hole is left in the VB.

$$T^+ \leftrightarrow \text{photon} + h \quad (4.1)$$

These transitions are allowed if the total z-component of the spin changes by +1 (σ^+) or -1 (σ^-) in Faraday geometry [SOS⁺95]. At low temperatures the excitation from the VB state $HH \downarrow$ in 4.2b is stronger than from the lower-energy state $HH \uparrow$ because of its higher hole population [SOS⁺95].

Compared to the photon energy of the exciton recombination, the photon energy of T^+ recombination is reduced by the amount of the binding energy of the second hole. The trion binding energy E_{Bind}^T is the required energy to "split" the trion into an unbound hole (called "left-over hole" in [BWM⁺08]) and a neutral exciton [SSA⁺05]. For the case of very diluted hole gas (hole concentration approaches zero) this energy corresponds to the energy difference between the exciton and the trion signal ($E_X - E_T$). For increasing hole concentration, ($E_X - E_T$) increases linearly with the Fermi energy E_F . According to [KCF⁺99] [RPV00] [HCS⁺00] the 2DHG-concentration can be determined using the following equation:

$$E_X - E_T = E_{Bind}^T + E_F \quad (4.2)$$

where the spectral distance of exciton and trion ($E_X - E_T$) is taken from "Zero-Tesla" PL-spectra. Then the 2DHG-concentration n_h can be calculated from the two-dimensional Fermi-energy

$$E_F \equiv E_F^{2D} = \frac{\pi \cdot \hbar^2 \cdot n_h}{m_e \cdot m_{in-plane}^*} \quad (4.3)$$

with m_e the free electron mass³ and the effective in-plane hole-mass $m_{in-plane}^* = 0.2$. The prediction, calculation and experimental confirmation of the positive- and negative-trion binding energy in heterostructures like QWs, are discussed in several publications (e.g. [SSA⁺05], [BSG⁺05], [SA89] et cetera) and goes beyond the scope of this thesis. The quintessence is a decreasing trion binding energy E_{Bind}^T with increasing well-width L. The trion binding energy E_{Bind}^T for the samples in this thesis is about 2.4meV [RPV00].

The increasing difference ($E_X - E_T$) with increasing hole concentration can be described with a simple model illustrated in Figure 4.3 according to [KCF⁺99] and [Haw91].

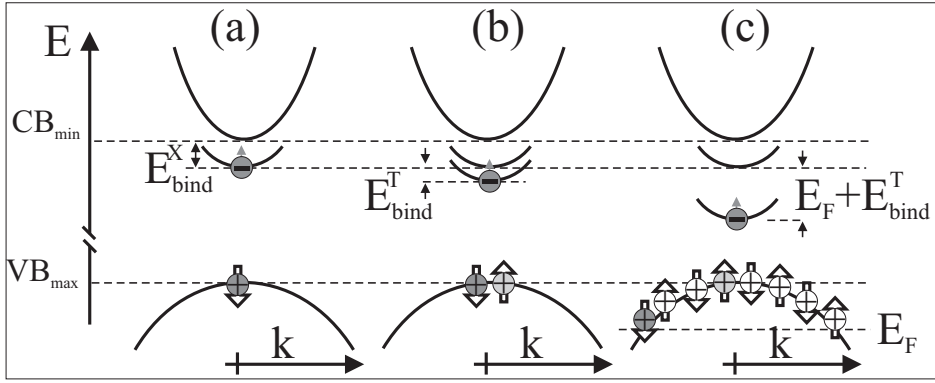


Figure 4.3: Scheme of the positive trion in the electron picture. (a) The common dispersion of an exciton with the in-plane wave vector k of the QW. E_{bind}^X is the exciton binding energy. (b) A trion scheme at the lower limit of the hole-concentration ($n_h \rightarrow 0$) i.e. providing only one additional hole (light-grey) of opposite spin to the photo-generated e-h pair (grey). Binding the additional hole to the e-h pair results in the decrease of transition energy by the trion binding energy E_{bind}^T . (c) Scheme of a trion in the presence of a 2DHG ($n_h > 0$) marked by the two grey and one light-grey spots representing the e-h pair and the additional hole out of the 2DHG.

In principle the reason for the coexistence of the neutral and charged excitons (trions) is the existence of bound levels that appears in the two-dimensional charge carrier gas in the presence of a carrier of opposite sign, i.e. here an electron in the presence of a 2DHG [KCF⁺99]. In this picture an exciton corresponds to a single occupancy of this level. The dispersion of the exciton is schematically shown in Figure 4.3(a) with its binding energy E_{bind}^X . Providing now one additional hole (light-grey) to this exciton (Figure 4.3(b)) the transition energy of the exciton is reduced by the binding energy of the second hole E_{bind}^T . In the presence of a 2DHG, the positive trion involves - in addition to the generation of the e-h pair from the Fermi-level E_F (grey e-h pair in Figure 4.3(c)) to the bound state - the binding of one hole with opposite spin (light-grey in Figure 4.3(c)) out of the 2DHG to the e-h pair with respect to the Fermi-level. Thus the transition of Figure 4.3(c) is smaller than the one in Figure 4.3(b).

This manifests in a red-shifting PL-trion signal with increasing hole concentration. In the following subsections 4.1.2 - 4.1.4 this effect is observed with increasing incident light power.

The identification of the trion as a positive one can be confirmed with the help of resonance measurements of the Multi-PR signals. That means the laser line is tuned from the blue shoulder of the PL-signal to the red one under an externally applied B-field by paying attention for the intensity of the Multi-PR signals and thus by their resonance behaviour which is shown in Figure 4.4. In the case of a negative trion the Multi-PR signal will appear both in the resonance of the exciton and the trion. On the contrary for a positive trion the Multi-PR signal will only appear in the resonance of the exciton.

The anisotropy of the QW and thus of the HH-states already discussed in subsections 2.3.2 to 2.3.3 and the phenomenon of the Multi-PR signals (subsection 2.4.5) helps to

³ $m_e = 9.1095 \cdot 10^{-31} \text{ kg}$ [HH85]

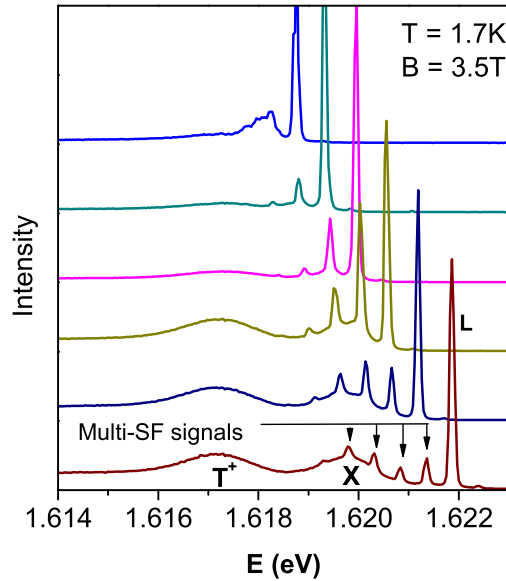


Figure 4.4: Multi-SF resonance spectra with varying Dye-Laser energy (1.6218-1.6180eV) at 1.7K and at an external B-field of 3.5T. Multi-PR signals appear only in resonance with the exciton PL-signal and disappear in resonance with the trion PL-signal. This is an indication for the existence of positive trions.

	h-spin	e-spin
exciton	\uparrow	\downarrow
negative trion	\uparrow	$\downarrow\uparrow$
positive trion	$\uparrow\downarrow$	\downarrow

Table 4.1: Spin system of the exciton and trion

explain this argumentation. The Multi-PR signals are caused (amongst other things) by the anisotropy of the HH-spin momentum and its resulting exchange field B_{exch} . Thus HHs are necessary to "observe" the Multi-PR signals. The resulting spin in a negative exciton is the HH-spin because the two electron-spins align antiparallel due to the PAULI-principle. On the contrary the electron spin is the resulting one in a positive trion shown in Table 4.1. Due to the latter case no Multi-PR signal can appear in resonance with the positive trion due to the absence of the HH-spin.

4.1.2 Below-barrier excitation

Using the Dye Laser for the below-barrier excitation by varying its illumination power the observed PL-behaviour is shown in Figure 4.5a. On the one hand with increasing Dye-power P_b the intensity of the trion signal increases at the expense of the exciton signal (intensity stealing/ oscillator strength stealing [GPK⁺04]). On the other hand

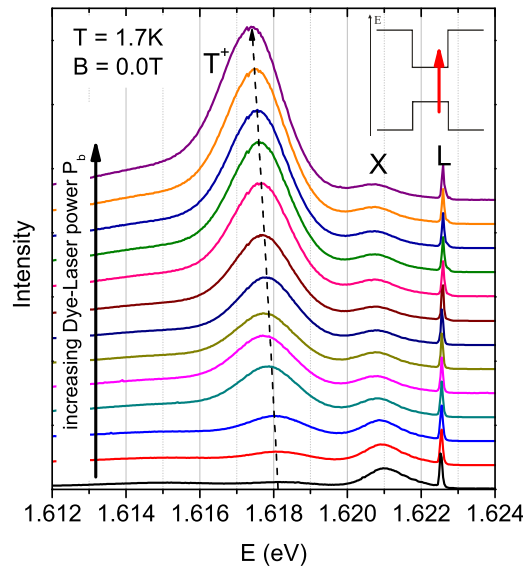


Figure 4.5: Below-barrier excitation of the QW with 12nm well width, 0.67% Mn-content and 17.5nm cap thickness at varying Dye-Laser power (P_b : 1 to $45\mu\text{W}$). The trion signal red-shifts (about 1meV) and increases in intensity at the expense of the exciton signal with increasing power of below-barrier excitation (dashed line as a guide of the eye). This indicates an increasing hole concentration inside the QW. The exciton signal also shows a small red-shift with increasing below barrier excitation. Its reason is discussed in the text.

the energetic position of the trion signal is red-shifted which is shown in detail in Figure 4.7a for more spectra than those presented in Figure 4.5. The exciton red shift saturates at about $10\mu\text{W}$ with an energetic position of 1.6207eV. The signal position is determined by fitting the PL-signals with Gaussian peak-functions⁴.

Three-Gaussian-peaks fitting procedure All PL-spectra were fitted with a three-Gaussian-peak fit which is shown for demonstration in Figure 4.6 for three different illumination powers. In general a clear and satisfying fitting result⁵ is achieved at each PL-spectrum where the exciton X and trion T^+ signal can be clearly observed i.e. the PL is excited by a "moderate" illumination shown in Figure 4.6(b). Only the low energy shoulder of the blue-coloured Gaussian fit misfit the experimental data. A significant discrepancy between the PL spectrum and its three-Gaussian-peak fit exist at spectra with either very low illumination power (absence of the trion signal) like in Figure 4.6(a) or at very high illumination power (absence of the exciton signal) like in Figure 4.6(c). These spectra should exemplarily demonstrate the problematic extrema concerning the fitting procedure.

The exciton X and the impurity-bound exciton A are the dominant signals in Figure 4.6(a) and can be fitted easily. In this spectrum it is difficult to determine the spectral

⁴Program: ORIGIN 7.5

⁵criterion: the envelope function (red curve in Figure 4.6) of the three-Gaussian-peak fit reproduces the measurement data as good as possible within the fitting region

position of the trion due to the fact of its very low intensity. In contrast, in Figure 4.6(c) the trion signal is the dominant one and the exciton is marginally observable. In addition, the low-energy side of the trion signal is asymmetric merging with the impurity-bound exciton A. Thus A cannot be fitted as a separate peak anymore. Due to this T^+ -A merging, the low energy side of the characteristic PL signal cannot be reproduced using symmetric Gaussian peaks. In this case an adequate fitting result is a well reproduced line shape of the high energy side of the experimental data via the two Gaussian peaks (Figure 4.6(c) magenta (T^+) and green peak (X)). This can be justified because the main focus within the fitting procedure is on the exciton X and trion T^+ especially on their spectral position in order to evaluate the hole concentration inside the QW. As a consequence of these fitting complications the error bars of the evaluated

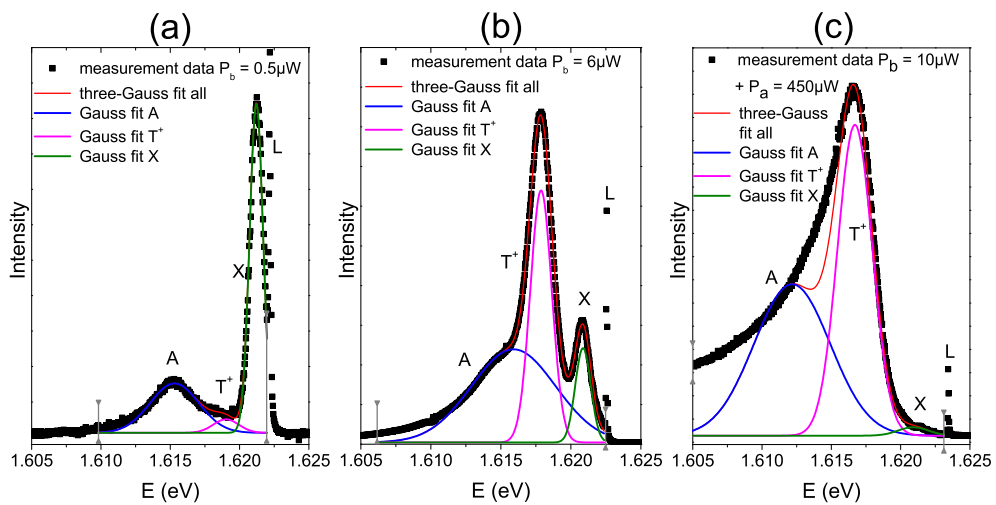


Figure 4.6: ORIGIN 7.5 Fitting procedure using three Gaussian functions demonstrated for three characteristic QW spectra with different illumination powers. (a) Very low-below barrier illumination power which results in an intense exciton signal X dominating the PL-spectrum. Here, the impurity-bound exciton A can be fitted as a separate peak. (b) "Moderate" and thus most common illumination power for the following Multi-PR measurements. In this PL-spectrum both the exciton X and the trion signal T^+ are prominent. (c) Large illumination power mainly caused by above-barrier illumination P_a resulting in a huge and asymmetric trion signal. In (b) and (c), T^+ and A merge which makes the fitting procedure with symmetric Gaussian functions more complicated. More details are discussed in the text.

hole concentration is larger at low illumination power (i.e. absence of the trion signal) and at large illumination power (i.e. absence of the exciton signal) compared to the error bars of the determined hole concentration evaluated at moderate illumination power where both the trion and the exciton signal are observable.

As already mentioned a small red-shift of the exciton was observed in Figure 4.5. The reason for this exciton red-shift could be the imbalance of the red-shifting correlation effect and the blue-shifting phase-space filling effect mentioned in section 4.1.1, i.e. the correlation effect is the dominant one up to about $P_b=10\mu W$. As already mentioned, the effect of screening plays a minor role in QWs. While the exciton red-shift is

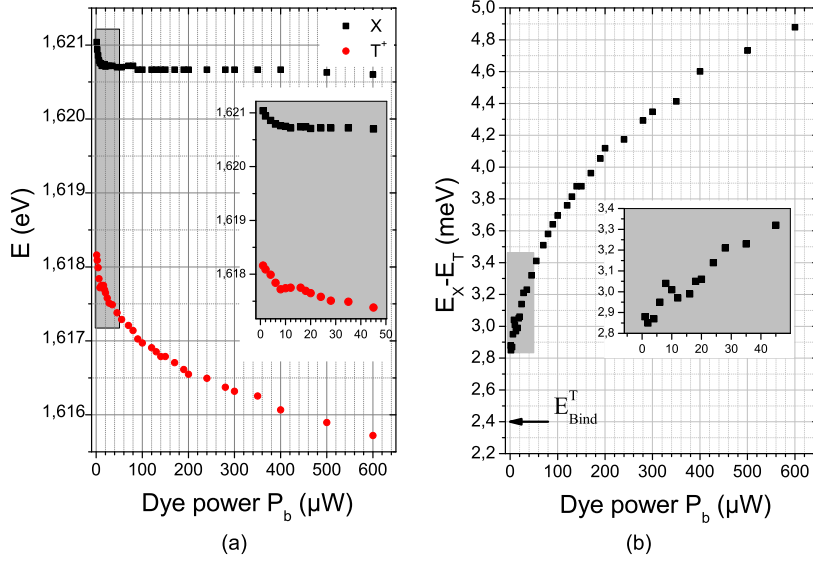


Figure 4.7: Dependence of the exciton X and trion position T^+ (a) as well as their energetic distance $E_X - E_T$ (b) on the increasing below barrier excitation P_b . (a) The filled squares (black) show the exciton position while the filled circles (red) represent the trion position with increasing P_b . The grey inset in (a) shows the magnified low power range up to $50\mu\text{W}$ which corresponds to the PL spectra representatively shown in Figure 4.5. (b) The energetic distance between X and T^+ with increasing P_b . The grey inset shows again the low power range of (a).

saturation, the trion red-shift is more pronounced with a continuous energy down-shift in this power range. Consequently, plotting now $E_X - E_T$ versus P_b like in Figure 4.7b, the spectral distance $E_X - E_T$ is increasing with increasing Dye-power and gives a direct access to estimate the hole concentration using (4.2).

The PL-behaviour of X and T^+ (intensity stealing) monitored in this subsection is analogue to several publications dealing with similar QW structures ([Kos03] [KBB⁺04] [KCF⁺99] [HCS⁺00]). A detailed discussion of the physical background is given in chapter 7.

It should be mentioned that the values of light power P_b and P_a in Figure 4.6 are a qualitative orientation of the photo-carrier generation rate. The minimum and maximum light power can differ due to adjustment details. The quantitative values of light power are subject to errors. A direct measure for the carrier density is the PL-shape, the energetic distance between exciton and trion ($E_X - E_T$), the intensity ratio of exciton and trion and the full width of half maximum (FWHM) of the trion, respectively. This is demonstrated in Figure 4.8 where the X-T area ratio (Figure 4.8b) decreases with increasing P_b while the trion FWHM increases (Figure 4.8c). Whereas the energetic distance $E_X - E_T$ is more useful concerning the evaluation of the hole concentration, the intensity ratio of exciton and trion is a more intuitive indication

directly seen from the spectrum by eye. The last possibility in the optical path to

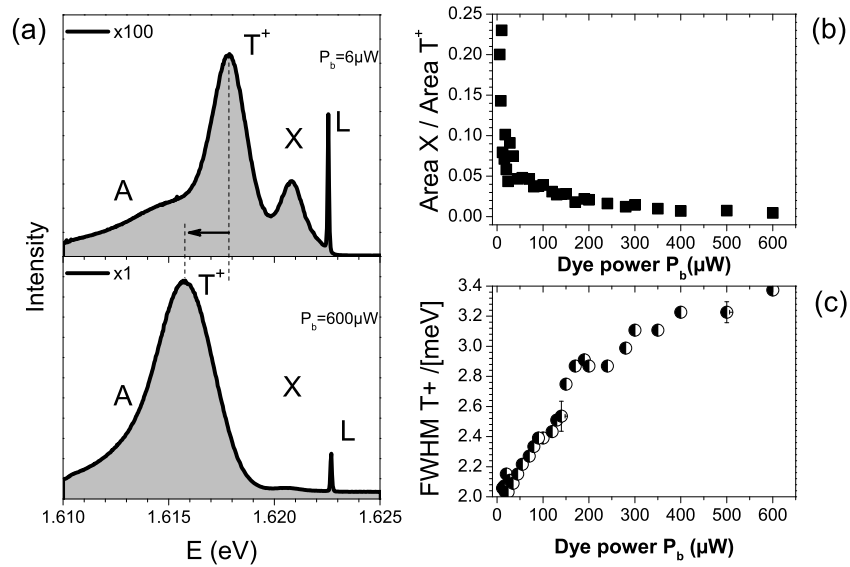


Figure 4.8: Overview of the PL-dynamics with increasing below-barrier excitation P_b . (a) A clear red shift of the trion signal (T^+) towards the impurity-bound exciton (A) can be observed. Besides the trion signal growth while the exciton signal (X) decreases. This X-T area ratio is plotted in (b). (c) In addition the FWHM of the trion signal increases.

measure the incident light power of both sources is just in front of the entrance window of the cryostat. At this point, the in-coming light beams are parallel to get them spot-in-spot on the sample in the ideal case. This means a total concentric arrangement and identical size of both light-spots. Both cannot be assured.

Summarized in Figure 4.7 and Figure 4.8, the increasing light power of the below barrier excitation causes a red-shifting trion signal T^+ , a decreasing X-T area ratio and an increasing FWHM of the trion signal in the PL-dynamics of the spectra. The content of the next subsection (4.1.3) will be the investigation of the influence of the increasing above-barrier excitation power of the QW PL-signal.

4.1.3 Above-barrier excitation

The 514nm-line of the Ar^+ -laser (2.41eV) is used for the above-barrier excitation (P_a) of the CdMnTe/CdMgTe QW (energy gap of the barrier layers: $\approx 1.94\text{eV}$). Under this condition a similar behaviour like in subsection 4.1.2 was observed which is shown Figure 4.9. This means that similar PL-behaviour concerning the PL-shape, the X-T-distance ($E_X - E_T$), X-T area ratio and trion-FWHM were observed. The PL-tuning efficiency of the above-barrier excitation is more pronounced compared to the below-barrier excitation. A certain line shape of the below barrier excited PL-signal is "reproducible" using the above-barrier excitation which is pointed out in Figure 4.9(a) but with lower power ($P_a \ll P_b$). An additional indication for the low power used for the green spectrum in Figure 4.9(a) is the minor signal-to-noise ratio, in spite of the long accumulation time ten times higher than for usual spectra.

For the below-barrier excitation, P_b must be a factor 60 higher for similar PL spectral

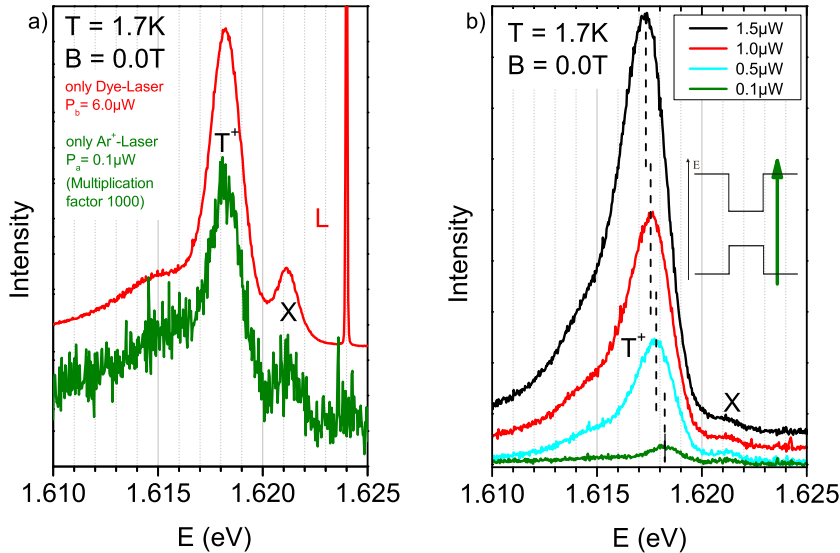


Figure 4.9: Above-barrier excitation: (a) Comparing above-barrier excitation with power P_a (green) and below-barrier excitation with power P_b (red), qualitatively the same PL-line shapes occur for different excitation powers $P_b > P_a$. Already at small values of P_a the trion is very dominant in the spectrum. Thus a similar but faster trend of increasing trion intensity and red-shifting trion position by above-barrier excitation compared to below-barrier excitation is shown in (b).

shape. This is demonstrated in Figure 4.9b where a clear change in the PL-dynamics can be observed within a small power range up to $1.5\mu\text{W}$ i.e. a smaller X-T area ratio and a wider trion FWHM was obtained than at comparable below-barrier illumination power, respectively. In Figure 4.10 the impact of the below and above-barrier excitation on the X-T energetic distance ($E_X - E_T$) and X-T-ratio is compared. As a result these plots confirm the observations of Figure 4.9a and the trend that the PL-behaviour is more sensitive on the above barrier excitation power. In Figure 4.10 the spectral X-T

distance ($E_X - E_T$) is plotted versus the Dye power P_b (a) and above barrier excitation P_a (b), respectively. Additionally, the X-T area ratio is plotted versus the excitation power. The ordinate of Figure 4.10 (a) and (b) as well as for (c) and (d) is presented at the same scale for comparing their behaviour with increasing P_b and P_a , respectively. As a matter of fact the impact of the above-barrier excitation for reaching the same values of $E_X - E_T$ and the X-T area ratio is much higher. Thus the same effect on the PL-dynamics is achieved with about one decade lower power than using the below barrier excitation P_b . The tuning of the hole concentration in the QW by the above-

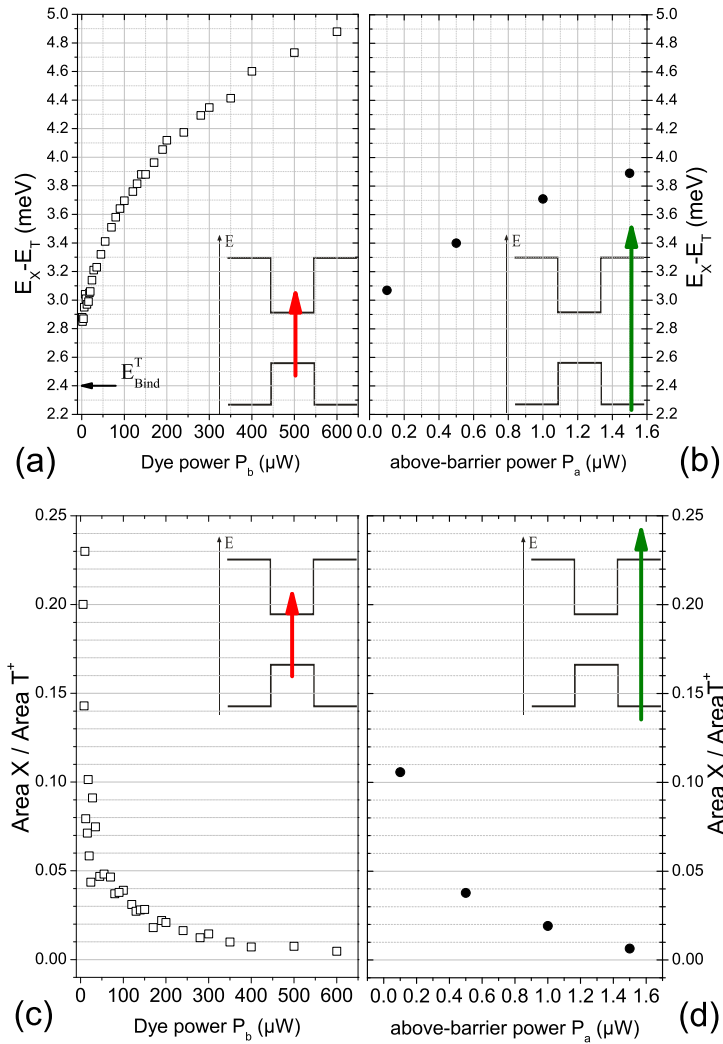


Figure 4.10: Comparison of below- and above-barrier excitation power with respect to the X-T energetic distance ($E_X - E_T$) ((a) and (b)), and X-T-ratio ((c) and (d)).

barrier illumination, which is proven by the trion PL behaviour, can be applied in the two-colour experiments together with the resonant PL- and Raman-excitation by the Dye-laser.

4.1.4 Two-colour excitation

Under the same conditions as in subsections 4.1.2 and 4.1.3 both sources were used to illuminate the sample simultaneously. This spot-in-spot optical alignment was already discussed in section 3.1. The PL behaviour of the QW was investigated by keeping the Dye power P_b at a constant (moderate) value ($\approx 10\mu\text{W}$) while the additional above-barrier illumination power from was increased. The experimental results are shown in Figure 4.11. The series starts with the pure Dye laser excitation below barrier of mod-

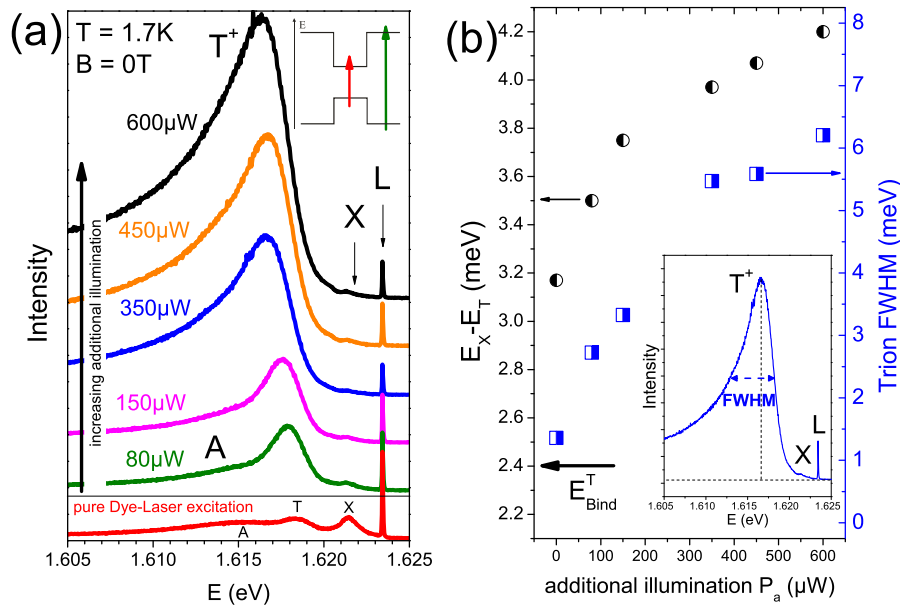


Figure 4.11: (a) PL behaviour with constant power of below barrier excitation (separate frame $P_b \approx 10\mu\text{W}$) and increasing additional illumination above barrier (P_a : from 0 to 600 μW). (b) Spectral separation between the exciton and trion lines (left axis) and the full width of half maximum (FWHM) of the trion signal (right axis) as a function of P_a with a constant $P_b = 10\mu\text{W}$

erate power ($P_b \approx 10\mu\text{W}$, separate frame in 4.11 (a)) subsequently the above-barrier illumination P_a was increased while keeping P_b constant at $10\mu\text{W}$. A similar behaviour concerning the spectral distance of the exciton and the trion ($E_X - E_T$) and the trion FWHM can be seen by tuning the additional illumination P_a like in subsections 4.1.2 and 4.1.3. Due to the fact that the trion signal becomes more and more asymmetric with increasing additional illumination its FWHM was determined by hand and not by using a fitting program (example of determination: see inset 4.11b).

The reason for using a moderate dye power is taking advantage of the resonance condition of the Multi-PR signals at the exciton signal pointed out in subsection 4.1.2. This is the vantage point for the investigation of the Multi-PR signals under the influence of increasing hole gas concentration in the following experiments (section 4.2).

4.1.5 Conclusion of the PL behaviour

The previous subsections presented the PL-spectra of the energetic lowest transitions of the QW (e1-HH transition) and their dependence on illumination power. Three significant PL-features appear in these spectra sorted according to decreasing spectral positions, namely

- the exciton X
- the positively charged trion T^+ and
- the impurity-bound exciton A.

With the help of the Multi-SF resonance spectra (Figure 4.4) tuning the excitation energy through the exciton and trion PL-signal, the trion was identified as a positive one, because of disappearing Multi-SF signals in resonant excitation on the trion PL-signal.

Due to the fact that the intensity of trion can be increased at the expense of the exciton intensity (also called oscillator-strength stealing (OSS) or intensity stealing [GPR⁺04]) with increasing illumination power using

- below-barrier excitation
- and above-barrier excitation
- the combination of below-barrier and above-barrier excitation, respectively.

it could be pointed out that an excess hole concentration in the QW can be induced with these excitation methods. In addition, when applying these three excitation methods the spectral distance between the centre of the exciton signal and the centre of the trion signal is increased with increasing illumination power. This fact also mirrors the existence of an excess hole concentration in the well and is a quantitative access for the determination of this hole concentration using equation (4.2).

Although the sample is nominally undoped, a p-doping in the QW can be achieved by illumination as presented in the previous sections. This excess hole concentration has its origin in the complexity of the sample structure combined with the above mentioned illumination methods. Concerning the sample structure, a thin capping layer positioning the QW close to the surface and the resulting surface states lead to a two-dimensional hole gas (2DHG) in the QW. This is called surface-state induced p-type doping [KAK⁺09].

A detailed discussion of the surface-state induced p-type doping, concerning the surface states, the tunnelling and diffusion processes of electrons and holes, respectively, and the resulting PL-behaviour is presented at the end of this thesis (see chapter 7). In addition, based on the previous results and the later on presented investigations of the PL-behaviour - under the aspect of different cap thicknesses - (see chapter 6), an

interpretation purely based on these PL-measurements and these mentioned aspects is presented in the same chapter 7.

The surface-state induced p-type doping of the sample influenced by the already mentioned two-colour illumination (cf. section 3.1) provides the opportunity to influence the Mn-g-factor which is demonstrated in the subsequent section.

4.2 Influencing the Mn-g-factor

4.2.1 Mn-g-factor determination

Typical spectra of Multi-PR signals for a moderate below-barrier illumination ($\approx 10\mu\text{W}$) and in an applied magnetic field (2.25-3.00T) are shown in Figure 4.12(a). The measurements were done at a temperature of 1.7K. Up to six linearly red-shifting PR-signals close to the exciton signal X in the increasing B-field could be observed. Emphasising the first three PR-signals in Figure 4.12(a) these peaks are presented as a typical Raman-plot in Figure 4.12(b) relative to the laser line called Spin Flip Raman signals (SFRS). The dashed lines serve as guides for the eye and underline the linear behaviour of the PR-signals in an increasing B-field. The peak position of each PR-

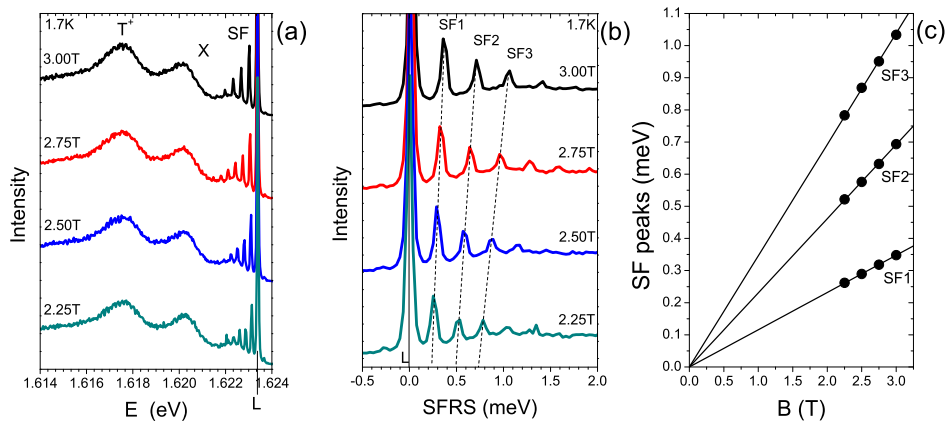


Figure 4.12: (a) Below barrier excited PL-spectra with applied magnetic field (2.25-3.00T) at 1.7K. L is the laser line, SF assigns the Multi-PR signal region and X and T⁺ are the exciton and positive trion, respectively. (b) The appropriate Raman plots with the Spin Flip Raman signals (SFRS) with respect to the laser line, numbered for the first three paramagnetic resonance signals. (c) The SF peak position of SF1, SF2 and SF3 determined from the presented spectra depending on the external magnetic field B.

signal is determined via Gaussian fit⁶ subtracting a linear background only beneath the relevant peak. The energetic position of the laser line was determined with the same

⁶using standard fits of ORIGIN 7.5

method. These determined positions relative to the laser line (SF peaks) were plotted versus the applied magnetic field and fitted with a straight line through the origin of the plot. The resulting slope of the "SF1"-fit ($\frac{\Delta E}{\Delta B}$) and using (2.8), the Mn-g-factor (g_{Mn}) can be evaluated:

$$g_{Mn} = \frac{1}{\mu_B} \cdot \left(\frac{\Delta E}{\Delta B} \right) \quad (4.4)$$

with

$$\mu_B = \frac{e \cdot \hbar}{2 \cdot m_e} \quad (4.5)$$

All subsequent Mn-g-factors presented in this thesis are determined in the similar

e	$1.60217733 \cdot 10^{-19} \text{ C}$	[HH85]
\hbar	$6.6262 \cdot 10^{-34} \text{ Js}$	[HH85]
m_e	$9.10938974 \cdot 10^{-31} \text{ kg}$	[HH85]

manner as discussed in this subsection.

4.2.2 Influencing the Mn-g-factor by varying above-barrier excitation power

The main question of thesis is the influence of the hole concentration on the Mn-g-factor and thus on the position of the Multi-PR signals. This subsection describes and discusses the experimental fine-tuning and the consequential results how the Mn-g-factor was systematically varied by changing the hole concentration via above-barrier excitation.

In order to exclude any significant influence of the B-field on the hole concentration the below-barrier excitation was kept at moderate excitation powers ($\leq 10 \mu\text{W}$). The reason for moderate excitation powers is well founded in section 4.1.1. On the one hand the Multi-PR signals appear only in resonance with the exciton PL-signal. On the other hand the presented PL-behaviour in this case for the below-barrier excitation (Figure 4.5) shows a dominating exciton PL-signal only at weak excitation powers. The criterion for a moderate below barrier excitation power (P_b) was the observation of a PL-spectrum with a still detectable exciton PL-signal (e.g.: Figure 4.8(a) ($6 \mu\text{W}$)). This holds the trade-off among the duty to work with lowest possible excitation powers but high enough in order to detect the Multi-PR peaks significantly.

Consequently the below barrier excitation is used as a probe for the Multi-PR signal while the above barrier excitation is responsible for varying the excess hole concentration in the QW.

Due to the necessity for observing the entire PL-signal of the QW at 0T in order to determine the hole concentration for each combination of constant below barrier excitation power and varying above barrier excitation power, the Dye-laser line is positioned close to the high energy shoulder of the exciton PL-signal at 0T ($E_L - E_X \cong 2 \text{meV}$, compare: Figure 4.8). The PL-signal is red shifting with increasing magnetic field due

to the GIANT ZEEMAN effect. As a consequence the appearing Multi-PR signals are off-resonant if the red-shift is too strong. On this account the discussed procedure for investigating the Mn-g-factor under the previous mentioned basic conditions is only possible for QW samples with low Mn-content ($\leq 2\%$). As a result this kind of measuring procedure is adequate for the samples investigated in this thesis with a maximum Mn-content of 1%.

The influence of varying above-barrier excitation power and increasing B-field on both the QW-PL and the Multi-PR signals is shown in Figure 4.13. All measurements were done at 1.7K and at 2.0T up to 4.5T. Figure 4.13(a)-(c) shows exemplarily the magneto-PL spectra without additional illumination (a) and two different above-barrier excitation power values (b) and (c). The increasing additional illumination from above barrier causes an intensity stealing at the exciton signal in favour of the trion signal T^+ . The hole concentrations determined via (4.2) at 0T for these three different above barrier illuminations are $(5.01 \times 10^{10})cm^{-2}$, $(7.15 \times 10^{10})cm^{-2}$ and $(10.94 \times 10^{10})cm^{-2}$, respectively. In addition the exciton virtually red-shifts which is likely because of spin-polarisation selective effects from above-barrier generated carriers. Consequently the Multi-PR signals lose their resonance, resulting in a decreasing PR-signal intensity. Focusing on the PL-behaviour with increasing B-field, no significant red shift is observed. The reason is an already almost saturated GIANT ZEEMAN splitting of the magneto-PL because of a small Mn-content (according to Table 3.1: 0.67% Mn-content at sample 030807A-I). The position of the exciton at 0T is marked with a dashed line in Figure 4.13(a)-(c).

Plotted to a larger intensity scale the Multi-PR signals of Figure 4.13(a)-(c) are presented separately in Figure 4.13(d)-(f), respectively. Up to seven Multi-PR signals can be observed with pure below barrier excitation (Figure 4.13(d)). With increasing above barrier illumination the number of well-defined PR-peaks decreases because of their disappearing exciton resonance (Figure 4.13(e), (f)). Thus the intensity scales of Figure 4.13(d)-(f) are zoomed with increasing additional illumination. The position of first the PR-peak of each spectrum and the Mn-g-factor were determined according to the procedure of subsection 4.2.1. The influence of the additional illumination on the PR-signals and the Mn-g-factor are exemplarily shown in Figure 4.14. In Figure 4.14(a) the comparison of the first PR-signal in a Spin-Flip Raman shift (SFRS) spectrum at a constant B-field of 3.0T and 1.7K for two different hole concentrations n_h is shown. A small but distinct shift of $10\mu eV$ towards the laser line was observed with increasing hole concentration from $n_h = 3.8 \times 10^{10}cm^{-2}$ to $1.3 \times 10^{11}cm^{-2}$. A Gaussian fit of the PR-signal (continuous line in Figure 4.14(a)) was used to determine the spectral centre position of each PR-peak. As discussed previously, for each hole concentration the peak positions were plotted versus B-field in order to determine the Mn-g-factor via the slope of the linear fit. In Figure 4.14(b) a distinct decrease of the slope with increasing hole concentration is observed within the B-field range from 2.25T to 3.00T. This leads to the conclusion that the Mn-g-factor is decreasing with increasing additional illumination P_a and hole concentration n_h , respectively.

The reason for representing the PR-signal positions only up to a maximum B-field of 3.00T in Figure 4.14(b) is a reduction of the Mn-g-factor decrease at B-fields $> 3.00T$. This B-field dependence is discussed in the next subsection 4.2.3 by determining Mn-g-factors depending on the corresponding hole concentration.

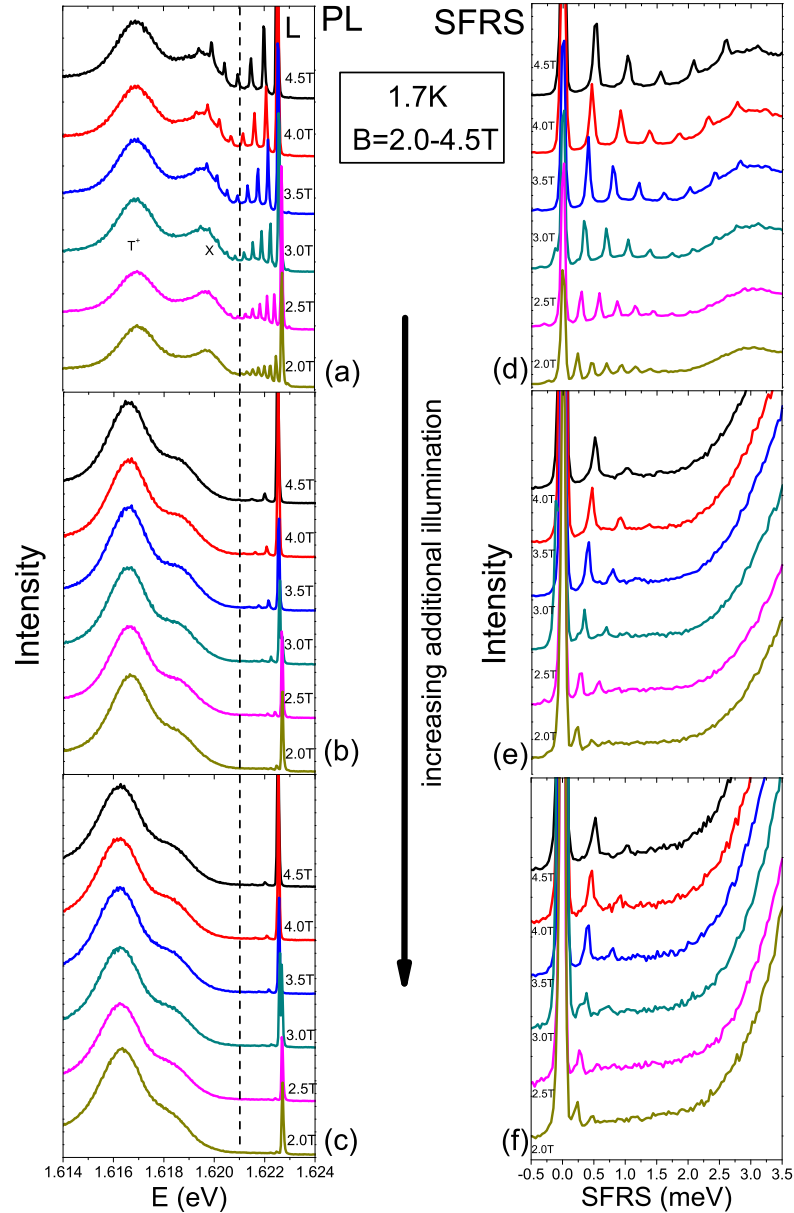


Figure 4.13: Influence of above-barrier excitation power on the PL-shape and the Multi-SF-signals in the external magnetic field range of 2.0T to 4.5T at 1.7K. The Dye-Laser (L) is in resonance with the exciton signal of the QW. Figures a-c show the PL-spectra under increasing additional illumination (0, 10 and $30\mu\text{W}$, respectively) while Figures d-f are the corresponding Multi Spin-Flip Raman spectra (SFRS). Figures a-c are presented with the same intensity scale. The dashed vertical line marks the exciton position at 0T (1.6209eV). Figures d-f have individually expanded intensity scales.

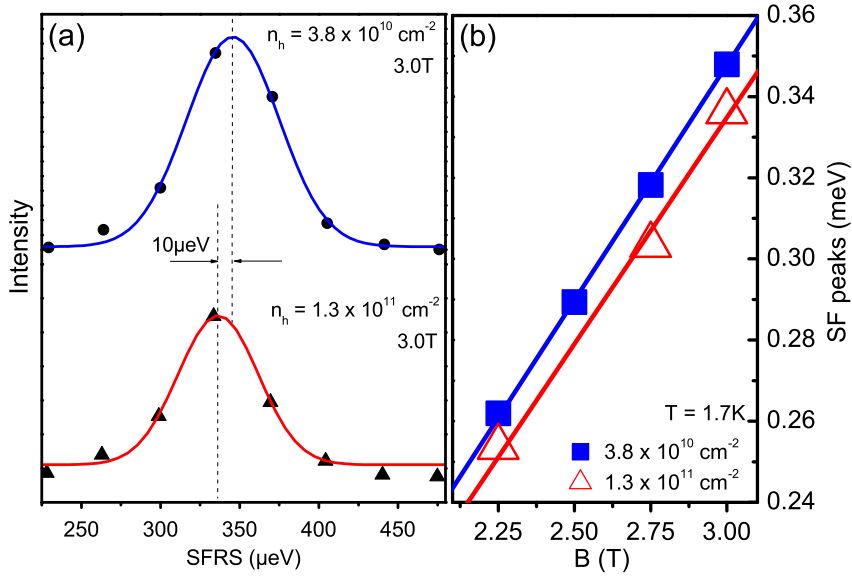


Figure 4.14: Influence of the hole concentration on the PR-signal and thus on the Mn-g-factor. (a) Comparison of the first PR-signal in a Spin-Flip Raman shift (SFRS) spectrum at a constant B-field of 3.0T and 1.7K under the influence of different hole concentrations. Increasing the n_h from $3.8 \times 10^{10} \text{ cm}^{-2}$ to $1.3 \times 10^{11} \text{ cm}^{-2}$ shifts the SF-peak by the order of $10 \mu\text{eV}$ at 3.0T closer to the laser line. (b) Comparison of the linear fits (straight lines) in the (SF peak(B))-plot at different n_h . A reduced slope with increasing n_h is observed. The squares and triangles represent the determined PR-peak positions

4.2.3 Dependence on external magnetic field

By varying the above barrier illumination power P_a in several steps the hole concentration dependence of the Mn-g-factor was measured and determined as discussed previously (section 4.2.2). This is summarized in Figure 4.15. The black squares and red solids correspond to the Mn-g-factor obtained from the linear fit in the B-field of 2.25 - 3.00T and 3.00 - 3.50T respectively. The decrease of the g-factor by the hole concentration is most pronounced in the low B-field range. The low-B-field value reduces down to $g_{Mn} = 1.89 \pm 0.02$ for $n_h = 1.4 \times 10^{11} \text{ cm}^{-2}$. The change⁷ $\Delta g_{Mn} \approx -0.10$ as compared with g_{Mn} at almost zero hole concentration is larger and of opposite sign compared to the KNIGHT SHIFT of g_{Mn} . This KNIGHT SHIFT is of the order of 10^{-3} [SSE+96] for the given concentrations in Figure 4.15. The increasing error of g_{Mn} originates from the fitting procedure of the decreasing PR-signals with increasing n_h (c.f. subsection 4.2.2).

The theoretical description of the effect is discussed in subsection 5.

⁷ $\Delta g_{Mn} = g_{Mn}^{n_h} - g_{Mn}^{(0)}$

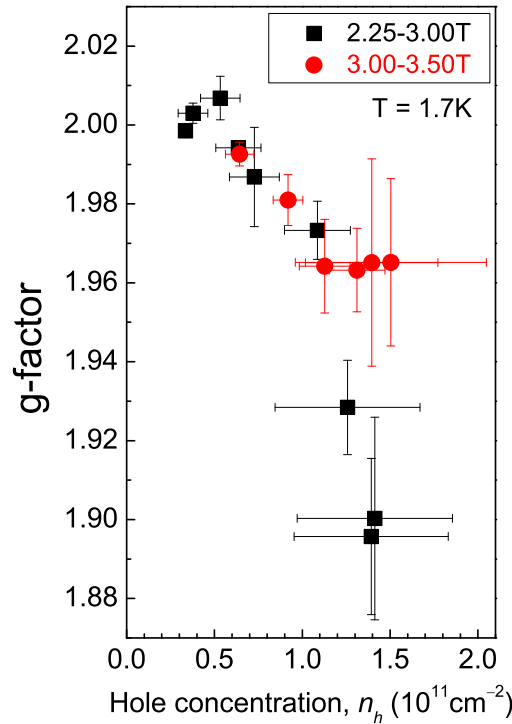


Figure 4.15: Mn-g-factor as a function of the 2DHG density obtained in the B-field ranges of 2.25-3.00T (black squares) and 3.00-3.50T (red circles) at 1.7K

4.2.4 Temperature dependence aspect

The influence of the hole concentration on the Mn-g-factor was investigated for different temperatures. Due to the fact of limited possibility of controlling the temperature at the previously presented setup the temperature dependent measurements were done as follows. The temperature was controlled by varying the liquid helium pressure. The vapour pressure curve of liquid helium serves as the calibration curve for the temperature. Because of the temperature drift effects, no systematic B-field variation at each T-value was possible. Therefore the Mn-g-factor was determined for each temperature from a single PR-spectrum at a constant B-field value (2.75T). Again the probe of the Multi-PR signals had a moderate power of about $10\mu\text{W}$ while the additional illumination was tuned to a constant power with maximum influence on the Mn-g-factor reduction but without losing the significant PR-signal.

The temperature was increased starting at 1.7K with a reduced Mn-g-factor of 1.92 influenced by a constant hole concentration of about $1.3 \times 10^{11} \text{ cm}^{-2}$. As demonstrated in Figure 4.16 the effect of the Mn-g-factor decrease is suppressed with increasing temperature almost reaching the atomic Mn-g-factor at 4.2K ($g_{Mn} = 1.99$). The determination of the Mn-g-factor at a constant B-field results in large error bars compared to determination method explained in subsection 4.2.1. Within these error bars the experimental results coincide up to $\approx 3.0\text{K}$ with the theoretical calculations of K.V. KAVOKIN ([KAK⁺09]) shown as a solid curve in Figure 4.16. The theoretical curve saturates (i.e. reaches $g_{Mn} = 2.00$) at 10.0K while the experimental determined value

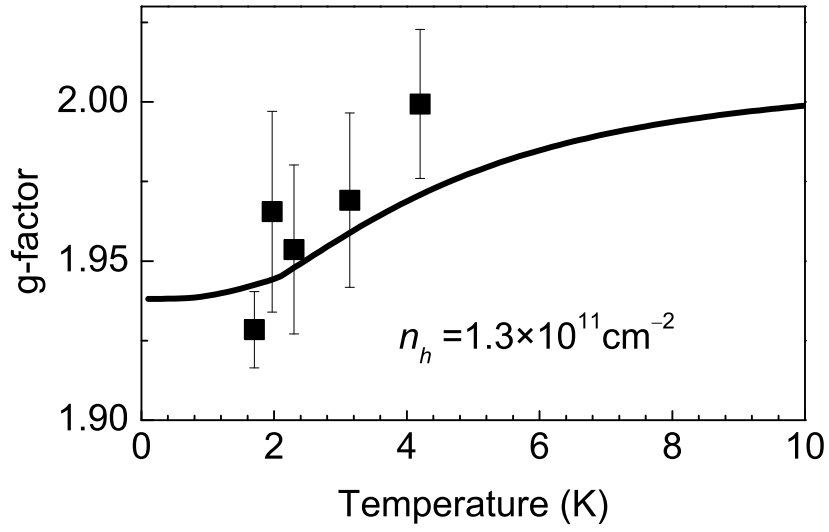


Figure 4.16: Mn-g-factors under two-colour illumination and at a constant B-field (2.75T) as a function of temperature. The continuous line represents the theoretical calculation of the temperature behaviour according to K.V. KAVOKIN ([KAK⁺09]).

reaches $g_{Mn} = 1.99 \pm 0.02$ at 4.2K.

Chapter 5

Magnetic soft mode behaviour of the Mn-g-factor - Interpretation and conclusion -

The frequency shift of Mn spin precession was qualitatively predicted by K.V. KAVOKIN [Kav99] and already discussed in section 2.5. It arises due to an additional torque exerted on the Mn spins by the hole spins [see Figure 5.1(b)]. Because of the g-factor anisotropy of the holes, the Mn spin component perpendicular to B_{ext} ($\equiv B$) induces a predominant polarisation of hole spins along the growth direction z . The oscillating exchange field B_{exch} of spin-polarised holes, applied to Mn spins, make them follow an ellipse, rather than circular, trajectories around B_{ext} , which slows down their Larmor precession shown in Figure 5.1(c) and (d) and discussed in more detail in section 2.5.

Two main issues which are specific for Spin Flip Raman Scattering/Multi-PR Raman scattering experiments have to be addressed here [KAK⁺09]:

1. The spin oscillations are excited by localized excitons and therefore they can have non-zero spatial frequencies ($k \neq 0$).
2. The experiments are performed in strong B-fields, therefore the Zeeman splitting of the holes in Voigt geometry is comparable to their Fermi energy (cf. PAULI-paramagnetism).

The resident 2D holes, as well as the localized exciton which initiates the Multi-PR Raman scattering, interact each with a large number of Mn^{2+} ions, i.e. the concentration

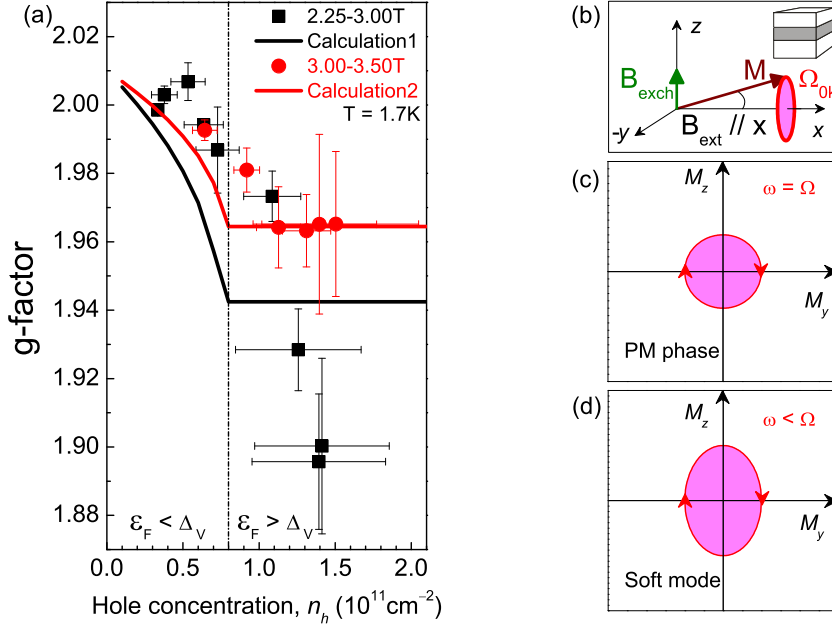


Figure 5.1: (a) shows again the experimental results (Figure 4.15) of the Mn-g-factor as a function of the photo-generated 2DHG for 2.25-3.00T (solid squares) and 3.00T-3.50T (solid circles), respectively. The solid lines represent K. V. KAVOKIN's calculations using two constant B-field values 2.60T and 4.00T, respectively. The drawing in (b) demonstrates the collective spin excitations. The exchange field of the spin-polarized holes B_{exch} creates an additional torque acting on the magnetic moment of the Mn-ions M (also cf. section 2.5). The $y - z$ plane of (b) is shown in detail for the oscillations of M in the paramagnetic phase (c) and the soft mode phase (d), respectively.

of Mn-ions is high compared to the interacting carrier concentration¹:

$$\begin{aligned}
 N_0 x &\gg \frac{k_F^2}{4\pi^2 L} \\
 \text{thus } N_0 x \frac{4\pi^2 L}{k_F^2} &\gg 1 \\
 \text{and } \pi L R^2 N_0 x &\gg 1
 \end{aligned} \tag{5.1}$$

(where L is the QW width, N_0 is the concentration of cations, x is the fraction of Mn-ions per N_0 , $R = \pi/k_F$ is the exciton localization radius). For this reason it is convenient to write the Hamiltonian of the spin system of Mn-ions in terms of spin density components S_{lk} :

$$\begin{aligned}
 H(\vec{S}_{l\vec{k}}) &= -g_{\text{Mn}}^{(0)} \mu_B \sum_l S_{l0}^x B - \frac{\beta}{3} \frac{g_{\perp}}{g_{\parallel}} J_x \sum_l \Psi_h^2(z_l) S_{l0}^x \\
 &\quad - \frac{g_{\perp}}{2} \mu_B A J_x B + \delta E_{\text{ex}}
 \end{aligned} \tag{5.2}$$

¹using the 2D-reciprocal space volume $V_k^{2D} = \pi \cdot k^2$

The subsequent terms represent (i) the Zeeman energy of the Mn spins (S_{l0} is the spin density of the l -th monolayer) and (ii) the exchange interaction energy between Mn-ions and holes (for Mn spins along x) where J_x is the x -component of the hole spin density and g_{\perp}/g_{\parallel} represents the anisotropy of the HH-g-factor, where g_{\perp} is the in-plane HH g-factor of the QW while g_{\parallel} is the g-factor along the growth direction. The term (ii) gives rise to a HH-spin splitting caused by the x-component of the exchange field of the Mn-ions ²

$$B_{exch,x}^{Mn} = \beta \sum_l \Psi_h^2(z_l) S_{l0}^x / A, \quad (5.3)$$

It can be assumed that the splitting of the HH spin-levels in B_{exch}^{Mn} is larger than the ZEEMAN splitting of the Mn-ion spins ($\mu_B g_{Mn} B$) caused by the external B-field B . Furthermore Term (iii) represents the Zeeman energy of HHs caused by the external magnetic B-field B along x (see Figure 5.1)(b) and A is the area of the structure. This term can be neglected considering term (ii).

The terms (i) and (ii) represent the Hamiltonian for the description of the Multi-PR Raman scattering processes according to STÜHLER et al. [SSD⁺95].

The exchange energy correction δE_{ex} (iv) added to the Hamiltonian (5.2) is due to the deflection of the Mn²⁺ spin-density components from the direction of x and thus out of the x-y plane [Figure 5.1(b)]. Since in equilibrium the mean spin direction of Mn-ions is along x, δE_{ex} is quadratic in the y and z components of the spin density³: these energy corrections arise because of the interaction of the Mn ion spins with the induced 2DHG polarization via spin-spin interaction, perpendicular to x . Thus a change in energy due to the polarisation of the 2DHG by the exchange field of Mn-ions can be written as

$$\delta E_{ex} \propto \chi_k (B_{exch}^{Mn})^2 \quad (5.4)$$

with the transverse (i.e. perpendicular to x) spin susceptibility χ_k of the 2DHG. Here B_{exch}^{Mn} is dependent on the y - and z -components of the Mn-spin density $S_{l,\vec{k}}^Y$ and $S_{l,\vec{k}}^Z$, respectively.

This means that the holes undergo the action of the stationary exchange field B_{exch}^{Mn} of the polarized Mn-ions, directed along the x-axis. Consequently, the two HH spin sub states are split by the value $\frac{g_{\perp}}{g_{\parallel}} \cdot \mu_B \cdot B_{exch}^{Mn}$. The z-component of the exchange field B_{exch}^{Mn}

with a certain wave vector \vec{k} causes a mixing of the two HH spin sub states, connected with a change in its total energy. Both the HH spin state splitting and its mixing are represented in the transverse spin susceptibility χ_k [KK09].

Assuming that the z-component of the exchange field B_{exch}^{Mn} is much smaller than the absolute value of B_{exch}^{Mn} , the transversal 2DHG spin susceptibility to the exchange field of magnetic ions at the spatial frequency k can be calculated, using perturbation theory. At low temperature ($k_B T \ll \Delta_V$, where Δ_V is the hole spin splitting in Voigt geometry caused by B_{exch}^{Mn}) it is given by ⁴:

$$\chi_k = \frac{m}{8\pi\hbar^2\varepsilon_k} \left[\varepsilon_k + \Delta_V - \sqrt{(\varepsilon_k + \Delta_V)^2 - 4\varepsilon_k\varepsilon_F} \right] \quad \text{for } \varepsilon_F \leq \Delta_V \quad (5.5)$$

²where the mean spin of Mn-ions is precessing around the external B-field

³like a 2D harmonic oscillator

⁴ $\Delta_V \propto \frac{g_{\perp}}{g_{\parallel}} \cdot B_{exch}^{Mn}$

and

$$\chi_k = \frac{m}{8\pi\hbar^2\varepsilon_k} [\varepsilon_k + \Delta_V - |\varepsilon_k - \Delta_V|] \quad \text{for } \varepsilon_F \geq \Delta_V \quad (5.6)$$

Here $\varepsilon_k = \frac{\hbar^2 k^2}{2m}$, and $\varepsilon_F = \frac{2\pi\hbar^2}{m} n_h$ is the 2DHG FERMI energy. For $\varepsilon_F \leq \Delta_V$ in (5.5) only one HH spin sub state is occupied, i.e. this state is fully spin-polarised (by the z-component of B_{exch}^{Mn}) leading to a twice larger FERMI energy than at zero external B-field.

Spins of different monolayers are coupled by indirect exchange via the 2DHG. The coupling strength is determined by the 2DHG spin susceptibility and by the mutual orientation of spins in different monolayers. Orthogonal linear combinations of spin densities of the monolayers form oscillatory modes corresponding to certain eigenfrequencies of the coupled spin system. As discussed in [Kav99], the pulsed exchange field of the photo-excited hole induces oscillations of the mode (see Figure 5.2), most strongly coupled with the 2DHG $\vec{\Phi}_{0\vec{k}} = \sum_l \Psi_l^2 \vec{S}_{l\vec{k}} / \sum_l \Psi_l^2$. Its eigenfrequency can be obtained by solving the Hamiltonian (5.2) for Φ_{0k} , where δE_{ex} is calculated using (5.5) and (5.6). Then, the eigenfrequency can be presented as $\Omega_{0k} = g_{0k}^* \mu_B B / \hbar$, with the effective g-factor

$$g_{0k}^* \approx g_{Mn}^{(0)} \sqrt{1 - \frac{\chi_k \beta^2}{\mu_B g_{Mn}^{(0)} B \tilde{L}} N_0 x \langle s_x \rangle} \quad (5.7)$$

Here, $\langle s_x \rangle$ is the mean spin of a Mn ion, $\tilde{L} = a (\sum_l \Psi_l^4)^{-1} \approx \frac{2}{3} L$, where L is the QW width, and a is the lattice constant. The dominating mode in SF-RS is the one with $|k| \simeq 1/r_h$, where r_h is the localization radius of the photo excited hole. As seen from equations (5.5)-(5.7), Ω_{0k} decreases with n_h for $\varepsilon_F \leq \Delta_V$ (besides the slope and shape of the curve depend on k), and does not depend on n_h for $\varepsilon_F \geq \Delta_V$ (see Figure 5.1(a)). Theoretical calculations were performed, using the experimentally obtained ratio $g_{\parallel}/g_{\perp} = 10$ (which defines Δ_V). Their results with $r_h = 10$ nm (shown by solid lines in Figures 5.1(a) and 4.16) describe all tendencies observed in our experiments. Yet a quantitative difference between the experimental data points and the theoretical calculations in Figure 5.1(a) occurs, which may be related to the B-field-dependent ratio of g_{\parallel}/g_{\perp} due to the mixing of HH- and LH-states, which was not considered in K.V. KAVOKIN's model. The used ratio $g_{\parallel}/g_{\perp} = 10$ was obtained by the comparison of the high B-field shifts of the trion line in the Faraday and Voigt geometries. From Figure 5.1(a) it can be recognised that the g-factor shift is larger for lower B-fields. The theory predicts that at very low B-fields, inaccessible in SF-Raman spectroscopy experiments⁵, g should turn to zero. This behaviour, high-field traces of which we detect in our experiment, is a fingerprint of the transition to the ferromagnetic phase.

In conclusion it was experimentally demonstrated that the g-factor of Mn-ions in a semimagnetic QW can be reduced from its atomic value ($g \approx 2.00$) by the photo-excited increase of the 2DHG concentration as first theoretically predicted in [Kav99] (already discussed in section 2.5 in a qualitative manner). This is called magnetic soft mode behaviour [KAK⁺09]. Furthermore the above discussed extended theory of K.V. KAVOKIN ending up with the main result in (5.7) enables to calculate this g-factor

⁵B-field must be >1.5 T for clearly observing a PR-signal

decrease which is in good agreement with the experimental results shown in Figures 5.1a and 4.16.

A more illustrative access to the previously mentioned theory combined with the discussed exchange-box model is given in Figure 5.2.

Starting with a sample without illumination, the magnetization of all the Mn-ions \vec{M}

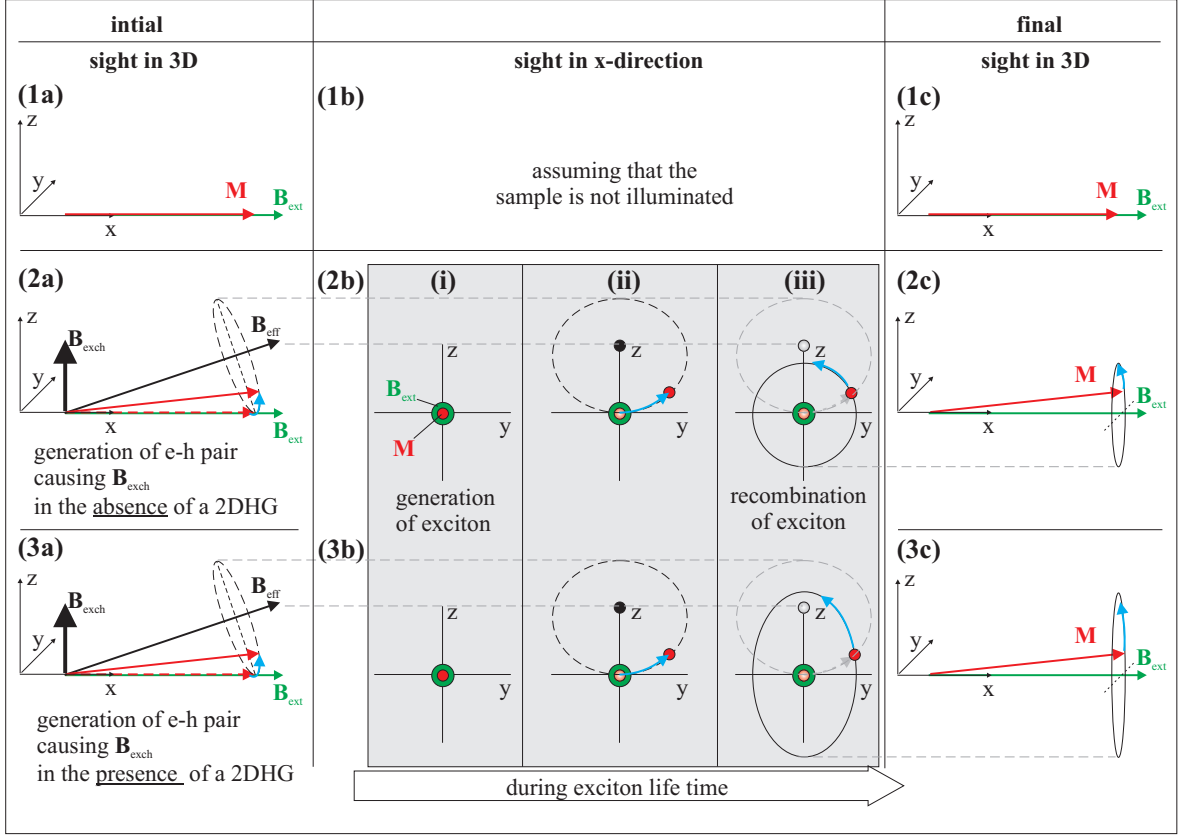


Figure 5.2: Overview of the Mn-ion precession model without ((1a)-(1c)) and with the generation of an e-h pair in the absence ((2a)-(2c)) and presence ((3a)-(3c)) of a 2DHG, respectively. The demonstration of the Mn-ion precessions - and its magnetisation \vec{M} - is assisted by 3D-view and a view parallel to the direction of the external magnetic field \vec{B}_{ext} , respectively. \vec{B}_{exch} is the exchange field induced by the heavy hole of the photo-generated e-h pair (exciton). \vec{B}_{eff} is the resulting effective B-field during the exciton life time.

is parallel to the external B-field \vec{B}_{ext} as shown in Figure 5.2(1a)-(1c).

A photo-generated e-h pair (exciton) excited in the semimagnetic QW causes a HH exchange field \vec{B}_{exch} along the growth direction (z) and perpendicular to the external B-field (Figure 5.2(2a)) resulting in an effective B-field \vec{B}_{eff} which exists during the exciton life time. Thus the magnetization of the Mn-ions \vec{M} within the photo-excited exciton (hole) volume starts to precess around \vec{B}_{eff} with an oscillating component perpendicular to the x-y plane till the exciton recombines. In the absence of a 2DHG and after the exciton recombination, \vec{M} precesses circularly around the external B-field \vec{B}_{ext} (Figure 5.2(2b,i-iii)). Now the Mn-ion system is in an excited state which manifests itself in the Multi-PR signals spectrally observed in this thesis and explained by the

exchange-box model in 2.4.5. The dedicated g-factor of the Multi-PR signals is of the same order than the atomic g-factor of Mn ($g \approx 2.00$).

In the presence of a 2DHG the deflection of \vec{M} out of the x-y plane leads to an interaction between the Mn-ions and the 2DHG via the exchange field caused by the Mn-ions \vec{B}_{exch}^{Mn} resulting in the spin polarisation of the 2DHG. Thus after the exciton recombination \vec{M} precesses elliptically around the external B-field (Figure 5.2(2c,i-iii)). This interaction can be seen as an additional torque for \vec{M} along the z-direction which acts as natural positive feedback between the Mn-ions and the 2DHG (also cf. section 2.5). This was meant by the mentioned explanation in this section, that the pulsed exchange field of the photo-excited hole (exciton) induces oscillations of the mode, most strongly coupled with the 2DHG $\vec{\Phi}_{0\vec{k}}$. Now the Mn-ion system is again in an excited state as already discussed for the case in the absence of a 2DHG (Figure 5.2(2a)-(2c)). However the resulting g-factor out of the Multi-PR signals of the Mn-ion system is reduced regarding to its atomic value.

Focusing now on the temperature and B-field aspect of the Mn-g-factor in Figure 4.16 and 5.1, respectively. The consequence of (5.7) is that the Mn g-factor of the calculated curve in this figure converges to its atomic value ($g \approx 2.00$) with increasing temperature and with increasing external magnetic field, respectively. In conclusion the phenomenon of magnetic soft mode behaviour is reduced in effectiveness with both the increasing external magnetic field and increasing temperature.

Chapter 6

Investigation of the impact of different cap-thicknesses

The main interest of this chapter is the investigation of the photo-generated carrier influence on the Mn-g-factor under the aspect of different cap thicknesses of the QW samples. In general, the QW-sample has to provide an opportunity to manipulate the hole concentration inside the QW with varying illumination power. This is the key condition for influencing the Mn-g-factor.

In literature MAŚLANA et al [MKB⁺03] observed that the cap thickness (15-100nm) influences the hole concentration inside a near-surface Cd_{0.99}Mn_{0.01}Te/Cd_{1-y-z}Zn_zMg_y-Te QW¹ of 10nm well width. The question is now, how this additional parameter of cap layer thickness influences the Mn-g-factor softening as already observed in chapter 4. Thus the sample series 031709B (I-IV) with cap thicknesses from 13nm up to 19nm will be investigated under the influence of the below-barrier excitation, the two-colour excitation and in consequence under the influence of the photo-generated hole concentration on the Mn-g-factor.

First the investigation of the sample with the lowest cap thickness of 13nm from the sample series 031709B I-IV consisting 1% manganese in the 10nm wide QW is presented in this chapter followed by the investigation of the 15nm, 17nm and 19nm capped samples.

6.1 Sample with 13nm Cap thickness (031709B-I)

Below-barrier excitation For the sample with the lowest cap thickness (13nm), the most distinctive part of the PL-behaviour for increasing below-barrier excitation power ($P_b = 60 - 150\mu W$) is shown in Figure 6.1(a) with the onset of the positive trion intensity increase (T^+)² at the expense of the exciton signal intensity X (accented with black arrows). Within about two decades of illumination power there is no significant

¹ $y = 0.22, z = 0.08$ and $y = 0.22, z = 0.00$, respectively; a brief discussion of MAŚLANA et al [MKB⁺03] will be presented in the next chapter

²the trion identified as a positive one, was checked with the same method as presented in section 4.1.1

change in the PL line shape. Represented here by spectra without the black arrows in Figure 6.1 (a). The additionally presented thinner grey PL spectrum ($P_b = 6\mu W$) followed by a PL spectrum with $P_b = 60\mu W$ (blue line) underlines this matter of fact. As well as previously observed at sample 030807A-I the trion signal red-shifts with increasing power P_b .

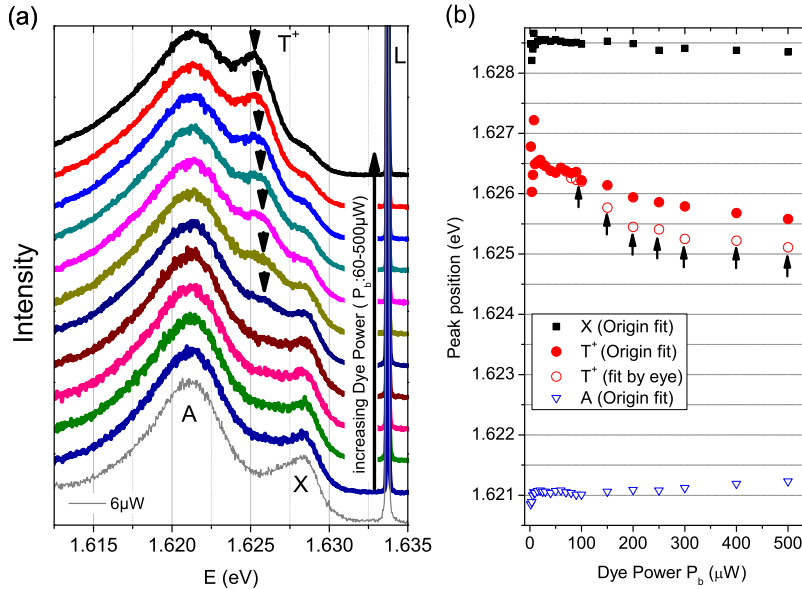


Figure 6.1: (a) Photoluminescence spectra for varying below-barrier excitation ($P_b = 60 - 150\mu W$) of the sample with 13nm cap thickness. The PL spectra are normalised to the maximum intensity of the impurity-bound exciton signal A. The lowest spectrum of the waterfall plot (thin grey line) represents a low excitation power spectrum of $P_b = 6\mu W$. Compared to its next neighbored spectrum of $P_b = 60\mu W$ there is no significant change in the PL-shape. At higher Dye power the trion signal T^+ appears (black arrows). (b) Spectral positions of the three characteristic PL-signals with increasing power. The empty circles represent the spectral positions of T^+ determined by eye and not by Gaussian fit. Again the black arrows mark the trion in the PL-spectrum.

The spectral positions of the three characteristic PL-signals with increasing power were determined again with a three Gaussian peak fit like demonstrated in Figure 4.6. Apart from the low-power region of the plot in Figure 6.1(b) the spectral position of both the exciton and the impurity-bound exciton stay constant at 1.6285eV and 1.6210eV, respectively. It is noticeable that the impurity-bound exciton signal is the dominant signal in the spectra over two excitation power decades. The already discussed discrepancies concerning the fitting procedure are mirrored here in the low power region of all three signals and specially for the trion signal also at high illumination power. This is represented by the comparison of the different ways of determining the spectral position of the trion on the one hand by Gaussian fit (filled circles) and on the other hand by eye³ (empty circles). This results in a discrepancy of about 0.5meV (see

³i.e. determining the spectral centre position of the trion by eye

Figure 6.1). In Figure 6.2(a) the black arrows mark the trion in the PL-spectrum. In summary it is possible to tune the hole concentration inside the QW, as demonstrated the PL spectra of below-barrier excitation.

Two-colour excitation The measurement series of the two-colour excitation starts without additional illumination, demonstrated by the black curve in Figure 6.2(a) using a below-barrier excitation power of $P_b = 10\mu W$. At this power only the exciton X and the impurity-bound exciton A appear in the spectrum. Again the impurity-bound exciton is the dominant signal. By switching on and increasing the additional illumination ($P_a = 1 - 110\mu W$) the positive trion T^+ signal appears and red-shifts. Additionally, with increasing P_a the trion signal more and more dominates and merges with the impurity-bound exciton signal to an asymmetric peak, while the exciton signal disappears. The red-shift of the positive trion signal is an indication for an increasing

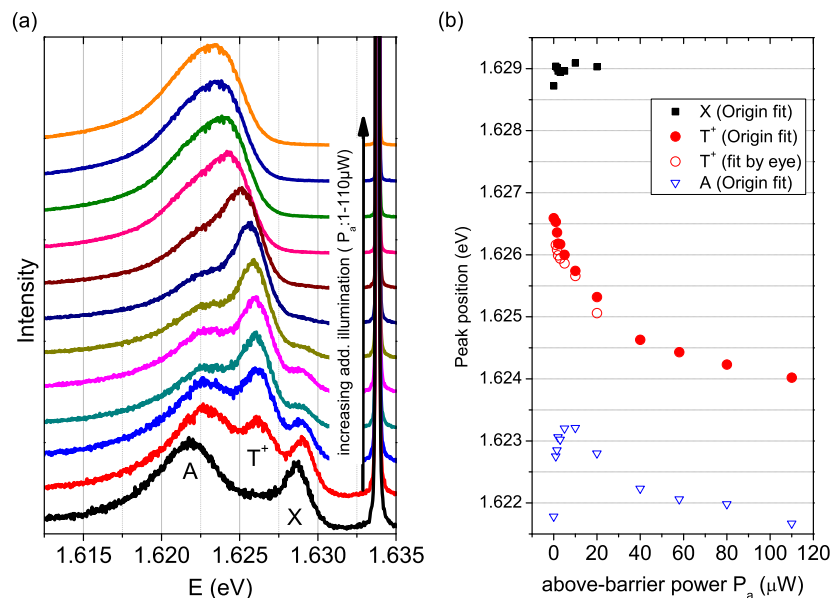


Figure 6.2: (a) PL-spectra of the 13nm-cap sample under two-colour excitation $P_b = 10\mu W$ and $P_a = 1 - 110\mu W$. (b) Fitted spectral positions of the characteristic PL-signals depending on the increasing additional illumination P_a . The PL spectra are normalised to the maximum intensity of the impurity-bound exciton signal A.

hole concentration inside the QW.

Figure 6.2(b) shows the spectral positions of the characteristic PL-signals with increasing additional illumination. The blue-shift of the X and A-signal can be ascribed to the phase-space filling as the predominant effect for $P_a < 10\mu W$. For $P_a > 10\mu W$ the exciton position converges to about 1.629eV while the A-signal starts to red-shift parallel to the trion signal. The filled and empty circles demonstrate here the small discrepancies between the Gaussian fit of the trion and the determination of the trion-maximum spectral position by eye.

In conclusion, the red-shifting behaviour of the positive trion signal with increasing

additional illumination is the indication for an increasing hole concentration inside the QW. This is a similar behaviour as demonstrated at sample 030807A-I in section 4.1. Thus the hole concentration in the QW can be controlled with the above-barrier excitation.

Multi-PR signals The two-colour excitation method in an external magnetic field is used for investigating the Multi-PR-signal and thus the Mn-g-factor under the influence of increasing hole concentration as already discussed in section 4.2. The below-barrier excitation power P_b is kept at $10\mu W$ ⁴, while the additional illumination from above-barrier P_a is varied stepwise from 0 to $100\mu W$ at different magnetic fields (2.25-4.50T) and at 1.7K. This is exemplarily shown in Figure 6.3 for three different situations of excitation in PL spectra (Figure 6.3(a),(c),(e)) and in Spin Flip Raman spectra (Figure 6.3((b),(d),(f)) where (a) and (b) demonstrate the case without additional illumination. Up to 10 Multi-PR signals appear in these spectra. The number and intensity of these signals is reduced like in section 4.2 with increasing additional illumination power (cf. Figure 6.3((c)-(e) and (d)-(f), respectively). At the maximum additional illumination power of $100\mu W$ in this measurement series only the 1PR-signal is left (f). In PL only the exciton and the impurity-bound exciton signal appear without additional illumination in Figure 6.3(a). With increasing additional illumination power the trion signal appears and simultaneously red-shifts while the exciton decreases ((c) and (e)). In Figure 6.3(e) the trion is merged to the impurity-bound exciton signal resulting in a broad and asymmetric PL-peak comparable to the FERMI-edge singularity.

⁴showing the dominant exciton PL-signal as the indication on the one hand for photo-generating as less holes as possible with the below-barrier exciton and on the other hand providing as much resonant background for the Multi-PR signals as possible

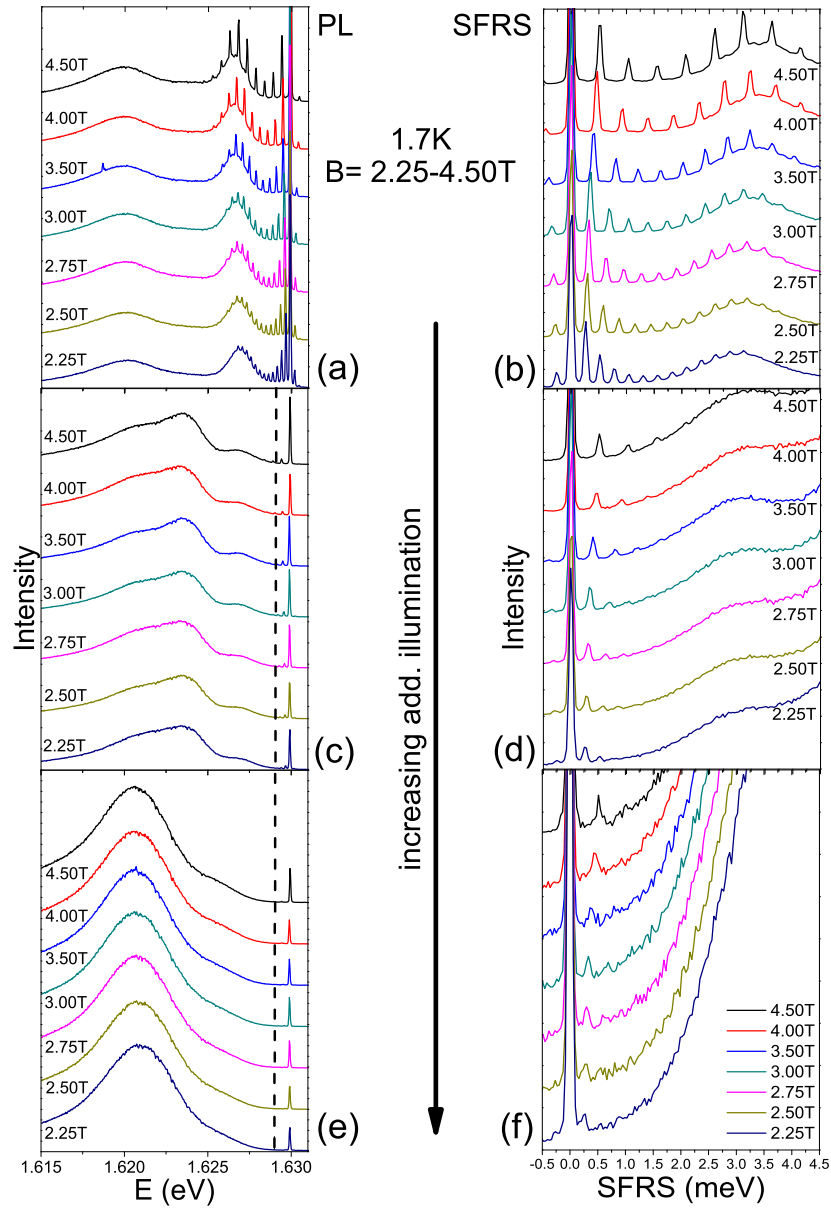


Figure 6.3: PL- and Multi-PR signals of the sample with 13nm cap thickness under above-barrier excitation 031907B-I influenced by the above-barrier excitation. (a) and (b) represent the starting point of the measurement series without additional illumination. The dashed line marks the exciton position at 0T.

Mn-g-factor Following along the procedure discussed in section 4.2 the Mn-g-factor is determined depending on the additional illumination and thus depending on the hole concentration. This is shown in Figure 6.4. This sample shows the same behaviour as

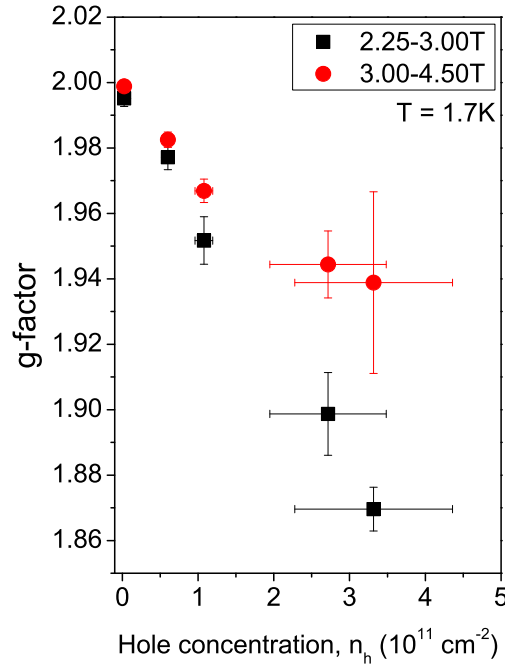


Figure 6.4: Mn-g-factor vs. hole concentration of sample 031907A-I (13nm cap) determined for low (2.25-3.00T) and high (3.00-4.50T) magnetic fields.

the one presented in section 4.2 (030807A-I). A similar down-shift ($\approx 7\%$) of the Mn-g-factor is observable with increasing hole concentration and dependent on the magnetic field. At "lower" B-fields (i.e. 2.25-3.00T) the lowest measured Mn-g-factor is ≈ 1.87 at $n_h = 3.3 \cdot 10^{11} \text{ cm}^{-2}$ (030807A-I: lowest Mn-g-factor ≈ 1.89 at $1.4 \cdot 10^{11} \text{ cm}^{-2}$). In contrast, for "high" B-fields (3.00-4.50T) the g-factor softening starts to converge to the value of about ≈ 1.94 at $2.7 \cdot 10^{11} \text{ cm}^{-2}$. This confirms the theoretical prediction of a saturating g-factor softening at large hole concentrations in high B-fields (cf. section 5).

A critical remark must be made concerning the determination of the hole concentration. The determination of the photo-generated hole concentration is only a rough estimation due to fitting procedure limitations. The reason for the limitations of this measurement series is that either the exciton is the dominant signal (pure below-barrier excitation) or the trion signal (high above-barrier excitation) in the PL-spectrum i.e. either the exciton signal is visible and not the trion or the other way round.

According to the exciton behaviour pointed out in Figure 6.1 where the exciton position essentially has a constant value in the larger part of the illumination range, the spectral position of the exciton is assumed to be constant. Thus the used exciton value is chosen from a PL-spectrum where both exciton and trion are detectable (blue coloured spectrum in Figure 6.2(a)). Due to this reason the determination of the hole concentration must be recognized as a rough estimation.

As an intermediate result this sample shows the same phenomenon of Mn-g-factor softening with increasing hole concentration like sample 030807A-I investigated in section 4.2, in spite of different Mn-content, well width and cap thickness.

6.2 Sample with 15nm Cap thickness (031709B-II)

The following sample of 15nm cap thickness is investigated under the same criteria as the sample with 13nm Cap thickness (031709B-I) starting with the PL-spectra under below-barrier excitation.

Below-barrier excitation The investigation of the PL-spectra at varying below-barrier excitation power and the spectral positions of the characteristic PL-signals are shown in Figure 6.5. In Figure 6.5(a) the increasing intensity of the positive trion signal

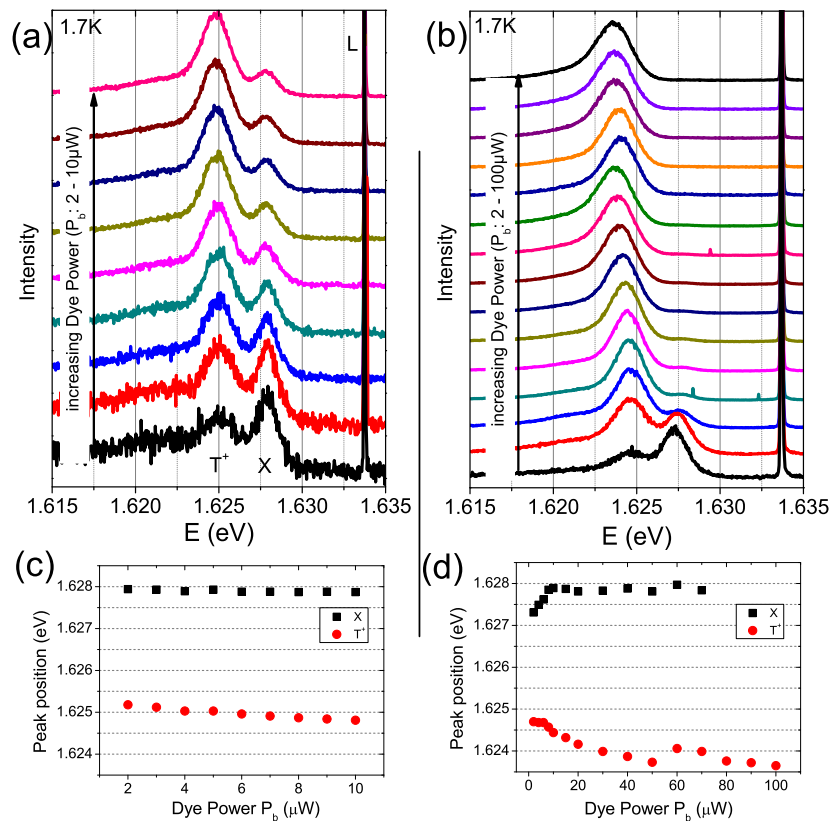


Figure 6.5: The PL spectra of sample 031709B-II (15nm cap) for below-barrier excitation with various laser power values. (a) Power range 2-10 μ W and (b) 2-100 μ W. The PL spectra are normalised to the maximum intensity of the T^+ signal.

T^+ at the expense of the exciton intensity is observed in detail by increasing the Dye

power P_b from 2 to $10\mu W$. In addition these measurements were repeated for a larger range of illumination power (2-100 μW) shown in Figure 6.5(b). Figures 6.5(c) and (d) show the spectral position of the exciton and trion versus Dye power evaluated from Figures 6.5(a) and (b), respectively. The impurity-bound signal A is considered in the fitting process but will not be discussed in the following because there is no significant impurity-bound exciton observable in Figure 6.5(a) and (b). This is different to the observations in Figure 6.1(a) and Figure 6.2(a) of sample 031709B-I (13nm cap).

A continuous decrease of the X-T ratio with increasing Dye power was observed in the power range from $P_b = 2 - 10\mu W$ without a significant red-shift of the trion signal (cf. Figures 6.5(a) and (c)). This red-shift is more pronounced (1meV from $P_b = 2\mu W$ to $100\mu W$) when P_b is further increased, so that the X-T ratio is reduced to its minimum when the exciton virtually vanishes. This is - in addition to the decrease of X-T ratio - the indication for an increasing hole concentration by photo-generated carriers.

Figure 6.5(d) shows that the spectral position of the exciton for the initial power values blue-shifts from about 1.6273eV up to its final spectral position at 1.6279eV due to phase space filling and screening. In contrast the trion position further red-shifts.

It is noticeable that in spite of the obvious intensity stealing from the exciton by the trion, the red-shift of the trion position is not as pronounced as in sample 031709B-I (13nm cap) and the trion signal is already present even at the lowest power $P_b = 2\mu W$. Assuming a constant exciton position at 1.628eV for varying Dye power it follows, the spectral distance of X and T at $P_b = 2\mu W$ is $\approx 3.2meV$, which is larger than the trion binding energy (2.4meV cf. section 4.1.1). This matter of fact and the already present trion signal even at low power, are the indication of an intrinsic hole concentration inside the QW (compared to the sample with 13nm cap). The origin of this intrinsic hole concentration will be discussed in section 6.5.

Two-colour excitation Using the two-colour excitation method, a drastic red-shift of the trion signal is observed with increasing additional illumination power up to $100\mu W$. Comparing the PL spectrum without additional illumination (black spectrum in Figure 6.6(a)) and the one with lowest above-barrier illumination power (red curve) the exciton signal disappears abruptly while the trion intensity increases with a simultaneous drastic red-shift. According to Figure 6.6(b) the most drastic red-shift of the trion appears in the range $0 < P_a < 20\mu W$. For $P_a > 20\mu W$ the signal starts to saturate (1.6205eV).

Multi-PR signals The two-colour method is used again in an external magnetic field to investigate the Mn-g-factor softening. This is presented in the same way as for the previously discussed samples and shown in Figure 6.7. At Dye power $P_b = 10\mu W$ without any additional illumination up to 4 PR-signals are observed (Figure 6.7(a),(b)), compared with the 13nm-cap sample the number of Multi-PR signals is reduced here by more than a factor one half at the same Dye power. With this condition the additional illumination power (P_a) is increased to only $1\mu W$ (Figure 6.7(e),(f)). Only the 1PR-signal is observable and it is very weak in intensity.

Comparing Figure 6.7(a),(c) and (e), in general the line shape of the whole PL-

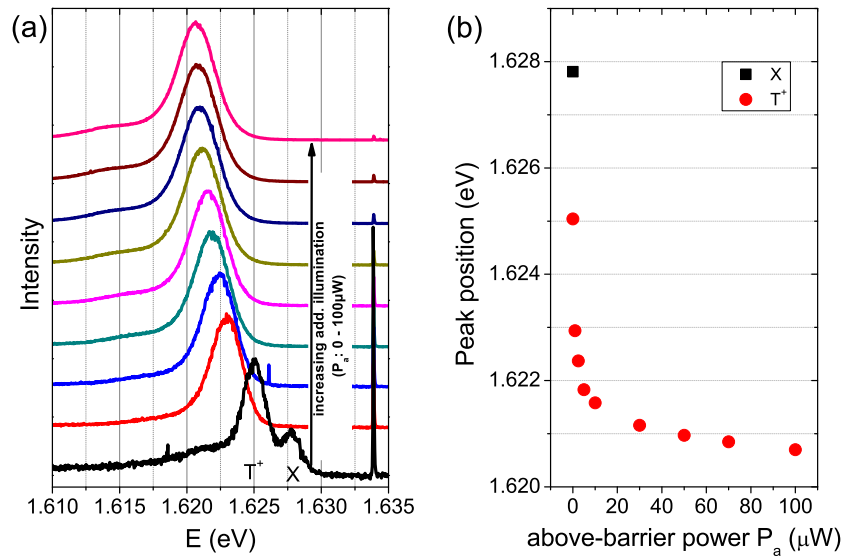


Figure 6.6: (a) PL of the two-colour excited sample 031709B-II (15nm cap). (b) The spectral positions of the characteristic peaks at above-barrier illumination.

spectrum does not change neither for increasing additional illumination nor for different B-fields, i.e. a large trion signal T^+ and a small exciton signal X are observed. Only the intensity and the spectral position of the trion changes with increasing additional illumination which mirrors an increasing hole concentration inside the QW.

Mn-g-factor The Mn-g-factor is determined from the spectra shown in Figure 6.7 ((b), (d), (f)) from the observed 1PR-signal. The results are plotted in Figure 6.8 as a function of the hole concentration n_h .

It is remarkable, that the largest Mn-g-factor without additional illumination is about 1.96(3) and not $g_{Mn} = 2.00$ as expected for the atomic value of Mn^{2+} . In addition the lowest determined g-factor at low B-fields (2.25-3.00T) is at $g_{Mn} = 1.77$. This is the lowest g-factor determined in this thesis.

The hole concentration is estimated in the same way as in section 6.1. The exciton is again assumed to be constant within the used power range of the two-colour method shown in Figure 6.6 justifying a larger error bar with increasing hole concentration in Figure 6.8.

Figure 6.8 shows no onset of Mn-g-factor saturation with increasing hole concentration at low and high B-fields in contrast to the Mn-g-factor of the 13nm capped sample in Figure 6.4, although the maximum range of photo-generated hole concentration is almost of the same order. From the experimental setup point of view the trion can still further red-shift resulting in the further increase of the hole concentration n_h in the QW but with the opposing effect of a virtually vanishing 1PR-signal. Hence, this avoids the determination of the Mn-g-factor at further increased hole concentration.

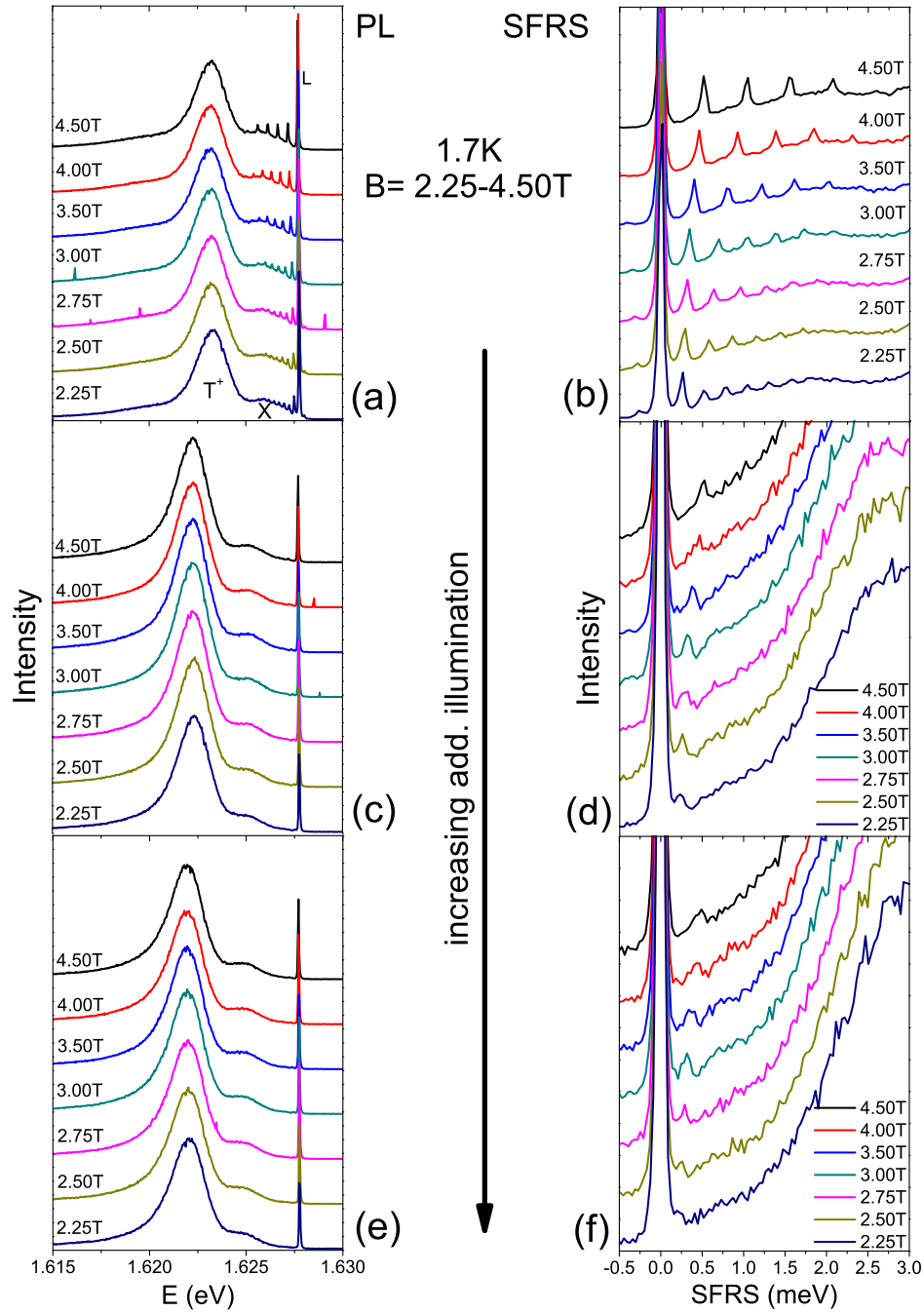


Figure 6.7: PL- and Multi-PR signals of 031907B-II (15nm cap) influenced by the above-barrier excitation. (a) and (b) represent the starting point of the measurement series without additional illumination. The dashed line marks the exciton position at 0T.

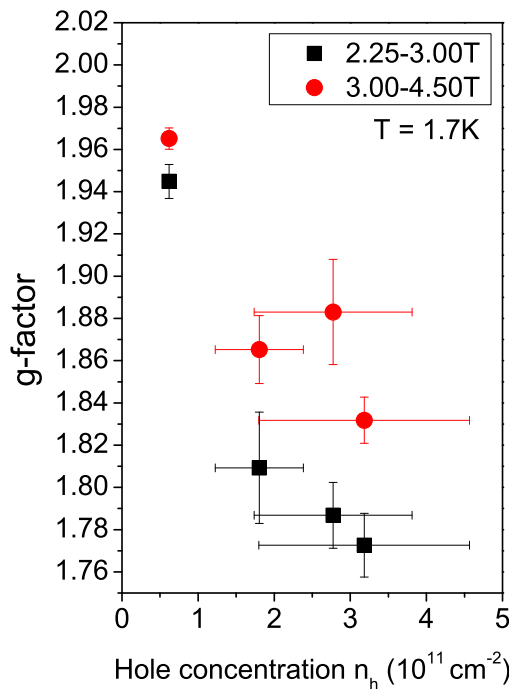


Figure 6.8: Mn-g-factor vs. hole concentration of sample 031907A-II (15nm cap) determined for low (2.25-3.00T) and high (3.00-4.50T) magnetic fields.

6.3 Sample with 17nm Cap thickness (031709B-III)

Below-barrier excitation For the 17nm cap sample within a large power range of the below-barrier excitation ($P_b=1-110\mu\text{W}$) no exciton signal appears in the PL spectrum (see Figure 6.9(a)). The trion signal T^+ is the omnipresent and dominating signal of the PL spectrum for all below-barrier illuminations. According to Figure 6.9(b) the saturation of the trion red-shift is not yet reached in this power range of investigation. The black arrow shown in (b) will be discussed in connection with the PL spectra of the two-colour exciton measurements.

Two-colour excitation The PL-line shape for the two-colour excitation in Figure 6.10(a) is very similar to the one using the below-barrier exciton shown in Figure 6.9(a). Again the trion signal T^+ dominates the PL-spectra with increasing power and no exciton signal appears. In contrast to that, the spectral position of the trion shows a different behaviour with increasing additional illumination power in the two-colour experiment. The signal saturates at about $10\mu\text{W}$ (cf. Figure 6.10(b)). The saturation value is 1.622eV for the trion signal. It is marked by the black arrow in Figure 6.9(b) for comparison. This points out that the saturation of the red-shift using two-colour illumination has an earlier onset with increasing illumination power from above the barrier. The below-barrier excitation leads to a larger red-shift of the trion than the influence of the two colour illumination.

This is different compared to the previously discussed PL-behaviour of samples 030807A-

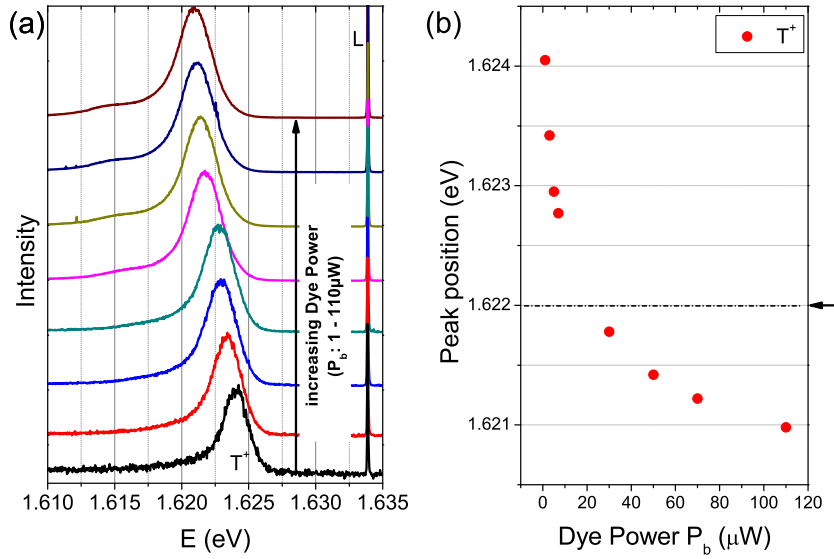


Figure 6.9: PL spectra at the below-barrier excitation of sample 031709B-III (17nm cap). The PL spectra are normalised to the maximum intensity of the trion signal T⁺

I (17.5nm cap) and 031709B-I (13nm cap), respectively. Thus the photo-generated charge carriers from below and above the barrier at this sample cap thickness affect the hole concentration of the 2DHG differently.

Multi-PR signals Again the Multi-PR signals and the corresponding Mn-g-factor are investigated via two-colour illumination in an external magnetic field up to 4.5T. For demonstration, Figure 6.11 shows the PL-spectra ((a),(c)) and the Spin Flip Raman spectra ((b),(d)) both without and with additional illumination, respectively. Without additional illumination and with a low below-barrier excitation power of $P_b=1\mu\text{W}$, only two PR-signals are observable. Using the additional light from above-barrier, only one weak 1PR-signal at high magnetic fields (4.00T and 4.50T) is left.

The corresponding Mn-g-factors for the case without additional illumination are:

- $g^{\text{low}B\text{-field}} = 1.93 \pm 0.01$ for 2.00T-3.00T and
- $g^{\text{high}B\text{-field}} = 1.94 \pm 0.01$ for 3.00T-4.50T.

The result of the Mn-g-factor determination for the case with additional illumination is not meaningful because at most two PR-signals at different B-fields can be used. Nevertheless a very rough estimation of the Mn-g-factor only at high magnetic fields (4.00T-4.50T) could be done: $g = 1.71 \pm 0.14$. An estimation of the hole concentration is impossible because in none of the detected spectra an exciton signal could be observed, even at technically realisable lowest illumination.

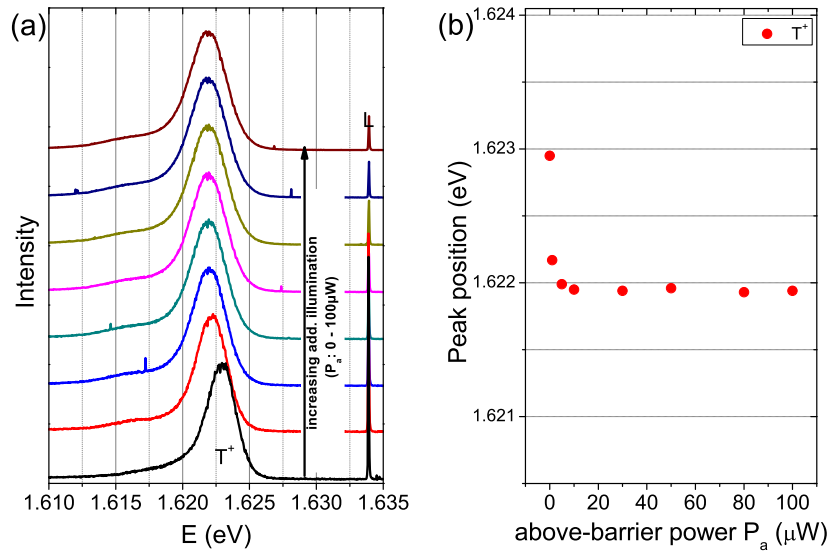


Figure 6.10: PL spectra at the two-colour excitation of sample 031709B-III (17nm cap). The below-barrier excitation is $P_b = 5\mu$ W. (b) Determined spectral positions of the dominant T^+ -signal in the spectra.

According to the previously shown PL-characteristics (Figure 6.9, Figure 6.10) and the determined Mn-g-factor even at low below-barrier excitation power, it can be concluded that a significant hole concentration already exists in the QW.

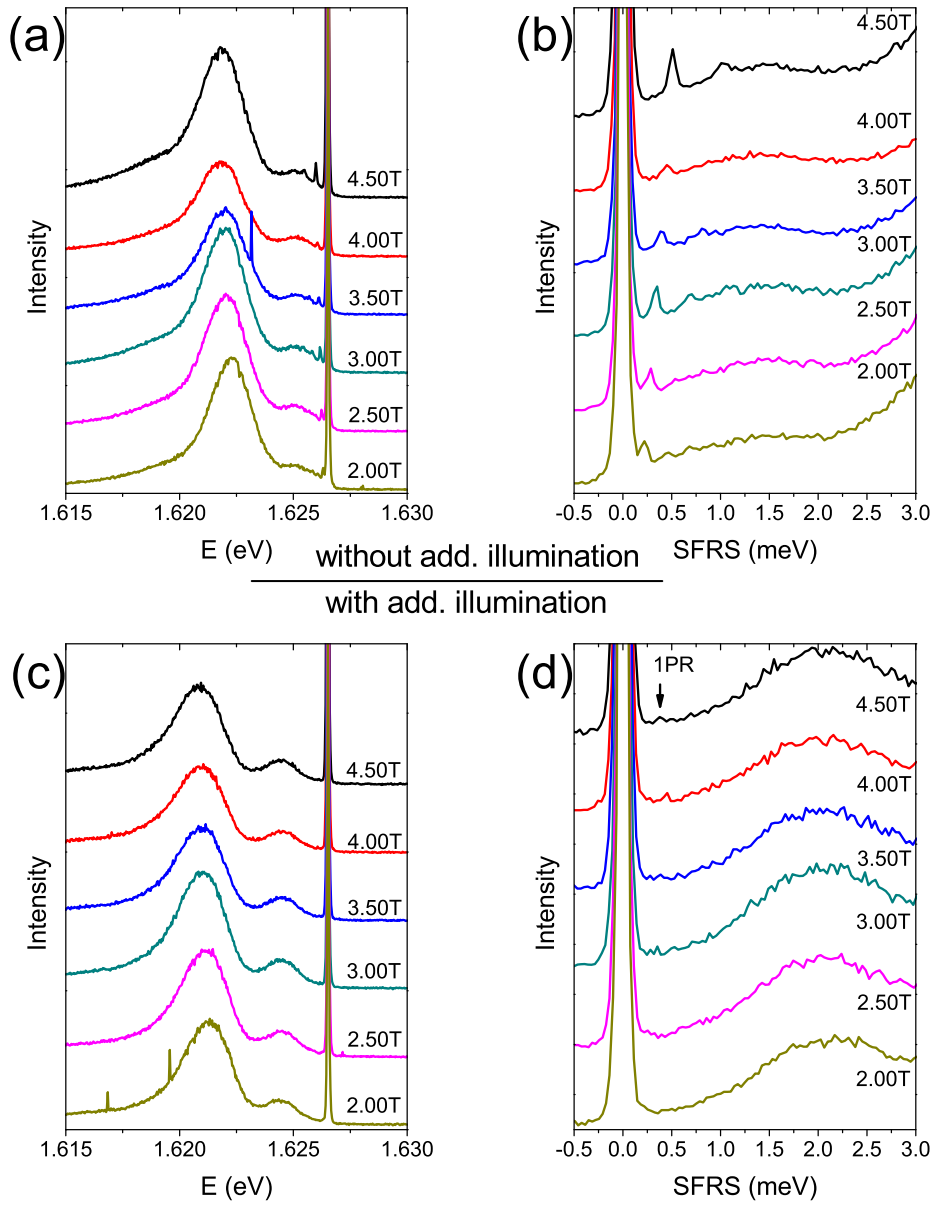


Figure 6.11: PL- and Multi-PR signals of sample 031907B-III (17nm cap) influenced by above-barrier excitation. (a) and (b) show the case without additional illumination while (c) and (d) are demonstrating the case with additional illumination.

6.4 Sample with 19nm Cap thickness (031709B-IV)

Below-barrier excitation For the below-barrier excitation at the sample with a cap of 19nm, in principle only the trion signal T^+ is observable in a large power range from 4 to $100\mu\text{W}$, as shown in Figure 6.12(a). No exciton signal could be observed. With the

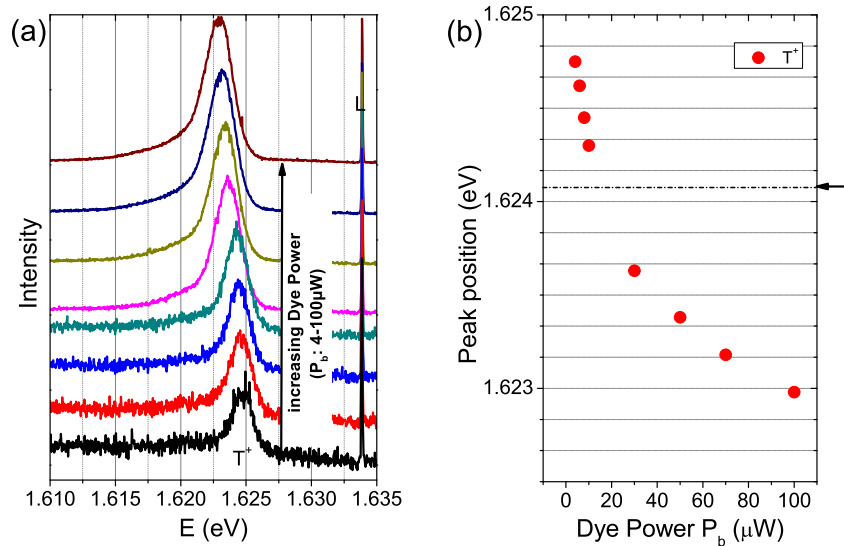


Figure 6.12: PL-spectra of the below-barrier excitation of sample 031709B-III (19nm cap).

help of a two-Gaussian fit procedure satisfying the asymmetric line shape of the trion signal, the spectral position of the trion was determined. The result is plotted in Figure 6.12(b). A clear red-shift without saturation of the spectral position of the trion peak was observed within this below-barrier excitation upper limit criterion. The black arrow marks the saturation values of the trion signal at the two-colour illumination presented next.

Two-colour excitation The two-colour experiment with a basic below-barrier illumination power of $P_b = 2\mu\text{W}$ starts at $P_a = 0\mu\text{W}$. Then P_a is increased to $110\mu\text{W}$. The dominating signal in this measurement series is again the trion signal T^+ . Comparing the two PL-spectra in Figure 6.13(a) without additional illumination (black) and with an additional illumination of $P_a = 1\mu\text{W}$ a clear red-shift of the trion signal is observed. Although starting with an additional illumination power of only $1\mu\text{W}$ the red-shift of the spectral position of the trion is already almost completely saturated in the first spectrum.

Multi-PR signals The PL- and Multi-PR spectra of the two-colour excitation in an external magnetic field (2.0-4.5T) of sample 031709B-IV are shown in Figure 6.14. (a) and (b) are the results of pure below-barrier excitation while (c) and (d) represent

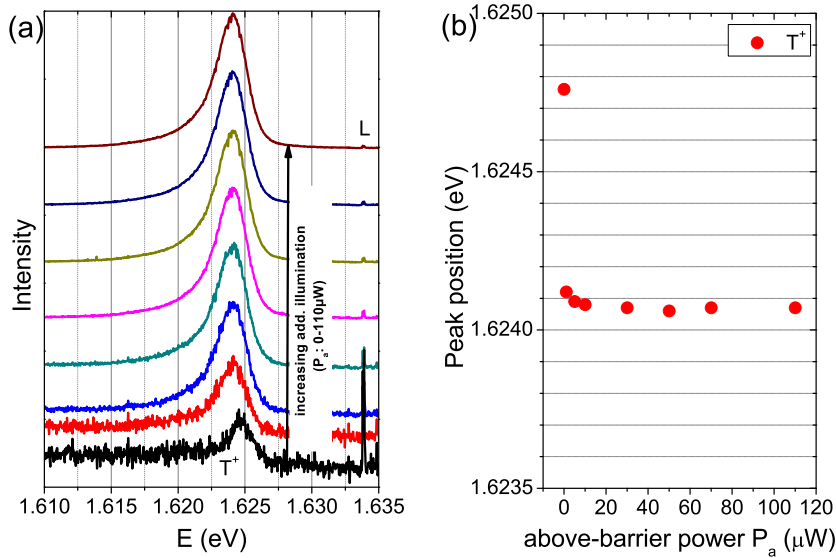


Figure 6.13: (a) PL spectra at the two-colour excitation of sample 031709B-IV (19nm cap). The below-barrier excitation is $P_b = 2\mu\text{ W}$. (b) Determined spectral positions of the dominant T^+ signals in the spectra.

spectra with additional illumination. It is noticeable that the number of PR signals is reduced to a single signal (1PR). This is the case both with and without additional above-barrier illumination. Additionally, the 1PR-signal is very weak and noisy although the exciton PL-signal X appears in the applied magnetic field (cf. Figure 6.14(a),(c)).

The PR-signals cannot be exactly fitted via Gaussian fits because their intensity is very low and noisy. Nevertheless, to get an orientation which Mn-g-factor belongs to these spectra, a rough estimation was done using the spectral positions of the 1PR-signal determined by eye. The estimated Mn-g-factors for high B-fields (3.0-4.5T) are $g = 1.80 \pm 0.02$ and $g = 1.77 \pm 0.06$ without and with additional illumination, respectively.

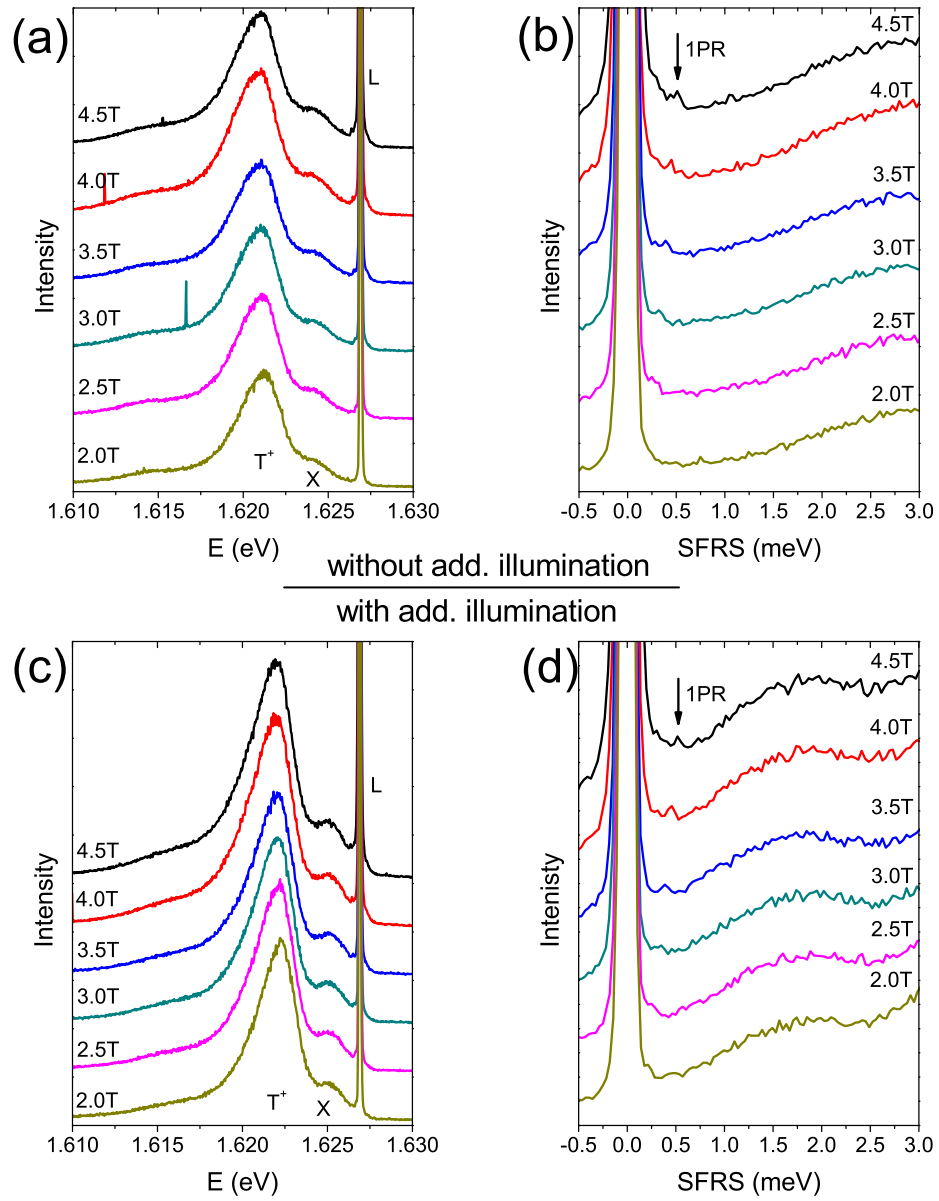


Figure 6.14: PL- and Multi-PR signals of sample 031907B-IV (19nm cap) influenced by the above-barrier excitation. (a) and (b) show the case without additional illumination while (c) and (d) are demonstrating the case with additional illumination.

6.5 Conclusion of the PL-behaviour depending on the cap layer thickness

As shown in the previous sections (6.1 - 6.4) the set of four $\text{Cd}_{0.99}\text{Mn}_{0.01}\text{Te}/\text{Cd}_{0.80}\text{Mg}_{0.20}\text{Te}$ QW samples (031709B-I-IV) with different cap thicknesses (13-19nm) was investigated with below-barrier illumination and with two-colour illumination. In general both types of illumination generate an excess hole concentration i.e. a 2DHG inside the QW. In the case of the two-colour illumination the below-barrier excitation was generally applied in moderate power for keeping its contribution to the photo-generated hole concentration as low as possible.

For the below-barrier illumination as well as for the two-colour illumination the positive trion increasingly becomes the dominating PL-signal with increasing cap thickness in the range between 13 and 19nm. This is an indication of increasing initial hole concentration in the QW from surface doping within this range of cap thicknesses (cf. section 4.1). This means at all of these samples, the hole concentration of the 2DHG can be influenced by illumination.

For both types of illumination the PL-spectra change their behaviour between the

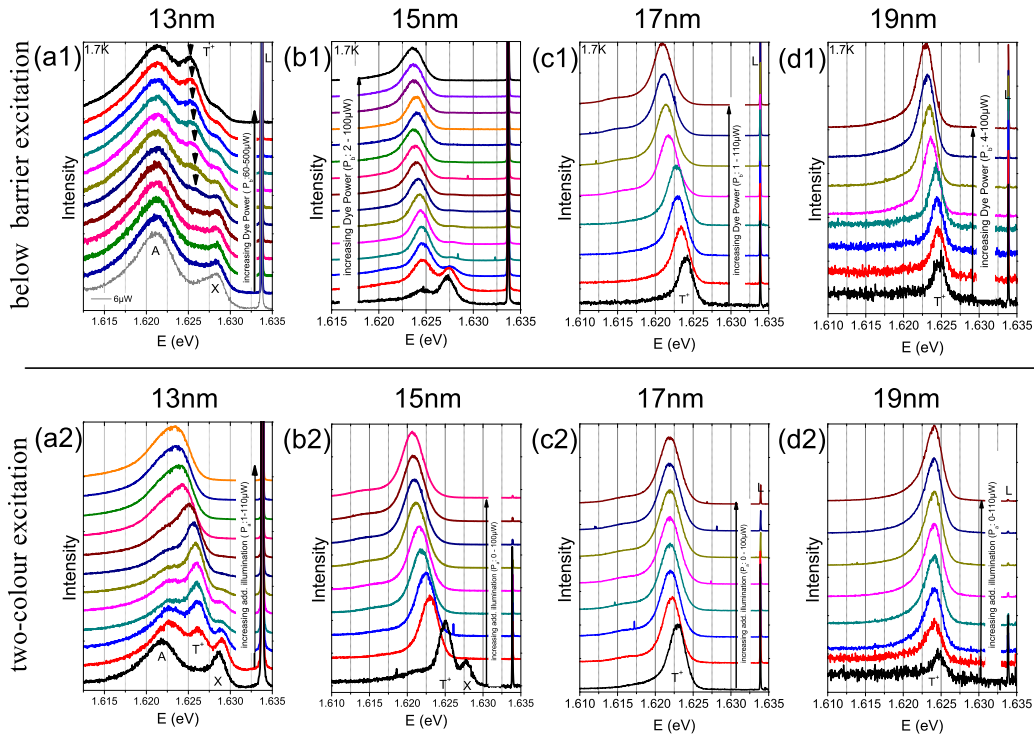


Figure 6.15: Overview of the PL-behaviour of the samples 031709BI - IV with a below-barrier illumination (a1)-(d1) and with a two-colour illumination (a2)-(d2), respectively.

15nm- and 17nm-cap sample concerning the influence on the PL-behaviour. On the one hand for the 13nm- and 15nm-capped sample it is possible to excite the PL-spectrum with a dominating exciton signal X at small illumination power and with none or a

small trion signal (see Figure 6.15). With increasing power the intensity stealing between the exciton- and trion-intensity can be observed. On the other hand no influence on the X-T ratio occurs for the 17nm- and 19nm-capped samples. Even if the illumination power is reduced to its setup-specific minimum, the trion PL-signal is the only observed feature in the PL-spectra (Figure 6.15 (c1-d1) and (c2-d2)).

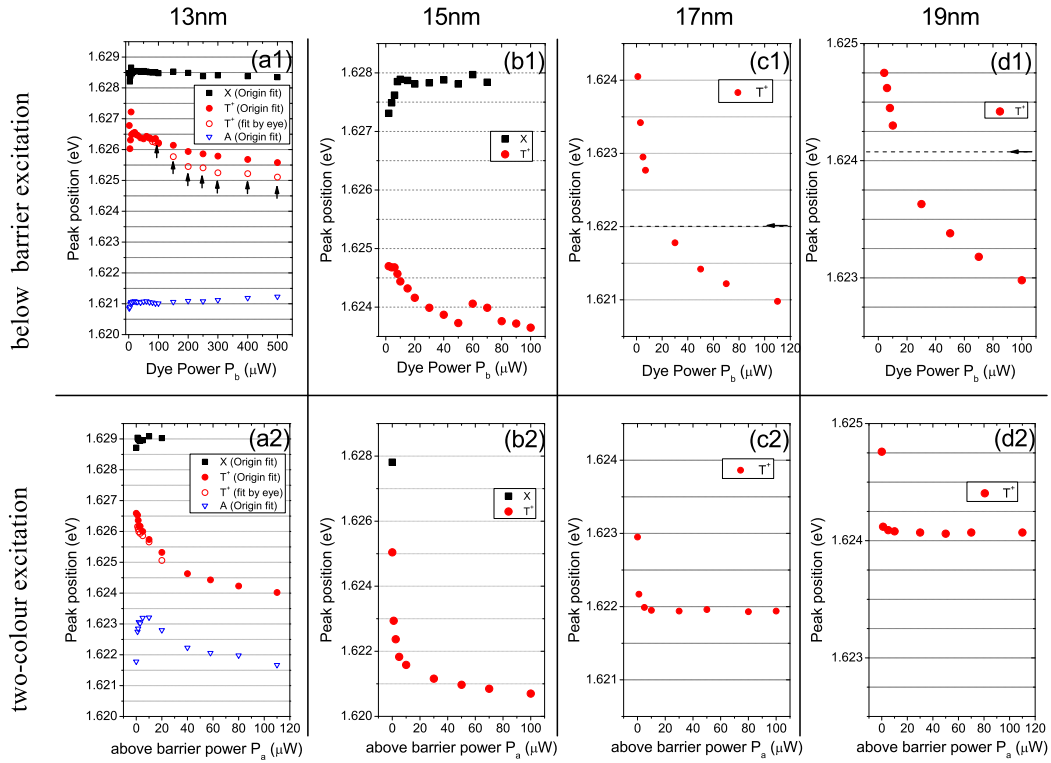


Figure 6.16: Summary of the determined spectral positions of the three significant PL-features of samples 031709BI - IV from Figure 6.15 without (a1)-(d1) and with additional illumination (a2)-(d2), respectively

The spectral positions of the PL-peaks in Figure 6.15 are summarised and compared for pure below-barrier excitation and for two-colour excitation in Figure 6.16, respectively. Due to the fact that the trion signal dominates the PL-spectrum at the 17nm- and 19nm-cap sample (cf. Figure 6.15 (c1)-(d1) and (c2)-(d2)), only the trion position is plotted in Figures 6.16 (c1)-(d1) and (c2)-(d2).

In the following, on the one hand the 13nm and 15nm capped samples and on the other hand the 17nm- and 19nm-cap samples are discussed.

13nm and 15nm cap thickness Referring to the 13nm and 15nm cap samples the converging exciton position⁵ of the below-barrier excitation has a discrepancy of about 0.5meV (13nm cap: $\approx 1.6284\text{eV}$, 15nm cap: $\approx 1.6279\text{eV}$) which is negligibly small. Similar values are determined for the two-colour excitation. The exception is the blue-shift of the exciton position in Figure 6.16 (a2) to 1.6290eV. The likely reason is the fitting error of the three-Gaussian peak fit, due to the disappearing exciton signal (see Figure 6.15 (a1) - fourth curve from below -).

Comparing now the behaviour of the trion position of Figure 6.16 (a1),(a2) and (b1),(b2), respectively the trion red-shift is stronger for the two-colour excitation than for the below-barrier excitation i.e. the above barrier excitation is more efficient for the hole diffusion into the QW.

17nm and 19nm cap thickness Although using setup-limited lowest possible below-barrier illumination, no exciton signal appears and thus no photo-generated influence on the X-T intensity ratio is possible. As mentioned earlier the trion signal is omnipresent in all of the PL-spectra of the 17nm- and 19nm-cap samples. This is the reason why Figures 6.16 (c1),(d1),(c2) and (d2) only represent the trion peak position versus illumination power. In contrast to the 13nm- and 15nm-capped samples the saturation of the trion red-shift caused by the two-colour excitation is at higher energy 1.6220eV in Figure 6.16 (c2) and 1.6243eV in Figure 6.16 (d2) compared to the pure below-barrier excitation in Figure 6.16 (c1) and (d1), respectively. This leads to the assumption that the below-barrier excitation triggers the maximum excess hole concentration in the two-colour excitation at the samples with the cap thicknesses of 17nm and 19nm, respectively.

In summary, according to the observed PL-behaviour at these sample thicknesses (17nm and 19nm) just small illumination power leads to a large excess hole concentration in the QW which coincides with a disappeared exciton signal and an intense and red-shifting trion PL-signal.

In principle in all four samples, the hole concentration can be influenced via illumination but not concerning the X-T intensity ratio which is important for the softening of the Mn-g-factor. The quintessence of the cap layer thickness and its influence on the Mn-g-factor is summarised in Table 6.1.

The observation by PR-Raman scattering of a quasi-continuous softening of the Mn-g-factor (i.e. the magnetic soft mode behaviour) by increasing the 2DHG is only possible as long as

- an exciton signal appears and
- the X-T intensity ratio and its spectral distance can be influenced by photo-generated carriers, respectively.

The first one can be seen as the resonance-"medium" for the Multi-PR signals. According to Figure 4.4 in section 4.1 the Multi-PR signals appear only in resonant

⁵at "high" power illumination

excitation with the exciton signal and not with the positive trion signal. The latter is the obvious indication for the photo-generated influence of the 2DHG in the QW.

sample 031709...	BI	BII	BIII	BIV
cap / [nm]	13	15	17	19
influencing X-T intensity ratio	yes	yes	no	no
2DHG-influence on Mn-g-factor	yes	yes	no	no

Table 6.1: Overview of spectroscopically observed properties at the samples 031709BI-IV.

Table 6.2 summarises the 2DHG-influenced Mn-g-factors obtained for different cap thicknesses. There is a tendency that coincides with the general influence of the 2DHG

sample 031709...	BI		BII		BIII		BIV	
cap / [nm]	13		15		17		19	
Mn-g-factor	min	max	min	max	min	max	min	max
at (2.50-3.00T)	1.87	2.00	1.77	1.95	x	1.94	x	x
at (3.00-4.50T)	1.94	2.00	1.83	1.97	≈1.71	1.94	≈1.77	≈1.80

Table 6.2: Determined Mn-g-factors of samples 031709BI-IV under the influence of the 2DHG and different cap layer thicknesses. "min" stand for the minimal Mn-g-factor at maximal additional illumination (i.e. maximum influence of the hole concentration) in a certain measurement series, "max" represents the maximal Mn-g-factor at a moderate below-barrier excitation and no additional illumination.

on the Mn-g-factor: the larger the hole concentration (which coincides here with: the thicker the cap) the larger the Mn-g-factor reduction at these investigated cap layer thicknesses. But as demonstrated in the previous sections the determination of the Mn-g-factor is more difficult with increasing cap layer thickness at all.

The next chapter discusses and interprets the complex mechanism how the photo-generated hole concentration of the QW is connected to the cap layer thickness.

Chapter 7

Discussion - PL-behaviour -

The observations of the previous sections 4.1 and 6.1 - 6.4 will now be interpreted and analysed concerning the PL-behaviour with (i) below-barrier excitation and (ii) the two-colour excitation.

It can be assumed that there are three recombination channels for e-h excitations:

- impurity-bound exciton A
- trion T
- exciton X

The impurity-bound exciton is most dominant in the PL-spectra of the sample with the smallest cap, i.e. 13nm (031709B-I). Its spectral relevance decreases with increasing cap layer thickness i.e. the A-signal intensity is reduced compared to the exciton signal and trion signal. The recombination channels causing this PL-signal could originate from impurities located both at the QW interface and the surface with a wave function extending into the QW. The latter is more likely due to the above mentioned observations. Due to non-ideal stoichiometry of the basic material CdTe a small background doping of the sample cannot be excluded as well [Kra07]. In bulk material this would be an n-type doping. Due to the fact that the A-signal is less relevant for the magnetic soft mode behaviour and does not increase its intensity with increasing hole concentration a detailed investigation and discussion would go beyond the scope of this thesis.

The trion signal was identified as a positive one in section 4.1. It is the main indicator for influencing the 2DHG (i.e. the hole concentration) of the QW because of its red-shift and its increased intensity at the expense of the exciton signal in the PL-spectra. In the following, two mechanisms are discussed which are of relevance for the photo-generated hole concentration tuning in nominally undoped near-surface positioned QWs which initially show a surface-state induced p-type doping [KAK⁺09]:

- surface-states and the resulting band bending
- tunnelling behaviour of electrons and holes depending on the cap layer thickness

Surface states In general, depending on the nature of the surface states (acceptor or donator) either an upward or downward band bending exists, and an above-barrier excitation is able to cause an accumulation of holes or electrons at the surface, respectively ([OLS⁺03], [Mön01]). On the other hand, for the case of a QW positioned close to the surface this leads to an accumulation of either photo-generated electrons (upward bending) or holes (downward bending) from above barrier in the QW. In addition, for thin cap layers, the tunnelling probability of charge carriers out of the well¹ to the surface or vice versa increases with decreasing cap layer thickness. The in-diffusion of carriers and the carrier tunnelling out of the well are competing processes. The connection of semiconductor surface states and a QW positioned close to the surface results in a complex interplay of these effects. The resulting band bending of the QW-cap layer depends on the one hand on the thickness of its cap layer and on the other hand on the energetic position of the surface states related to the FERMI energy between the VB and CB. In the following, different band bendings which result of these mentioned properties will be discussed (satisfying the PL-dynamics observed in this thesis).

This discussion will be preceded by a brief introduction of surface states in general. Surface states are caused by unsaturated chemical bonds lacking of binding partners at the surface. For the case that the atoms remain at their former lattice sites at the surface (surface relaxation) and the bonds are covalent this results in unsaturated bonds perpendicular to the surface, called dangling bonds [Czy08]. Surface relaxation means that the 2D translation invariancy parallel to the surface is conserved i.e. surface atoms can either be stucked out of the surface or pushed in. In contrast, the surface reconstruction causes the development of new bonds between the unsaturated orbitals of the surface, resulting in new lattice structures at the surface.

The surface of a crystal causes electronic states which are energetically located in the forbidden region of the electronic band structure i.e. in the energy gap. It must be distinguished between intrinsic and extrinsic surface states. The intrinsic ones are caused by unsaturated chemical bonds and the extrinsic ones have their origin in impurities or adsorbed atoms at the surface [Czy08]. For the samples investigated in this thesis it is assumed that both intrinsic and extrinsic surface states exist.

Mašlana et al ([MKB⁺03]) published studies of CdTe and Cd_{1-x}Mn_xTe quantum wells which were p-type doped from surface states. They showed that this doping method was as efficient as usual modulation doping with nitrogen acceptors². It was pointed out that the resulting hole concentration systematically depends on the cap layer thickness. According to Figure 7.1(a), starting from a rather high cap layer thickness ($\approx 60nm$) the hole concentration increases with decreasing cap layer thickness and reaches its maximum at 25nm. Thus, in this range of cap layer thickness, a thinner cap layer in the surface doping makes the mechanism of the increasing hole density more efficient. But for thicknesses below 25nm the reverse effect was observed i.e. the hole concentration decreases and virtually vanishes at about 15nm (orange region in Figure 7.1(a)).

The carrier concentration of the QW was determined via Moss-Burstein shift (MB). The Moss-Burstein shift is the difference of the transition energies between PL and blue-

¹see paragraph: tunnelling behaviour of electrons and holes

²nitrogen-doping layer is located between the QW and the substrate

shifted absorption (or PLE³). Therefore it is a fingerprint of the presence of a carrier gas in the QW but without making any assumptions on the nature of the carriers (either holes or electrons). According to Mašlana the surface states were identified as acceptor surface states due to CdTeO₃-surface oxidation⁴ and thus trapping electrons. A scheme of the likely resulting near-surface band bending of the VB is shown in Figure 7.1(b). The energy position of the surface states is defined by the distance ΔE at flatband

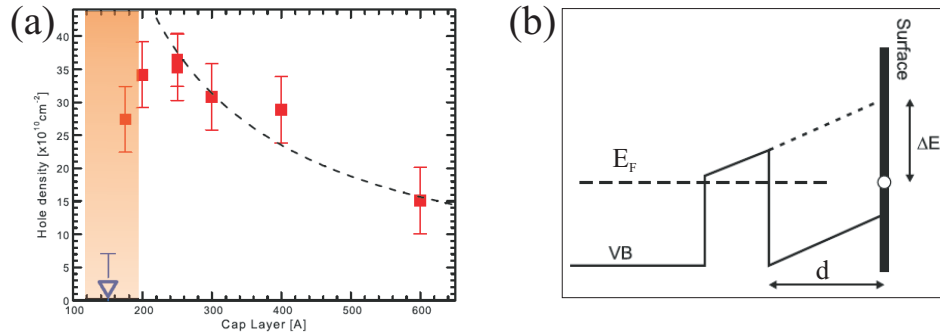


Figure 7.1: (a) shows the plot of the 2DHG-concentration vs. cap thickness which was experimentally determined on $Cd_{0.99}Mn_{0.01}Te / Cd_{1-y-z}Zn_zMg_yTe$ QW samples ($y = 0.22, z = 0.08$ and $y = 0.22, z = 0.00$, respectively) by MAŠLANA et al [MKB⁺03] [Maš07]. The relevant part of the plot for this thesis is orange-coloured. (b) shows the possible band bending which affects the hole concentration inside the QW according to MAŠLANA et al [MKB⁺03].

condition between the acceptor states and the level confined in the QW. Assuming now ΔE as the only adjustable parameter the hole density is mostly determined by the effect of the electric field between the QW and the surface. Using Gauss' theorem⁵ the QW hole density p writes [MKB⁺03]:

$$p = \frac{\epsilon\epsilon_0}{e \cdot d} \cdot \Delta E \quad (7.1)$$

with the dielectric constant of the cap material $\epsilon=10$, the permittivity of vacuum ϵ_0 , the electron charge e and the cap layer thickness d . This assumption mirrors the experimentally determined hole concentration with increasing cap layer thickness in the range between 25nm and 60nm in good agreement represented by the fitting plot (dashed curve) in Figure 7.1(a). Due to the fact that (7.1) neglects any tunnelling or diffusion processes it is more difficult to get a theoretical access to the cap layer thicknesses between 15nm and 25nm. Nevertheless it can be assumed that the discrepancy for cap thicknesses smaller than 25nm in the simple model used for equation (7.1) originates from the interplay of the carrier tunnelling and the surface states, because at these small cap thicknesses the carrier tunnelling is more likely. In principle, electrons trapped by the surface acceptor states can tunnel from the surface to the QW until a new equilibrium between in- and out-tunnelling processes is achieved and thus decreasing ΔE , resulting in a reduced hole concentration p in the QW. This could explain the opposite trend of hole concentration as a function of cap layer thickness compared to

³photoluminescence excitation

⁴CdTeO₃ is energetically favourable to TeO₂ [Maš07]

⁵also called divergence theorem: $div \vec{E} = \rho/\epsilon_0$ Maxwell equations

caps larger than 25nm.

In Mašlana's thesis the influence of the illumination on a surface doped QW sample with a well width of 10nm and a cap thickness of 25nm depends on the excitation energy of the light. For this sample three different cases occur: (i) below-barrier excitation has no effect on the carrier density, (ii) above barrier excitation with an energy close to the barrier band gap causes a depletion of the hole gas in the QW due to the fast in-diffusion of electrons into the well and much slower hole tunnelling into the well. (iii) In contrast, an illumination energy much higher than the barrier band gap increases the hole gas density [Maš07]. This can be explained by a decrease of the electron trapping efficiency by the QW for high energy electrons, combined with an enhancement of the hole tunnelling probability at high kinetic energies. The high energy electrons penetrate deep in the sample while the holes tunnel into the QW (Figure 7.1(b)).

Comparing now the PL-behaviour of the samples discussed previously in this thesis with the mentioned one of Mašlana et al [MKB⁺03] there are some differences in spite of the similarity of the sample structures. In contrast to Mašlana, at sample 030807A-I as well as at the sample series 031709B-I-IV both the below-barrier illumination and above-barrier illumination cause an increasing hole concentration demonstrated in subsections 4.1.2-4.1.3 and 6.1-6.4, respectively. The reason for the different effects of the below-barrier excitations may be the lower cap thickness (13-19nm), which causes a higher tunnel efficiency of the electrons through the barrier to the surface states. It could also be an indication of the upward bending of the electronic bands between the QW and the surface with acceptor states of sample 030807A-I.

The possibility of a downward bent cap band can be discussed as follows. This could be the case for mid-gap pinning and a nominally undoped QW with a VB-band offset of about 40% shown in Figure 7.2. Under below-barrier excitation, but dependent on the electron tunnelling efficiency and thus on the cap layer thickness, photo-generated electrons can tunnel to the surface states leaving a majority of holes in the QW. Due to the potential slope of the cap band an above barrier excitation causes an electron diffusion to the surface states while the holes "fall" into the QW. Under both kinds of illumination a steady state of hole excess density in the QW is achieved and thus satisfying the experimental observations. In the case of the existence of weak pinning shown in Figure 7.2(b) the slope of the band bending is assumed to be constant (in contrast to a mid gap pinning). An exemplary sketch of strong and weak pinning for the down-bent cap bands with varying cap thickness is shown in Figure 7.2(c) and (d), respectively. According to [CCHH98] the available unoccupied surface states decrease with decreasing cap layer thickness by crossing the FERMI energy (E_F) as demonstrated in Figure 7.2(b). Thus the photo-generated carriers diffusing or tunnelling through the barrier find a decreasing number of free surface states with decreasing cap thickness. For the QW with a downward band bending in the cap, this would also explain the influence of the cap layer thickness on the (steady state) hole concentration in the QW.

Based on the PL-spectra of 031709B-I-IV for the two different excitation methods the spectral difference of the exciton spectral position between different cap thicknesses is

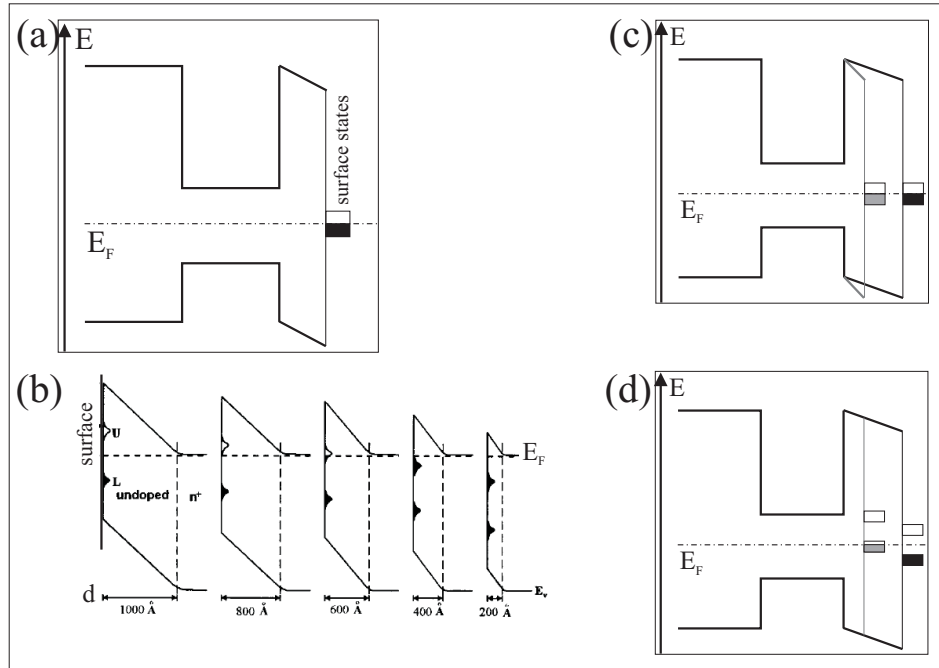


Figure 7.2: (a) Scheme of a downward bent cap band due to mid gap pinning. (b) Weak pinning dependent on the cap layer thickness according to CHOU et al [CCHH98]. (c) Scheme of the influence of the varying cap thickness on a strong pinning. (d) Scheme of the influence of the varying cap thickness on a weak pinning with respect to (b) adapted to the sample structure investigated in this thesis.

less than 1meV and thus it can be assumed that the Quantum Confined Stark Effect (QCSE) can be neglected in this sample series according to [CTZ⁺93]. Due to the neglect of the QCSE, a pinning of surface states close to the CB can be excluded and thus a downward bending of the cap bands can be excluded [CTZ⁺93].

The near-surface induced p-doping of the QW is one of two different processes of relative importance to achieve and explain the existence of an excess hole concentration in the QW. The second process which explains this excess hole concentration is based on the consideration of the different tunnelling behaviour of the photo-generated electrons and holes. This is discussed below.

Tunnelling behaviour of electrons and holes For the discussion of this phenomenon, the band bending at the surface is disregarded. CHANG et al [CTZ⁺93] used a simple model to estimate the tunnelling time of the electron and the hole from the well to the surface dependent on the cap layer thickness d . Their calculated results are confirmed by experimental data using below barrier excitation. CHANG et al assumed that all photo-generated carriers rapidly thermalize to the ground state of the QW before they either recombine in the well with the lifetime τ_r or tunnel to the surface with the time τ_t . This situation is comparable with a resonant excitation in the QW performed in this thesis. The tunnelled electrons and holes find empty states available at the surface and recombine non-radiatively. To calculate τ_r the knowledge of the density of surface states as a function of energy is needed but not available.

Dealing with this problem CHANG et al replaced the surface states by a second QW with the same parameters like the one under investigation. A weak coupling between these wells is assumed, i.e. a small overlap of the wavefunctions. The two lowest energy states of the coupled wells are the eigenstates of interest for the calculations. From the energy splitting of the even and odd-parity states (cf. the hydrogen molecule energy states) the tunnelling time of electrons and holes can be calculated using the equation [CTZ⁺93]:

$$\tau_{tunnel} \approx \frac{h}{4V_j} \cdot \frac{(\alpha_i^2 + k_{zi}^2)(1/\alpha_i + L/2)}{\alpha_i} \cdot \exp(\alpha_i \cdot d) \quad (7.2)$$

with

$$\alpha_i = \sqrt{\frac{2m_i^*(V_j - E_{0i})}{\hbar^2}} \quad (7.3)$$

$$k_{zi} = \sqrt{\frac{2m_i^*E_{0i}}{\hbar^2}} \quad (7.4)$$

the wave number values of the states in the barrier and the well, respectively. For the weak coupling approximation, it is assumed: $\exp(-\alpha \cdot d) \ll 1$. The index "i" stands for the electron "e" and hole "h", respectively. L is the well width, d the cap layer thickness and m_i^* is the effective mass. V_j is the well depth of the CB (V_C) and VB (V_V) considering a band-offset $V_C/V_V = 60/40$, respectively. E_{0i} represents the confinement energy of the QW which was labelled as V_e and V_h in Figure 3.3. The application of this scheme to our series of samples yields the corresponding tunnelling times of electrons and holes. The tunnelling time of electrons and holes was calculated for the parameters of a $\text{Cd}_{0.99}\text{Mn}_{0.01}\text{Te}/\text{Cd}_{0.80}\text{Mg}_{0.20}\text{Te}$ QW with $L = 10\text{nm}$, $m_e^* = 0.0992$ and different effective hole masses found in literature. Figure 7.3 shows the results of the calculated tunnelling times for different effective hole masses and LUTTINGER parameters plotted versus the cap layer thickness. According to Figure 7.3 within the region of interest for the cap layer thickness ($d = 13\text{nm} - 19\text{nm}$), the slope of the hole tunnelling time is larger than the electron tunnelling time. Thus the tunnelling time of the holes is about four (13nm) to six (19nm) decades higher than the one of the electrons. This means predominantly electrons can tunnel to the surface, resulting in an excess hole concentration in the QW. In principle the electron tunnelling rate triggers the photo-generated influence on the 2DHG in the QW.

In the following the PL-spectra of the below-barrier excitation and the two-colour excitation dependent on the cap layer thickness from 13nm to 19nm are discussed and interpreted under the previously presented aspects of near surface-induced p-doping of the QW and the different tunnelling behaviour of electrons and holes. Figure 7.4 serves as the key feature for the interpretation. Observed by MAŚLANA et al [MKB⁺03] the intrinsic hole concentration p in the QW caused by near surface-induced p-doping increases with increasing cap layer thicknesses up to 25nm.

13nm cap According to Figure 7.4 (a) the intrinsic hole concentration p in the sample with 13nm cap is zero, which is verified with the observed PL-spectra in Figure

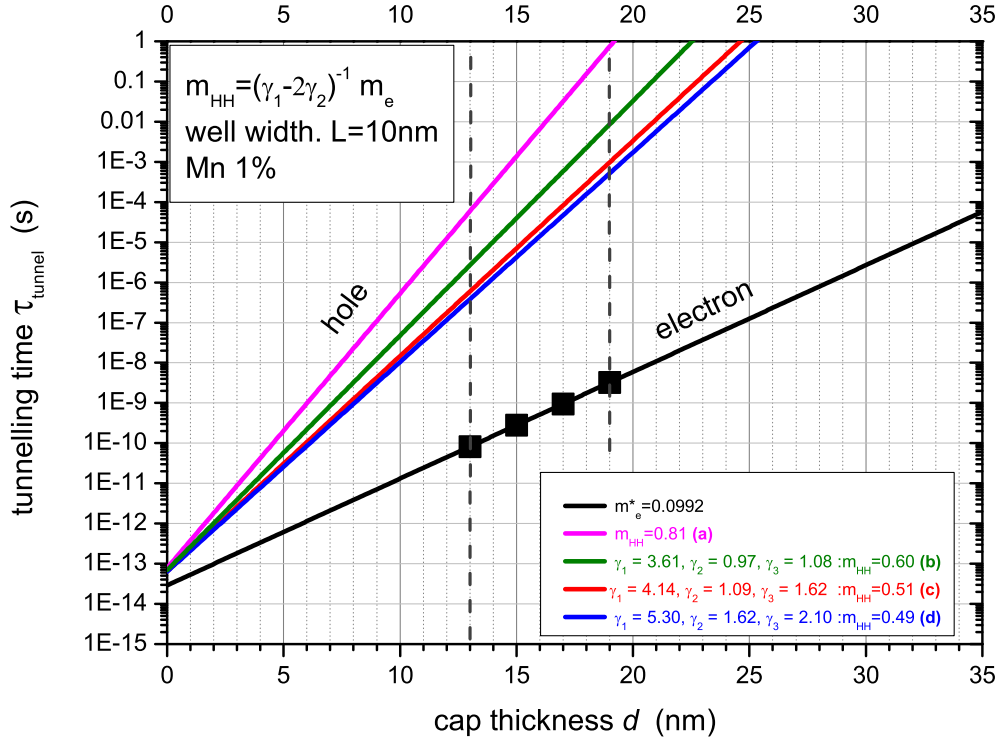


Figure 7.3: The tunnelling times calculated according to CHANG et al. [CTZ⁺93] for electron and heavy holes, respectively. The tunnelling time of holes is calculated for four different sets of hole masses and LUTTINGER parameters according to (a) [DNR82], (b)[LHHS97], (c)[FKM⁺94] and (d) [SK90], respectively. The vertical dashed lines define the cap layer thickness region of interest (13-19nm). The black squares represent the electron tunnelling times for the sample series of this thesis.

6.15 (a1-2) and Figure 7.4 (c) because no trion signal appears for low excitation power. The prominent signals are the exciton and the impurity-bound signal A. This is only the case for the 13nm cap sample.

The recombination channels caused by the impurities are not yet saturated because of the small photo-generated carrier concentration at low illumination power and because of the exciton life time which will be discussed below. This saturation sets in with increasing illumination power and thus with increasing hole concentration. The reason for the latter is the different tunnelling behaviour of photo-generated electrons and holes (cf. Figure 7.4 (b)). The increasing hole concentration n_h with increasing illumination power results in the increase of trion formation and recombination. Consequently the trion becomes the dominant signal in the high illumination power spectra. With increasing illumination power (below-barrier and two-colour excitation), it is possible to tune the T-X ratio of PL-spectrum from zero to infinity (i.e. to a virtually vanishing exciton signal).

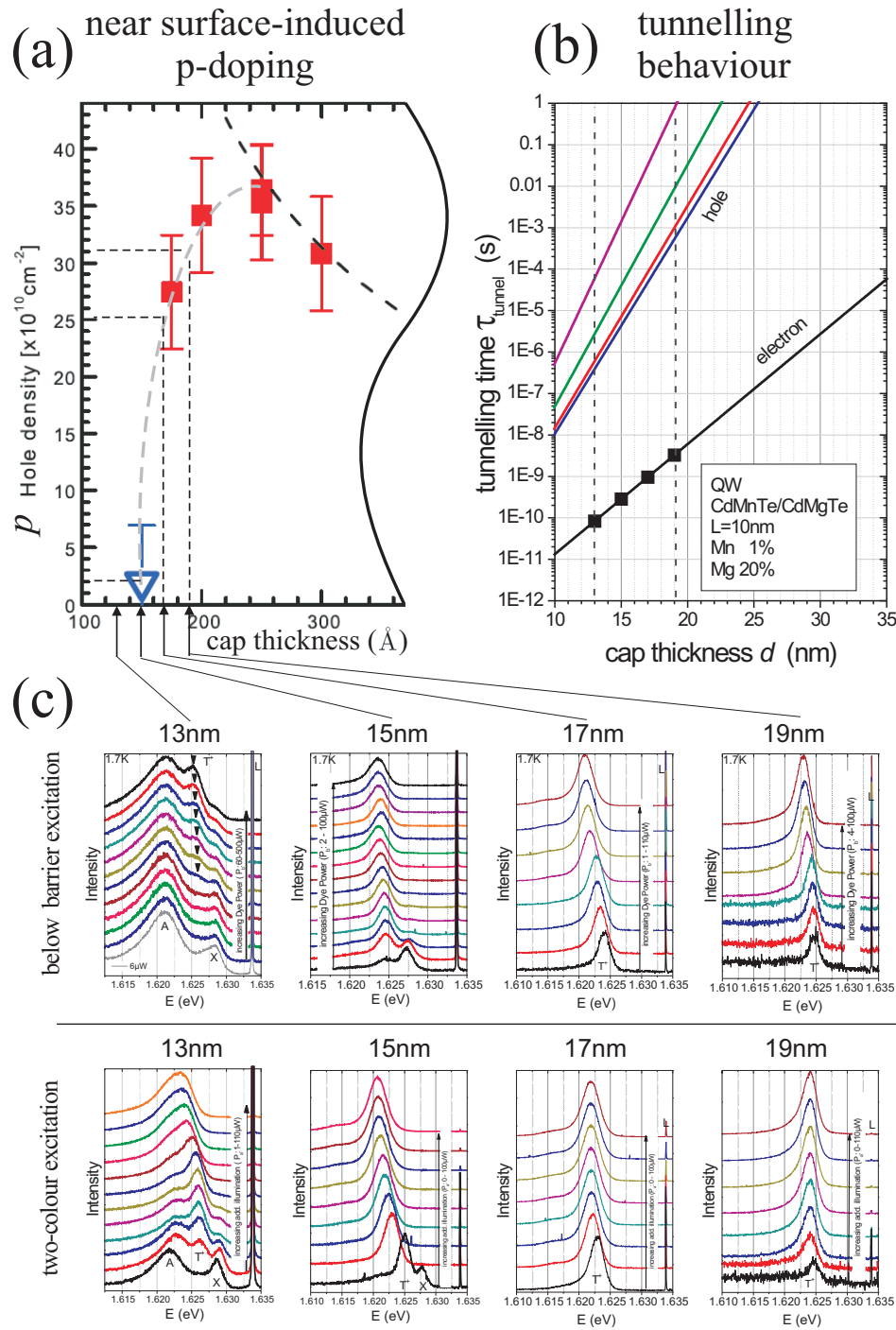


Figure 7.4: The interpretation of the cap layer impact. The reasons for the 2DHG in the QW: (a) the near surface-induced p-doping shown in this figure is the relevant detail for this thesis out of MAŠLANA’s plot (cf. [MKB⁺03], [Maš07]). The grey dashed line serves as a guide for the eye for the hole density p vs. cap thickness d in the range of 15nm to 25nm. The black arrows mark the relevant cap thicknesses of this thesis connected to its surface-induced (intrinsic) hole concentration p . (b) The different tunnelling behaviour of the photo-generated charge carriers depending on the cap layer thickness (cf. Figure 7.3) and its impact on the PL-spectra (c). A detailed interpretation is given in the text.

15nm cap Even at low excitation power a prominent trion signal was observed in the PL-spectrum of the 15nm cap sample (Figure 7.4 (c)). This mirrors an already existing hole concentration p induced by surface doping. The evaluated hole concentration n_h at low power⁶ from the spectral distance of X and T⁺ ($n_h \approx 1.67 \times 10^{10} \text{cm}^{-2}$) coincides with the one evaluated by MASLANA et al at 15nm cap thickness in Figure 7.4 (c) within the error bars ($p = (0 - 5) \times 10^{10} \text{cm}^{-2}$). This intrinsic hole concentration p can be increased by photo-generated carriers n_h from increasing illumination power. The reason is the already explained difference in tunnelling behaviour of photo-generated electrons and holes shown in Figure 7.4 (b). This difference is increased with increasing cap layer thickness resulting in a more efficient influence on the hole concentration in the QW.

17nm and 19nm cap Guiding the eye on the grey dashed line in Figure 7.4 (a) to the 17nm and 19nm cap layer thickness a surface-induced p-doping of the QW of $p = 2.8 \times 10^{11} \text{cm}^{-2}$ and $p = 3.1 \times 10^{11} \text{cm}^{-2}$ is reached, respectively. According to this Figure this is close to the maximum surface-induced p-doping ($\approx 3.5 \times 10^{11} \text{cm}^{-2}$) at 25nm cap layer thickness. This large amount of intrinsic hole concentration explains the domination of the trion signal in the PL-spectra for the whole illumination high-power range of the 17nm and 19nm cap samples.

Exciton life time Additionally, the exciton life time with respect to the electron tunnelling time must be discussed. The exciton life time $\tau_{X,lifetime}$ plays a major role concerning the tunnelling time of the 13nm and 15nm cap thickness because of equivalent time scales. The grey dense pattern in Figure 7.5 delimits the known life times of excitons in QWs from literature (43ps – 550ps). Compared to the QWs in this thesis the most common QW structure and material in literature is the investigated CdTe/CdMnTe QW by Polhmann et al [PHG⁺92] with $\tau_{X,lifetime} = 140\text{ps}$ and $\tau_{X,lifetime} = 170\text{ps}$ for well width of 3.4nm and 30.0nm, respectively (marked with a red arrow in Figure 7.5). For the case that $\tau_{X,lifetime} < \tau_{tunnel}$ most photo-generated electrons tunnel to the surface. In contrast, for $\tau_{X,lifetime} > \tau_{tunnel}$ most of these electrons recombine as excitons. Consequently, for the PL-behaviour of the 13nm cap where $\tau_{X,lifetime} < \tau_{tunnel}$ most of the photo-generated electrons either tunnel to the surface or recombine via the impurity bound exciton channel (assuming a rapid decay time of less than 80ps). This results in a prominent A-signal compared to the exciton signal for lowest possible excitation power. In contrast, for cap thicknesses larger than 15nm where $\tau_{X,lifetime} > \tau_{tunnel}$ the exciton signal is more prominent compared to the A-signal (cf. 15nm cap Figure 7.5). By further increasing excitation power the trion becomes the dominant signal of the PL-spectrum as already mentioned.

In conclusion the two main reasons for influencing the hole concentration (2DHG) in a near-surface QW were discussed. This is on the one hand the near surface-induced p-doping of the QW caused by the sample parameters, which can be seen as the "2DHG offset" or intrinsic hole concentration p of the QW. On the other hand this already existing hole concentration can be increased by photo-generated carriers n_h (up to

⁶here: $n_h \approx p$

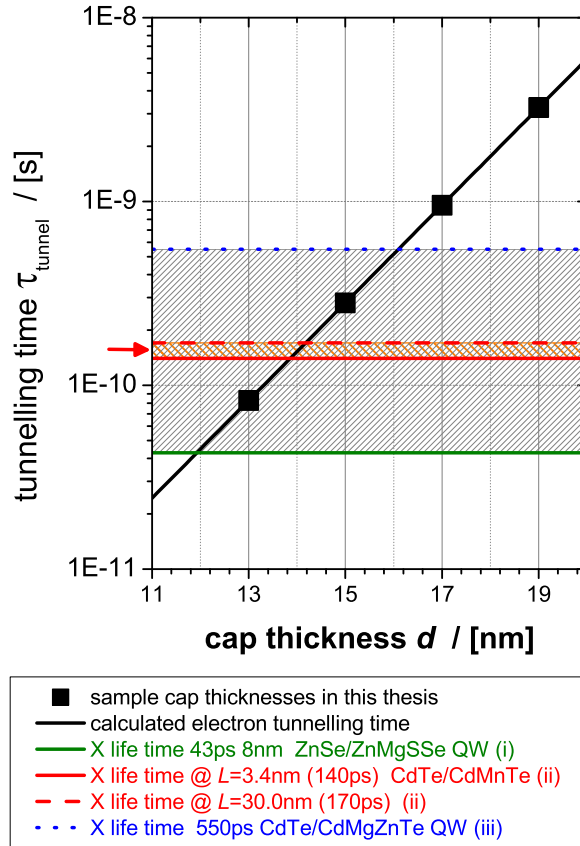


Figure 7.5: Tunnelling time of the photo-generated electron vs. cap layer thickness from Figure 7.3 in comparison to the exciton (X) life times for similar QW systems found in literature from (i) $43ps$ [YPM⁺00], (ii) $140 - 170ps$ at $3.4 - 30.0nm$ well width [PHG⁺92] up to (iii) $550ps$ [BKV⁺98].

19nm) due to the different tunnelling behaviour of electrons and holes as a function of cap layer thickness.

For cap thicknesses above 25nm the hole concentration of the QW is mainly caused by the influence of the near surface-induced doping while at cap thicknesses below 25nm (orange region in Figure 7.1(a)) the tunnelling behaviour of electrons and holes plays the major role.

In contrast to the observed PL-behaviour at cap layer thicknesses smaller than 25nm in this thesis, an increasing above-barrier illumination at cap thicknesses larger than 25nm causes a decreasing hole concentration [WDS⁺09] [Maś07] [KKW⁺09].

Finally, for this thesis the different tunnelling behaviour of electrons and holes enables the experimental access for influencing the hole concentration in the QW.

Chapter 8

Summary

In the context of the ongoing discussion about a carrier-induced ferromagnetic phase transition in diluted-magnetic II-VI semiconductors (DMS) through RKKY-interaction [HWA⁺97], theoretical studies on coherent dynamics of localized spins coupled with a two-dimensional hole gas (2DHG) in DMS quantum wells (QWs) were done by K.V. KAVOKIN [Kav99]. His key for studying the exchange interaction of the localized spin ensemble (e.g. Mn²⁺) with the 2DHG is the Larmor frequency of the localized Mn²⁺ spins and thus their Mn-g-factor. It was shown that the 2DHG affects a time evolution of the (Mn²⁺) spin system in an in-plane magnetic field resulting in the reduction of its Larmor frequency (Mn-g-factor) under the influence of an oscillating effective field of holes. This is called magnetic soft mode (behaviour) [KAK⁺09]. The experimental access for demonstrating this Mn-g-factor reduction with increasing hole concentration is the method of Multi-Paramagnetic Resonance (PR) Raman scattering (Multi-Spin-Flip Raman scattering) combined with the variation of the carrier concentration by photo-excitation with an additional light source (two-colour experiment).

The main motivation for this thesis was the experimental confirmation of the theoretically predicted magnetic soft mode and the analysis of its dependence on the hole concentration and external B-field, as well as its disappearance with increasing sample temperature. For that purpose, Cd_{1-x}Mn_xTe/Cd_{0.80}Mg_{0.20}Te QWs ($x = 0.006, 0.010$) positioned close to the sample surface (13 – 19nm) were investigated in an in-plane applied external magnetic field B_{ext} (up to 4.5T in Voigt-geometry) via a two-colour experiment i.e. using two light sources. This two-colour experiment allows the observation of the spin excitation of Mn-ions by simultaneously tuning the hole-concentration towards the ferromagnetic phase transition by photo-generated carriers. This means, one tuneable laser is responsible for resonant below-barrier excitation as a probe for Multi-PR Raman scattering. The other laser excites photo-generated carriers from above barrier (2.41eV) for tuning the hole concentration in the QW. Positioning the QW close to the sample surface causes a surface-induced p-doping of the QW [MKB⁺03] (intrinsic hole concentration in the QW) and enables the active tuning of the hole concentration by photo-generated carriers due to different tunnelling behaviour of electrons and holes from the QW to the surface.

The Mn-g-factor was determined from the slope of the 1PR-Raman signal position versus the external magnetic field B_{ext} (2.0 – 4.5T). The Mn-g-factor was decreased by quasi-continuously increasing the above-barrier illumination (and thus the hole concentration), while the below-barrier excitation (Multi-PR probe) was kept at a constant low power. This results in a Mn-g-factor reduction starting from its atomic value $g_{Mn} = 2.01$ to lowest evaluated Mn-g-factor in this thesis $g^* = 1.77 \pm 0.01$ (19nm cap sample: 031709B-IV). This is a magnetic softening of $\approx 12\%$.

In general, the concentration of the photo-generated 2DHG in the QW was determined via spectral distance of the exciton and trion position. The increase of the hole concentration up to a sample specific maximum value leads to a saturation in the Mn-g-factor downshift. This mirrors the critical point when the 2DHG spin susceptibility is independent on the hole concentration because at this point the FERMI energy equals the hole spin splitting in Voigt geometry caused by the exchange field B_{exch}^{Mn} of the Mn-ion mean spin.

Apart from the general magnetic soft mode behaviour at low temperatures, one of the main experimental results in this thesis is the confirmation of the theoretical prediction that the magnetic soft mode behaviour in the external B-field does not only depend on the carrier concentration but also on the B-field strength itself. This means the Mn-g-factor downshift is larger for lower B-fields, as it was confirmed by comparing the ranges around 4.0T and around 2.5T of the 13nm cap sample (031709B-I) with $g^* = 1.97 \pm 0.03$ and $g^* = 1.89 \pm 0.02$, respectively. This is a fingerprint of the transition towards the ferromagnetic phase for vanishing B-field. However, very low B-field values are intrinsically inaccessible for the Multi-PR Raman spectroscopy, because in this case the PR-signals would merge with the laser line.

An additional aspect is the temperature dependence of the magnetic soft mode. The Mn-g-factor decrease is suppressed with increasing temperature almost reaching the atomic Mn-g-factor at 4.2K ($g_{Mn} = 1.99$). This behaviour is due to the T-induced weakening of the transverse 2DHG spin susceptibility.

The results of the investigations concerning the cap layer thickness impact on the QW carrier characteristics were investigated in the cap thickness range of 13nm to 19nm. The cap thickness configures on the one hand the intrinsic hole concentration of the QW ("2DHG offset") due to the surface-induced p-doping and sets the "starting point" for the Mn-g-factor reduction. On the other hand the cap thickness determines the probability of electron tunnelling to the surface and thus the efficiency of the hole tuning by light. The latter is the criterion for the range of Mn-g-factor reduction by light. This two dependences were pointed out by the photo-generated hole influence on the QW PL-spectra which results in tuning the exciton-trion ratio. This tuning, from a virtually vanishing and weak trion signal at small illumination powers to a virtually vanishing exciton signal at high illumination powers can be observed for 13nm-capped and 15nm-capped sample, respectively. In contrast, the samples with 17nm and 19nm cap thickness show a dominant trion signal even at smallest possible illumination powers. The reason for these observations is on the one hand the increasing intrinsic hole concentration p - caused by surface doping - with increasing cap layer thickness up to 25nm from $p \approx 0$ to $p \approx 3.1 \times 10^{11} \text{cm}^{-2}$ for 13nm and 19nm cap thickness, respectively. On the other hand, using a model calculation for estimating the electron

and hole tunnelling time out of these QWs [CTZ⁺93], it could be shown that the electron tunnelling time is a few decades larger than the hole tunnelling time and that the tunnelling times of both carrier types increase with increasing cap thickness but with different slopes¹. As a result, the electron tunnelling time controls the hole tuning in the QW and becomes less efficient the more the cap layer is increased.

In summary both mechanisms are of relevance for the hole tuning and thus for the magnetic soft-mode behaviour. The mechanism of tunnelling time prevails at small cap layer thicknesses while the surface-induced p-doping plays the major role for larger cap thicknesses ($> 25nm$ [MKB⁺03]).

As a consequence, the Mn-g-factor reduction is as follows. The Mn-g-factor can be quasi-continuously decreased at the 13nm cap sample starting close to its atomic value of $g^* \approx 2.00$ to $g^* \approx 1.87$ in contrast to e.g. the 19nm cap sample where g^* already starts at $\approx 1.80^2$ due to larger intrinsic hole concentration and decreases down to ≈ 1.77 by increasing hole concentration.

In conclusion, the presented method in this thesis is a sensitive tool to study the dynamics of the spin excitations and the paramagnetic susceptibility in the vicinity of the hole-induced ferromagnetic phase transition.

¹larger slope for holes than for electrons

²even at lowest possible illumination power

Chapter 9

Zusammenfassung

Im Zusammenhang mit den aktuellen Diskussionen über einen ladungsträgerinduzierten ferromagnetischen Phasenübergang in verdünnt-magnetischen II-VI Halbleitern¹ durch RKKY-Wechselwirkung [HWA⁺97] wurden von K.V. KAVOKIN [Kav99] theoretische Untersuchungen zu kohärenter Dynamik von lokalisierten Spins durchgeführt, welche mit dem zweidimensionalen Lochgas² im DMS Quantentrog (QT) koppeln. Die Larmorfrequenz der lokalisierten Mn²⁺ Spins und der damit verbundene Mn-g-Faktor sind dabei der experimentelle Zugang, um die Wechselwirkung des lokalisierten Spinensembles (z.B. Mn²⁺) mit dem zweidimensionalen Lochgas zu untersuchen. Das 2DHG ruft eine zeitliche Entwicklung des (Mn²⁺) Spinsystems in einem in der Quantentrogenebene angelegten äußeren Magnetfeld hervor. Dies hat die Verringerung der Larmorfrequenz und damit des Mn-g-Faktors, beeinflusst durch ein oszillierendes effektives Austauschfeld der Löcher zur Folge. Dies wird magnetisches Softmode-Verhalten genannt [KAK⁺09]. Multi-PR-(Paramagnetische Resonanz) Raman-Spektroskopie (Multi-Spin-Flip-Raman-Spektroskopie) in Verbindung mit einer zusätzlichen Lichtquelle (genannt Zwei-Farben-Experiment) ist das probate Mittel, um diese Reduzierung des Mn-g-Faktors durch die photo-generierte Erhöhung der Lochkonzentration des 2DHG zu demonstrieren.

Die experimentelle Bestätigung des theoretisch vorhergesagten magnetischen Softmode-Verhaltens, sowie dessen Abhängigkeit von der Lochkonzentration und dem externen B-Feld, also auch dessen Verschwinden mit steigender Proben temperatur zu analysieren, war die Motivation dieser Arbeit. Aus diesem Grund wurden nahe (13-19nm) an der Probenoberfläche liegende Cd_{1-x}Mn_xTe/Cd_{0,80}Mg_{0,20}Te Quantentröge (x \cong 0,6%; 1,0%) in einem parallel zur Quantentrogenebene angelegten externen Magnetfeld B_{ext} (mit bis zu 4,5T) mittels Zwei-Farben-Experiment (d.h. mittels zweier Laser-Lichtquellen) untersucht. Dieses Zwei-Farben-Experiment ermöglicht die Untersuchung der Mn²⁺-Spin-Anregung bei gleichzeitiger Erhöhung der Lochkonzentration in Richtung zum ferromagnetischen Phasenübergang durch photogenerierte Ladungsträger. Dabei dient ein durchstimmbarer Laser zur resonanten Anregung im Quantentrog als Lichtquelle für die Multi-PR Raman Streuung. Der andere Laser hingegen erzeugt photogenerierte Ladungsträger oberhalb der Quantentrogbarriere (2,41eV), um die Lochkonzentration

¹engl.: Diluted Magnetic Semiconductor (DMS)

²engl.: two-dimensional hole gas 2DHG

im Quantentrog einzustellen.

Der Mn-g-Faktor wurde mittels der Steigung der 1PR-Raman-Signalposition, aufgetragen über dem externen Magnetfeld B_{ext} (2,0-4,5T) bestimmt. Die Reduzierung des Mn-g-Faktors erfolgte durch quasikontinuierliche Erhöhung der Beleuchtung oberhalb der Barriere und folglich auch der Lochkonzentration, während die resonante Anregungsleistung im Quantentrog (d.h. die Multi-PR-Sonde) niedrig und konstant gehalten wurde. Hiermit wurde tatsächlich die Verringerung des Mn-g-Faktors nachgewiesen, ausgehend von dessen atomaren Wert $g_{Mn} = 2,01$ hin zu dem, in dieser Arbeit kleinsten ermittelten Wert von $g^* = 1,77 \pm 0,01$ (19nm-Cap-Probe: 031709B-IV). Dies entspricht einem magnetischen "softening" von $\approx 12\%$.

Im Allgemeinen wurde die Konzentration des photo-generierten zweidimensionalen Lochgases im QT über den spektralen Abstand zwischen Exziton- und Trionposition bestimmt. Eine Erhöhung der Lochkonzentration über einen probenspezifischen Maximalwert hinaus hat eine Sättigung der Mn-g-Faktor-Reduzierung zur Folge. Dieses Verhalten spiegelt den kritischen Punkt wider, an dem die 2DHG-Spin-Suszeptibilität unabhängig von der Lochkonzentration wird. An diesem Punkt gleicht die FERMI-Energie der, durch das Mn^{2+} -Austauschfeld B_{exch}^{Mn} des gemittelten Spins der Mn-Ionen hervorgerufenen, energetischen Aufspaltung der Lochspinniveaus in Voigt-Geometrie.

Neben dem allgemeinen magnetischen Softmode-Verhalten bei niedriger Temperatur, war eines der wichtigsten experimentellen Ergebnisse dieser Arbeit die Bestätigung der theoretisch vorhergesagten Abhängigkeit des magnetischen Softmode-Verhaltens von der Magnetfeldstärke selbst und nicht nur von der Lochkonzentration im externen Magnetfeld. Die Mn-g-Faktor-Reduzierung wirkt sich bei kleinen B-Feldern stärker aus. Dies wurde durch den Vergleich der ermittelten Mn-g-Faktor-Reduzierung in der Umgebung von 4,0T sowie im Bereich um 2,5T an der 13nm Cap-Probe (031709B-I) mit $g^* = 1,97 \pm 0,03$ bzw. $g^* = 1,89 \pm 0,02$ bestätigt und ist ein charakteristischer Hinweis für den Übergang in Richtung ferromagnetische Phase bei verschwindendem B-Feld. Allerdings sind sehr kleine B-Feldstärken für Multi-PR-Raman-Spektroskopie an sich nicht zugänglich, da dann die PR-Signale mit der Laserlinie verschmelzen.

Ein weiterer experimenteller Aspekt ist die Temperaturabhängigkeit des magnetischen Softmode-Verhaltens. Mit steigender Temperatur wird die Mn-g-Faktor-Reduzierung unterdrückt und der g-Faktor erreicht bei 4,2K mit $g_{Mn} = 1,99$ fast seinen atomaren Wert. Grund dafür ist die temperaturinduzierte Abschwächung der transversalen 2DHG-Spin-Suszeptibilität.

Die Auswirkung der Cap-Schichtdicke auf das Verhalten der Ladungsträger-charakteristik im Quantentrog wurde für Cap-Dicken im Bereich von 13nm bis 19nm untersucht. Die Cap-Dicke legt einerseits, durch die oberflächeninduzierte p-Dotierung, die intrinsische Lochkonzentration des Quantentrogs fest ("2DHG offset") und damit den "Startpunkt" für die Mn-g-Faktor-Reduzierung. Andererseits bestimmt die Cap-Dicke die Tunnelwahrscheinlichkeit der Elektronen zur Oberfläche und damit wiederum die Effizienz der Lochkonzentrationsbeeinflussung durch das eingestrahlte Licht. Letzteres

ist das Kriterium dafür, wie groß der Einflussbereich ist, in dem eine Mn-g-Faktor-Reduzierung durch Licht stattfinden kann. Durch den Einfluss der photogenerierten Löcher auf das Quantentrog-PL-Spektrum und der damit verbundenen Beeinflussung des Exziton-Trion-Verhältnisses, konnten die beiden oben genannten Abhängigkeiten herausgearbeitet werden. In der 13nm- bzw. 19nm-Cap-Probe konnten somit die PL-Spektren von einem nahezu verschwindenden bzw. schwachen Trion-Signal bei kleiner Anregungsleistung bis zu einem geradezu verschwindenden Exziton-Signal bei hohen Anregungsleistungen durchgestimmt werden. Bei der 17nm- und 19nm-Cap-Probe hingegen, zeigte sich ein dominantes Trion-Signal über den gesamten Anregungsleistungsbereich, selbst bei den messplatzspezifischen niedrigsten Anregungsleistungen. Die Gründe dafür sind zum einen die ansteigende Lochkonzentration p - verursacht durch die oberflächen-induzierte Dotierung des QT - mit Steigerung der Cap-Schicht bis zu einer Dicke von 25nm, das heißt für die hier verwendeten Proben, von $p \approx 0$ bei 13nm bis $p \approx 3,1 \times 10^{11} \text{cm}^{-2}$ bei 19nm. Andererseits konnte, mittels einer Modellrechnung zur Abschätzung der Elektron- und Loch-Tunnelzeiten aus den untersuchten Quantentrögen heraus [CTZ⁺93], gezeigt werden, dass Elektron-Tunnelzeit um mehrere Dekaden größer ist als die Tunnelzeit der Löcher und dass zudem die Tunnelzeiten bei Ladungsträgersorten mit steigender Cap-Dicke zunehmen, allerdings mit unterschiedlicher Steigung³. Aus diesem Grund bestimmt die Elektron-Tunnelzeit die Einstellung der Lochkonzentration im QT. Ihre Wirksamkeit nimmt mit steigender Cap-Dicke ab.

Zusammenfassend sind beide Mechanismen für die Loch-Abstimmung im QT und damit für das magnetische soft-mode Verhalten von Bedeutung. Während der Mechanismus der Tunnelzeit bei schmalen Cap-Dicken überwiegt, spielt die oberflächeninduzierte p-Dotierung des Qms bei größeren Cap-Stärken ($> 25\text{nm}$ [MKB⁺03]) die Hauptrolle. Dies wirkt sich wie folgt auf die Mn-g-Faktor-Reduzierung aus. Bei der 13nm-Cap-Probe kann der Mn-g-Faktor startend bei seinem atomaren Wert von $g^* \approx 2.00$ bis hin zu $g^* \approx 1.87$ quasi-kontinuierlich reduziert werden. Im Gegensatz dazu startet g^* z.B. bei der 19nm-Cap-Probe bereits bei $\approx 1.80^4$ auf Grund der höheren intrinsischen Lochkonzentration und sinkt bis auf ≈ 1.77 mit steigender Lochkonzentration ab.

Fazit ist, dass die in dieser Arbeit präsentierte Methode ein sensibles Werkzeug darstellt, um die Dynamik der Spin-Anregungen und der paramagnetischen Suszeptibilität im Hinblick auf den Loch-induzierten ferromagnetischen Übergang zu untersuchen.

³ Steigung für Löcher größer als für Elektronen

⁴ selbst bei niedrigster Anregungsleistung

Chapter 10

Indices



Bibliography

- [AJBM01] M. Abolfath, T. Jungwirth, J. Brum, and A. H. MacDonald. Theory of magnetic anisotropy in $\text{III}_{1-x}\text{Mn}_x\text{V}$ ferromagnets. *Phys. Rev. B*, 63(5):054418, Jan 2001.
- [Bas88] G. Bastard. *Wave mechanics applied to semiconductor heterostructures*. Halsted Press from J. Wiley & Sons, Avenue du Hoggar, Zone Industrielle Courtaboeuf, B.P112, 91944 Les Ulis Cedex, France, 1988. les edition de physique.
- [BFC83] A.K. Bhattacharjee, G. J. Fishman, and B. Coqblin. Virtual bound-state model for the exchange interaction in semimagnetic semiconductors such as CdMnTe. *Physica B*, 117–118:449–451, 1983.
- [BKV⁺98] D. Brinkmann, J. Kudrna, E. Vanagas, P. Gilliot, R. Lévy, A. Arnoult, J. Cibert, and S. Tatarenko. Dynamical properties of trions and excitons in modulation doped CdTe/CdMgZnTe quantum wells. *Thin Solid Films*, 336(1-2):286 – 290, 1998.
- [Blo46] F. Bloch. Nuclear induction. *Phys. Rev.*, 70(7-8):460–474, Oct 1946.
- [Blu04] Stephen Blundell. *Magnetism in Condensed Matter*. Oxford University press, New York, 2004. Oxford Master Series in Condensed Matter Physics.
- [BRH⁺87] G. Barilero, C. Rigaux, Nguyen Hy Hau, J.C. Picoche, and W. Giriat. High Field Magnetization Step in $\text{Zn}_{1-x}\text{Mn}_x\text{Te}$. *Solid State Com.*, 62(5):345–350, 1987.
- [BSG81] N. Bottka, J. Stankiewicz, and W. Giriat. Electroreflectance studies in $\text{Cd}_{1-x}\text{Mn}_x\text{Te}$ solid solutions. *J.Appl.Phys.*, 52(6):4189–4193, 1981.
- [BSG⁺05] A. S. Bracker, E. A. Stinaff, D. Gammon, M. E. Ware, J. G. Tischler, D. Park, D. Gershoni, A. V. Filinov, M. Bonitz, F. Peeters, and C. Riva. Binding energies of positive and negative trions: From quantum wells to quantum dots. *Phys. Rev. B*, 72(3):035332, Jul 2005.
- [BWM⁺08] L. Bryja, A. Wójs, J. Misiewicz, P. Plochocka-Polack, and M. Potemski. Energy and recombination spectra of free and impurity-bound positive trions in high magnetic fields. *Physica E: Low-dimensional Systems and*

-
- Nanostructures*, 40(5):1386 – 1388, 2008. 17th International Conference on Electronic Properties of Two-Dimensional Systems.
- [CAB⁺97] S. A. Crooker, D. D. Awschalom, J. J. Baumberg, F. Flack, and N. Samarth. Optical spin resonance and transverse spin relaxation in magnetic semiconductor quantum wells. *Phys. Rev. B*, 56(12):7574–7588, Sep 1997.
- [CC76] J.R. Chelikowsky and M.L. Cohen. Nonlocal pseudopotential calculations for the electronic structure of eleven diamond and zinc-blende semiconductors. *Phys. Rev. B*, 14:556, 1976.
- [CCHH98] W. Y. Chou, G. S. Chang, W. C. Hwang, and J. S. Hwang. Analysis of fermi level pinning and surface state distribution in InAlAs heterostructures. *Journal of Applied Physics*, 83(7):3690–3695, 1998.
- [CTDL99] C. Cohen-Tannoudji, F. Diu, and F. Laloe. *Quantum Mechanics*. J. Wiley & Sons, NewYork, 1999. Vol.1.
- [CTZ⁺93] Ying-Lan Chang, I-Hsing Tan, Yong-Hang Zhang, D. Bimberg, James Merz, and Evelyn Hu. Reduced quantum efficiency of a near-surface quantum well. *Journal of Applied Physics*, 74(8):5144–5148, 1993.
- [Czy08] G. Czycholl. *Theoretische Festkörperphysik*. Springer, Berlin, Heidelberg, 2008. 3. Auflage.
- [Dav98] J.H. Davies. *The Physics of low-dimensional Semiconductors—An Introduction*. Cambridge University Press, The Edinburgh Building, Cambridge CB2 2RU, UK, 1998.
- [DDJ08] M.S. Dresselhaus, G. Dresselhaus, and A. Jorio. *Group Theory*. Springer, Berlin, Heidelberg, 2008. Application to the Physics of Condensed Matter.
- [DNR82] Le Si Dang, G. Neu, and R. Romestain. Optical detection of cyclotron resonance of electron and holes in CdTe. *Solid State Communications*, 44(8):1187 – 1190, 1982.
- [DS83] T. Dietl and J. Spalek. Effect of thermodynamic fluctuations of magnetization on the bound magnetic polaron in dilute magnetic semiconductors. *Phys. Rev. B*, 28(3):1548–1563, Aug 1983.
- [Dya08] M.I. Dyakonov, editor. *Spin Physics in Semiconductors*. Springer, Berlin, Heidelberg, 2008.
- [Dzy58] I. Dzyaloshinski. A thermodynamic theory of weak ferromagnetism of antiferromagnetics. *Phys. Chem. Solids*, 4:241, 1958.
- [EBW04] R.R. Ernst, G. Bodenhausen, and A. Wokaun. *Principles of Nuclear Magnetic Resonance in One and Two Dimensions*. Oxford University Press, Oxford, NewYork, 2004. International Series of Monographs on Chemistry 14.

-
- [FKM⁺94] T. Friedrich, J. Kraus, M. Meininger, G. Schaack, and W.O.G. Schmitt. Zeeman levels of the shallow lithium acceptor and band parameters in Cadmium Telluride. *Journal of Physics-Condensed Matter*, 6(23):4307–4316, 1994.
- [FSN96] W. Farah, D. Scalbert, and M. Nawrocki. Magnetic relaxation studied by transient reflectivity in Cd_{1-x}Mn_xTe. *Phys. Rev. B*, 53(16):R10461–R10464, Apr 1996.
- [Fur88] J.K. Furdyna. Diluted magnetic semiconductors. *J.Appl.Phys.*, 64(4):R29–R64, 1988.
- [GGG78] J.A. Gaj, R. Ginter, and R.R. Galazka. Exchange Interaction of Manganese 3d⁵ States with Band Electrons in Cd_{1-x}Mn_xTe. *phys. stat sol. (b)*., 89:655–662, 1978.
- [GPF79] J.A. Gaj, R. Planel, and G. Fishman. Relation of magneto-optical properties of free excitons to spin alignment of Mn²⁺ ions in Cd_{1-x}Mn_xTe. *Solid State Com.*, 29:435–438, 1979.
- [GPK⁺04] J.A. Gaj, P. Plochocka, P. Kossacki, W. Maslana, J. Cibert, and S. Tatarenko. Neutral and charged excitons in CdTe-based quantum wells. *Low Temperature Physics*, 30(11):848–852, 2004.
- [GPR⁺04] J. A. Gaj, P. Plochocka, C. Radzewicz, P. Kossacki, W. Maslana, J. Cibert, and S. Tatarenko. Neutral and charged excitons in a CdTe-based quantum well. *Low Temperature Physics*, 30(11):848–852, 2004.
- [Haw91] Pawel Hawrylak. Optical properties of a two-dimensional electron gas: Evolution of spectra from excitons to Fermi-edge singularities. *Phys. Rev. B*, 44(8):3821–3828, Aug 1991.
- [HCS⁺00] V. Huard, R. T. Cox, K. Saminadayar, A. Arnoult, and S. Tatarenko. Bound States in Optical Absorption of Semiconductor Quantum Wells Containing a Two-Dimensional Electron Gas. *Phys. Rev. Lett.*, 84(1):187–190, Jan 2000.
- [He91] Xing-Fei He. Excitons in anisotropic solids: The model of fractional-dimensional space. *Phys. Rev. B*, 43(3):2063–2069, Jan 1991.
- [HH85] A. Hammer and K. Hammer. *Sammlung physikalischer Formeln und Konstanten*. Lindauer Verlag, München, 1985.
- [HL78] W. Hayes and R. Loudon. *Scattering of light by crystals*. John Wiley and Sons, NewYork, 1978. B:II-VI and I-VI-Compounds; Semimagnetic Compounds.
- [HWA⁺97] A. Haury, A. Wasiela, A. Arnoult, J. Cibert, S. Tatarenko, T. Dietl, and Y. Merle d’Aubigné. Observation of a Ferromagnetic Transition Induced by Two-Dimensional Hole Gas in Modulation-Doped CdMnTe Quantum Wells. *Phys. Rev. Lett.*, 79(3):511–514, Jul 1997.

-
- [Kac91] T.Z. Kachlishvili. On some magnetic field induced effects in 2-D $\text{Cd}_{1-x}\text{Mn}_x\text{Te}$. *Solid State Com.*, 80(4):369–371, 1991.
- [KAK⁺09] C. Kehl, G. V. Astakhov, K. V. Kavokin, Yu. G. Kusrayev, W. Ossau, G. Karczewski, T. Wojtowicz, and J. Geurts. Observation of the magnetic soft mode in (Cd,Mn)Te quantum wells using spin-flip Raman scattering. *Phys. Rev. B*, 80(24):241203, Dec 2009.
- [Kav99] K.V. Kavokin. Coherent dynamics of localized spins coupled with a two-dimensional hole gas in diluted-magnetic quantum wells. *Phys. Rev. B*, 59(15):9822–9825, 1999.
- [KBB⁺04] P. Kossacki, H. Boukari, M. Bertolini, D. Ferrand, J. Cibert, S. Tatarenko, J. A. Gaj, B. Deveaud, V. Ciulin, and M. Potemski. Photoluminescence of p -doped quantum wells with strong spin splitting. *Phys. Rev. B*, 70(19):195337, Nov 2004.
- [KCdA⁺93] K. Kheng, R. T. Cox, Merle Y. d’ Aubigné, Franck Bassani, K. Saminadayar, and S. Tatarenko. Observation of negatively charged excitons $x-$ in semiconductor quantum wells. *Phys. Rev. Lett.*, 71(11):1752–1755, Sep 1993.
- [KCF⁺99] P. Kossacki, J. Cibert, D. Ferrand, Y. Merle d’Aubigné, A. Arnoult, A. Wasiela, S. Tatarenko, and J. A. Gaj. Neutral and positively charged excitons: A magneto-optical study of a p -doped $\text{Cd}_{1-x}\text{Mn}_x\text{Te}$ quantum well. *Phys. Rev. B*, 60(23):16018–16026, Dec 1999.
- [Kel04] D. Keller. *Optische Eigenschaften ZnSe-basierter zweidimensionaler Elektronengase und ihre Wechselwirkung mit magnetischen Ionen*. PhD thesis, Universität Würzburg, Institut für experimentelle Physik, 2004. Dissertation.
- [KG02] H. Krenn and P. Granitzer. Magnetische Halbleiter: Spintronik. *Physik in unserer Zeit*, 33(5):218–225, 2002.
- [KK09] K.V. Kavokin and Yu. G. Kusrayev. private communication, 2009.
- [KKW⁺09] A. V. Koudinov, Yu. G. Kusrayev, D. Wolverson, L. C. Smith, J. J. Davies, G. Karczewski, and T. Wojtowicz. Giant modulation of resonance Raman scattering from (Cd,Mn)Te quantum wells by secondary illumination. *Phys. Rev. B*, 79(24):241310, Jun 2009.
- [Kli07] C. Klingshirn. *Semiconductor Optics*. Springer, Berlin Heidelberg NewYork, 2007.
- [KM97] K. V. Kavokin and I. A. Merkulov. Multispin raman paramagnetic resonance: Quantum dynamics of classically large angular momenta. *Phys. Rev. B*, 55(12):R7371–R7374, Mar 1997.

-
- [KMY98] K.V. Kavokin, I.A. Merkulov, and D.R. Yakovlev. Magnetic polarons in semimagnetic-semiconductor-based heterostructures. *Physics of the Solid State*, 40(5):734–736, 1998.
- [Kos03] P Kossacki. Optical studies of charged excitons in II-VI semiconductor quantum wells. *Journal of Physics: Condensed Matter*, 15(13):R471–R493, 2003.
- [Kra07] G. Kraczewski. oral information, 2007.
- [Lam58] Murray A. Lampert. Mobile and Immobile Effective-Mass-Particle Complexes in Nonmetallic Solids. *Phys. Rev. Lett.*, 1(12):450–453, Dec 1958.
- [LE89] B.E. Larson and H. Ehrenreich. Anisotropic superexchange and spin-resonance linewidth in diluted magnetic semiconductors. *Phys. Rev. B*, 39:1747, 1989.
- [LHE88] B.E. Larson, K.C. Hass, and H. Ehrenreich. Theory of exchange interactions and chemical trends in diluted magnetic semiconductors. *Phys. Rev. B*, 37:4137, 1988.
- [LHEC85] B.E. Larson, K.C. Hass, H. Ehrenreich, and A.E. Carlsson. Exchange mechanisms in diluted magnetic semiconductors. *Solid State Communications*, 56(4):347 – 350, 1985.
- [LHHS97] Fei Long, W. E. Hagston, P. Harrison, and T. Stirner. The structural dependence of the effective mass and Luttinger parameters in semiconductor quantum wells. *Journal of Applied Physics*, 82(7):3414–3421, 1997.
- [Liu61] S.H. Liu. Exchange interaction between conduction electrons and magnetic shell electrons in rare-earth metals. *Phys. Rev.*, 121:451, 1961.
- [LK55] J.M. Luttinger and W. Kohn. Motion of Electrons and Holes in Perturbed Periodic Fields. *Phys. Rev.*, 97(4):869–883, 1955.
- [LR84] Y.R. Lee and A.K. Ramdas. A piezomodulation study of the absorption edge and Mn^{++} internal transition in $CdMnTe$, a prototype of diluted magnetic semiconductors. *Solid State Communications*, 51(11):861–863, 1984.
- [Lut56] J. M. Luttinger. Quantum Theory of Cyclotron Resonance in Semiconductors: General Theory. *Phys. Rev.*, 102(4):1030–1041, 1956.
- [Maś07] W. Maśłana. *Carrier induced ferromagnetism in (Cd,Mn)Te quantum wells: a spectroscopic study*. PhD thesis, Institute of Experimental Physics, Faculty of Physics, University of Warsaw, 2007. PhD thesis, <http://en.ifd.fuw.edu.pl>.
- [MDP⁺09] X. Mathew, J. Drayton, V. Parikh, N.R. Mathews, Liu Xiangxin, and A. D. Compaan. Development of a semitransparent $CdMgTe/CdS$ top cell for applications in tandem solar cells. *Semicond. Sci. Technol.*, 24(1):015012, Aug 2009.

-
- [MDSW97] R. Meyer, M. Dahl, G. Schaack, and A. Waag. Spin-flip Raman scattering from donor-bound electrons in $\text{Cd}_{1-x}\text{Mn}_x\text{Te}/\text{Cd}_{1-y}\text{Mg}_y\text{Te}$ single quantum wells. *Phys. Rev. B*, 55(24):16376, Feb 1997.
- [MK95] I. A. Merkulov and K. V. Kavokin. Two-dimensional magnetic polarons: Anisotropic spin structure of the ground state and magneto-optical properties. *Phys. Rev. B*, 52(3):1751–1758, Jul 1995.
- [MKB⁺03] W. Maslana, P. Kossacki, M. Bertolini, H. Boukari, D. Ferrand, S. Tatarenko, J. Cibert, and J. A. Gaj. p-type doping of II–VI heterostructures from surface states: Application to ferromagnetic $\text{Cd}_{1-x}\text{Mn}_x\text{Te}$ quantum wells. *Applied Physics Letters*, 82(12):1875–1877, 2003.
- [MLC92] H. Mathieu, P. Lefebvre, and Ph. Christol. Simple analytical method for calculating exciton binding energies in semiconductor quantum wells. *Phys. Rev. B*, 46(7):4092–4101, Aug 1992.
- [Mön01] W. Mönch. *Semiconductor Surfaces and Interfaces*. Springer, Berlin, Heidelberg, NewYork, 3. edition, 2001.
- [Mor60] T. Moriya. Anisotropic superexchange interaction and weak ferromagnetism. *Phys. Rev.*, 120:91, 1960.
- [MOY⁺94] G. Mackh, W. Ossau, D. R. Yakovlev, A. Waag, G. Landwehr, R. Hellmann, and E. O. Göbel. Localized exciton magnetic polarons in $\text{Cd}_{1-x}\text{Mn}_x\text{Te}$. *Phys. Rev. B*, 49(15):10248–10258, Apr 1994.
- [MOY⁺95] G. Mackh, W. Ossau, D.R. Yakovlev, R. Hellmann, E.O. Göbel, A. Waag, and G. Landwehr. Exciton Magnetic Polarons in Semimagnetic Quantum Wells with Nonmagnetic Barriers. *Materials Science Forum*, 182–184:775–778, 1995. II-VI Compounds and Semimagnetic Semiconductors.
- [NNL88] Ch. Neumann, A. Nöthe, and N. O. Lipari. Two-photon magnetoabsorption of ZnTe, CdTe, and GaAs. *Phys. Rev. B*, 37(2):922–932, 1988.
- [OLS⁺03] K. Oura, V.G. Lifshits, A.A. Saranin, A.V. Zotof, and M. Katayama. *Surface Science*. Springer, Berlin, Heidelberg, NewYork, 1. edition, 2003. An Introduction.
- [ope08] opensource. jmol. website, 2008. <http://jmol.sourceforge.net/>.
- [PHG⁺92] A. Polhmann, R. Hellmann, E. O. Gobel, D. R. Yakovlev, W. Ossau, A. Waag, R. N. Bicknell-Tassius, and G. Landwehr. Exciton lifetimes in CdTe/CdMnTe single quantum wells. *Applied Physics Letters*, 61(24):2929–2931, 1992.
- [PPV⁺83] A. Petrou, D. L. Peterson, S. Venugopalan, R. R. Galazka, A. K. Ramdas, and S. Rodriguez. Raman scattering study of the magnetic excitations in diluted magnetic semiconductors in the presence of an external magnetic field. *Phys. Rev. B*, 27(6):3471–3482, Mar 1983.

-
- [PWMd⁺93] P. Peyla, A. Wasiela, Y. Merle d'Aubigné, D. E. Ashenford, and B. Lunn. Anisotropy of the Zeeman effect in CdTe/Cd_{1-x}Mn_xTe multiple quantum wells. *Phys. Rev. B*, 47(7):3783–3789, Feb 1993.
- [RK54] M. A. Ruderman and C. Kittel. Indirect Exchange Coupling of Nuclear Magnetic Moments by Conduction Electrons. *Phys. Rev.*, 96(1):99, Oct 1954.
- [RMW88] L. R. Ram-Mohan and Peter A. Wolff. Energetics of acceptor-bound magnetic polarons in diluted magnetic semiconductors. *Phys. Rev. B*, 38(2):1330–1339, Jul 1988.
- [RNPZ74] J.M. Row, R.M. Nicklow, D.L. Price, and K. Zanio. Lattice dynamics of cadmium telluride. *PRB*, 10(2):671–675, 1974.
- [RPV00] C. Riva, F. M. Peeters, and K. Varga. Excitons and charged excitons in semiconductor quantum wells. *Phys. Rev. B*, 61(20):13873–13881, May 2000.
- [RS83] S. M. Ryabchenko and Y. G. Semenov. Spin-correlation effects for a large-radius electron center in a magnetically mixed semiconductor. *Sov. Phys, JETP*, 57(4):825–832, Mar 1983.
- [RVV06] P.G. Riewald and L.H. Van Vlack. Deformation and fracture of MnTe and MnSe-MnTe solid solutions. *Journal of the American Ceramic Society*, 53(4):219–223, 2006.
- [SA89] B. Stébé and A. Ainane. Ground state energy and optical absorption of excitonic trions in two dimensional semiconductors. *Superlattices and Microstructures*, 5(4):545 – 548, 1989.
- [SHSW94] J. Stühler, M. Hirsch, G. Schaack, and A. Waag. Raman spectroscopy of the paramagnetic spin flip in Cd_{1-x}Mn_xTe, the role of band-gap excitons as intermediate states, and optically detected electron-nuclear double resonance. *Phys. Rev. B*, 49(11):7345–7356, Mar 1994.
- [SK90] M. Said and M. A. Kanehisa. Excited Acceptor States in II–VI and III–V Semiconductors. *phys. stat. sol. (b)*, 157(1):311–321, 1990.
- [Sli96] C.P. Slichter. *Principles of Magnetic Resonance*. Springer, Berlin, Heidelberg, NewYork, 3. edition, 1996. Third Enlarged and Upgraded Edition.
- [SLT⁺86] J. Spal/ek, A. Lewicki, Z. Tarnawski, J. K. Furdyna, R. R. Galazka, and Z. Obuszko. Magnetic susceptibility of semimagnetic semiconductors: The high-temperature regime and the role of superexchange. *Phys. Rev. B*, 33(5):3407–3418, Mar 1986.
- [SOS⁺95] A.J. Shields, J.L. Osborne, M.Y. Simmons, M. Pepper, and D.A. Ritchie. Magneto-optical spectroscopy of positively charged excitons in GaAs quantum wells. *Phys. Rev. B*, 52(8):R5523–R5526, Aug 1995.

-
- [SPRM95] A.J. Shields, M. Pepper, D.A. Ritchie, and Simmons M.Y. Influence of excess electrons and magnetic fields on Mott-Wannier excitons in GaAs quantum wells. *Advances in Physics*, 44(1):47–72, Aug 1995.
- [SSA⁺05] R. A. Sergeev, R. A. Suris, G.V. Astakhov, Ossau W., and D. R. Yakovlev. Universal estimation of X⁻ trion binding energy in semiconductor quantum wells. *The European Physical Journal B - Condensed Matter and Complex Systems*, 47(4):541–547, Oct 2005.
- [SSD⁺95] J. Stühler, G. Schaack, M. Dahl, A. Waag, G. Landwehr, K. V. Kavokin, and I. A. Merkulov. Multiple Mn²⁺-spin-flip Raman Scattering at High Fields via Magnetic Polaron States in Semimagnetic Quantum Wells. *Phys. Rev. Lett.*, 74(13):2567–2570, Mar 1995.
- [SSD⁺96] J. Stühler, G. Schaack, M. Dahl, G. Landwehr, K. V. Kavokin, I. A. Merkulov, and A. Waag. Polarization properties of multiple Mn²⁺-Spin-Flip Raman Scattering in semimagnetic quantum wells. *Journal of Crystal Growth*, 159(1):1001–1004, Mar 1996.
- [SSE⁺96] T. Story, C. H. W. Swüste, P. J. T. Eggenkamp, H. J. M. Swagten, and W. J. M. de Jonge. Electron paramagnetic resonance knight shift in semimagnetic (diluted magnetic) semiconductors. *Phys. Rev. Lett.*, 77(13):2802–2805, Sep 1996.
- [Stü95] J. Stühler. *Resonante Ramanstreuung an Anregungen der Mn²⁺-Ionen in Cd_{1-x}Mn_xTe und Cd_{1-x}Mn_xTe/Cd_{1-y}Mg_yTe Quantentrogstrukturen*. PhD thesis, Universität Würzburg, Institut für experimentelle Physik, 1995. Dissertation.
- [TBF⁺94] D. Tönnies, G. Bacher, A. Forchel, A. Andreas Waag, T. Litz, and G. Landwehr. Optical Study of Intermixing in CdTe/CdMgTe Quantum Wells. *Japanese Journal of Applied Physics*, 33(Part 2, No. 2B):L247–L249, 1994.
- [WDS⁺09] D. Wolverson, J.J. Davies, L.C. Smith, A.V. Koudinov, Yu. G. Kusrayev, M. Wiater, G. Kraczewski, and T. Wojtowicz. Competition between above- and below-barrier excitation in QW photo-modulation. In *14th International Conference on II-VI Compounds St. Petersburg/ Russia*, 2009. Conference presentation.
- [WHS⁺93] A. Waag, H. Heinke, S. Scholl, C.R. Becker, and G. Landwehr. Growth of MgTe and Cd_{1-x}Mg_xTe thin films by molecular beam epitaxy. *Journal of Crystal Growth*, 131(3-4):607 – 611, 1993.
- [Wol88] P.A. Wolff. *Semiconductors and Semimetals*, volume 25. Academic Press, INC., Boston, San Diego, New York, London, Tokyo, 1988. Theory of Bound Magnetic Polarons in Semimagnetic Semiconductors.
- [YC01] P.Y. Yu and M. Cardona. *Fundamentals of Semiconductors*. Springer Berlin Heidelberg New York, 3. edition, 2001. Physics and Materials Properties.

-
- [Yos57] Kei Yosida. Magnetic Properties of Cu-Mn Alloys. *Phys. Rev.*, 106(5):893–898, Jun 1957.
- [YPM⁺00] D.R. Yakovlev, J. Puls, G.V. Mikhailov, G.V. Astakhov, V.P. Kochereshko, W. Ossau, J. Nürnberger, W. Faschinger, F. Henneberger, and G. Landwehr. Charged Exciton Dynamics in ZnSe/ZnMgSSe QWs. *phys. stat. sol. (a)*, 178(1):501–505, 2000.
- [ZE96] P.S. Zory and Editors. *Quantum Well Lasers*. Academic press inc, 24-28 Oval Road, London NW1 7DX, UK, 1996. Quantum Electronics - Principles and Applications.
- [Zeh98] U. Zehnder. *Magnetooptische Untersuchungen an neuartigen und semi-magnetischen II-VI-Halbleiter-Heterostrukturen*. PhD thesis, Universität Würzburg, Institut für experimentelle Physik, 1998. Dissertation.
- [ZLR10] A. Zunger, S. Lany, and H. Raebiger. The quest for dilute ferromagnetism in semiconductors: Guides and misguides by theory. *Physics*, 3:53, Jun 2010.



List of Figures

1.1	Introducing chart	2
2.1	Zinc blende CdTe crystal	5
2.2	Electronic structure of CdTe	6
2.3	Mn energy states	10
2.4	BRILLOUIN function: Discussion	17
2.5	Schematic Γ_6 - and Γ_8 -splitting in B-field	18
2.6	Energy vs. lattice constant	19
2.7	QW scheme	20
2.8	Schematic overview: bulk to QW	22
2.9	Theoretical calculations: 2D exciton binding energy	24
2.10	QW VB-splitting dependent on B-field directions	25
2.11	Calculated B-field dependence of VB states in Voigt geometry	30
2.12	Feynman diagram of Raman scattering	35
2.13	bulk PR scheme	38
2.14	Selection rules for PR-Raman scattering	38
2.15	2PR Raman scattering	39
2.16	Scheme of magnetic polaron	40
2.17	Scheme of Multi-PR-Raman scattering	42
2.18	B-field directions according to K.V. Kavokin's paper	45
2.19	Mn-ion precession	47
3.1	Two-colour Raman setup	52
3.2	QW	53

3.3	QW sample scheme	54
4.1	Below-barrier excitation (constant Dye-Laser power)	56
4.2	X and T states in B-field	58
4.3	Scheme of the positive Trion	60
4.4	Multi-SF resonance spectra	61
4.5	Below-barrier excitation (varying Dye-Laser power)	62
4.6	Gauss Fitting procedure	63
4.7	Exciton and trion position	64
4.8	X-T-ratio and FWHM of the trion (Dye)	65
4.9	Above-barrier excitation	66
4.10	Comparing X-T-ratio and energetic distance (Dye-, Ar-Laser)	67
4.11	Two-colour excitation	68
4.12	Linear behaviour of Multi-PR signals in B-field	70
4.13	Influence of above-barrier excitation power on PL- and Multi-SF-signals	73
4.14	Influence of the hole concentration on the PR-signal and Mn-g-factor .	74
4.15	Mn-g-factor vs. hole concentration 030807A-I	75
4.16	Temperature-influence on Mn-g-factor reduction	76
5.1	Mn-g-factor reduction: Comparing experiment and theory	78
5.2	Overview of the Mn-ion precession model	81
6.1	PL below-barrier excitation 031709B-I	84
6.2	PL two-colour excitation 031709B-I	85
6.3	PL- and Multi-PR signals under above-barrier excitation 031907B-I . .	87
6.4	Mn-g-factor vs. hole concentration 031907B-I	88
6.5	PL below-barrier excitation 031709B-II	89
6.6	PL two-colour excitation 031709B-II	91
6.7	PL- and Multi-PR signals under above-barrier excitation 031907B-II . .	92
6.8	Mn-g-factor vs. hole concentration 031907B-II	93
6.9	PL below-barrier excitation 031709B-III	94
6.10	PL two-colour excitation 031709B-III	95

6.11	PL- and Multi-PR signals under above-barrier excitation 031907B-III	96
6.12	PL below-barrier excitation 031709B-IV	97
6.13	PL two-colour excitation 031709B-IV	98
6.14	PL- and PR-Raman signals under above-barrier excitation 031907B-IV	99
6.15	PL-behaviour 031709BI-IV -summary-	100
6.16	Spectral positions 031709BI-IV -summary-	101
7.1	2DHG-concentration vs. cap thickness (Maślana)	107
7.2	Downward bended cap band	109
7.3	Calculated HH tunnelling times	111
7.4	Interpretation of cap layer impact	112
7.5	Tunnelling time and exciton life time	114
A.1	Temperature dependence of the band splitting	144
A.2	Dependence of the band splitting on the total angular momentum S	145
A.3	2D magnetic polaron in B-field	147
A.4	Exciton spin splitting	152



List of Tables

2.1	Basis Bloch functions of Γ_6^- , Γ_8^- and Γ_7^- -band	14
2.2	Energy gap and lattice constant of CdMnTe- and CdMgTe-bulk material	19
2.3	CdMnTe free-exciton energies	23
3.1	Sample list	53
3.2	Sample properties	54
4.1	Spin system: Exciton and trion	61
6.1	Summary of samples 031709BI-IV	103
6.2	Mn-g-factors of samples 031709BI-IV	103
A.1	Optical transitions	152

Appendix A

Physical and mathematic add-ons

A.1 $k \cdot p$ theory

Starting with the one electron SCHRÖDINGER equation (SE) which describes identical motion of each electron [YC01]:

$$H \Phi_n(\vec{r}) = \left(\frac{p^2}{2m} + V(\vec{r}) \right) \Phi_n(\vec{r}) = E_n \Phi_n(\vec{r}) \quad (\text{A.1})$$

The $k \cdot p$ method can be derived from (A.1). By using the BLOCH theorem¹, the solution of (A.1) in the reduced zone scheme is:

$$\Phi_{n\vec{k}} = e^{i\vec{k}\vec{r}} u_{n\vec{k}}(\vec{r}) \quad (\text{A.2})$$

\vec{k} is within the first Brillouin zone, n is the band index and $u_{n\vec{k}}(\vec{r})$ has the periodicity of the lattice.

Converting the operator \vec{p} from momentum space to position space² (A.1) changes to:

$$\left(\frac{\hbar^2 \nabla^2}{2m} + V(\vec{r}) \right) \Phi_n(\vec{r}) = E_n \Phi_n(\vec{r}) \quad (\text{A.3})$$

Pasting (A.2) in (A.3) and using:

$$\nabla_{\vec{r}} \Phi_n(\vec{r}) = i\vec{k} e^{i\vec{k}\vec{r}} \cdot u_{n\vec{k}}(\vec{r}) + e^{i\vec{k}\vec{r}} \cdot \nabla_{\vec{r}} u_{n\vec{k}}(\vec{r}) \quad (\text{A.4})$$

$$\nabla_{\vec{r}}(\nabla_{\vec{r}} \Phi_n(\vec{r})) = \left[\nabla_{\vec{r}}^2 + 2i\vec{k} \nabla_{\vec{r}} - \vec{k}^2 \right] u_{n\vec{k}}(\vec{r}) e^{i\vec{k}\vec{r}} \quad (\text{A.5})$$

and $-i\hbar \nabla \rightarrow \vec{p}$

The result is:

$$\left(\frac{p^2}{2m} + V(\vec{r}) \right) + \left(\frac{\hbar \vec{k} \cdot \vec{p}}{m} + \frac{\hbar^2 \vec{k}^2}{2m} \right) u_{n\vec{k}}(\vec{r}) = E_{n\vec{k}} u_{n\vec{k}}(\vec{r}) \quad (\text{A.6})$$

¹Def: $V(x)$ is a periodic potential and its periodicity x_0 ($V(x+x_0) = V(x)$). Thus the stationary solution of the SE is forced to have the form $\psi(x) = e^{ikx} \cdot u_k(x)$ where $u_k(x)$ is a periodic function periodic in x_0 ($u_k(x+x_0) = u_k(x)$).

² $\vec{p} \rightarrow -i\hbar \nabla$ and $\vec{p}^2 \rightarrow \hbar^2 \nabla^2$

At $\vec{k} = (0, 0, 0)$ the equation (A.6) is much easier due to periodic functions of $u_{n\vec{0}}$ and its solutions form a complete and orthogonal set of basis functions. Now, both $E_{n\vec{0}}$ and $u_{n\vec{0}}$ can be determined. As a consequence the second summand in brackets in (A.6) can be treated as perturbations using either degenerate or non-degenerate perturbation theory [YC01].

A particular band n , which should not be degenerate with any other band at $\vec{k} = \vec{0}$ is given by second order perturbation theory:

$$E_{n\vec{k}} \approx E_{n\vec{0}} + \frac{\hbar^2 k^2}{2m} + \frac{\hbar^2}{m^2} \sum_{q, q \neq n} \frac{|\langle q\vec{0} | \vec{k} \cdot \vec{p} | n\vec{0} \rangle|^2}{E_{n\vec{0}} - E_{q\vec{0}}} \quad (\text{A.7})$$

The diagonal elements $\langle n\vec{0} | \vec{k}\vec{p} | n\vec{0} \rangle$ of (A.7) vanish.

Its application is the calculation of electronic band dispersion and is known as the **k·p-theory**. This method works best for small values of k when the perturbations terms are proportional to k .

For more details: [YC01] or [Dav98]

A.2 BRILLOUIN function and band splitting

The simulations of the CB and VB band bending under the aspect of two different parameters S (total angular momentum) and T (Temperature) are calculated using the following equations for the band bending

$$\Delta E_{\Gamma_6} = xN_0\alpha \langle S_z \rangle m_s \quad \text{with} \quad m_s = \pm \frac{1}{2} \quad (\text{A.8})$$

$$\Delta E_{\Gamma_8} = \frac{1}{3}xN_0\beta \langle S_z \rangle m_j \quad \text{with} \quad m_j = \pm \frac{1}{2}, \pm \frac{3}{2} \quad (\text{A.9})$$

with the expectation value

$$\langle S_z \rangle = -S \cdot \mathfrak{B}_S \left(\frac{g_{Mn}\mu_B SB}{k_B T} \right) \quad (\text{A.10})$$

where \mathfrak{B}_S is the BRILLOUIN function. Discussing the BRILLOUIN function the following aspects can be pointed out:

- high B-field or small temperature ($y \gg 1$): $\mathfrak{B}_S(y) = \frac{2S+1}{2S} \coth\left(\frac{2S+1}{2S} \cdot y\right) - \frac{1}{2S} \coth\left(\frac{1}{2S} \cdot y\right)$
- low B-field or high temperature ($y \ll 1$): $\mathfrak{B}_S \approx \frac{S+1}{3S} \cdot y$ [Dya08]

The latter case shows a linear dependence at low B-fields or high temperature.

$$N_0\alpha = 0.22eV \quad \text{and} \quad N_0\beta = -0.88eV \quad (\text{A.11})$$

are the exchange constants of the CdMnTe conduction band and valence band, respectively. All plots are simulated in "MATHEMATICA 7.0" .

Temperature The results of the temperature dependent calculations are plotted in Figure A.1(a) for the CB and the VB presented in different energy scales. For more details, the HH and LH splitting are plotted separately in Figure A.1(b) and (c) as full and dashed lines, respectively. In general the black thick lines (and black dashed lines for LHs)) represent the case of Cd_{0.99}Mn_{0.01}Te bulk material with $S=5/2$ at 1.7K.

Total angular momentum S At a constant temperature of 1.7K and varying the parameter S from 1/2 to 7/2 in 1/2-steps the band splitting of a virtual Cd_{0.99}A(S)_{0.01}Te bulk material is plotted in Figure A.2(a). Only A($S=5/2$) \equiv Mn²⁺ (black thick/dashed line) represents the case of Cd_{0.99}Mn_{0.01}Te bulk material. Figure A.2(b) shows in more detail the VB splitting of the HH and LH band under varying total angular momentum S .

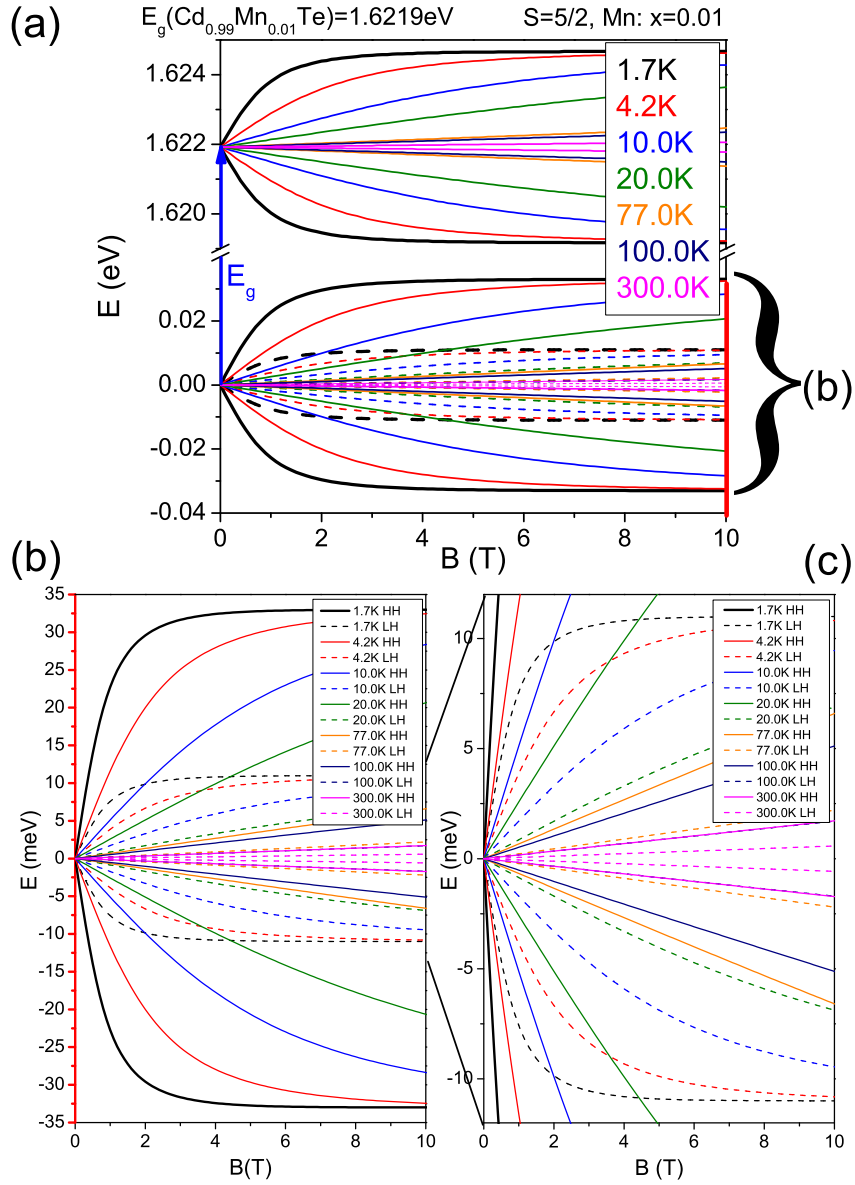


Figure A.1: Temperature dependence of the band splitting. (a) Overview of the CB splitting (1.6219eV at 0T) and the VB splitting (0.0eV at 0T). (b) and (c) Detailed presentation of the HH and LH state splitting.

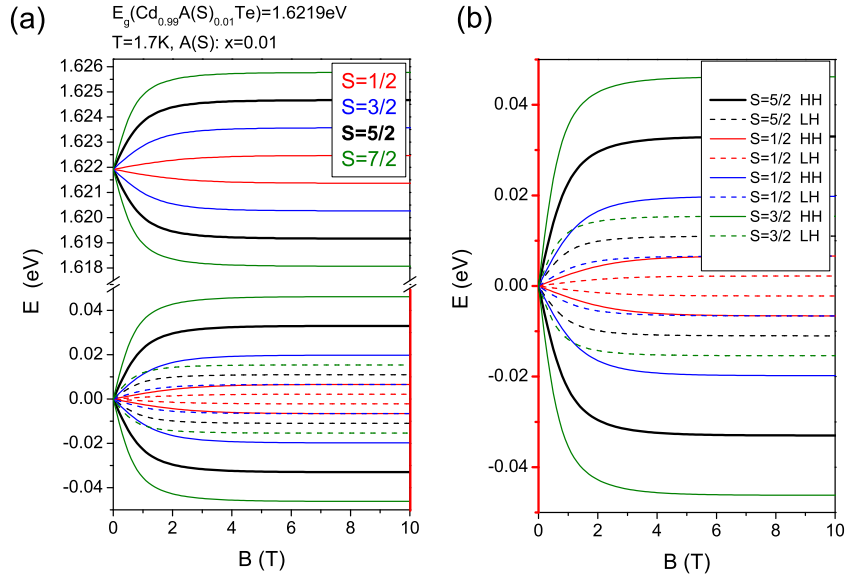


Figure A.2: Dependence of the band splitting on the total angular momentum S .

A.3 Magnetic polaron in 2D in its exchange field

A magnetic polaron (MP) is a system of aligned Mn-spins within the expansion of a charge carrier wave function in general (discussed in [Kli07], [DS83], [RMW88], [MK95], [Wol88]). This alignment of the Mn-spins due to an exchange field (a few Tesla) is on the one hand caused by the strong exchange interaction among the spins of the charge carriers in the VB and CB and on the other hand caused by the spins of the Mn-ions. The stronger case is the charge carrier interaction (here: hole) due to a larger exchange constant. In summary the formation of a magnetic polaron is the alignment of Mn-ions in the presence of a charge carrier or exciton caused by the strong s/p-d exchange interaction.

It can be distinguished between three types of magnetic polarons:

- **bound magnetic polarons (BMP)**: charge carrier or exciton is bound to a defect (acceptor or donator) via Coulomb interaction. Thus dynamics of polaron formation can be neglected.
- **localized magnetic polaron (LMP)**: polaron formation due to non-magnetic potential located exciton caused by well width fluctuations or alloy disorder
- **free magnetic polarons (FMP)**: formation of Mn-ions due to excitons or charge carriers which are not bound to Coulomb-defects

A polaron can be described with a wave function Φ using envelope function approximation [Wol88] as a product of :

$$\Phi = \Psi(\vec{r})u_0(\vec{r})X(\vec{J}, \vec{S}_i) \quad (\text{A.12})$$

with

- $\Psi(\vec{r})$: slowly varying envelope function defined by the non-lattice-periodic localization potential
- $u_0(\vec{r})$: lattice periodic band edge Bloch function
- $X(\vec{J}, \vec{S}_i)$: spin function

This function expresses the localized charge carrier with angular momentum \vec{J} and location \vec{r} interacting with an ensemble of Mn-ions (Spin \vec{S}_i location \vec{R}_i). From the coupled SCHRÖDINGER equation for polarons $\Psi(\vec{r})$ and $X(\vec{J}, \vec{S}_i)$ can be determined separately.

A formal description of a donor-bound magnetic polaron is given in [Wol88] using the wave function above:

$$\left\{ \frac{p^2}{2m^*} - \frac{e^2}{4\pi\epsilon\epsilon_0 r} - \alpha \sum_i \langle X | (\vec{J}\vec{S}_i) | X \rangle \delta(\vec{r} - \vec{R}_i) \right\} \Psi(\vec{r}) = E\Psi(\vec{r}) \quad (\text{A.13})$$

$$- \alpha \sum_i \left[(\vec{J}\vec{S}_i) |\Psi(\vec{R}_i)|^2 \right] X(\vec{J}, \vec{S}_i) \equiv H_{exch} X(\vec{J}, \vec{S}_i) = (E - E_0) X(\vec{J}, \vec{S}_i) \quad (\text{A.14})$$

$$E_0 = \int \Psi^*(\vec{r}) \left(\frac{p^2}{2m^*} - \frac{e^2}{4\pi\epsilon\epsilon_0 r} \right) \Psi(\vec{r}) d^3r \quad (\text{A.15})$$

The s/p-d exchange Hamiltonian for localized band states (described by an envelope function) $\Psi(\vec{r})$ can then be expressed by

$$H_{exch} = -\alpha \sum_i |\Psi_e(\vec{r})|^2 \vec{S}_i \vec{J}_e \quad \text{for electrons} \quad (\text{A.16})$$

$$H_{exch} = -\frac{1}{3}\beta \sum_i |\Psi_h(\vec{r})|^2 \vec{S}_i \vec{J}_h \quad \text{for holes} \quad (\text{A.17})$$

As a result the exchange interaction of a charge carrier with a single spin depends on the probability of the charge carrier to be at the location \vec{R}_i of this Mn-ions. These two operators act only on the spin function $X(\vec{J}, \vec{S}_i)$.

Due to the huge number of individual spin states, the properties of the polaron are described by an ensemble average. Now self consistent solutions for $\Psi(\vec{r})$ can be found by minimizing the free energy with respect to $\Psi(\vec{r})$ ³. At the formation of BMP the wave function is shrinking and thus decreasing the free energy but the main influence

³A detailed analysis solving the above equations is given in [Wol88]

of the expansion of the wave function is the Coulomb potential. In contrast during the formation of a LMP the wave function of the exciton is shrinking strongly because the localized potential (roughness of the band edge) is weak.

The dynamic of the polaron formation is dependent on the *polaron formation time* τ_f and on the *exciton recombination time* τ_X . Depending on the Mn-concentration the τ_X is 180ps at x=12% and 480ps at x=33% while τ_f is decreasing simultaneously from 125ps to 55ps [MOY+94].

For bulk material in general:

Increasing temperature weakens the alignment of Mn-spins by charge carriers. An external field aligns the Mn-spins in the whole sample so that the contribution of the additional spin polarization by excitons or holes is more and more decreasing with increasing external magnetic field. For these reasons the temperature or an external magnetic field suppress the magnetic polaron effect.

2D magnetic polarons In quantum wells with a strong anisotropic character, two different phenomena of the (2D) magnetic polarons for extreme B-field directions (in-plane and out of plane) are shown in Figure A.3. In the case of an applied external B-field in growth direction (i.e. Faraday geometry) the polaron energy shows the same behaviour like in bulk material with increasing B-field. However in Voigt geometry (i.e.

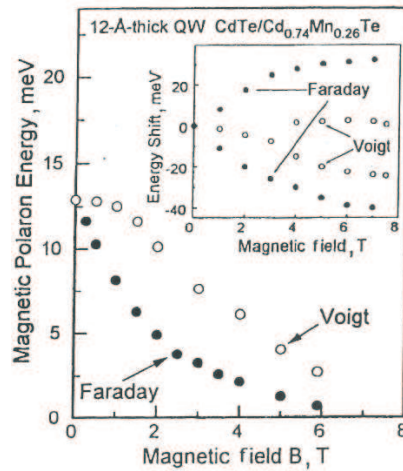


Figure A.3: [KMY98]: "Anisotropy of the depression of the two-dimensional magnetic polaron by an external magnetic field. Inset shows the spin splittings of states of the free exciton formed by a 2D electron and a heavy hole in a magnetic field perpendicular to the quantum-well plane (Faraday geometry) and in an in-plane magnetic field (Voigt geometry)"

B-field || QW plane) the "suppression" of the polaron by the applied magnetic field is much smaller than in Faraday geometry. Even at high B-fields the polaron effect is detectable, especially at extreme anisotropic QWs [MOY+95].

To get an easier access to the formal description of these phenomena I.A. MERKULOV and K.V.KAVOKIN ([MK95]) made the assumption that the 2D polaron in a magnetic field can be described by an anisotropic g-factor which represents the anisotropy of the VB. Thus, also the anisotropy of the VB in Voigt geometry can be expressed by an

anisotropic g-factor. In this case the strong polaron effect in Voigt geometry does not need to be described by an additional polarization of the Mn^{2+} -spins in the charge carrier environment. Instead it can be seen as a reorientation of the Mn^{2+} -spins in a direction which is not parallel to the external B-field followed but permitting a reduction in energy of the system.

For the case of total anisotropy of the VB-states discussed in subsection 2.3.3 and an external B-field along z-direction, equation (A.14) can be written:

$$H = \sum_i g_{Mn} \mu_B \vec{S}_i \vec{B}_{ext} - \frac{\beta}{3} \sum_i \left[(\vec{J} \vec{S}_i) |\Psi(\vec{R}_i)|^2 \right] \quad (\text{A.18})$$

The first term represents the influence of the external B-field on the Mn^{2+} -spin within the localized hole volume (Zeeman term). The second one is the exchange interaction of hole and the Mn^{2+} -spin. This Hamiltonian describes the precession of periodic energy transfer among polaron energy and Zeeman energy which can only take place by anisotropy in an external B-field. Using the eigenvalues of the HHs $J_z = \pm 3/2$ the above equation converts to:

$$H = \sum_i g_{Mn} \mu_B \vec{S}_i \left(\vec{B}_{ext} + \vec{B}_{exch} \right) \quad (\text{A.19})$$

with the exchange field

$$\vec{B}_{exch}(\vec{R}_i) = - \frac{1}{g_{Mn} \mu_B} \frac{\beta}{3} \cdot |\Psi(\vec{R}_i)|^2 \vec{J} \quad (\text{A.20})$$

which describes the exchange interaction of HH and Mn^{2+} -spins.

In summary the exchange interaction among HHs and Mn^{2+} -spins is interpreted as an exchange field \vec{B}_{exch} . This exchange field is caused by the HH ($J_z = \pm 3/2$) at the location of the Mn^{2+} -spin \vec{S}_i and is oriented along the z-axis (i.e. the growth axis). The energy of the whole system is lowered due to the reorientation of the Mn^{2+} -spins along $\vec{B}_{eff} \equiv \vec{B}_{ext} + \vec{B}_{exch}$ (where $|\vec{B}_{eff}| > |\vec{B}_{ext}|$) during the polaron formation [MK95].

A.4 Bloch equations

The Bloch equations are macroscopic equations that are used e.g. to calculate the temporal development magnetization $\vec{M} = (M_x, M_y, M_z)$ with specific relaxation times T_1 and T_2 . These are phenomenological equations that are used e.g. in **N**uclear **M**agnetic **R**esonance or **E**lectron **S**pin **R**esonance. According to [EBW04] ([Sli96] [Blo46]), the equations of motion of nuclear magnetization can be written in a general form:

$$\frac{d}{dt} \vec{M}(t) = \gamma \vec{M}(t) \times \vec{B}(t) - \bar{R} \cdot (\vec{M}(t) - \vec{M}_0) \quad (\text{A.21})$$

with

$$\bar{R} = \begin{pmatrix} 1/T_1 & 0 & 0 \\ 0 & 1/T_2 & 0 \\ 0 & 0 & 1/T_2 \end{pmatrix} \quad (\text{A.22})$$

which assumes $\vec{B}(t) = (B, 0, 0)$.

- T_1 : longitudinal/spin-lattice relaxation time
- T_2 : transversal/spin-spin relaxation time ($T_2 > T_1$) [Sli96]
- \vec{M}_0 : thermal equilibrium magnetization of the static susceptibility χ_0 and the static magnetic field \vec{B}_0 ($\vec{M}_0 = \chi_0 \cdot \vec{B}_0$)

With no relaxation (i.e. $T_1, T_2 \rightarrow \infty$) the above equations simplify to the equation for Larmor precession of the magnetization \vec{M} in an external magnetic field $B(t)$. Thus $\vec{R} \cdot (\vec{M}(t) - \vec{M}_0)$ are called the relaxation terms.

Under the conditions shown in Figure 2.18 $\vec{B}(t)$ can be expressed:

$$\vec{B}(t) = \vec{B}_{eff} = \vec{B} + \vec{b}_{hi}(t) = \begin{pmatrix} B \\ 0 \\ b_{hi}(t) \end{pmatrix} \quad (\text{A.23})$$

where $B \gg b_{hi}$ and $\vec{M}_0 = (M_{0x}, 0, M_{0z})$. Now the BLOCH equations can be rewritten:

$$\begin{aligned} \dot{M}_x &= \gamma M_y b_{hi}(t) - \frac{M_x - M_{0x}(B)}{T_1} \\ \dot{M}_y &= \gamma M_z B - M_x b_{hi}(t) - \frac{M_y}{T_2} \\ \dot{M}_z &= -\gamma M_y B - \frac{M_z - M_{0z}}{T_2} \end{aligned} \quad (\text{A.24})$$

For the case $B \gg b_{hi}$ follows that $\gamma M_y b_{hi}(t)$ in (A.24) can be neglected and in the stationary state $\dot{M}_x = 0$. Thus it can be compared to (2.95):

$$\begin{aligned} M_x &= M_{0x} \Leftrightarrow s_{ix} = s_{0x}(B) \\ \dot{M}_y &= \gamma M_z B - M_x b_{hi}(t) - \frac{M_y}{T_2} \Leftrightarrow \dot{s}_{iy} = B s_{iz} - b_{hi}(t) s_{ix} - \frac{s_{iy}}{T_2} \\ \dot{M}_z &= -\gamma M_y B - \frac{M_z - M_{0z}(b_{hi}(t))}{T_2} \Leftrightarrow \dot{s}_{iz} = -B s_{iy} - \frac{s_{iz} - s_{0z}[b_{hi}(t)]}{T_2} \end{aligned} \quad (\text{A.25})$$

A.5 Auxiliary calculations for KAVOKIN PRB 59 p. 9822 1999

A.5.1 Differential equation of \vec{s}_i

Given: Again, the mean fields are expressed by:

$$\text{Mean field of holes: } \vec{b}_{hi}(t) = a |\psi_h(z_i)|^2 \vec{j} \quad (\text{A.26})$$

$$\text{Mean field of Mn-ions: } \vec{B}^I(t) = a \sum_i |\psi_h(z_i)|^2 \vec{s}_i \quad (\text{A.27})$$

According to Figure 2.18 the following ratio is valid:

$$\frac{s_{0z}(b_{hi})}{s_{0x}(B)} = \frac{b_{hi}}{B} \quad (\text{A.28})$$

Furthermore:

$$j(t) = j[B_z^I(t)] \quad (\text{A.29})$$

and

$$W \equiv \sum_i |\psi_h(z_i)|^4 \quad (\text{A.30})$$

z-component

$$\begin{aligned} \dot{s}_{iz} &= -Bs_{iy} - \frac{s_{iz} - s_{0z}[b_{hi}(t)]}{T_2} \left| *a |\psi_h(z_i)|^2, \sum_i \right. \quad (\text{A.31}) \\ a \sum_i |\psi_h(z_i)|^2 \dot{s}_{iz} &= -aB \sum_i |\psi_h(z_i)|^2 s_{iy} \\ &\quad - \frac{a \sum_i |\psi_h(z_i)|^2 s_{iz} - a \sum_i |\psi_h(z_i)|^2 s_{0z}[b_{hi}(t)]}{T_2} \end{aligned}$$

Using now (A.27), (A.28), (A.30) and (A.29) one ends up with

$$\dot{B}_z^I = -BB_y^I - \frac{1}{T_2} \left[B_z^I - a^2 \cdot W \cdot s_{0x}(B) \cdot \frac{j(B_z^I)}{B} \right] \quad (\text{A.32})$$

y-component

$$\begin{aligned} \dot{s}_{iy} &= Bs_{iz} - b_{hi}(t)s_{ix} - \frac{s_{iy}}{T_2} \left| *a |\psi_h(z_i)|^2, \sum_i \right. \quad (\text{A.33}) \\ a \sum_i |\psi_h(z_i)|^2 \dot{s}_{iy} &= a \sum_i |\psi_h(z_i)|^2 Bs_{iz} - a \sum_i |\psi_h(z_i)|^2 b_{hi}(t)s_{ix} \\ &\quad - \frac{a \sum_i |\psi_h(z_i)|^2 s_{iy}}{T_2} \end{aligned}$$

Using (A.26), (A.27), (A.30) and $s_{ix} = s_{0x}(B)$ it can be written:

$$\dot{B}_y^I = BB_z^I - a^2 \cdot W \cdot s_{0x}(B) \cdot j(B_z^I) - \frac{B_y^I}{T_2} \quad (\text{A.34})$$

A.5.2 Stationary State with one solution

Due to the stationary states of the spin system $B_y^I = 0$, (2.99) leads to:

$$B_z^I = a^2 W \frac{s_{0x}(B)}{B} j(B_z^I) \quad (\text{A.35})$$

and

$$\frac{dB_z^I}{dB} = a^2 W \left[\left(\frac{1}{B} \cdot \frac{ds_{0x}(B)}{dB} - \frac{s_{0x}(B)}{B^2} \right) j(B_z^I) + \frac{s_{0x}(B)}{B} \frac{dj(B_z^I)}{dB} \right] \quad (\text{A.36})$$

(A.35) has only one solution for $B_z^I = 0$. The borderline case $B_z^I = 0$ corresponds to an applied strong magnetic field along the x-axis with the consequence of totally aligned Mn^{2+} -spins in x-direction. Thus the susceptibility of the equilibrium spin-density of Mn-ions⁴ $\frac{ds_{0x}(B)}{dB}$ converges to very small values.

$$\left. \frac{dB_z^I}{dB} \right|_{B_z^I=0} = a^2 W \left[\underbrace{\left(\frac{1}{B} \cdot \frac{ds_{0x}(B)}{dB} - \frac{s_{0x}(B)}{B^2} \right)}_{\kappa < 0} j(B_z^I) + \frac{s_{0x}(B)}{B} \frac{dj(B_z^I)}{dB} \frac{dB_z^I}{dB} \right] \Bigg|_{B_z^I=0} \quad (\text{A.37})$$

Dividing both sides of (A.37) by its left-hand side, it follows:

$$1 = a^2 W \left[\kappa j(B_z^I) \left(\left. \frac{dB_z^I}{dB} \right|_{B_z^I=0} \right)^{-1} + \frac{s_{0x}(B)}{B} \frac{dj(B_z^I)}{dB} \right] \Bigg|_{B_z^I=0} \quad (\text{A.38})$$

Now, the more the external B-field is increased the more Mn-ions are aligned by following a Brillouin-function i.e. B_z^I converges to a constant value and $\left. \frac{dB_z^I}{dB} \right|_{B_z^I=0} \geq 0$ thus the first term in (A.37) is negative resulting in the already presented equation (2.100):

$$\zeta = a^2 \cdot W \cdot \frac{s_{0x}(B)}{B} \cdot \left. \frac{dj(B_z^I)}{dB_z^I} \right|_{B_z^I=0} \leq 1$$

Concluding that this equation has only one solution under these circumstances.

⁴following a Brillouin-like function

A.6 QW Exciton spins in an external B-field

In this appendix section two types of schematic spin presentations of an exciton in an external magnetic field in Faraday geometry are introduced. Figure A.4a presents the individual spin presentation of the exciton only concerning the HH-states. The two spin sub bands are labelled as $+3/2$ for the spin-up holes and $-3/2$ for the spin-down holes corresponding to the normal momentum of holes (not electrons) in the VB. Due to this convention, a σ^+ -transition involves the creation of a $-1/2$ electron ($m_J = -1/2$) and of a $+3/2$ heavy hole ($m_J = -3/2$) and a σ^- -transition vice versa [KCF⁺99].

The optical transitions σ^+ and σ^- with the corresponding net spins and the corre-

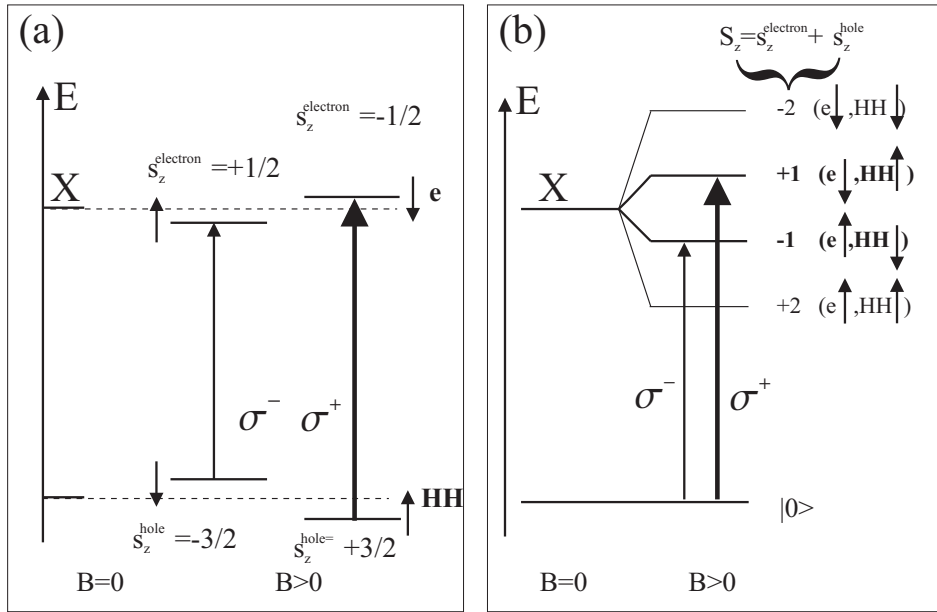


Figure A.4: Schematic diagram of the exciton spin splitting including the allowed optical transitions in an external B-field in Faraday geometry. Figure (a) shows the electron spins and heavy hole spins of the exciton separately [KCF⁺99]. Figure (b) shows the net spin of the exciton of both the allowed optical transition $S_z = s_z^{electron} + s_z^{hole} = \pm 1$ and the optical "forbidden" net spin states $S_z = \pm 2$.

	$\Delta m_J = m_J^{final} - m_J^{initial}$	$S_z = s_z^{electron} + s_z^{hole}$	m_J^{final}	$m_J^{initial}$	$s_z^{electron}$	s_z^{hole}
σ^+	+1	+1	-1/2	-3/2	-1/2	+3/2
σ^-	-1	-1	+1/2	+3/2	+1/2	-3/2

Table A.1: Optical transitions in Faraday geometry with the net-spins and their corresponding z-component of their total angular momentum.

sponding total angular momentum of the involved electron and hole are presented in Table A.1. s_z^{hole} and its corresponding m_J change their algebraic sign under the convention above. The energetic position depending on the spin-state (i.e. if the energy of spin-up level is higher than of the spin-down level or vice versa) is chosen here arbitrarily. This positioning is dependent on the character of the QW (e.g.: strained grown layers) and is defined by the algebraic sign of the band-electron (-hole) g-factor.

Appendix B

Formality

Danksagung

An dieser Stelle möchte ich mich herzlichst bei allen bedanken, die mich im Rahmen dieser Arbeit unterstützt und gefördert haben. Mein Dank gilt:

- meinem Doktorvater Prof. Dr. Jean Geurts für die Möglichkeit, in seiner Arbeitsgruppe meine Dissertation anfertigen zu können, für seine Unterstützung, die fruchtbaren Diskussionen und die kollegiale Atmosphäre in seiner Arbeitsgruppe. "Dank u wel!!!"
- dem Lehrstuhlinhaber für Experimentelle Physik III Herrn Prof. Dr. Laurens Molenkamp für die Arbeitsmöglichkeit an seinem Lehrstuhl.
- der AG Geurts: Sven Issing, Utz Bass, Dr. Michael Lentze, Hedwig Müller, Sina Zapf und Franziska Fricke für die gute und kollegiale Zusammenarbeit, für ihre Zuverlässigkeit und die zahlreichen Diskussionen. Allen noch mal das größte auszusprechende fränkische Lob: DOCH!!!
- der AG Ossau: Prof. Dr. Wolfgang "Sepp" Ossau, Dr. Georgy Astakhov, Dr. Tobias Kießling und allen anderen AG-Mitglieder für die gute und unkomplizierte Kommunikation zwischen unseren Arbeitsgruppen, die Hilfsbereitschaft in technischer und fachlicher Hinsicht und die zahlreichen fruchtbaren Diskussionen. Besonderer Dank an Georgy für seine Betreuung, seine Beratung und die "Russian connections" nach St.Petersburg.
- Prof. Dr. Yuri Kusrayev und Dr. Kiril Kavokin (IOFFE Physical Technical Institute, St Petersburg, Russian Federation) für die fruchtbaren Diskussionen, die Unterstützung und die Bereitstellung der theoretischen Grundlagen und Interpretationen im Rahmen dieser Arbeit.
- Prof. Dr. Grzegorz "Greg" Kraczewski (Institute of Physics PAS, Warsaw, Poland) für die Bereitstellung der Proben und die vielen hilfreichen und fruchtbaren Diskussionen.
- Herrn Dr. Claus Schumacher für die interessanten Diskussionen und die guten Ratschläge.
- dem Freistaat Bayern für der finanzielle Förderung durch das Promotions-Stipendium nach dem Bayerischen Eliteförderungsgesetz und die finanzielle Unterstützung für die Konferenzteilnahme an der "14th International Conference on II-VI Compounds" im August 2009 in St. Petersburg.
- unserer Lehrstuhlsekretärin Anja Brück für die bürokratische Hilfe.
- "Mr. Helium-Verflüssiger" Roland Ebert für die stete und zuverlässige Bereitstellung von Helium, den technischen Rat v.a. bzgl. unseres Kryostaten und seine generelle Hilfsbereitschaft.

- der Mechanikwerkstatt für die schnelle Bearbeitung meiner Aufträge.
- meinen Studienkollegen und Freunden für die vielen unvergessenen interdisziplinären Diskussionen.
- meiner Freundin für die Unterstützung und das Verständnis während der ganzen Arbeit.
- ganz besonders meinen Eltern und Großeltern, die mir das Physik-Studium und das Promotions-Studium ermöglicht und mich in jeder Lebenslage unterstützt haben.

Allen noch einmal ein herzliches "Vergelt's Gott!".

Publications and conferences

- *Observation of the magnetic soft mode in (Cd,Mn)Te quantum wells using spin-flip Raman scattering*, C. Kehl, G. V. Astakhov, K. V. Kavokin, Yu. G. Kusrayev, W. Ossau, G. Karczewski, T. Wojtowicz, J. Geurts, Phys. Rev. B 80, 24, p241203, 2009, DOI:10.1103/PhysRevB.80.241203
- *"Laser controlled magnetization in bulk Zn_{1-x}Mn_xTe"* ;Le Van Khoi, A. Avdonin, R.R. Galazka, M. Lentze, C.Kehl, J. Geurts, M. Eyring, G. Astakhov, W. Ossau; phys. stat.sol. (b), 1-5(2007)/DOI 10.1002/pssb.200675131
- *"Raman scattering by phonons and electronic excitations in In(Ga)As/Al(Ga)As quantum dot structures"*; A. Milekhin, A. Toropov, A. Bakarov, C. Kehl, M. Lentze, J. Geurts, D. Zahn; Beitrag zur Konferenz, "PHONONS 2007, Paris"
- *"Magneto-optic photoluminescence and Spin-Flip-Raman-spectroscopy on Cd_{1-x}Mn_xTe/Cd_{1-y}Mg_yTe quantum well samples"*, Beitrag zur Konferenz, Frühjahrstagung der Deutschen Physikalischen Gesellschaft 2008
- *"Influence of photo-generated carriers on the Mn-Spins in CdMnTe Quantum Well studied by Spin-Flip-Raman-Spectroscopy"*, Beitrag zur "International Conference on the Physics of Semiconductors" (ICPS) im Juli 2008 in Rio de Janeiro
- *"Influence of photo-generated carriers on the Mn-Spins in CdMnTe Quantum Wells studied by Spin-Flip-Raman Spectroscopy in a Two-Colour Experiment"*, Beitrag zur "14th International Conference on II-VI Compounds" im August 2009 in St. Petersburg (finanziell gefördert vom Stipendium nach dem Bayerischen Eliteförderungsgesetz)
- *"Influence of photo-generated carriers on the Mn-Spins in CdMnTe Quantum Wells studied by Spin-Flip-Raman Spectroscopy in a Two-Colour Experiment"*, Beitrag zum "Symposium Spin Manipulation in Solid State Systems" im Oktober 2009 in Würzburg

Lebenslauf

Zur Person

Christian Kehl
geboren: 04.10.1979
Geburtsort: Werneck
Familienstand: ledig

Julius-Maximilians Universität Würzburg	2000 - 2010
<u>Promotion in Physik</u>	
Angestellt an der Universität Würzburg	seit 01.11.2009
Promotionsförderung durch das Stipendium nach dem Bayerischen Elite Förderungsgesetz (BayEFG)	Nov.2006-Okt.2009
Beginn der Promotion in Physik	seit Juni 2006
<u>Diplomstudium Physik</u> <i>Diplom-Physiker Univ.</i> Diplomarbeit <i>"Raman-spektroskopische Untersuchung der Gitterschwingungen von dotiertem $Zn_{1-x}Mn_xTe$ und $Zn_{1-x}Cr_xSe$"</i>	verliehen am 19.06.2006 Abgabe 09.06.2006
<u>Industriepraktikum: INFINEON technologies</u> <i>"Communications Fiber Optics Development Gloss on Silicon"</i>	02.09.2002-25.10.2002
Diplom-Vorprüfung	26.08.2002
Studienbeginn	01.10.2000

Auslandstudium	2003-2004
Heriot-Watt University Edinburgh/ Scotland	
Abschluss	13.07.2004
<i>Master of Physics in Optoelectronics and Lasers with Honours of the First Class</i>	
Beginn	28.09.2003
Grundwehrdienst	01.09.1999-30.06.2000
AVZ 1.Pz.Gren.Btl. 352 Mellrichstadt AGA 1.Pz.Art.Btl. 355 Wildflecken	
Regiomontanus-Gymnasium Hassfurt	1990-1999
Abitur	25.06.1999

Würzburg,

(Christian Kehl)

Ehrenwörtliche Erklärung

gemäß § 5 Abs. 1 Ziff. 2, 3 und 5
der Promotionsordnung der
Fakultät für Physik und Astronomie
der Universität Würzburg

Hiermit erkläre ich ehrenwörtlich, dass ich die Dissertation selbständig und ohne Hilfe eines kommerziellen Promotionsberaters angefertigt und keine anderen als die angegebenen Quellen und Hilfsmittel benutzt habe.

Die Dissertation wurde bisher weder in gleicher noch in anderer Form in einem anderen Prüfungsfach vorgelegt.

Am 19. Juni 2006 wurde mir von der Julius-Maximilians-Universität Würzburg der akademische Grad
Diplom-Physiker Univ.
verliehen.

Des Weiteren wurde mir am 13. Juli 2004 von der Heriot Watt University in Edinburgh / Schottland der akademische Grad
Master of Physics in Optoelectronics Lasers with Honours of the First Class
verliehen.

Weitere akademische Grade habe ich weder erworben noch versucht zu erwerben.

Würzburg,

(Christian Kehl)